PRELIMINARY INTERPRETATIONS
— WORKSHOP #4 —

APPROACHES TO FAULT-DISPLACEMENT METHODOLOGY

E. Anderson, W. Arabasz, A. Ramelli

January 8, 1997

PREMISES

- **Probability of new faulting is negligible.**

- **An internally consistent approach to fault-displacement hazard can be developed based on "events" as "displacement happenings"—without characterizing size in terms of magnitude**

  ("What you see is what you get" approach)

- **Fractal, rock mechanics, empirical, and theoretical considerations dealing with fault populations can provide key guidance:**

  - **dip-slip faults are characteristically longer in strike-direction than dip direction (aspect ratios guide subsurface dip extent)**
  - **total cumulative displacement on a fault scales linearly with length**
  - **in theory, single-event slip scales linearly with rupture length (for constant stress drop), and nearly linearly in empirical relation of Wells & Coppersmith (1994)**
  - **from above, single-event slip should scale linearly with total cumulative displacement**

  ("Is this all the repository engineer needs to know?)

Sources of Displacement

Tectonic/ Structural Model

Sources of Primary Displacement

Geometry

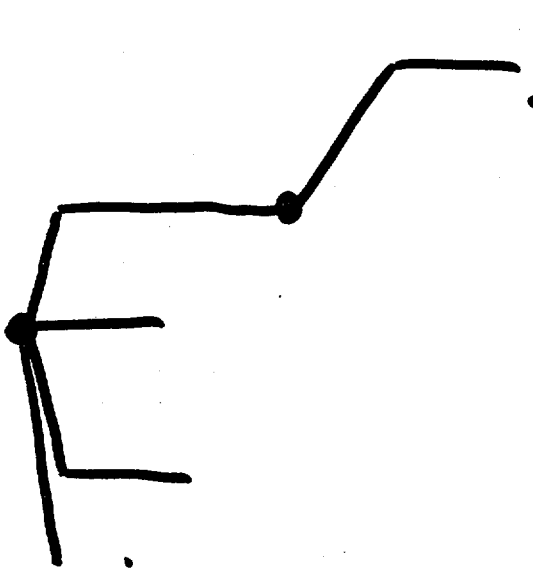

Solitario
Dune Wash ?
Bow Ridge ?
Iron Ridge
Fatigue Wash
Paintbrush/Stagecoach
Windy Wash
Crater Flat
Bare Mtn.
.
.
.

NOT SOURCES OF PRIMARY DISPLACEMENT

Ghost Dance
Sundance
Drill Hole Wash
Pagany Wash
Sever Wash

Pergamon

Journal of Structural Geology, Vol. 18, Nos 2/3, pp. 235 to 248, 1996

0191-8141/96 $15.00 + 0.00

0191-8141(96)00115-8

The shapes, major axis orientations and displacement patterns of fault surfaces

A. NICOL, J. WATTERSON, J. J. WALSH and C. CHILDS

Fault Analysis Group, Department of Earth Sciences, University of Liverpool, Liverpool L69 3BX, U.K.

(*Received* 9 *January* 1995; *accepted in revised form* 23 *August* 1995)

Abstract—Displacement contour diagrams constructed using seismic reflection data and coal-mine plans are analysed to establish the factors determining the dimensions, shapes and displacement patterns of normal faults. For blind isolated normal faults in layered sequences the average aspect ratio is 2.15, with sub-horizontal major axes. Earthquake slip-surface aspect ratios range from 0.5 to 3.5 and are independent of slip orientation. The principal control on the shape of blind isolated faults is mechanical anisotropy associated with rock layering, resulting in layer-parallel elongation of fault surface ellipses. Faults that intersect the free surface and/or interact with nearby faults have aspect ratios ranging from 0.5 to 8.4, and are referred to as restricted. Restriction of fault growth has various effects including: (i) reduced curvature of the tip-line and of displacement contours; and (ii) increased displacement gradients in the restricted region. Many faults are restricted at more than one place on their tip-line loop and so have highly irregular shapes and displacement patterns. Subsequent linkage of interacting faults produces combined faults with aspect ratios within the normal range for unrestricted faults. Lateral interaction between faults does not necessarily lead to a change in the power-law exponent of the fault population.

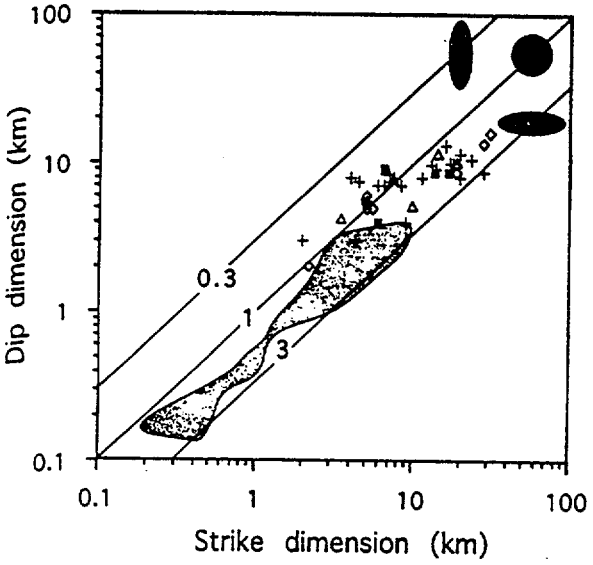

Fig. 4. Dip dimension vs strike dimension for 40 main-shock slip-surfaces as defined by aftershock loci, for normal dip-slip (filled squares), strike-slip (crosses), reverse dip-slip (open diamonds) and oblique-slip (open triangles) slip-surfaces associated with moderate magnitude (M = 4.2–6.8) events. Data sources are listed in Table 2. The field of nominal unrestricted faults in Fig. 3 is shown stippled. Straight lines correspond to aspect ratios of 0.3, 1.0 and 3.0.

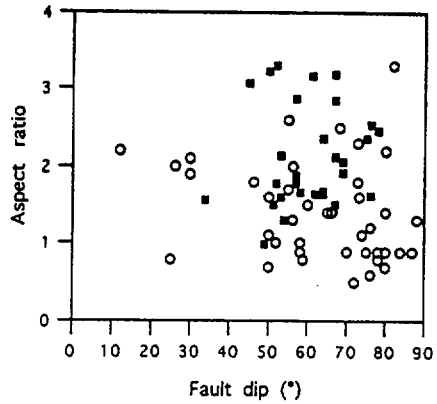

Fig. 5. Aspect ratio vs dip for unrestricted fault surfaces (filled squares) and earthquake main-shock slip-surfaces (open circles). Earthquake data sources are listed in Table 2.

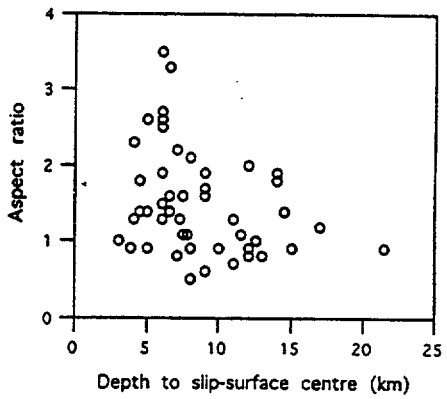

Fig. 6. Aspect ratio vs depth to the centre, for all earthquake slip-surfaces in Table 2.

NICOL ET AL. (1996) (CONT)

From their Table 2, ASPECT RATIOS OF MAINSHOCK SLIP SURFACES DEFINED BY AFTERSHOCK DISTRIBUTIONS

- ALL DATA N = 54, M = 4.2-6.8

  MEAN = 1.54 std dev = 0.67

- NORMAL-FAULTING EQ's

  MEAN = 1.56 std dev = 0.64

  N = 7, M = 4.2 - 6.0

- SURFACE-FAULTING EQ's

  N = 14, M = 5.6 - 6.7

  MEAN = 1.89 std dev = 0.65

ASPECT RATIO	FAULT LENGTH	FAULT WIDTH	DEPTH OF PENETRATION (DIP=60°)	
1.5	5	3.3	2.9	
	10	6.7	5.8	
	15	10	8.7	
→	20	13	12	←
	25	17	14	
	30	20	17	
2.0	5	2.5	2.2	
	10	5	4.3	
	15	7.5	6.5	
	20	10	8.7	
	25	12.5	10.8	←
→	30	15	13.0	

FAULT LENGTH TO PENETRATE TO, SAY, 12 KM

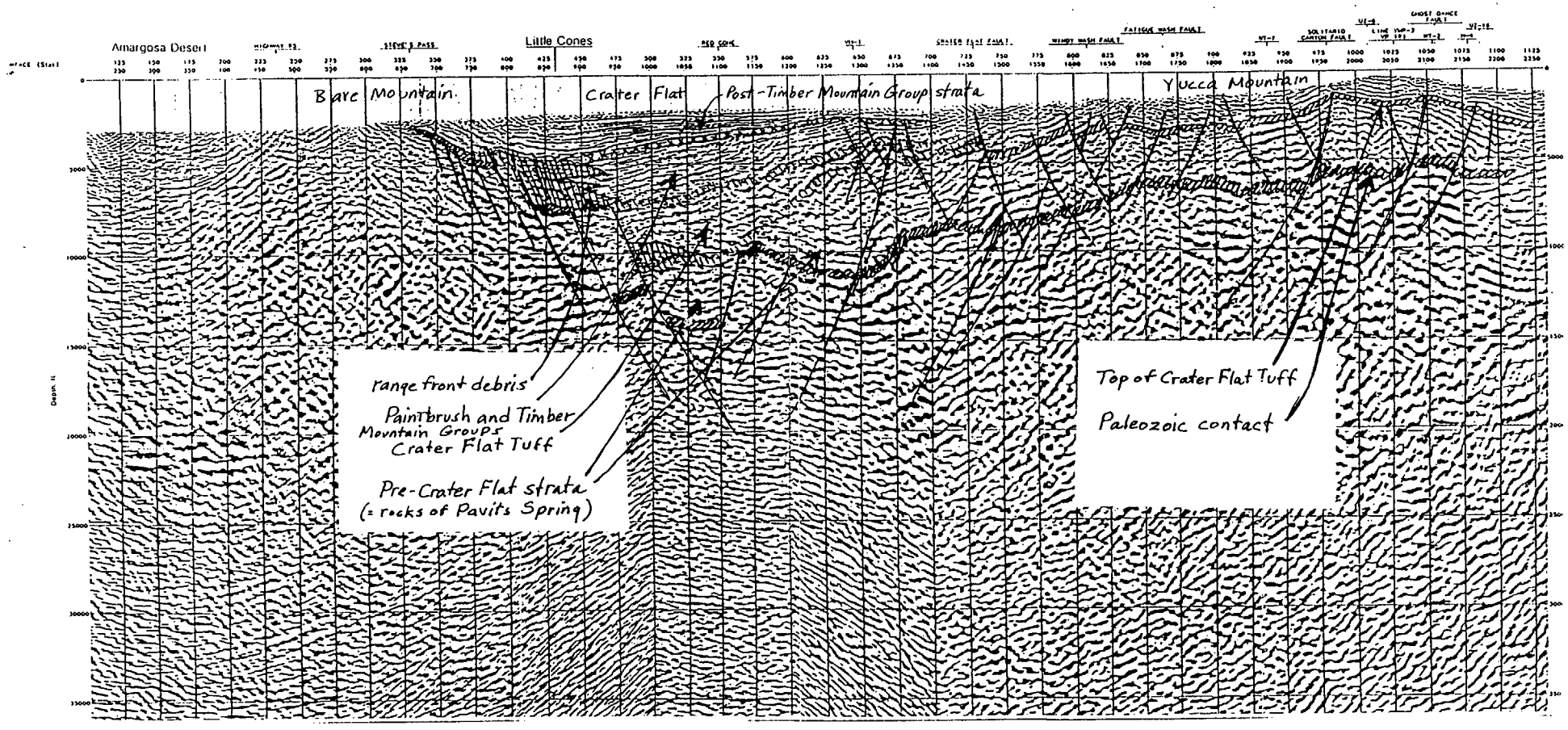

Figure 8.11. Western segment of Crater Flat seismic reflection profile (Brocher and others, 1966). See figure 8.6 for location. Interpretations shown here are for this report. Subvertical solid lines indicate faults.

FROM O'LEARY (CH. 8 OF SYNTHESIS REPT.)

1 Nm = 10^7 dyne-cm

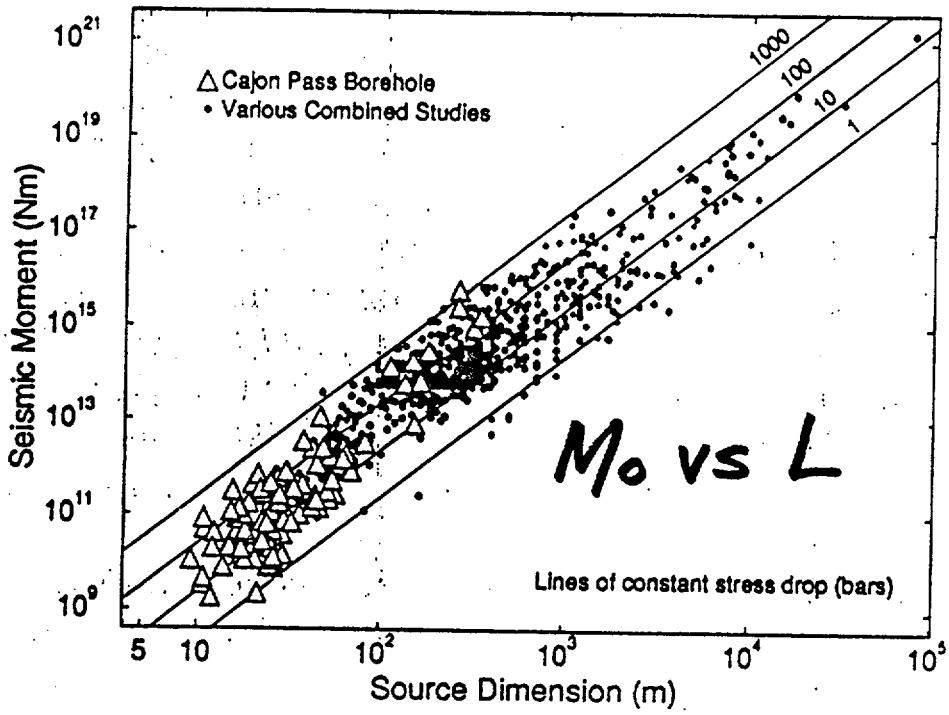

Figure 4. Scaling of seismic moment as a function of source size (log-log plot) after *Abercrombie* [1995], who also gives the original references for the combined studies indicated. The solid lines represent the scaling predicted at different stress drops (in bars) from a simple dislocation model for the seismic source. The high-resolution borehole data from the Cajon Pass borehole (open triangles) show no strong systematic difference from earthquake data at larger scales (solid circles) within the scatter of the data; i.e., there is no systematic "f_{max}" effect.

FROM MAIN (1996: REV. OF GEOPHYSICS, 34 (4), 433-462

$M_o \propto L^2$

For constant stress drop,

u (slip) $\propto$ L

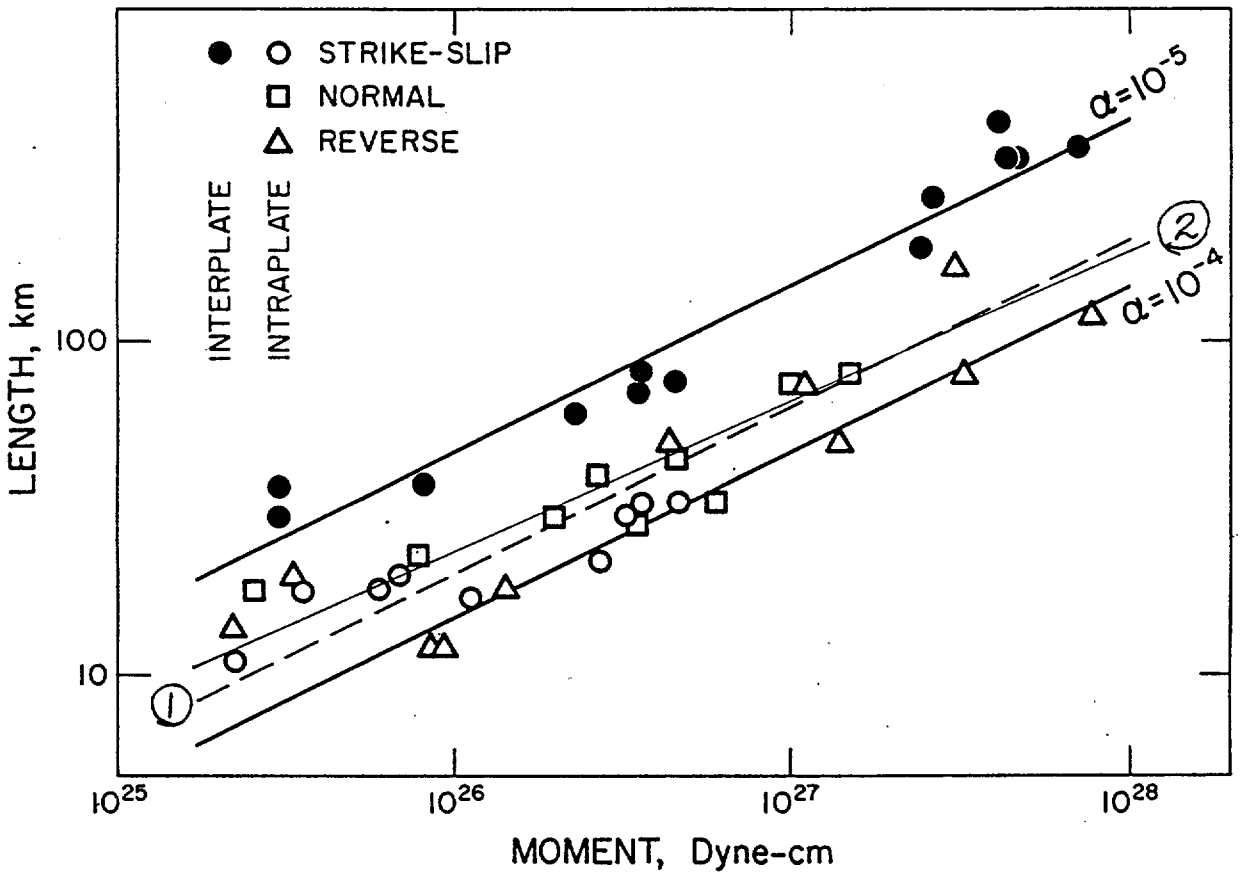

FIG. 1. Log fault-length versus log moment for large interplate and intraplate earthquakes.

FROM SCHOLZ ET AL. (1986: BULL. SEISMOL. SOC. AM., 76 (1), 65-70

$u = \alpha L$

u — slip

① = best-fit line by Scholz et al to large intraplate earthquakes

② = Wells & Coppersmith (1994)

$\log SRL = -3.22 + 0.69\,M$

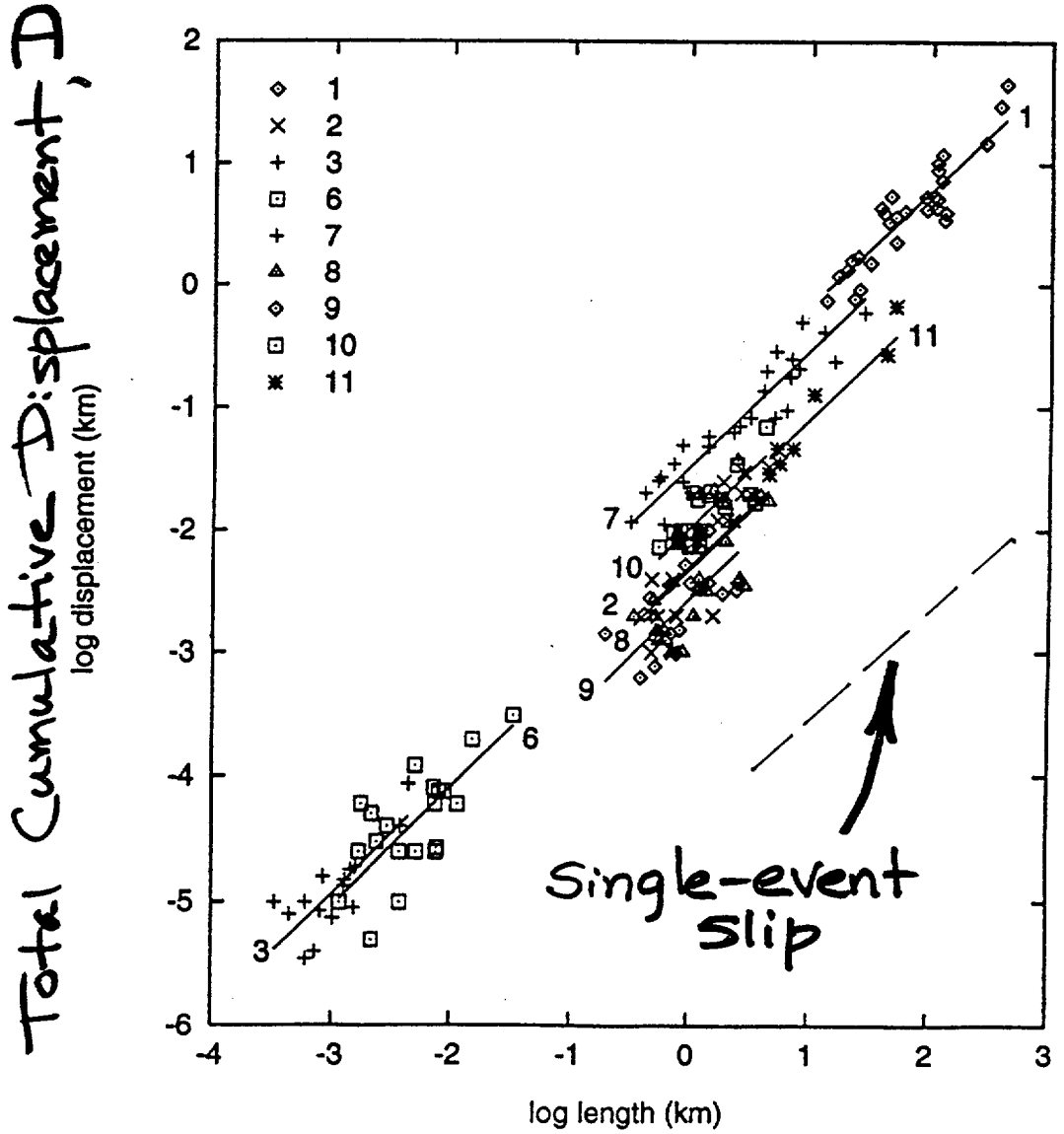

Fig. 1. Results of the combined analysis of nine data sets (lines), with the source data (symbols). Group numbers as in Table 1.

D & L [FROM CLARK & COX, 1996: J. Structural Geol. 18 (2/3), 147-152]

Single-event slip (Wells & Coppersmith, 1994)

$$\log(AD)_m = -1.43 + 0.88 * \log(SRL)_{km}$$

Scaling of single-event slip vs cumulative total displacement

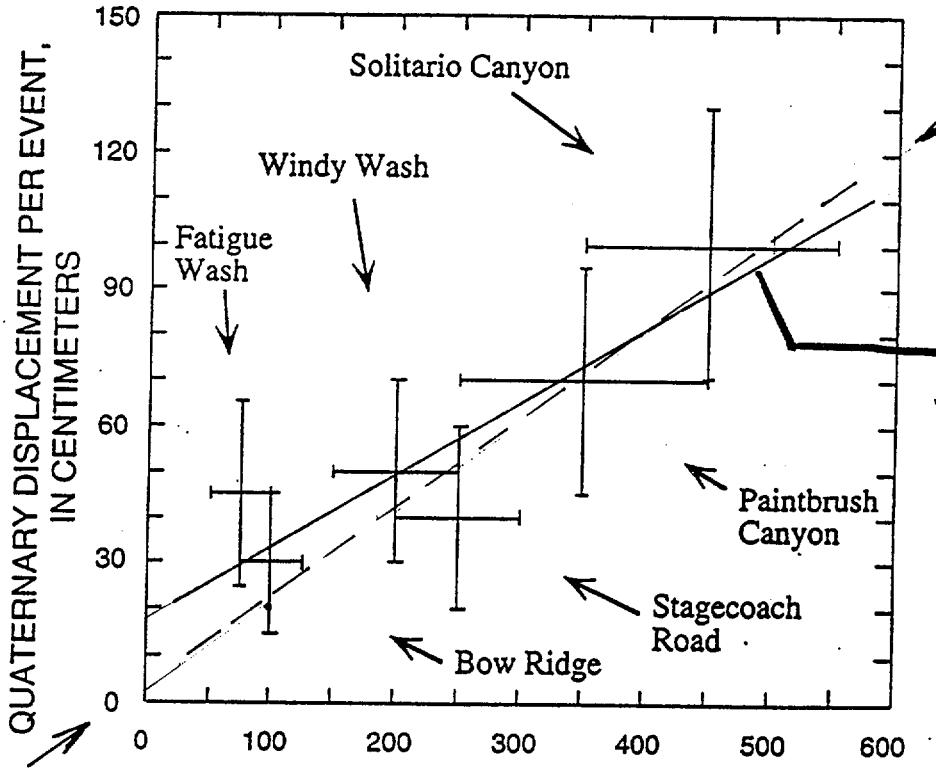

u

linear regression

D

dashed line predicted by simply assuming $u \propto D$ from previous figure (assumed rupture length = fault length)

Figure 9-20. Example of site-specific scaling relation between cumulative vertical slips and displacements per event for Yucca Mountain faults. The ranges of cumulative dip-slip displacement (in m) are plotted against Quaternary displacements per event (in cm).

10

Table 4-1. Fault lengths and throws for dip-slip faults of the Yucca Mountain region

Fault		Length (km)	Length Range (km)	Throw (km)	Throw Range (km)
Airport Lake	(P)	45.00	±15.00	0.550	±0.0500
Ash Hill	(P)	38.50	± 6.50	0.122	—
Bare Mountain	(P)	15.50	—	2.600	±0.200
Belted Range	(P)	46.00	±8.00	0.610	—
Bow Ridge	(P)	8.00	± 2.00	0.220	±0.0050
Carpetbag	(P)	23.25	± 6.75	0.600	—
Deep Springs	(P)	27.00	—	1.575	±0.050
Emigrant Peak	(P)	36.00	±10.00	0.654	±0.245
Ghost Dance	(P)	9.00	± 3.00	0.030	±0.015
Grapevine	(P)	25.00	± 5.00	4.270	—
Hot Creek Reveille	(P)	51.50	±21.50	0.458	—
Kawich Range	(P)	82.00	± 2.00	1.068	±0.153
Midway Valley	(S)	4.50	± 3.50	0.050	±0.010
Oak Springs	(P)	20.00	± 1.00	0.458	—
Paintbrush	(P)	20.00	±10.00	0.375	±0.120
Saline Valley	(P)	17.25	± 4.00	6.000	—
Solitario Canyon	(P)	12.50	± 0.50	1.000	—
Solitario Canyon	(S)	19.00	—	0.500	—
Stagecoach Road	(S,P)	15.00	11.00	0.75	±.25
Towne Pass	(P)	38.00	—	2.380	—
West Spring Mt.	(P)	45.00	±15.00	3.500	—
Windy Wash	(P)	19.50	± 5.50	0.040	—
Windy Wash	(S)	14.00	11.00	0.500	—
Yucca	(P)	31.00	± 9.00	0.450	±0.150
Yucca Lake	(P)	17.00	—	0.610	—

(P) Data from Piety (1996) and (S) Data from Simonds et al., (1995).

FROM MCKAGUE ET AL (MCKAGUE, L., J.A. STAMATAKOS, & D.A. FERRILL)
TYPE I FAULTS IN THE YUCCA MOUNTAIN REGION.

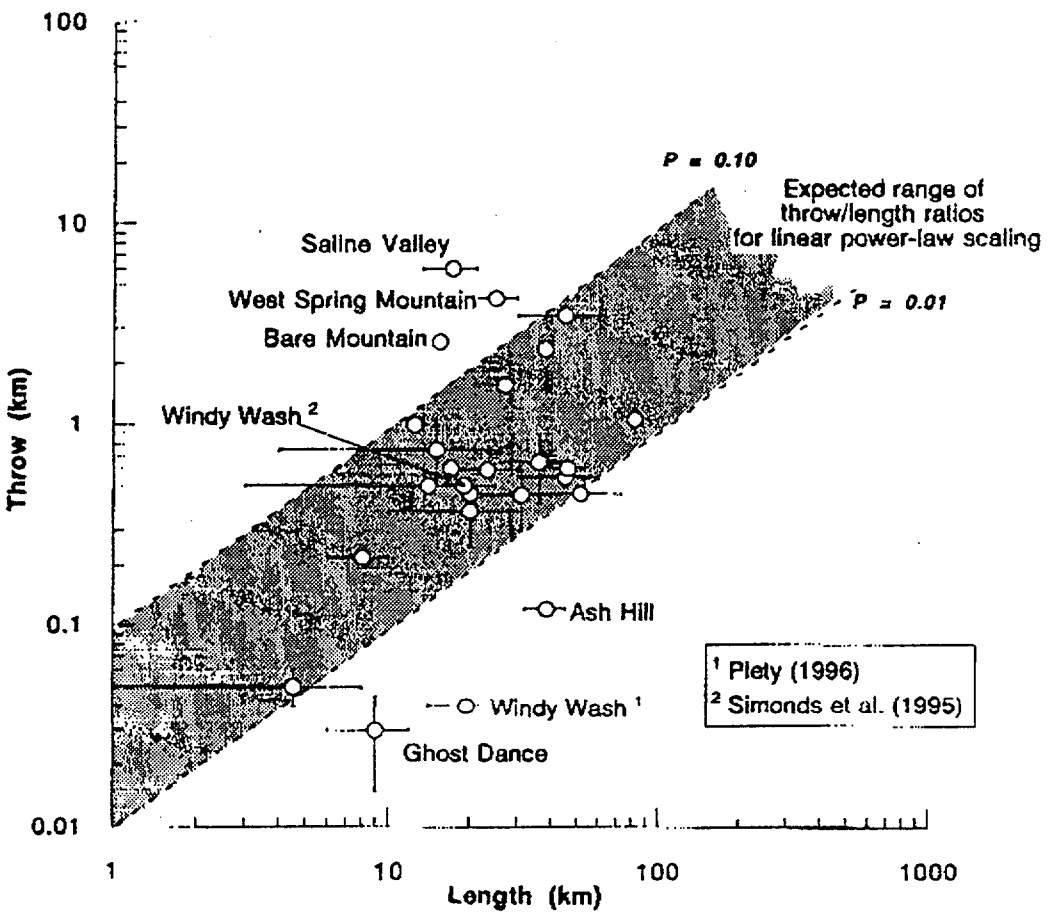

PLOT ACCOMPANYING TABLE ON PRECEDING PAGE FROM McKAGUE ET AL, CENTER FOR NUCLEAR WASTE REGULATORY ANALYSIS REPORT (1997)

MAXIMUM "EVENT" METHODOLOGY

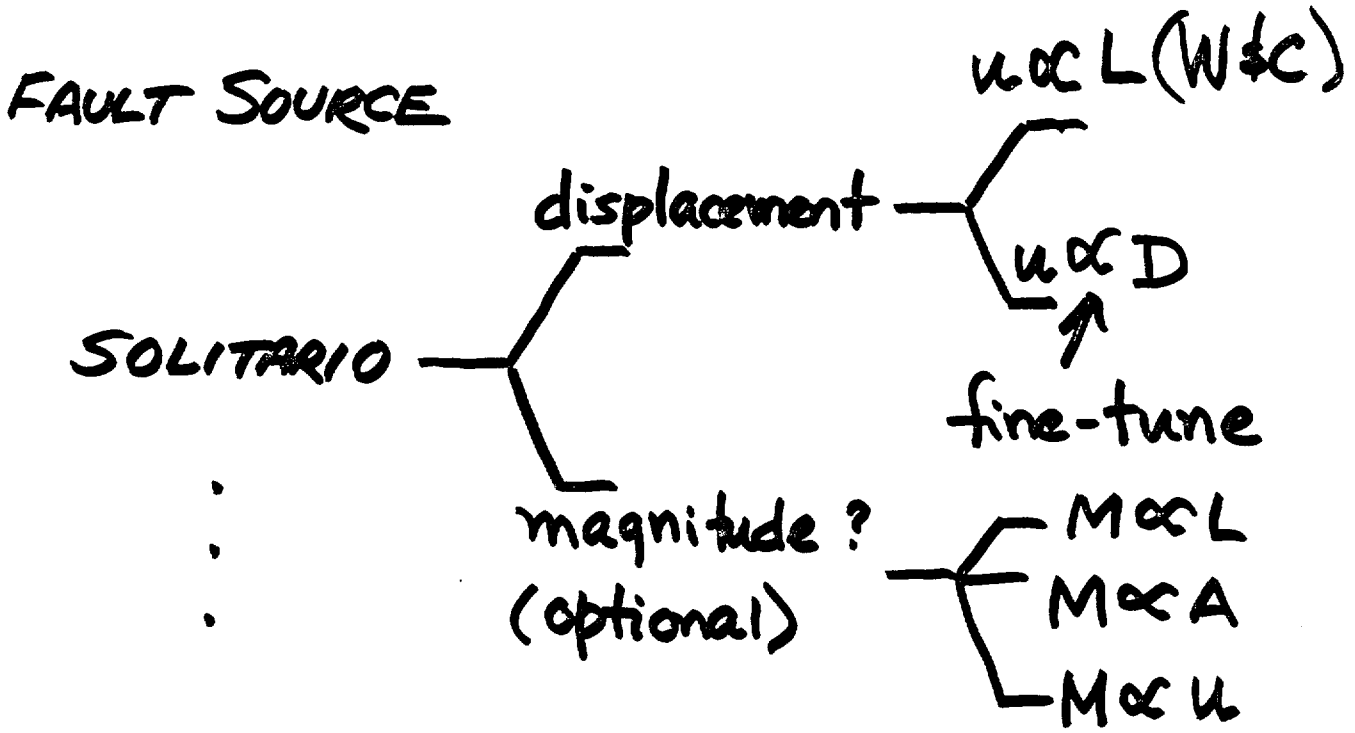

IN DISPLACEMENT APPROACH, TRACK BOTH AVG & MAX DISPLACEMENT

FREQUENCY OF PRIMARY RUPTURE EVENTS

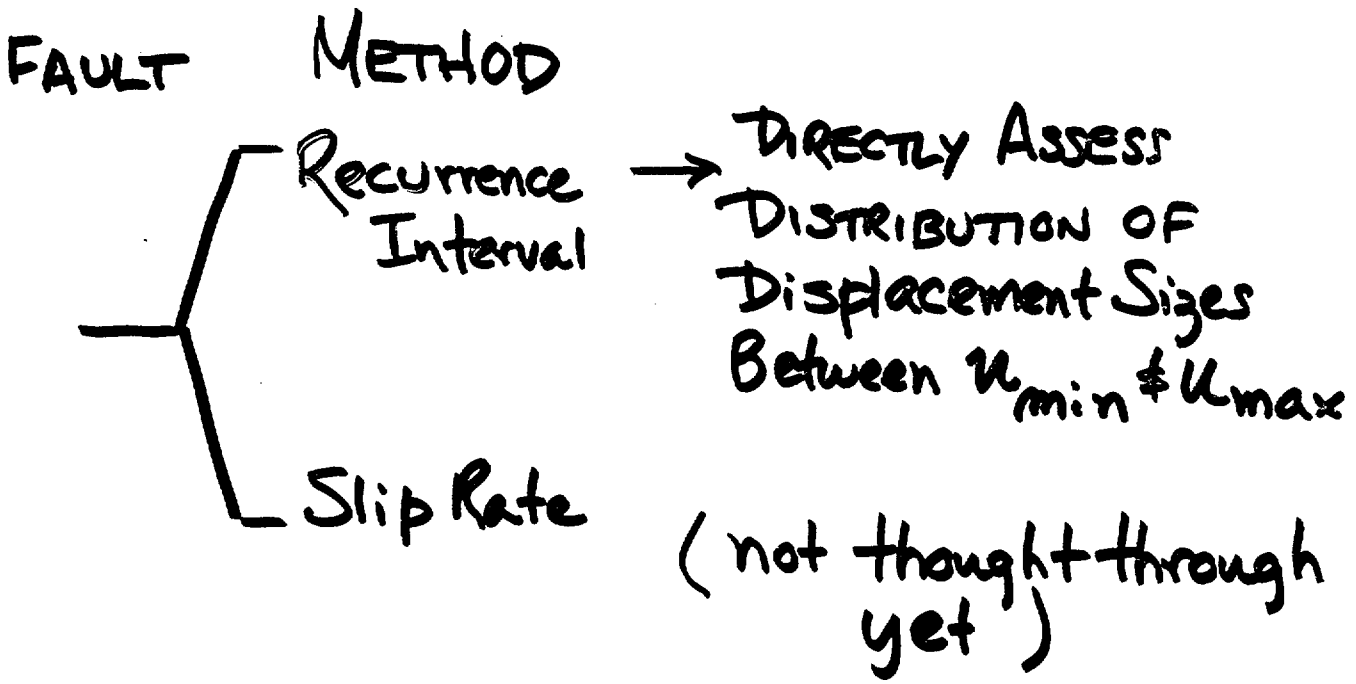

DISPLACEMENT WITHIN REPOSITORY

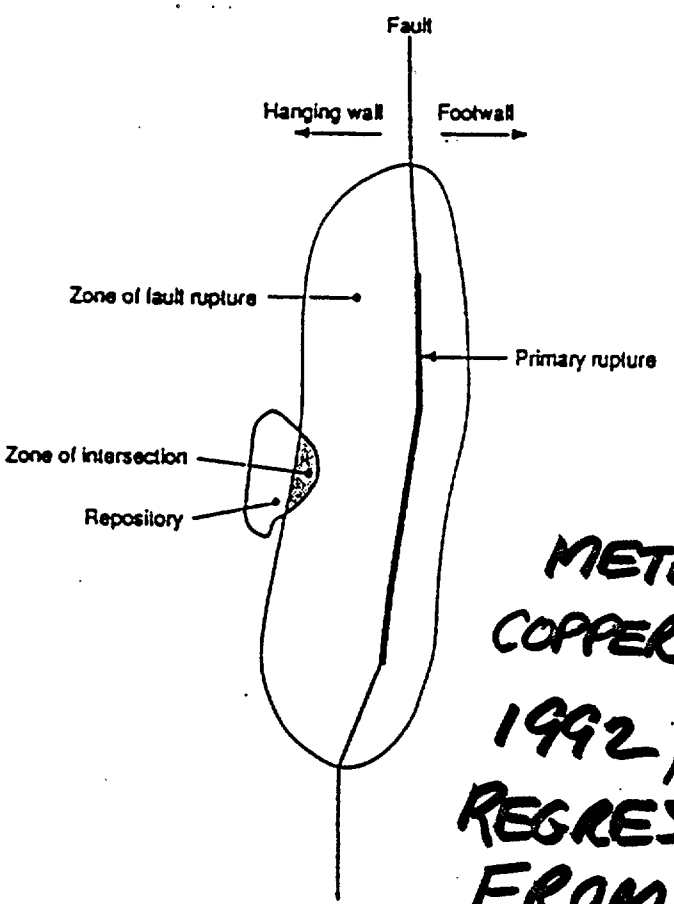

FOLLOW METHODOLOGY OF COPPERSMITH & YOUNGS 1992, ADDING REGRESSION INFO. FROM CH. 9 FOR

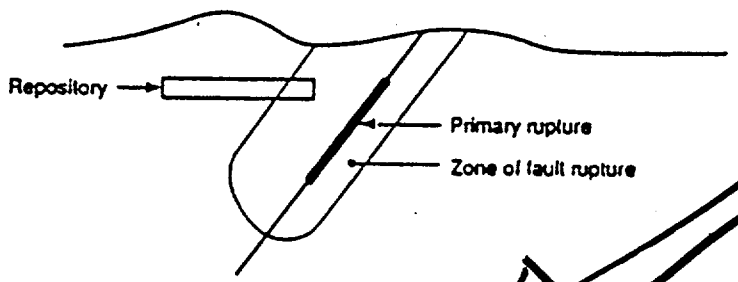

- max width of surface rupture zone
- max displacement within repository (scaled to primary surface displacement
- total length of rupture within repository
- variable approach to amount of displacement at various points in repository

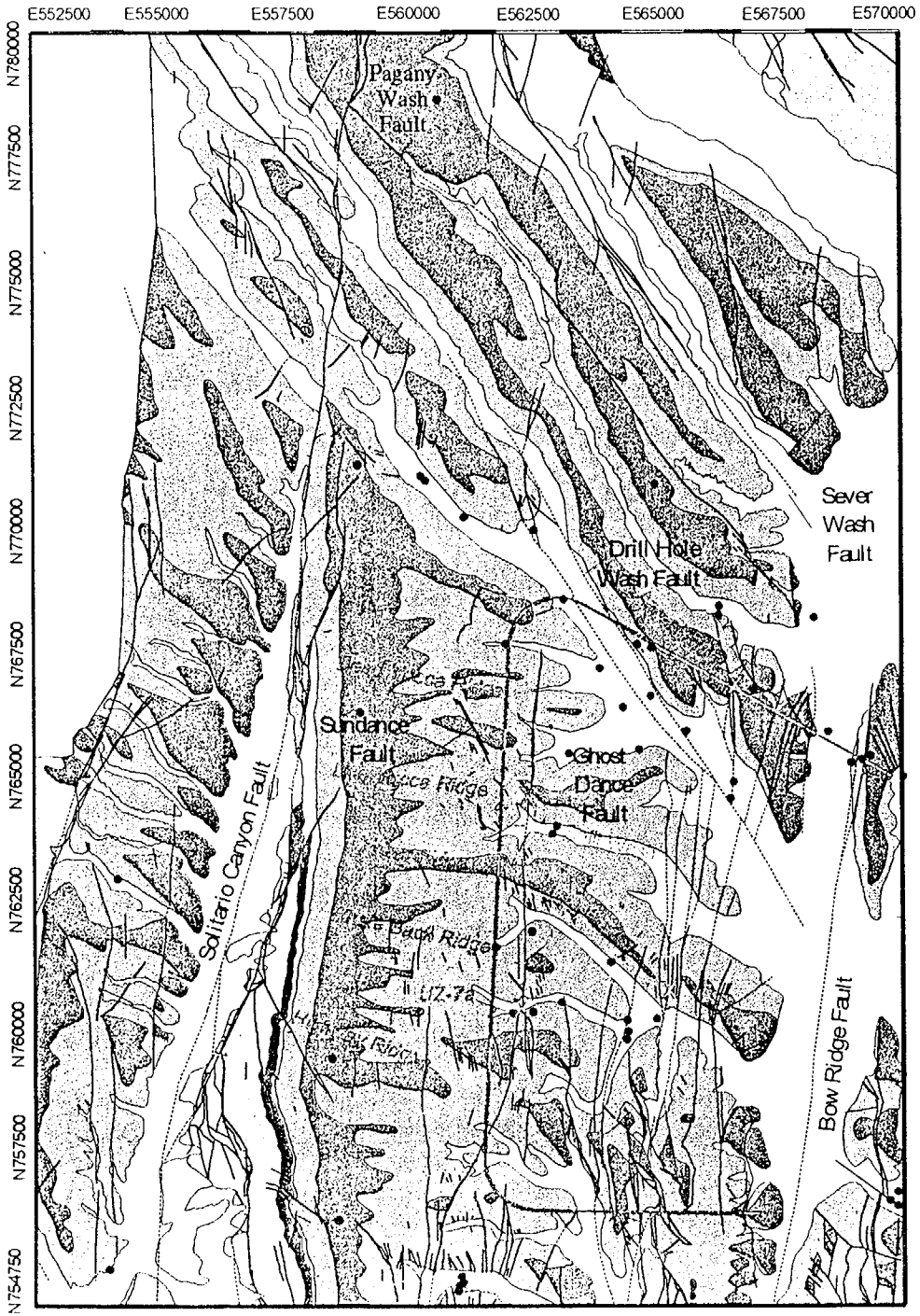

Bedrock Geologic Map of the Central Block Area, Yucca Mountain, Nevada

by

W.C. Day, C.J. Potter, D.S. Sweetkind, and R.P. Dickerson

0 2,500 Feet

Explanation

Quaternary

- Alluvium & Colluvium

Tertiary

- Rainier Mesa Tuff
- Comb Peak Rhyolite
- Tiva Canyon & Topopah Spring Tuff

Tiva Canyon Tuff

- Crystal - rich member
- Crystal - poor member

- **Pah Canyon, Yucca Mountain Tuffs - undivided**

Topopah Spring Tuff

- Crystal - rich member
- Crystal - poor member

Field Trip Outcrop Stop

Field Trip Trench Stop

FROM WORKSHOP #3

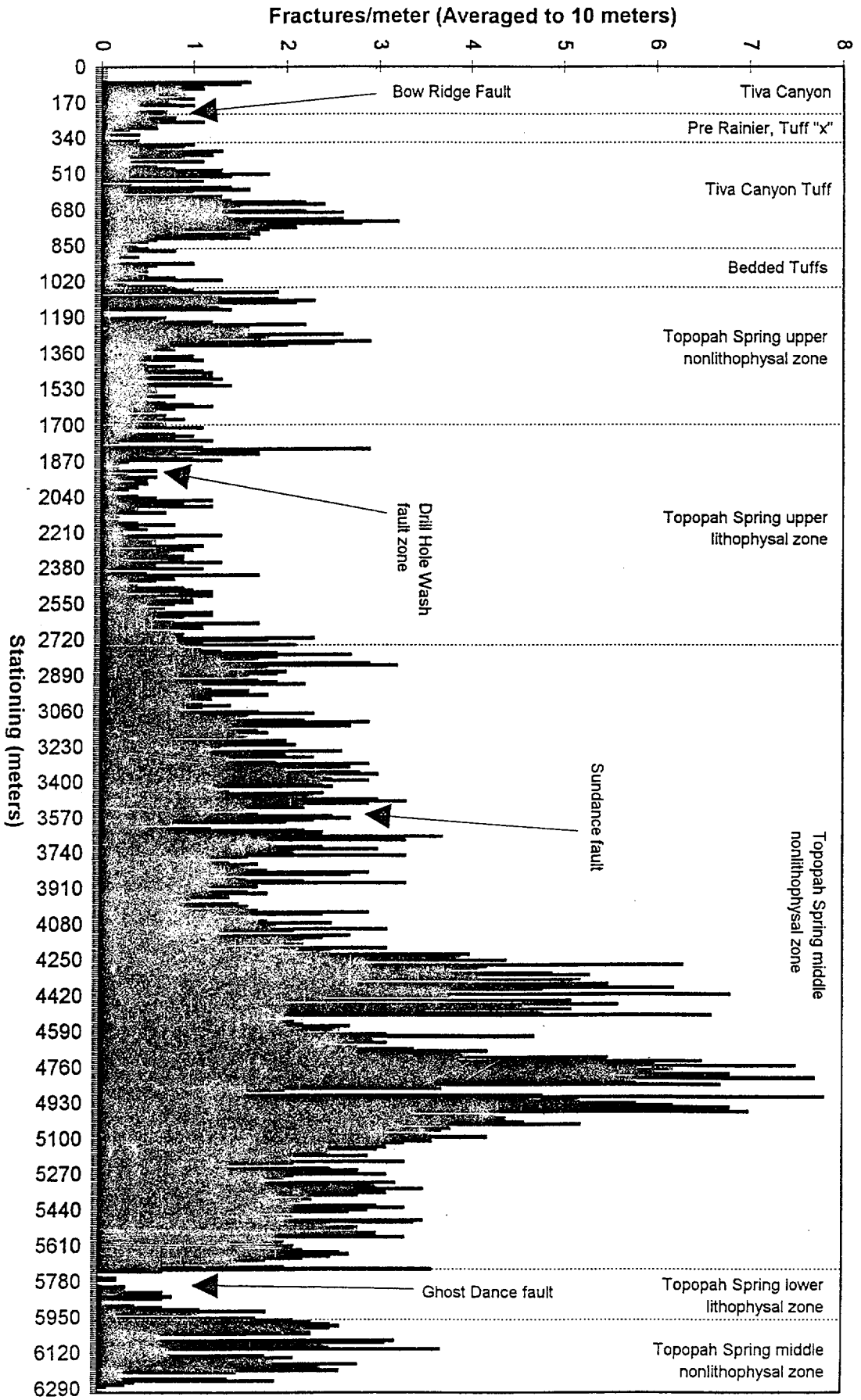

Fracture Density in the ESF
Station 0+60 to 62+70

FROM WORKSHOP #3

Fault and Shear density in the ESF
Station 0+60 to 62+70

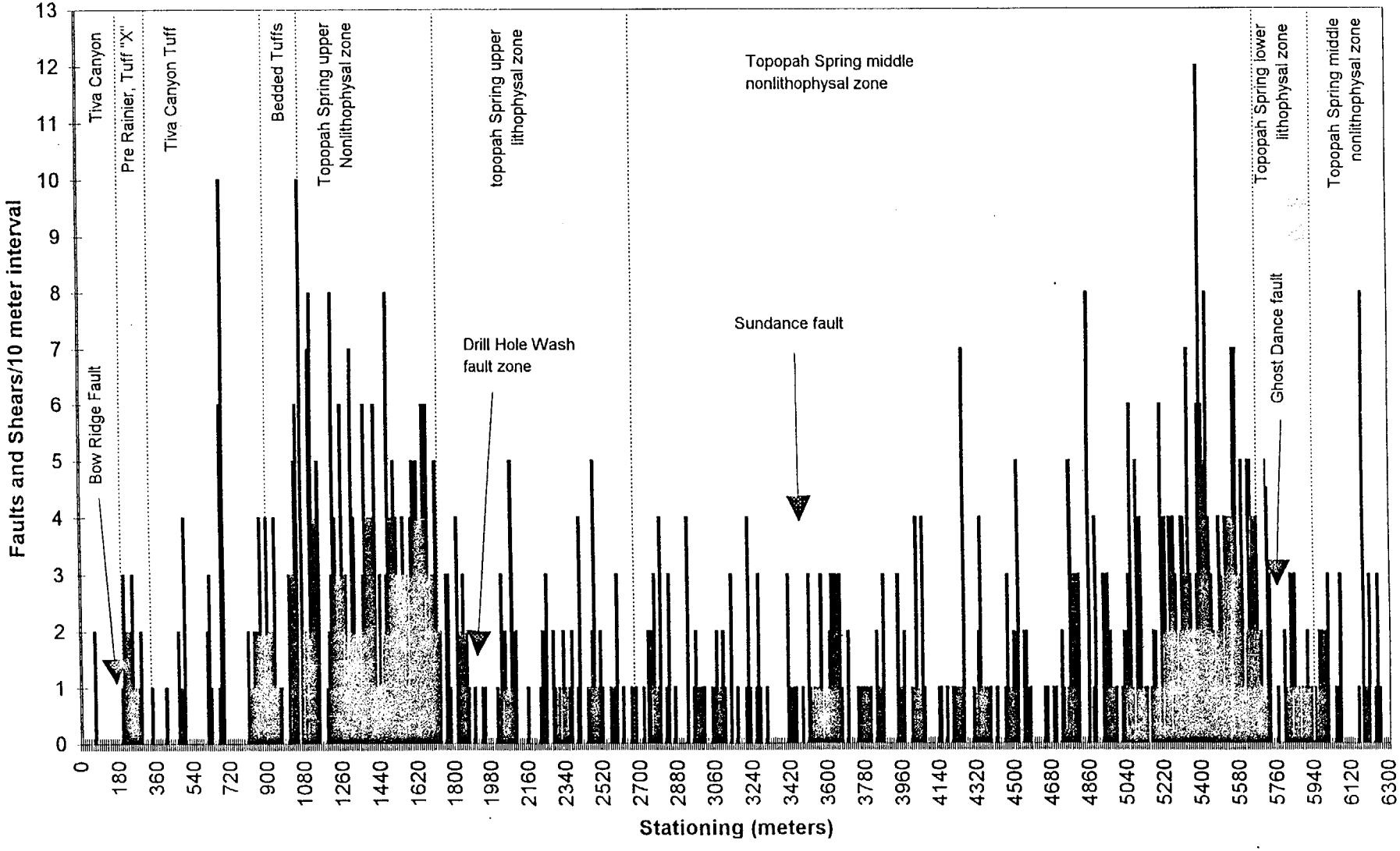

FROM WORKSHOP #3

21

PROTOTYPING A FAULT DISPLACEMENT HAZARD METHODOLOGY

OUTLINE

1) FAULT DISPLACEMENT HAZARD: WHAT ARE WE TRYING TO DO?

2) WHAT DOES AN ANALOG RESERVOIR - REPOSITORY LOOK LIKE IN CHALK (LAEGERDORF, GERMANY)

3) FAULT SCALING RELATIONSHIPS OF INTEREST

4) A PROTOTYPE METHOLDOLOGY (SCAN LINE)

   A) THE GEOMETRICAL PROBLEM & SOLUTION

   B) THE TEMPORAL PROBLEM

5) ALTERNATIVE FORMULATIONS
   A) PREVIOUS WORK
   B) RETURN TO LAEGERDORF

Ken.

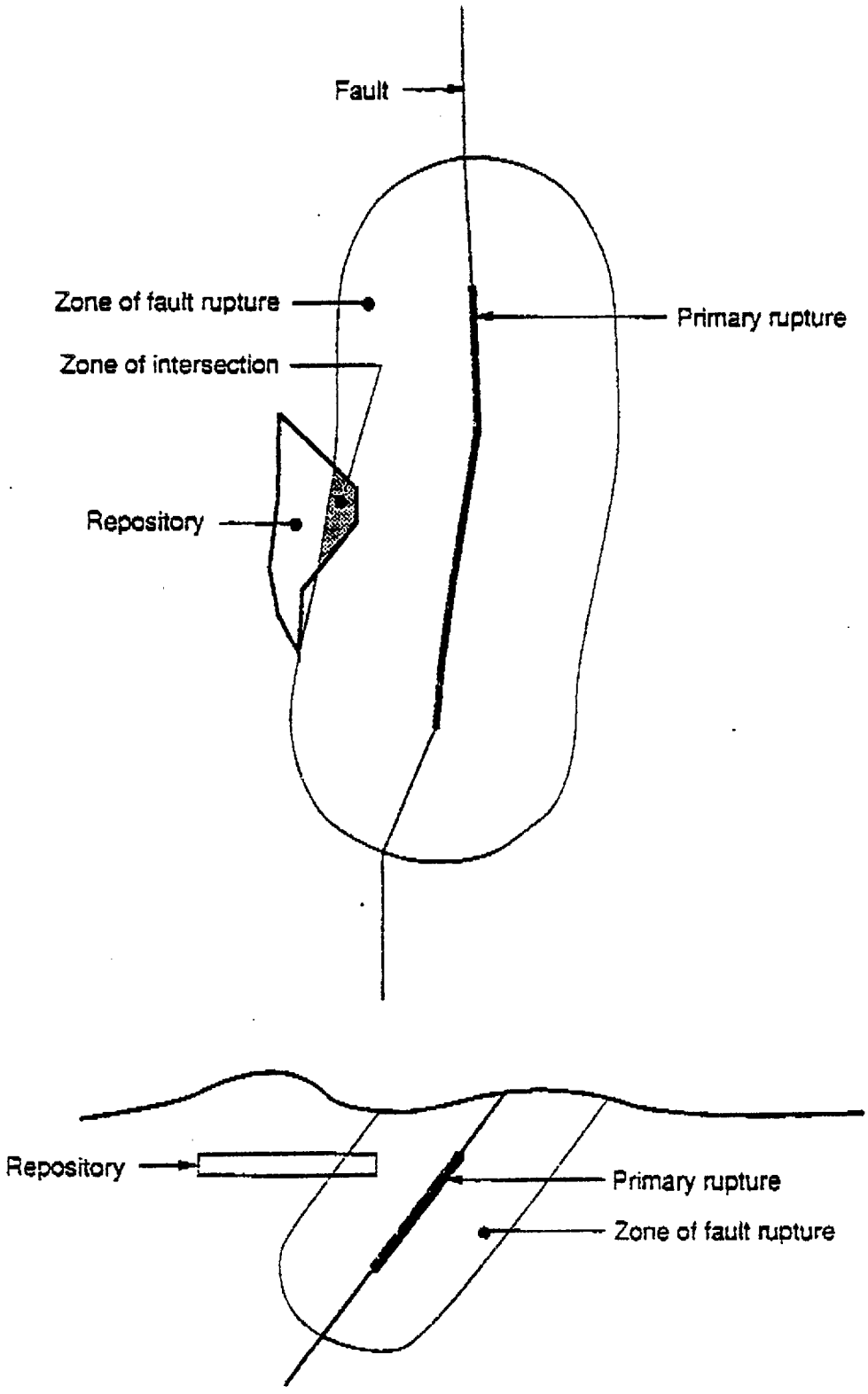

7 8b (part 1)

Figure ~~3-6~~ Illustration of simulation of a zone of faulting for a single event occurring on a fault near the repository. Shaded area represents the area of interSection of the rupture zone with the repository footprint.

LÄGERDORF QUARRY FRACTURE MODEL

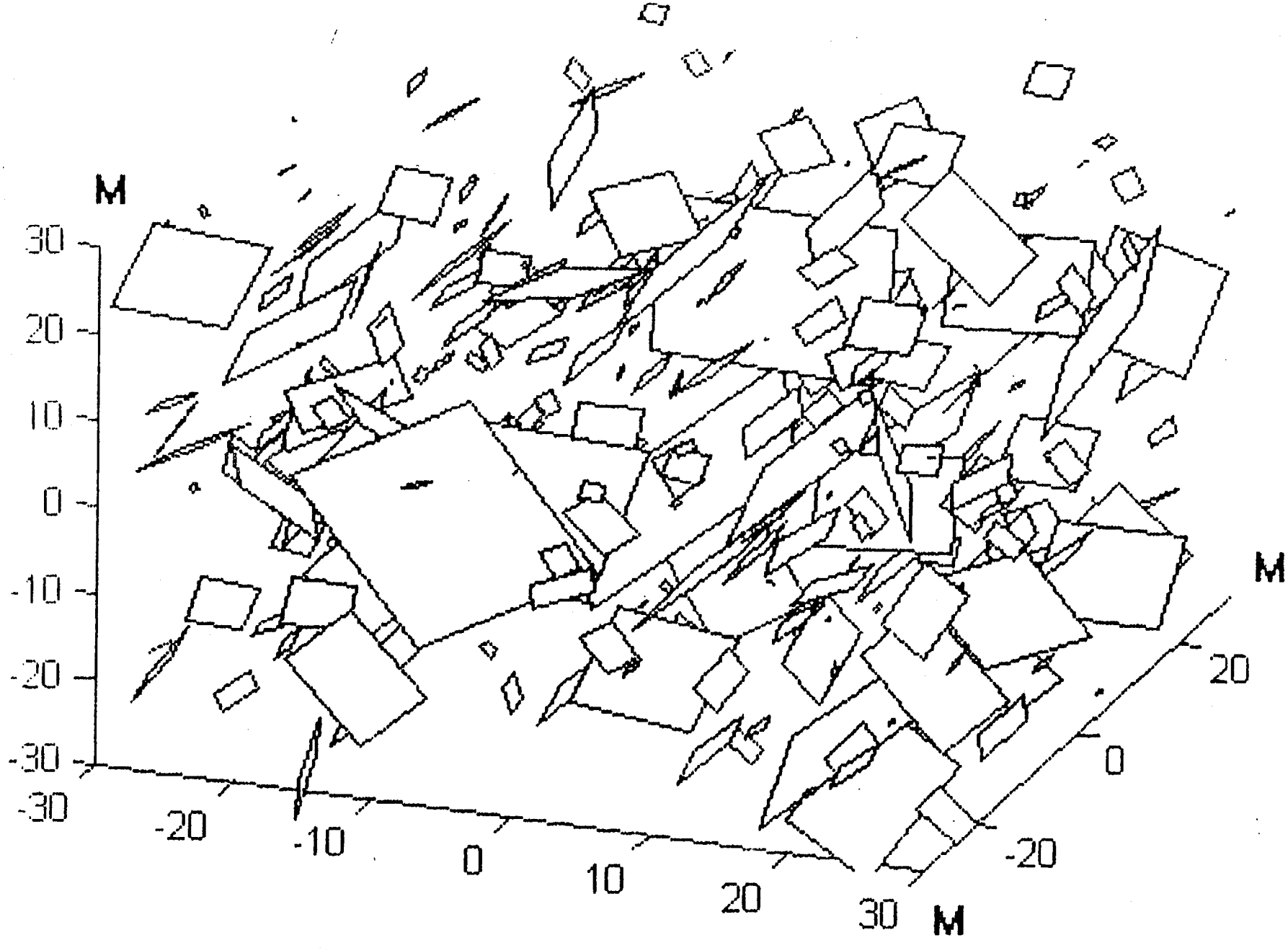

FAULT DISPLACEMENT HAZARD CALCULATION: A PROTOTYPE ENGINEERING METHOD

R.L. Bruhn
Department of Geology and Geophysics
University of Utah
Salt Lake City, Utah
84112 (rlbruhn@mines.utah.edu)

Goal: Estimate the # of faults per meter along a line (tunnel, survey line (scan) capable of slip exceeding some specified value.

1) Estimate the number of faults that intersect a length of scan line based on the statistical properties of faults in the rock mass of interest.

2) Estimate the fraction of these faults capable of generating a displacement D or greater.

3) Estimate the # faults in (2) where the scan line intersects the surface at a point of displacement equal to or exceeding D.

Required Information or Parameters:

1) # faults (centers or centroids) / unit volume (ρ) & a known or assumed spatial distribution function of centers (random?, but other assumptions can be used (clustered, etc)).

2) Distribution function (P(L)) for fault size and a shape assumption: circles, squares, ellipses. (P(L) could be a negative exponential, a lognormal, or power law distribution).

3) An orientation function (P(β)), where β = angle between fault pole and scan line. I fix β for the prototype.

4) A single slip event scaling law Dmax = α L, say, where α is about 1e-4 to 1e-5.

5) A function describing the manner in which slip is distributed on a fault surface from Dmax to 0.

6) Either solve analytically or simulate 'Las Vegas' fashion.

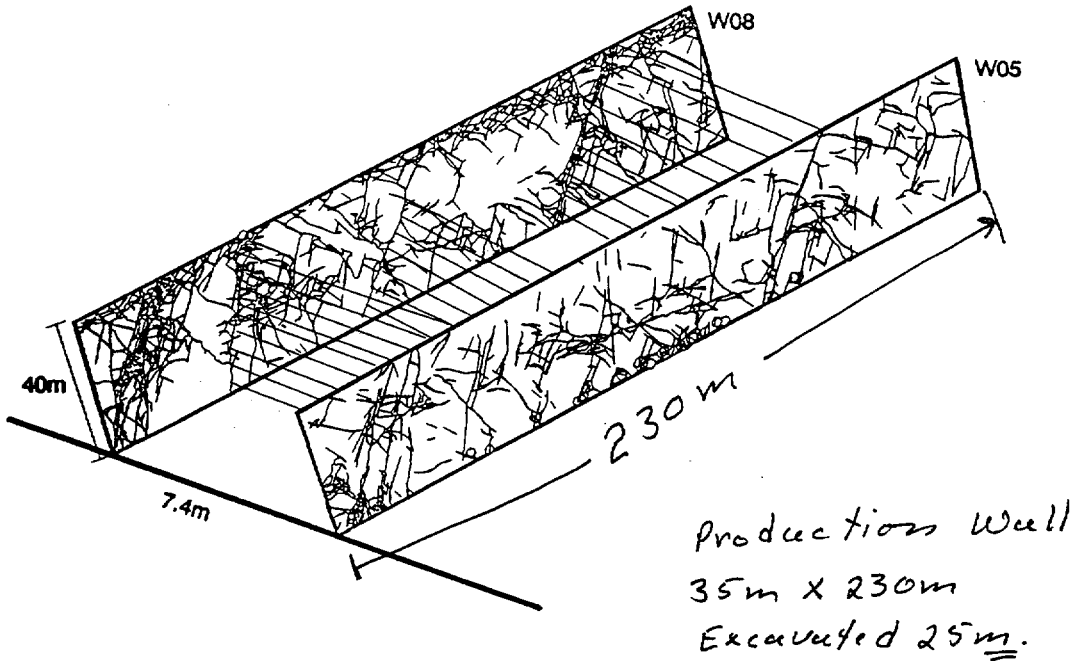

*Fig. 8 **Isolines** linking fractures between two wall sections mapped in the field.* Vol ~ 200,000 m^3

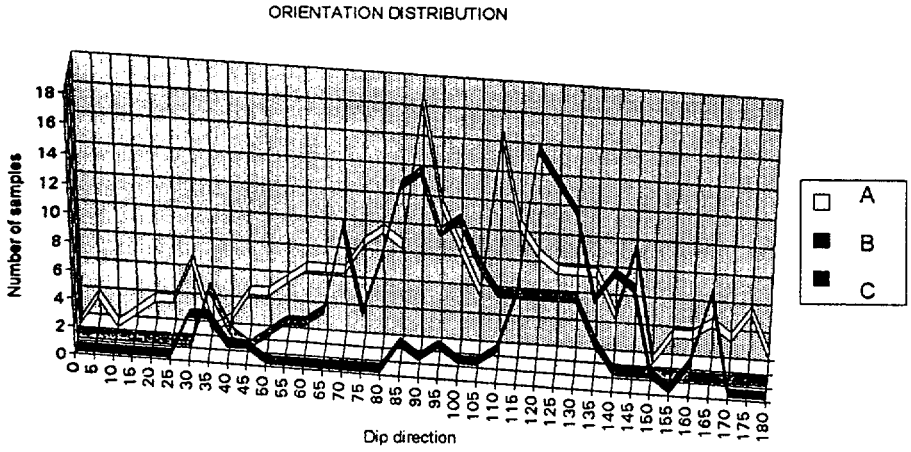

*Fig. 9 **Dip direction** distributions of fracture orientations measured by compass plotted in the interval **0 to 180** degrees (A), and constructed from links of two fractures between different wall **sections** (B and C). Note the similarity of the three curves.*

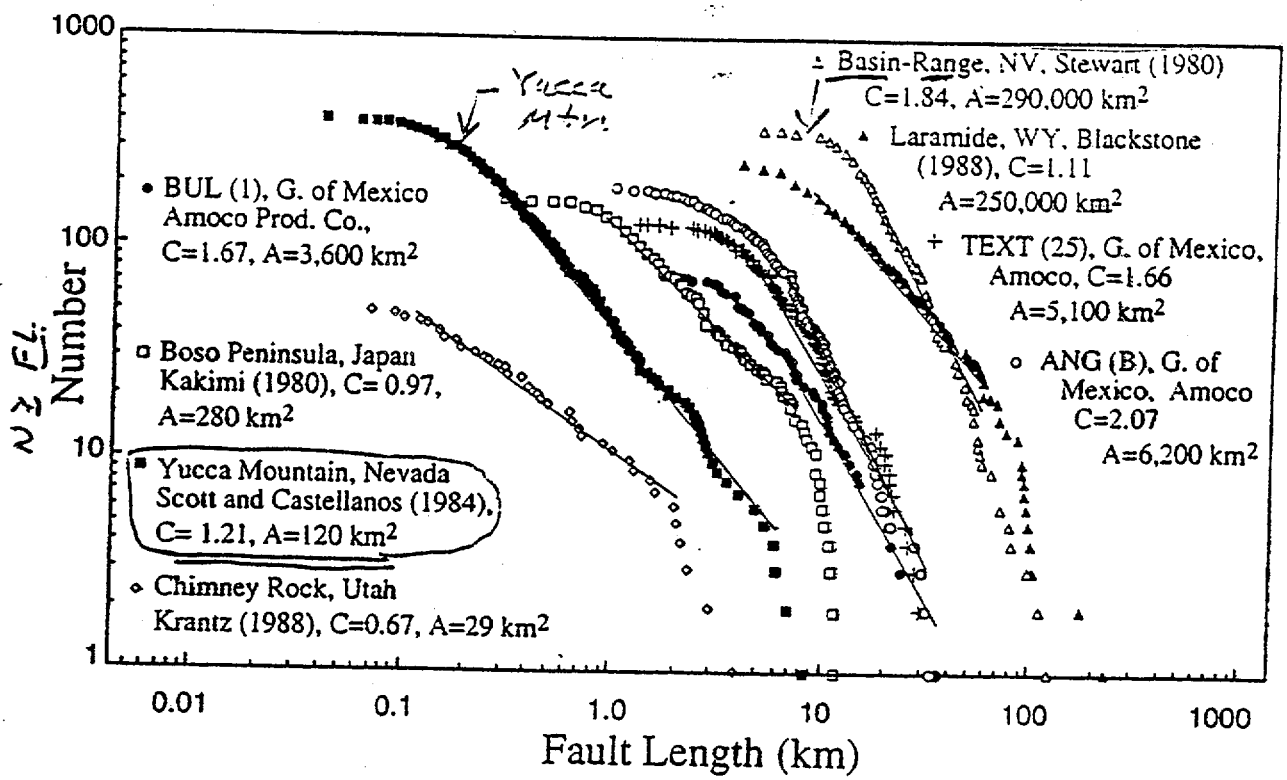

Fig. 1. Eight fault length data sets derived from the maps published in the references given on the figure. Thin lines show the portions of the curves which fit lines with slopes of C. Because these data were collected from two-dimensional samples of three-dimensional volumes, equation (1) and the data in Fig. 1 describe two-dimensional fault populations. The actual (three-dimensional) power-law exponent for small faults is $C + 1$ (Marrett & Allmendinger 1991). Also shown are the areas (A) in square kilometers of the maps from which the data were collected.

Total Displacement

Clark & Cox 1996

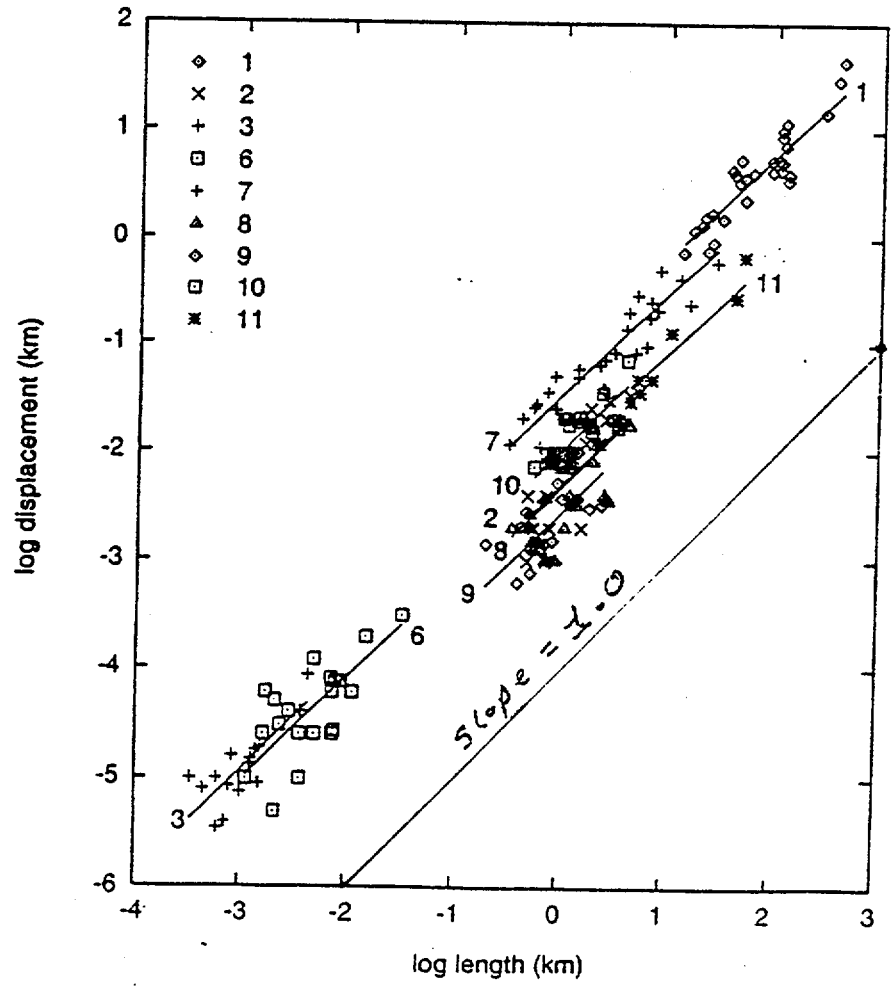

Fig. 1. Results of the combined analysis of nine data sets (lines), with the source data (symbols). Group numbers as in

FIGURE 1: Tensile Crack Arrays at Edges of Normal Fault

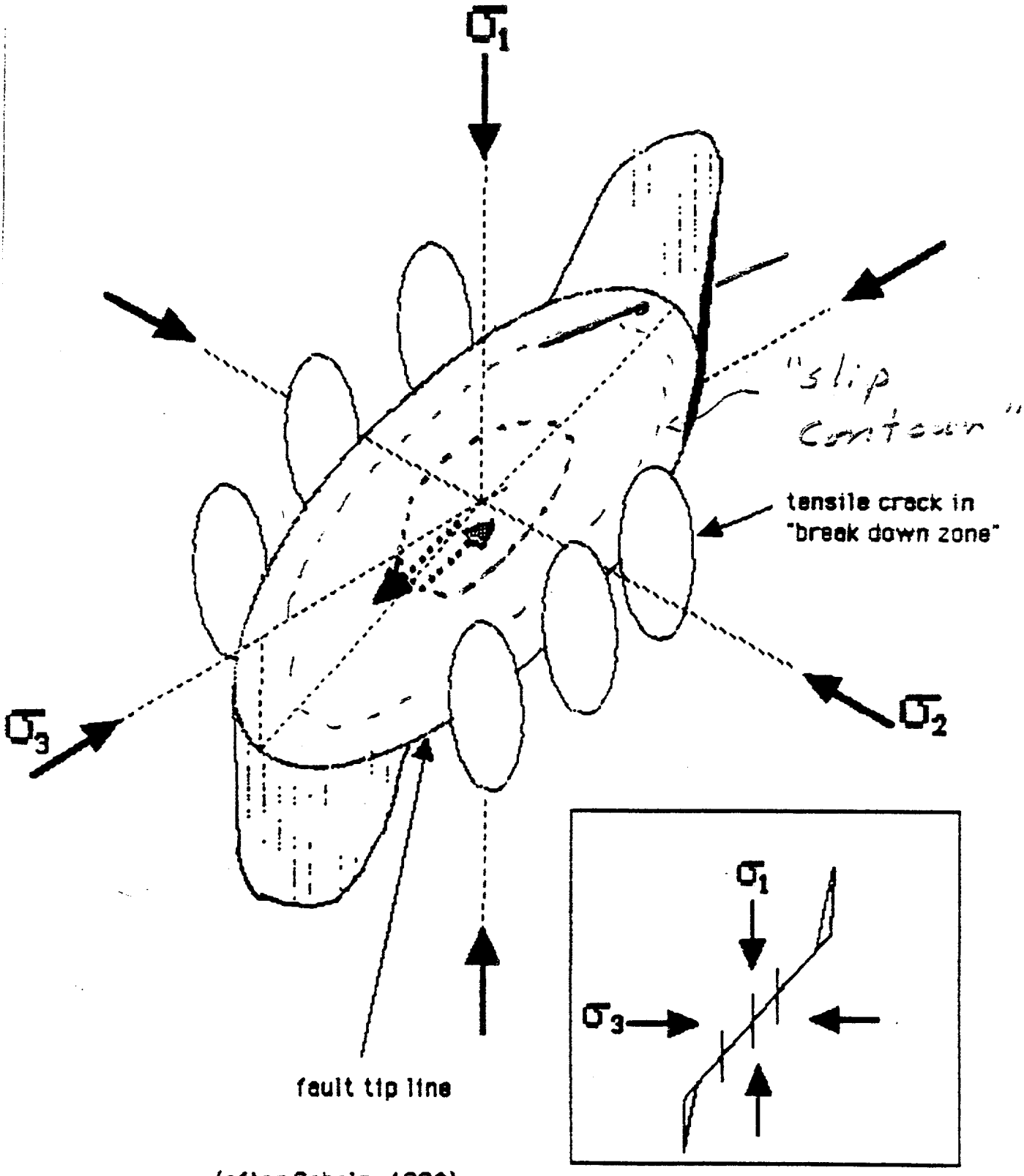

(after Scholz, 1990)

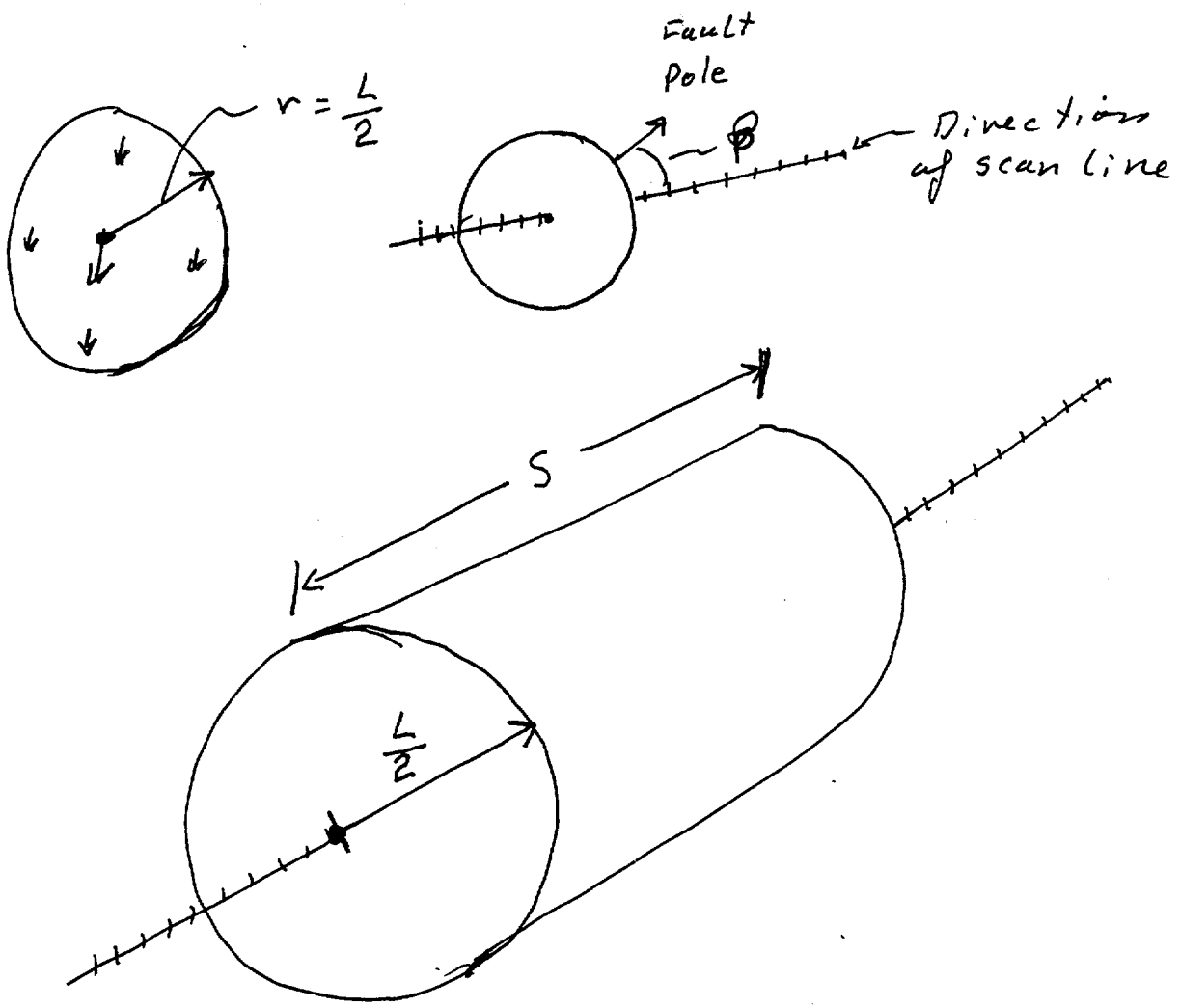

Trick: A fault of length (Diameter = $L/2$) will intersect the scan line if its center is located in the volume of the cylinder of face area = $\pi/4\ L^2$ & length S. How many intersections are expected?

$$\frac{\#\ \text{Faults}}{\text{Volume}} \times \text{Volume of cylinder} \times P(L) = \text{Fraction of all faults of diameter } L$$

The solution for circular faults with a linear slip gradient.
D = Dmax, r = 0, D = 0, r = L/2, r = radius. Scan length = S

Max. Displacement on a fault of diamter L:

$$(Dmax = \alpha L) \qquad (1)$$

Displacement as a function of distance from center:

$$D(r) = Dmax\ (\ 1 - 2r/L),\quad 0 <= r <= L/2\ ) \qquad (2)$$

 # Faults of diameter L to dL expected to be intersected.

$$\#\ F(L) = (\pi/4)\ \rho\ S \cos(\beta)\ L^2\ P(L)\ dL \qquad (3)$$

 # Total # of expected fault intersections L = D/α & larger.

$$\#FI = (\pi/4)\ \rho\ S \cos(\beta) \int_{L_d = D/\alpha}^{L_{max}} L^2\ P(L)\ dL \qquad (6)$$

Fault radius for area in which displacement >= D

$$r = L/2 - D/(2\alpha) \qquad (7)$$

Chance of cutting a point with displacement >= D on fault.

$$P(D|L(Dmax > D)) = Ar/AL = 1 - 2D/\alpha L + D\ /(\alpha^2 L^2\ ) \qquad (8)$$

The estimated number of points along the scan line where slip may exceed D during faulting is then (9)

$$\#FI(\ S > D) = (\pi/4)\ \rho\ S \cos(\beta) \int_{L_d = D/\alpha}^{L_{max}} L^2\ P(L)\ P(D|L(Dmax > D))\ dL$$

FAULT DISPLACEMENT HAZARD ANALYSIS: PROTOTYPE SOLUTION

Fault Diam. (m) Min.	Max.	Angle β	Fault Density	Disp/Length Ratio (α) :	PDF slope (abs value)
$Lmin := 1$	$Lmax := (1 \cdot 10)^4$	$\beta := 25$	$rho := 0.1$	$\alpha := 1 \cdot 10^{-4}$	$c := 3$

Fault Displacement (m): $D := 0.1$

Normalizing Factor for PDF ----------> NT := $\int_{Lmin}^{Lmax} L^{-c}\, dL$

---------- **SOLUTIONS** ----------

1: Expected # of faults per meter intersecting the scan line:

$$\frac{\pi}{4} \cdot rho \cdot \cos(\beta \cdot deg) \cdot \int_{Lmin}^{Lmax} \left[\frac{L^{(2-c)}}{NT} \right] dL = 1.19$$

2: Expected # of fault intersections of faults with maximum displacement >= D m

$$\frac{\pi}{4} \cdot rho \cdot \cos(\beta \cdot deg) \cdot \int_{\frac{D}{\alpha}}^{Lmax} \left[\frac{L^{(2-c)}}{NT} \right] dL = 0.028$$

3: Expected # intersections per meter at points where displacement may exceed D (m)

$$\frac{\pi}{4} \cdot rho \cdot \cos(\beta \cdot deg) \cdot \int_{\frac{D}{\alpha}}^{Lmax} \left[\frac{L^{(2-c)}}{NT} \cdot \left(1 - 2 \cdot \frac{D}{\alpha \cdot L} + \frac{D^2}{\alpha^2 \cdot L^2} \right) \right] dL = 0.012$$

R.L. Bruhn, Dept. Geology & Geophysics, University of Utah,
Salt Lake City, Utah 84112 : rlbruhn@mines.utah.edu
Dec. 1996

Real Problem !

a) what fraction of faults are "active"

b) At what rate are they activated?

Direct - Slip Rate = $\frac{\text{Displacement}}{\text{Age of Rocks}}$

Indirect -

a) Look at "strain" distribution around block bounding or other larger fault. Estimate # small faults needed to accom. strain at a point.

b) Use Silvio's data set: strain generated by distributed faulting during analog quakes.

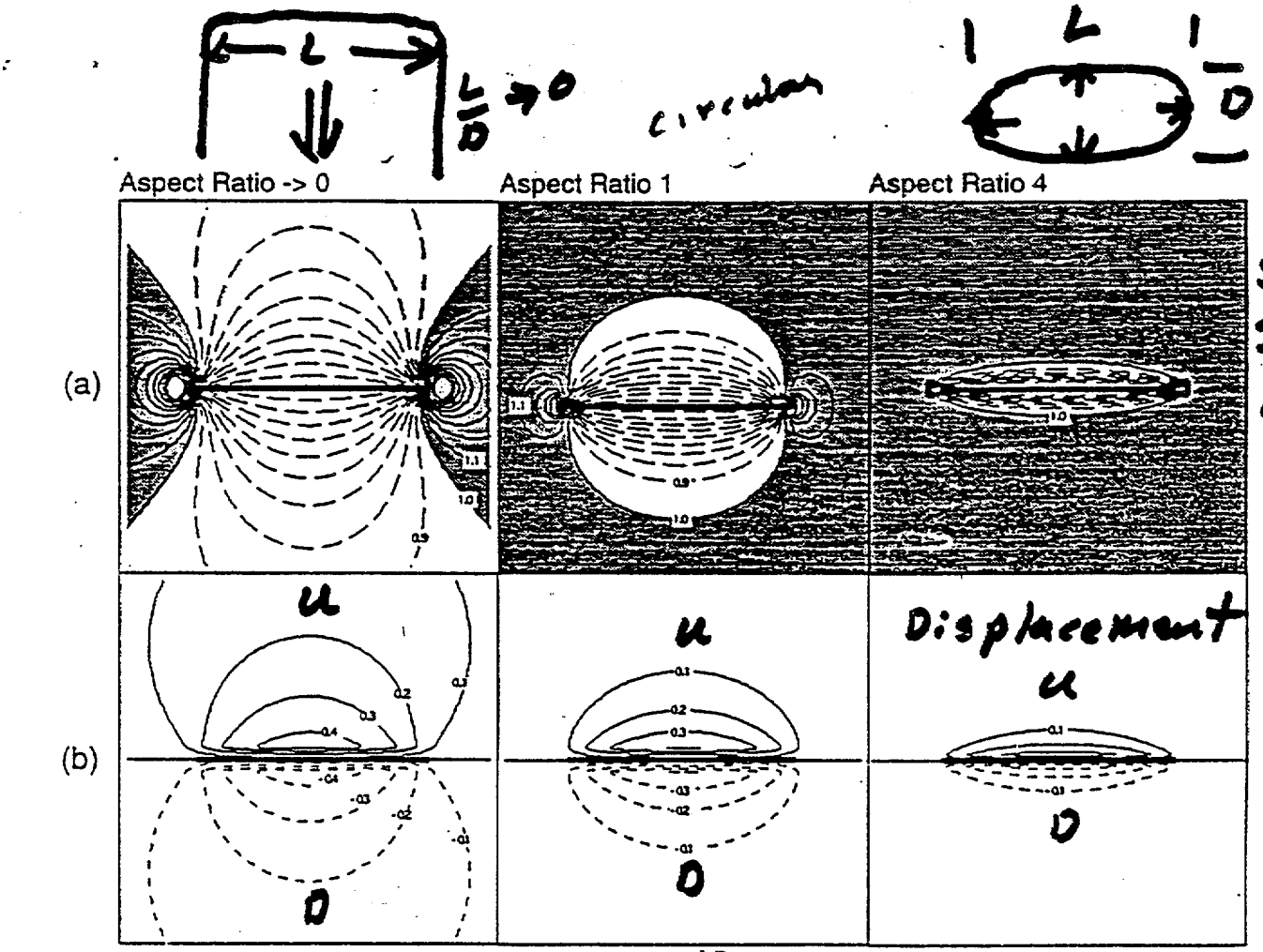

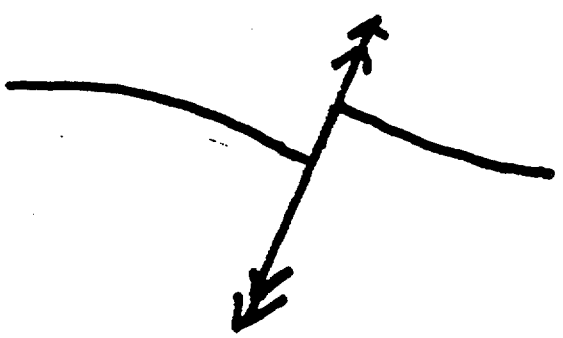

From Willemse & Pollard (96).

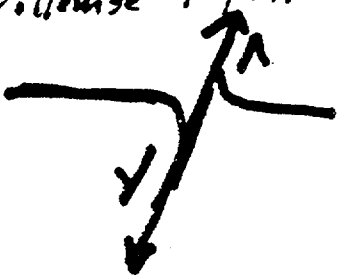

THE TEMPORAL PROBLEM (?)

HOW IS SLIP TRIGGERED?
VIBRATORY GROUND MOTION, STRUCTURAL LINKAGES.
Direct

A) SLIP TRANSFER FROM LARGE TO SMALL FAULTS.

B) LARGE FAULT SLIP (BLOCK BOUNDING) CHANGES STATIC OR DYNAMIC STRESS FIELD.

C) SLIP TRIGGERED BY 'REMOTE' FAULT SLIP (BARE MTN FAULT, CHALFONT VALLEY TYPE)

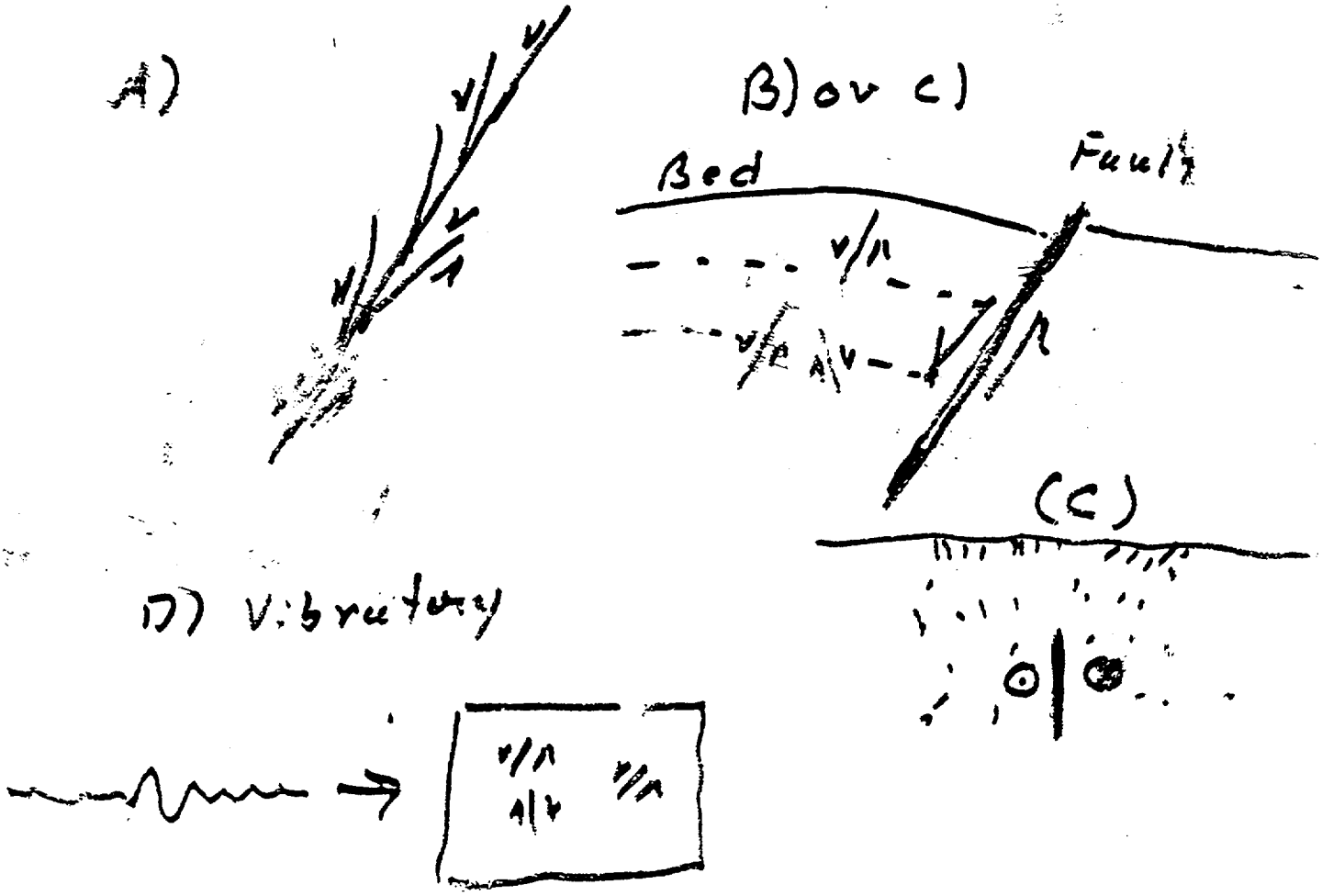

The Thorny Issue:

If an "event" occurs what fraction of the "small" faults will fail? or alternatively - how often will they fail?

1] Time (Direct) $= \frac{\text{Displacement}}{\text{Age of rocks}}$

Recurrence Interval =

2) strain changes associated with blocks bounding slip.

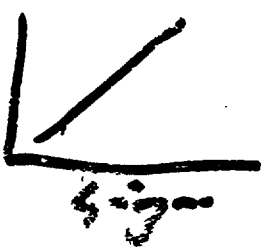

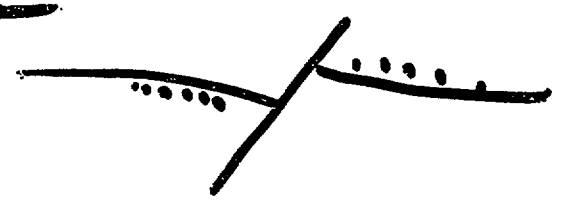

3) strain created by ~~Int~~ distributed faulting analog earthquake.

$e_s = \frac{d}{2kL}$ ⇐ ⇒

FAULT DISPLACEMENT HAZARD CALCULATION: A PROTOTYPE ENGINEERING METHOD

R.L. Bruhn
Department of Geology and Geophysics
University of Utah
Salt Lake City, Utah
84112 (rlbruhn@mines.utah.edu)

(NOT FOR GENERAL DISTRIBUTION - DRAFT DOCUMENT, Dec. 26, 1996)

Introduction

We must estimate the probability of exceedance of a specified fault displacement at a point in a rock mass during some interval of time. Our goal is to develop an algorithm that relies primarily on the structural and statistical properties of faults observed within the rock mass as determined from surface and underground mapping, and studies of Quaternary and longer-term fault recurrence. A second part that deals specifically with estimates of faulting recurrence is not included with this FAX.

Conceptual Framework

We wish to develop an algorithm that predicts the expected number of potential fault displacements greater than or equal to some specified displacement (D) per meter of length in the rock mass. That is, imagine a survey line (scan line) that cuts through the rock mass in some given direction. We estimate the number of fault displacements >= D averaged per meter along the scan line. The scan line could be the center line of a tunnel floor, a drill hole, or a tape measure extended across an outcrop.

We proceed in three steps: 1) Estimate the number of faults that intersect a length of scan line based on the statistical properties of faults in the rock mass of interest. 2) Estimate the fraction of these faults capable of generating a displacement D or greater. 3) Estimate the chance that the scan line cuts the fault at a point where the displacement will equal or exceed D.

Step #1: This part of the algorithm is taken from the work of Oda et al., (1987), and requires statistical information and assumptions concerning (a) the number of fault centers per unit volume of rock (ρ), (b) the statistical distribution of the fault centers in space (assumed to be random for simplicity), (c) the probability density distribution P(L) of fault diameters (for circular faults of diameter L), and (d) the orientation of the faults with respect to the scan or sampling line. Fault orientation is defined by the acute angle between the normal to the fault surface and the scan line. The required parameters and statistical distribution functions may be derived from geological maps and bore hole logs, with the caveat that sampling biases must be taken into account (Oda et al., 1987).

Step #2: An estimate of the fraction of faults that both intersect the scan line and are capable of generating displacements >= D requires a displacement vs fault size scaling law. We are interested in single event displacements (co-seismic, say), not in cumulative fault displacement that develops by multiple slip events. Displacement vs fault length or size scaling laws may be taken from the work of Wells and Coppersmith (199?) for surface rupturing, or from physical models developed by seismologists and tectonophysicists (Scholz and Cowie, 1990; Walsh et al., 1991).

Step #3: Fault slip or displacement varies over a fault surface, usually reaching a maximum near the center and decreasing outwards towards the edges. If the fault is a dislocation buried in the rock mass, then the displacement must be zero around its perimeter. Fault surface displacement fields may be modeled using empirical data from field and laboratory studies, or fracture mechanics theory (Scholz, 1991). In this

prototype we assume circular faults on which the displacement dies out linearly from a maximum Dmax at the center of the fault to zero at the perimeter.

Technical Description

Make the following assumptions:
1) Consider a population of circular faults of diameter Lmin <= L <= Lmax, with randomly distributed centers embedded in the rock mass. A 'fault set' is a group of similarly oriented faults with a well defined average orientation described by a mean fault pole, and a PDF which describes the fraction of faults with diameter L between Lmin and Lmax. The acute angle between the average fault pole and the scan line is defined as β. The scan line length is S. Single event fault slip is described by two functions, the first relating the maximum displacement at the fault center to fault diameter

$$(D_{max} = \alpha L) \qquad (1)$$

and the second describing the linear decay of displacement D from the fault center radially outward to the fault perimeter

$$D(r) = D_{max} (1 - 2r/L), \quad 0 <= r <= L/2) \qquad (2)$$

Step 1: Let ρ = # faults/ unit volume for the fault set of interest, let P(L) describe the fraction of faults of diameter L. We seek the number of faults of diameter L expected to intersect the scan line of length S. Following the derivation by Oda et al. (1987):

Consider a circular cylinder of diameter $L\cos(\beta)$ centered about the scan line of length S. Faults of diameter L with centers within this cylinder must intersect the scan line. What is the number of such faults expected to cut the scan line?

$$\#F(L) = (\pi/4)\, \rho\ S \cos(\beta)\, L^2\, P(L) \qquad (3)$$

Note that the volume of the circular cylinder is $(\pi/4)\, S \cos(\beta)\, L^2$, and the total number of faults with centers in the cylinder is the product of the fault density (ρ) and the cylindrical volume given by (3). The number of faults of diameter L is then the total number of fault centers in the cylindrical volume multiplied by P(L), the fraction of faults in the fault set or population with diameter L.

How many faults of the total population are expected to intersect the scan line? Integrate (3) over the range of diameters Lmin <= L <= Lmax.

$$\#FI = (\pi/4)\, \rho\ S \cos(\beta) \int_{L_{min}}^{L_{max}} L^2\, P(L)\, dL \qquad (4)$$

The PDF of fracture diameters is determined from field or tunnel observations. Usually, natural fault populations contain many more small faults than large ones, motivating the use of negative exponential, fractal or lognormal distribution functions.

2) What fraction of the faults that intersect the scan line can generate single event slip D or greater? Assume the slip scaling relation $D_{max} = \alpha L$. Surface slip during normal faulting earthquakes produces maximum slip between 3 m and 4 m on faults about 30 km long, suggesting a value of about $\alpha = 1 \times 10^{-4}$. The minimum diameter fault that can generate slip D is then estimated as

$$L_d = D/\alpha \qquad (5)$$

Integrating (4) from Ld <= L <= Lmax estimates the number of scan line intersections with faults capable of generating a displacement greater than or equal to D.

$$\#FI(L_d <= L <= Lmax) = (\pi/4)\,\rho\, S\cos(\beta) \int_{L_d = D/\alpha}^{Lmax} L^2\, P(L)\, dL \qquad (6)$$

However, some of these intersections presumably occur at a point on the fault surfaces where the slip is less than D. Remember, we assume that Dmax is located at the center of a fault and decays linearly outward to zero at the fault's perimeter. This means that the scan line may intersect a large fault with Dmax > D, but if the intersection occurs near the fault perimeter, the amount of slip at that point may be less than D. This motivates us to make an additional correction as described below.

3) We take the product between the integrand in (6) and the probability that the scan line intersects the fault a point on the fault surface where slip equals or exceeds D. That is we seek the conditional probability P(D|L(Dmax > D)) for a circular fault with the assumed slip distribution function in equation (2).
By P(D|L(Dmax > D)) we mean the chance that the fault is intersected by the scan line at point where slip equals or exceeds D. This requires that the fault have diameter L sufficiently large so that Dmax >= D.

P(D|L(Dmax > D)) is simply the area Ar of the fault surface on which slip exceeds D, divided by the total area of the fault surface (AL). Substituting the expression for Dmax in equation (1) into equation (2) and solving for the radius r of the circular patch on the fault surface in which slip equals or exceeds D gives

$$r = L/2 - D/(2\alpha) \qquad (7)$$

and

$$P(D|L(Dmax > D)) = Ar/AL = 1 - 2D/\alpha L + D/(\alpha^2 L^2) \qquad (8)$$

The estimated number of points along the scan line where slip may exceed D during faulting is then

$$\#FI(\text{ Slip} > D) = (\pi/4)\,\rho\, S\cos(b) \int_{L_d = D/\alpha}^{Lmax} L^2\, P(L)\, P(D|L(Dmax > D))\, dL \qquad (9)$$

Example

The algorithm is implemented in the attached MathCad 5.0 document. MathCad is a mathematical program that allows one to generate a text document with embedded, working mathematical equations. The diameters of the simulated faults are described by a fractal distribution of form

$$P(L) = L^{-c} \qquad (10)$$

This PDF is normalized in the document to ensure an area of 1.0 when integrated from Lmin to Lmax.

In the example, 1 m <= L <= 10,000 m, the fault set is oriented at β = 25 degrees to the scan line, the fault density is 0.1 faults/m3, $\alpha = 1\text{x}10^{-4}$, and c = 3. This is a sample solution using reasonable values for natural fault populations, but it is not based on data from the Yucca Mountain repository. The results are expressed as the number of fault intersections per meter of scan line:

1) The expected number of fault intersections is 1.19 / meter.

2) The expected number of intersections of faults capable of displacement D > 0.1 meter is 0.028 / m.

3) The expected number of fault intersections where D > 0.1 m at the scan line if the fault is activated is 0.012 / m. This is the final and desired result.

We estimate that on average there are 1 to 2 faults capable of generating 10 cm or more of displacement in a 100 meter section of a repository or tunnel center line. If there is more than one fault set in the rock mass, the calculation is repeated for each fault set, and the number of fault intersections are summed together. A reminder - these results are from an imagined fault population, they do not use any data from the Yucca Mountain region.

The probability that fault displacement occurs during a given time interval can be estimated from information on faulting recurrence intervals, and is not discussed in detail in this preliminary report. One could estimate recurrence by dividing the total slip on a observed fault, or set of faults, by the age of the rocks in which they occur. An alternative method, or methods, may use information on recurrence of Quaternary slip events on several of the larger faults in the population. The likelihood of fault activation could also be weighted by the ratio of shear to normal stress on faults computed from knowledge of the present-day stress field (slip-tendency analysis).

Further Applications

The algorithm is fairly general, and can be implemented with different fault geometry, statistical distribution functions, and fault scaling laws. Application to a repository area instead of a sampling line should be possible. Implementation in practice is hindered by problems in deriving the PDF describing the fault population from geological data, and by uncertainty in the appropriate fault size and fault slip scaling laws. One strength is that the algorithm relies on site-specific data obtained from the rock mass of interest. This means that predictions may be tested and modified as new information becomes available during repository exploration and development. This is perhaps an 'engineering' advantage over methods that use analogs from surface faulting earthquakes.

References

Oda, M., Y. Hatsuyama, and Y. Ohnishi, Numerical experiments on permeability tensor and its application to jointed granite at the Stripa Mine, Sweden. J. Geophys. Res., **92**, 8037-8048, 1987.

Scholz, C.H., The Mechanics of Earthquakes and Faulting (Cambridge Uiversity Press, 1991)

Scholz, C.H., and P. A. Cowie, Nature, **346**, 837-839, 1990.

Walsh, J., J. Watterson, and G. Yielding, The importance of small-scale faulting in regional extension, Nature, **351**, 391-393, 1991.

FAULT DISPLACEMENT HAZARD ANALYSIS: PROTOTYPE SOLUTION

Fault Diam. (m) Min.	Max.	Angle β	Fault Density	Disp/Length Ratio (α) :	PDF slope (abs value)
Lmin := 1	Lmax := $(1 \cdot 10)^4$	β := 25	rho := 0.1	α := $1 \cdot 10^{-4}$	c := 3

Fault Displacement (m): D := 0.1

Normalizing Factor for PDF ----------> NT := $\int_{Lmin}^{Lmax} L^{-c}\, dL$

---------- **SOLUTIONS** ----------

1: Expected # of faults per meter intersecting the scan line:

$$\frac{\pi}{4} \cdot rho \cdot \cos(\beta \cdot deg) \cdot \int_{Lmin}^{Lmax} \left[\frac{L^{(2-c)}}{NT} \right] dL = 1.19$$

2: Expected # of fault intersections of faults with maximum displacement >= D m

$$\frac{\pi}{4} \cdot rho \cdot \cos(\beta \cdot deg) \cdot \int_{\frac{D}{\alpha}}^{Lmax} \left[\frac{L^{(2-c)}}{NT} \right] dL = 0.028$$

3: Expected # intersections per meter at points where displacement may exceed D (m)

$$\frac{\pi}{4} \cdot rho \cdot \cos(\beta \cdot deg) \cdot \int_{\frac{D}{\alpha}}^{Lmax} \left[\frac{L^{(2-c)}}{NT} \cdot \left(1 - 2 \cdot \frac{D}{\alpha \cdot L} + \frac{D^2}{\alpha^2 \cdot L^2} \right) \right] dL = 0.012$$

**R.L. Bruhn, Dept. Geology & Geophysics, University of Utah,
Salt Lake City, Utah 84112 : rlbruhn@mines.utah.edu**
Dec. 1996

Spatial distribution of faulting w/in repository

1) given secondary-faulting halos of some defined widths, how does potential for secondary faulting vary across the area?
   - uniform throughout (very low)
   - decreasing w/distance from primary faults (high)

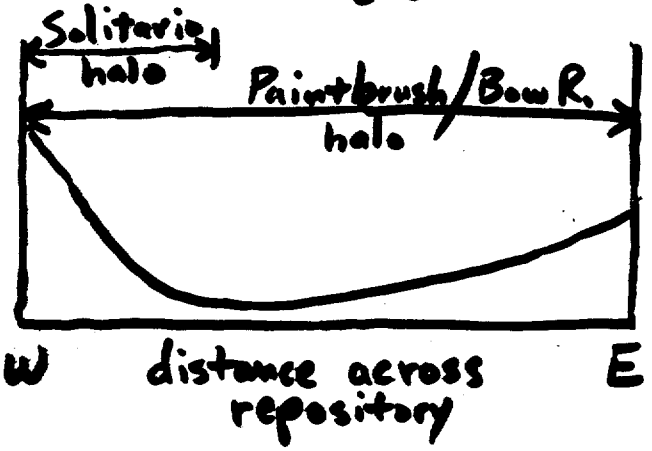

2) can areas of relatively high (or low) potential be defined?
   - selected faults (Solitario splay; "faults & shears" adjacent to Ghost Dance bend; Sundance fault; others?)
   - intensely-fractured zone (most fracture variations lithologically bound, but this zone may be associated w/ mapped intrablock faults ∴ structural?)
   - remainder of area

? - area north of Drillhole Wash?

E. Anderson, Arabasz, Ramelli

Clover Mts Analog

Similarities

1) Seismotectonic setting (SNSB)
2) "Magmatectonic" setting
3) age of rocks + deformation
4) style of deformation including:
   a) faulting, tilting, and structural "lumpiness"
   b) steep-axis bending
   c) length of faulting (to ≈10 km)
   d) depth of penetration of faults ?

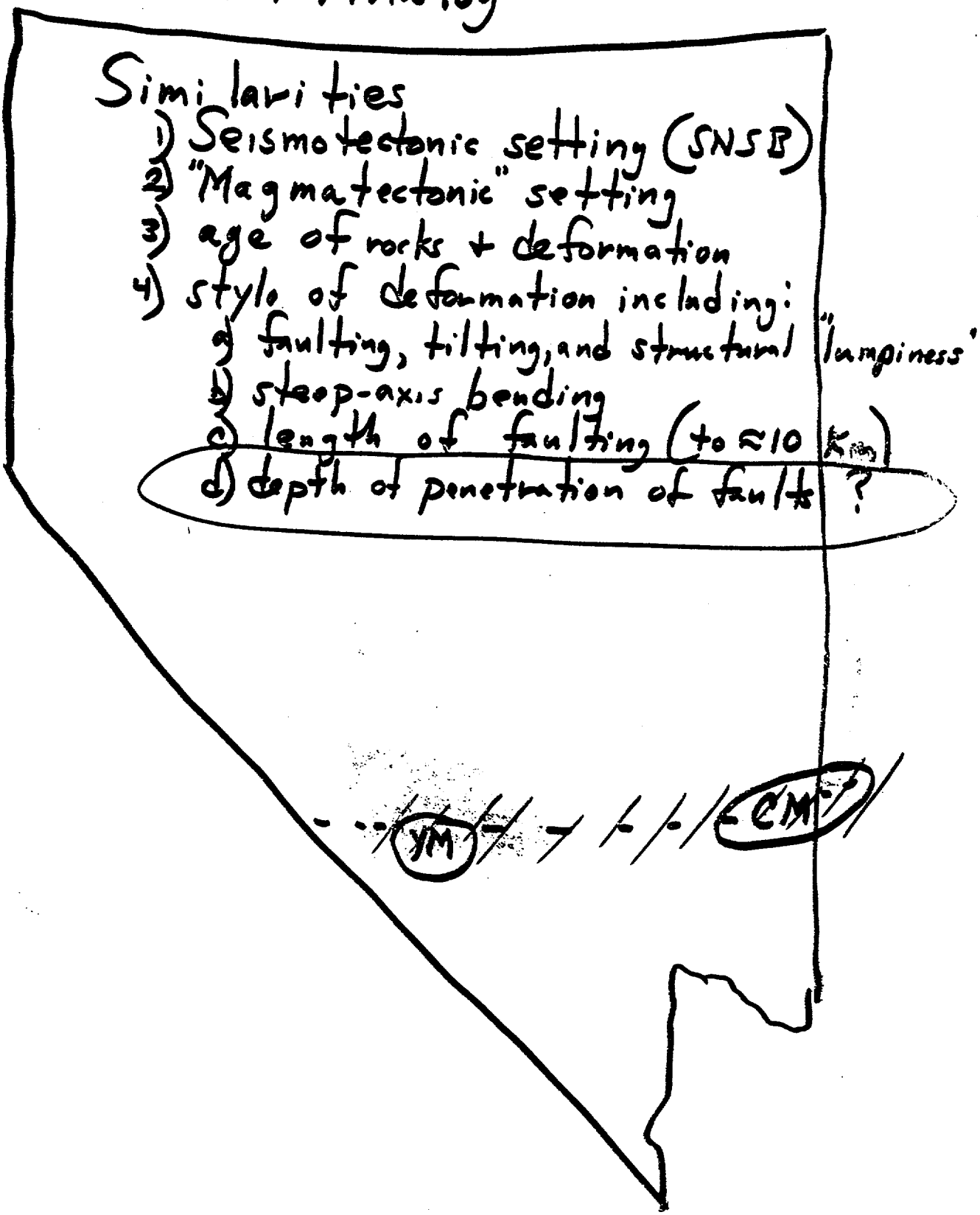

Fault Displacement Hazard

The 100 km Seismicity Catalog and the Background Earthquake

Ken Smith
January 8, 1997
Workshop #4
Salt Lake City, Utah


0 10 20 30
Kilometers
25
24
22
20
18
16
Log Mo

94 Year - 100 KM Seismicity Catalog

- b = .907
- a = $10^{5.3}$ M(0)
- M > 3 removed from area around Pahute Mesa and Yucca Flat
- Fit to M > 3
- Seismicity Strain Rate (*Slip Rate*) = 0.36 mm/yr
- Mw = 6.24

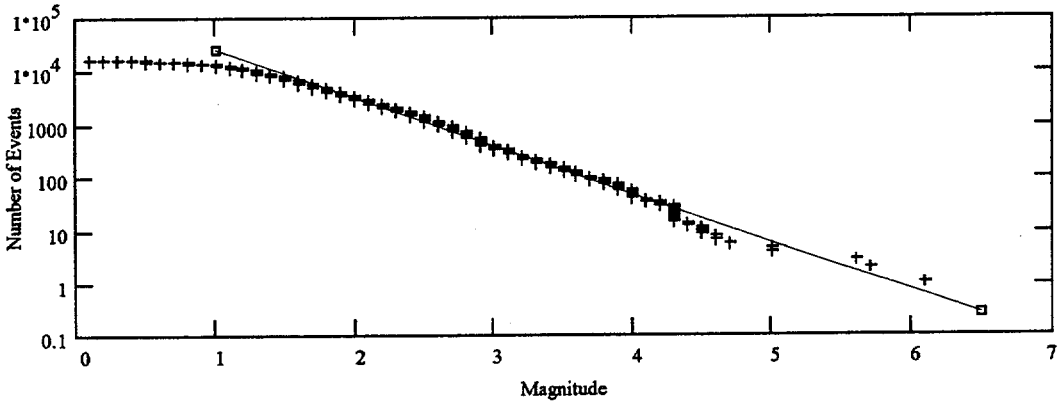

Estimated 94 Year Recurrence

- Mmax = 7
- a = $10^{4.7}$ M(1)
- Strain Rate (*Slip Rate*) = 1.2 mm/yr
- Mw = 6.6

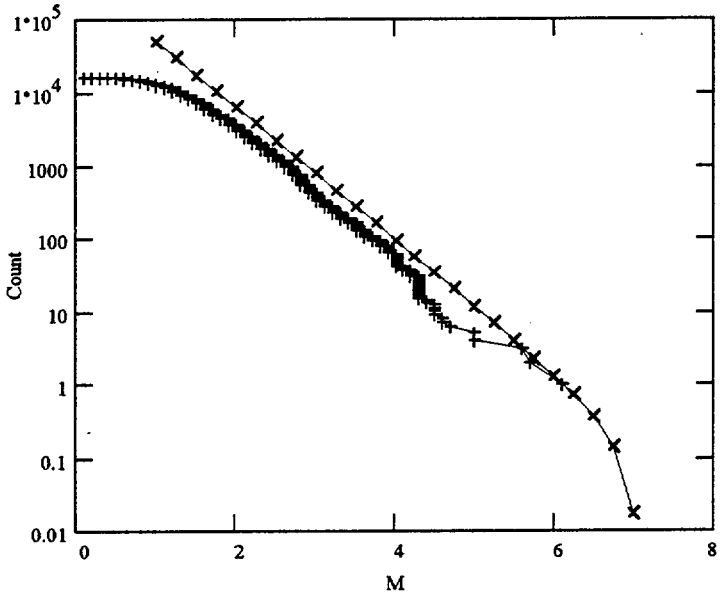

Estimated Yearly Recurrence

- $a = 10^{2.7}(M(1))$
- Mw = 5.2

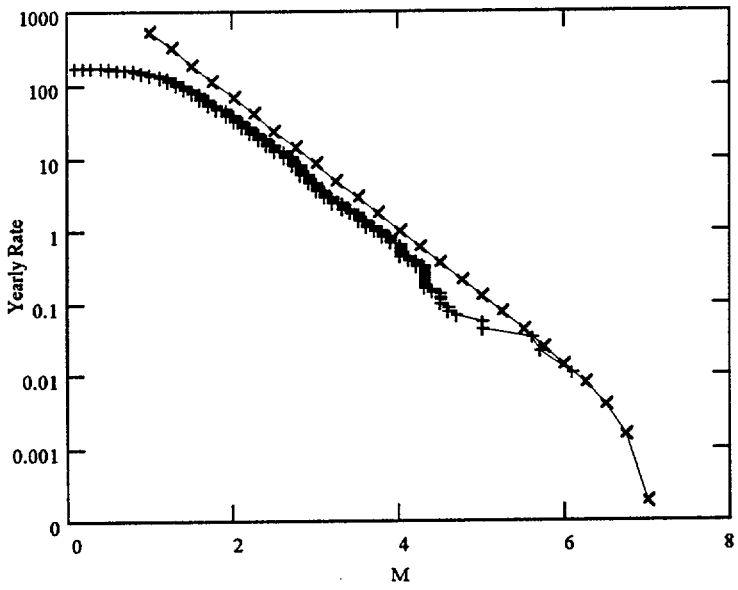

Estimated Yearly Recurrence (25x20 km area)

- a = $10^{0.9}$ (M (1))
- Strain Rate (*Slip Rate*) = 0.16 mm/yr
- Mw = 4.1

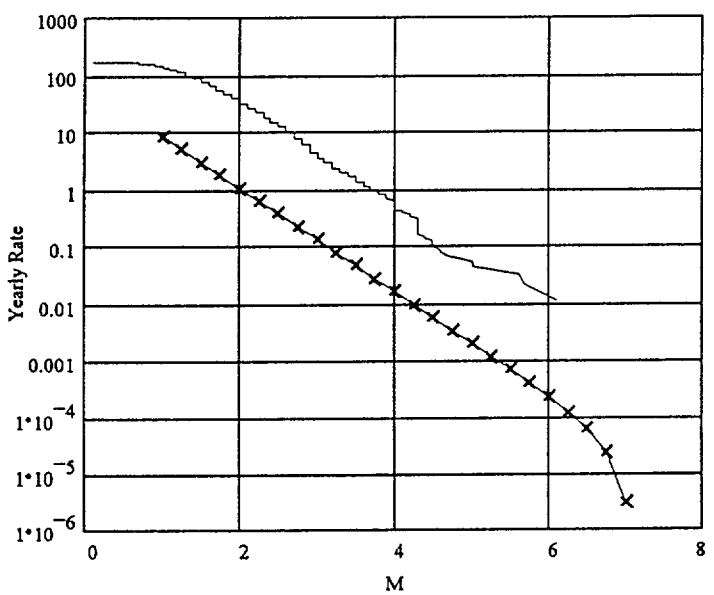

Yearly Recurrence Rate - Model-3 Chapter 5

- 9 Earthquakes
- 150k Years

Model-3 Earthquakes

- Strain Rate (*Slip Rate*) = 0.06 mm/yr
- Mw = 3.8

From Recurrence Curve

- $a = 10^{0.6}$ (M(1))
- Strain Rate (*Slip Rate*) = 0.08 mm/yr
- Mw = 3.9

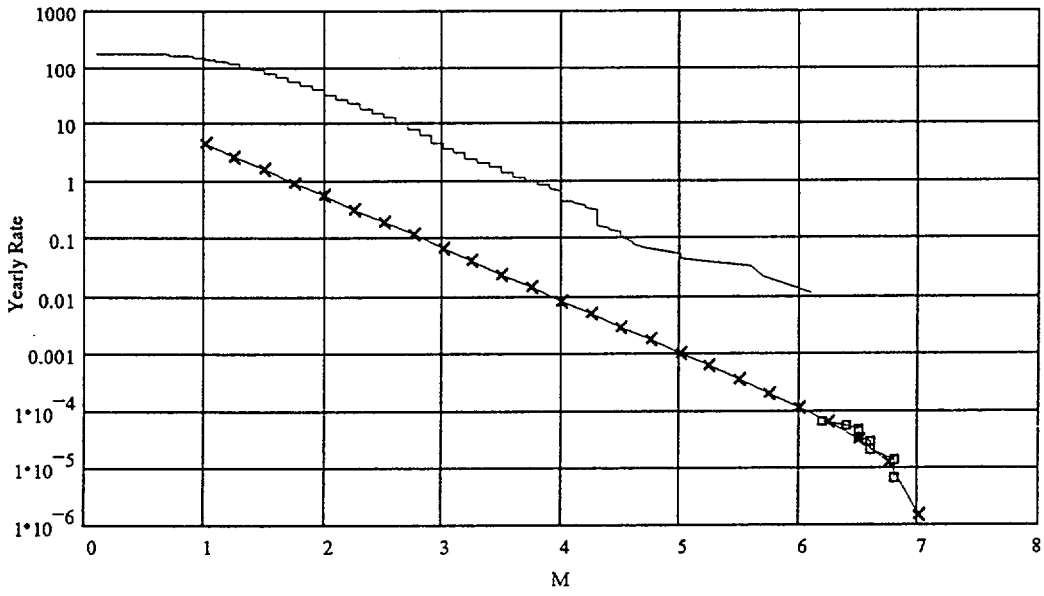

Q: are we trying to predict what's in the REPOSITORY:
or, what might happen given what's known to be in the REPOSITORY?

Workshop #4 - Wed. am

Fault Displ. Hazard

McCALPIN
Wed. 11:15 am
Jan. 8, 1997
Workshop #4

Anderson
- dip-slip faults longer along strike than down dip
- net slip scales w/ length (linear relation)
- single-event slip scales w/ rupture length (linear regression, WC 94)
- ∴ single-event slip should scale linearly with total cumulative displ

NOT SOURCES OF PRIMARY DISPL.
- Sundance – NW
- Drill Hole Wash – NW
- Pagany Wash – NW
- Severi Wash

} transfer faults?

- confined faults = ~~blind~~ hit surface + are bounded
- unconfined faults = dips out below surface is reached · totally within crust

- TYPICAL ASPECT RATIOS in historic ruptures 1.5–1.8

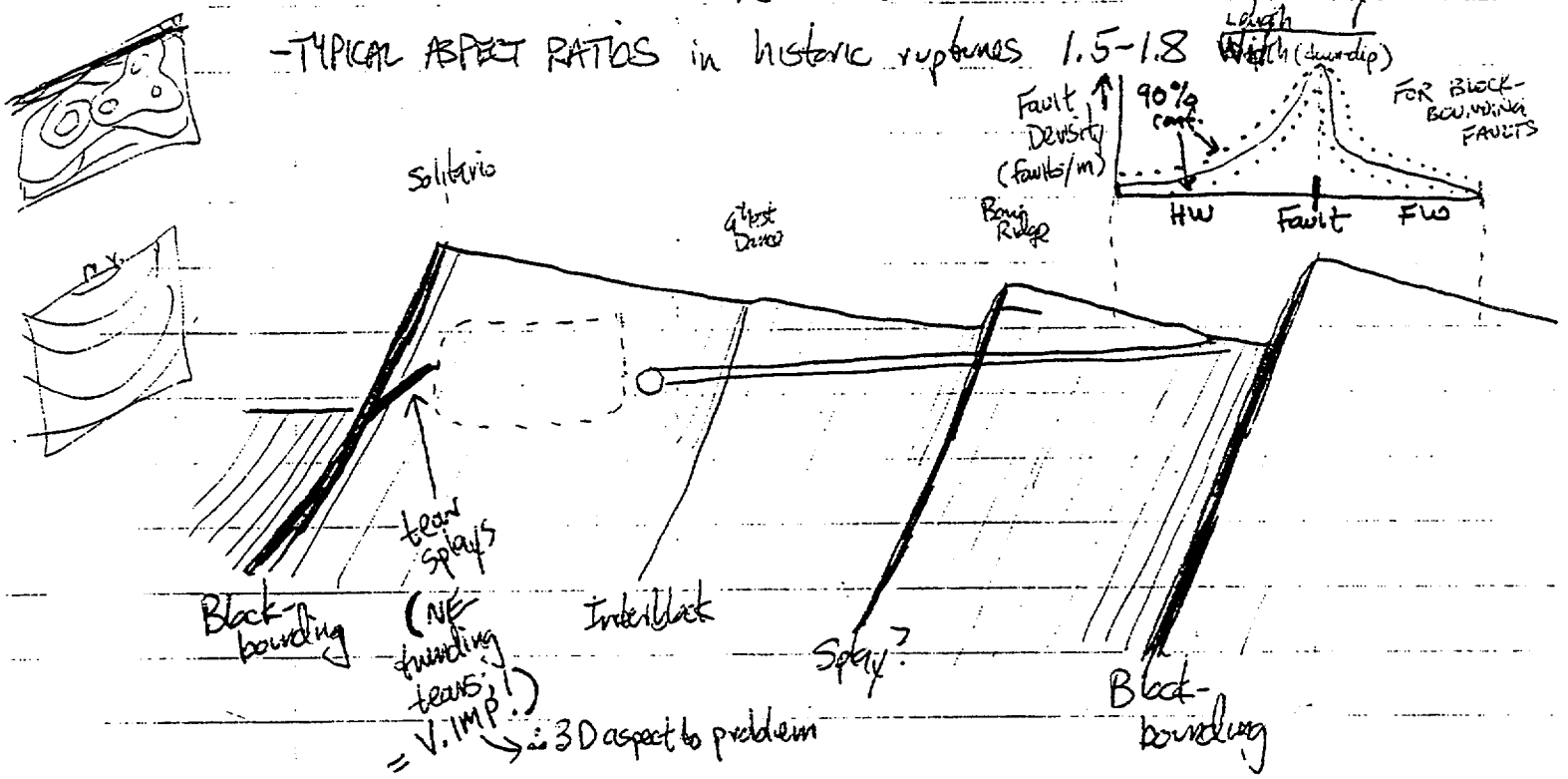

∴ 3D aspect to problem

Q: is the shape of the Fault Density PDF the same for all fault types
- Block bounding faults? IF SO, WE CAN SCALE UP OBSERVED PDFs to Solitario Cyn
- Splay faults? BOW RIDGE
- Interblock faults? GHOST DANCE
- Tear Faults SUNDANCE

# of faults created per event? ⇐ Total # of faults (fractures) / # of paleo-disp sites

[ESF penetrates]

ULTIMATE QUESTION: how much faulting occurs in a single event?

Brahin

$$\frac{D_{fract}}{D_{max}} = R$$

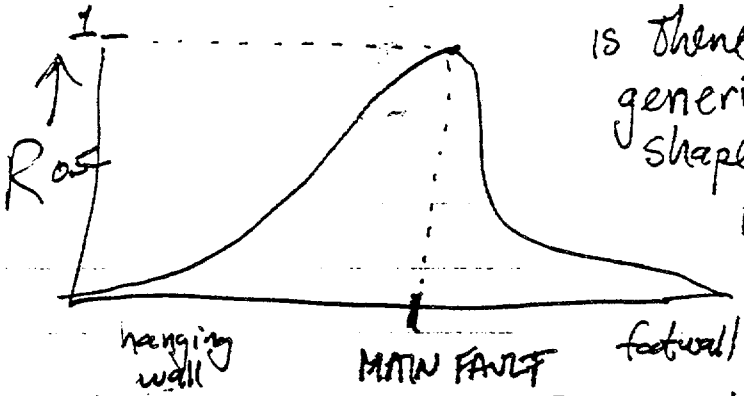

Is there a generic shape to this PDF?

Going from the Cumulative Fracture PDF to the Individual Event Fracture PDF ⇒

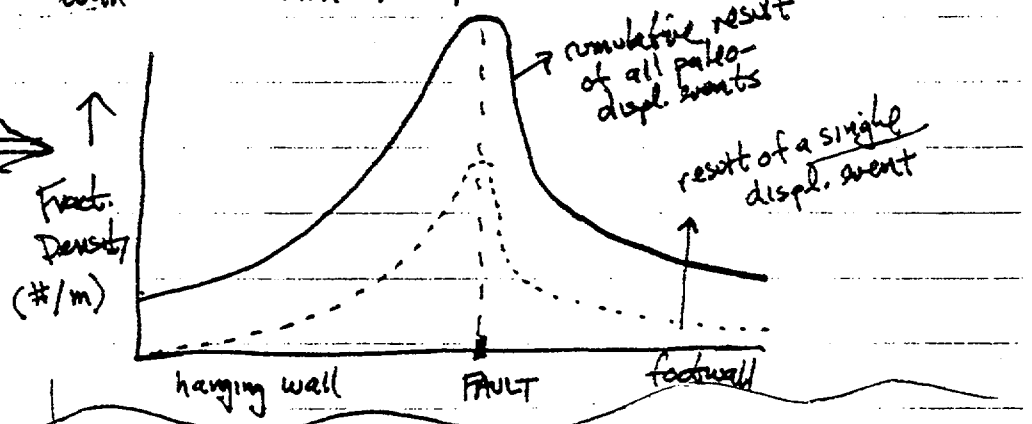

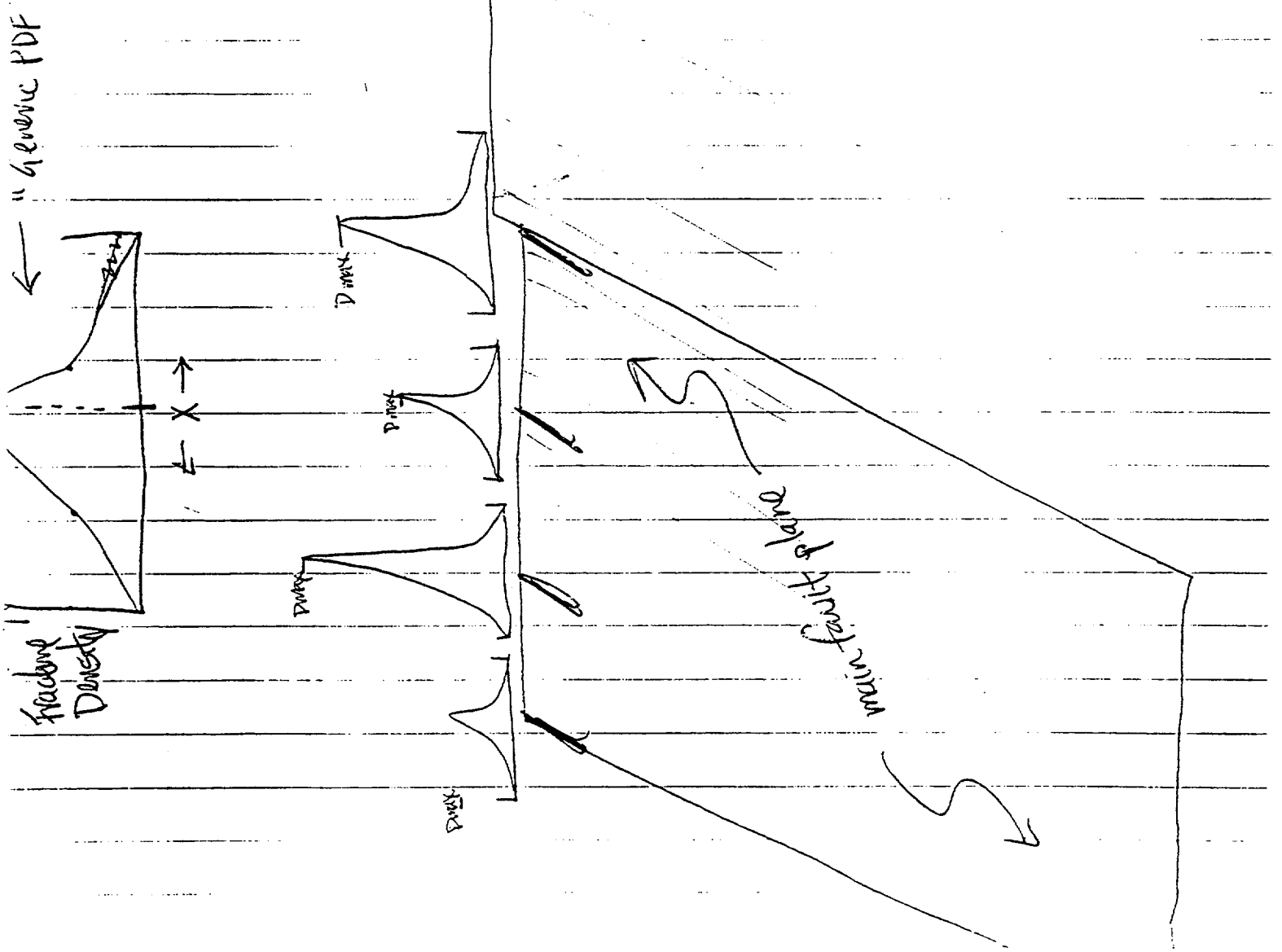

E. Anderson – in Clover Mtns, faults < 5 km long die out downward + do not penetrate the entire thickness of T. vols, or die out in underlying Paleozoics

– could use to de-convolve the net fracture density in the ESF into footwall + hanging wall components assignable to indiv. faults

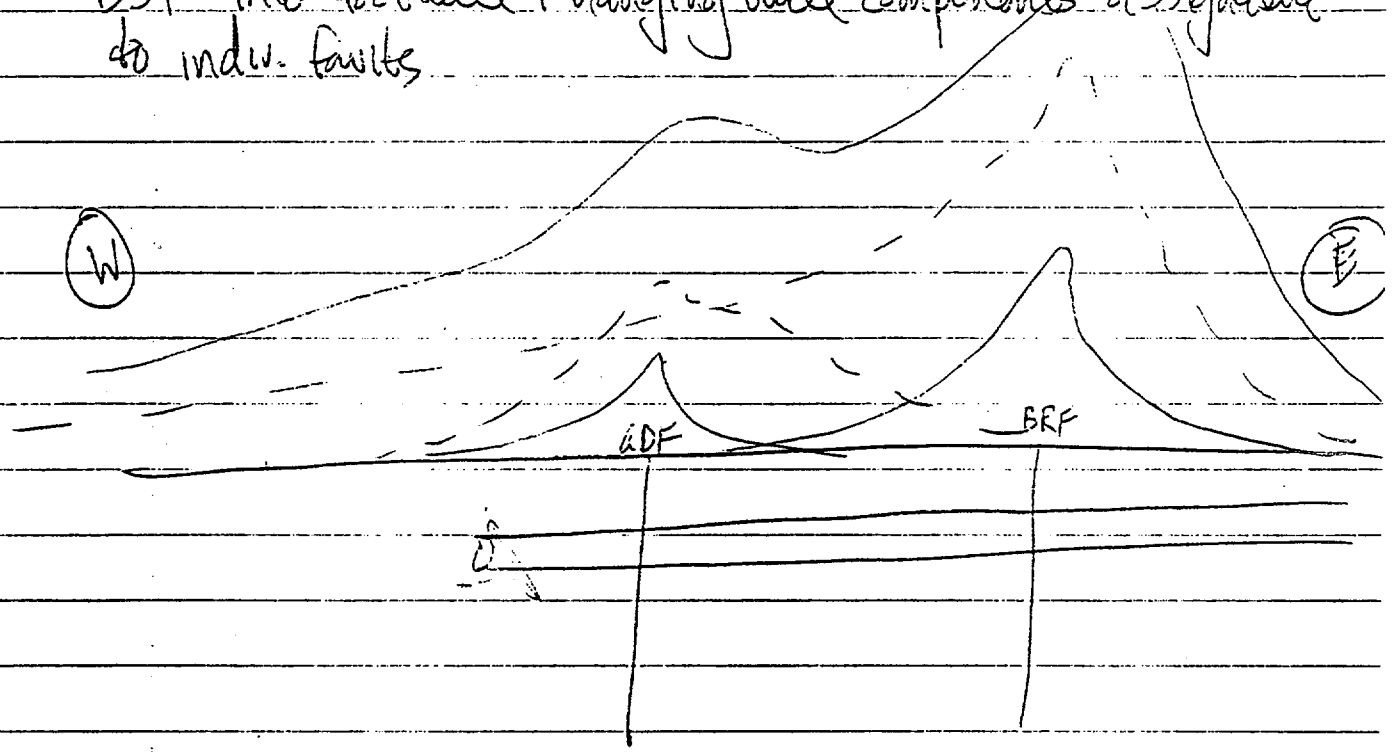

MODERN ANALOGS = tunnels cut by historic surface ruptures

1) San Andreas, 1906 – water tunnel
2) Kern Co., 1952 – railroad tunnel
3) San Fernando, 1971 – water tunnel

4) Chalk Mtn – (Fairview Pk) – mining tunnel

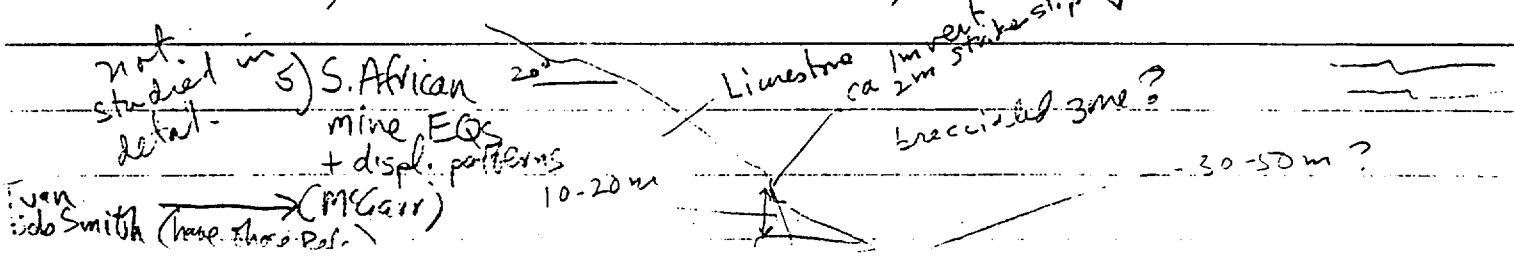

1) Inventory fracture density + displ. + orientations in ESF
2) throw out cooling fractures
3) throw out Miocene fractures/faults
4) calculate post-Miocene displ. on major faults ≥ SCF, GDF, BRF
5) deconvolve (if overlap) density + displ. data into separate populations ≥ GDF, BRF → any other big faults
6) establish a "generic PDF" for cumulative (post-Miocene) Fracture Density and Normalized Displ ($\frac{D\,fract}{D\,max} = R$)
7) scale up "generic cumulative PDFs" for Fract. Dens + Norm. Displ. for SCF (based on net post-Mio. displ.)
8) estimate number of post-Mio. characteristic EQs on SCF = N
9) divide "generic cumulative PDF" for Fract. Density by N, to establish "predicted, single-event PDF" for Fract. Density for SCF

- for Norm. Displ., no need to divide by N ? because $\frac{D\,fract}{D\,max}$ should remain constant at a given distance from main fault = TIME INVARIANT

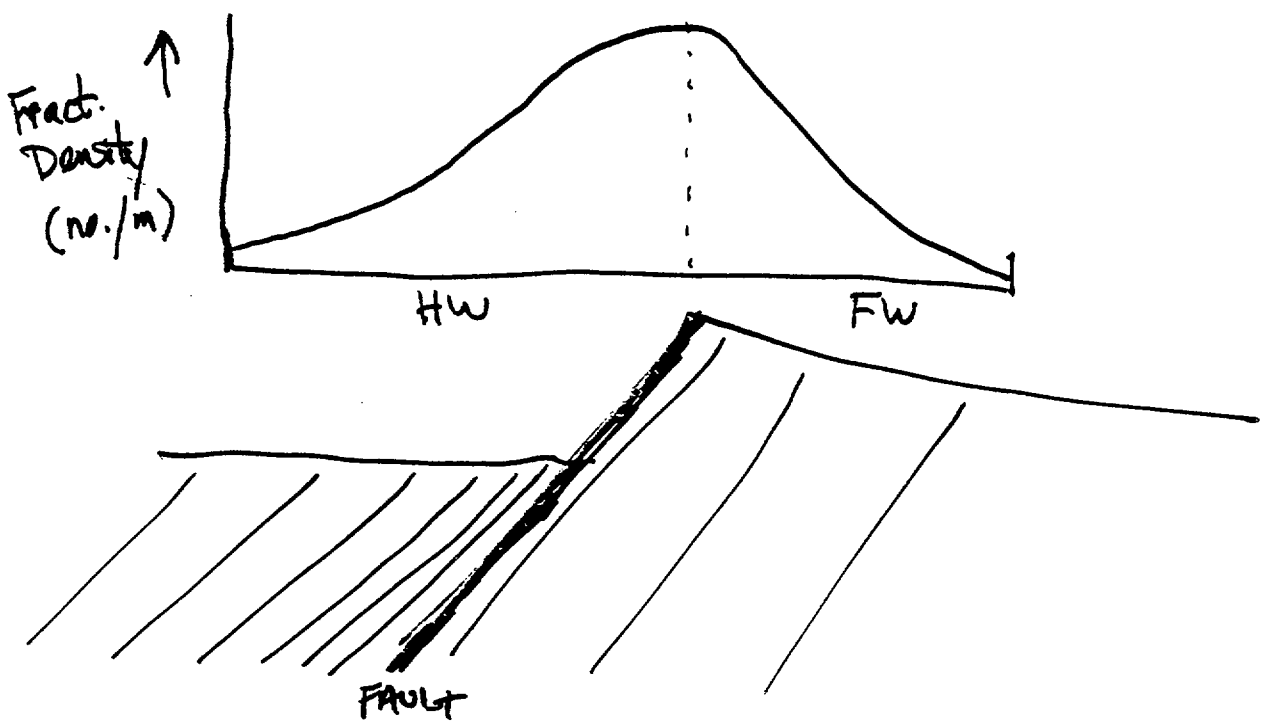

Fault Displacement Hazard

Bob Youngs

Jan. 8, 1997

Example GIS Characterization of the
Summed Length of Distributed Faulting versus Distance to the Principal Rupture Zone
for Surface Ruptures of the 1959 Hebgen Lake, Montana, M 7.4 Earthquake

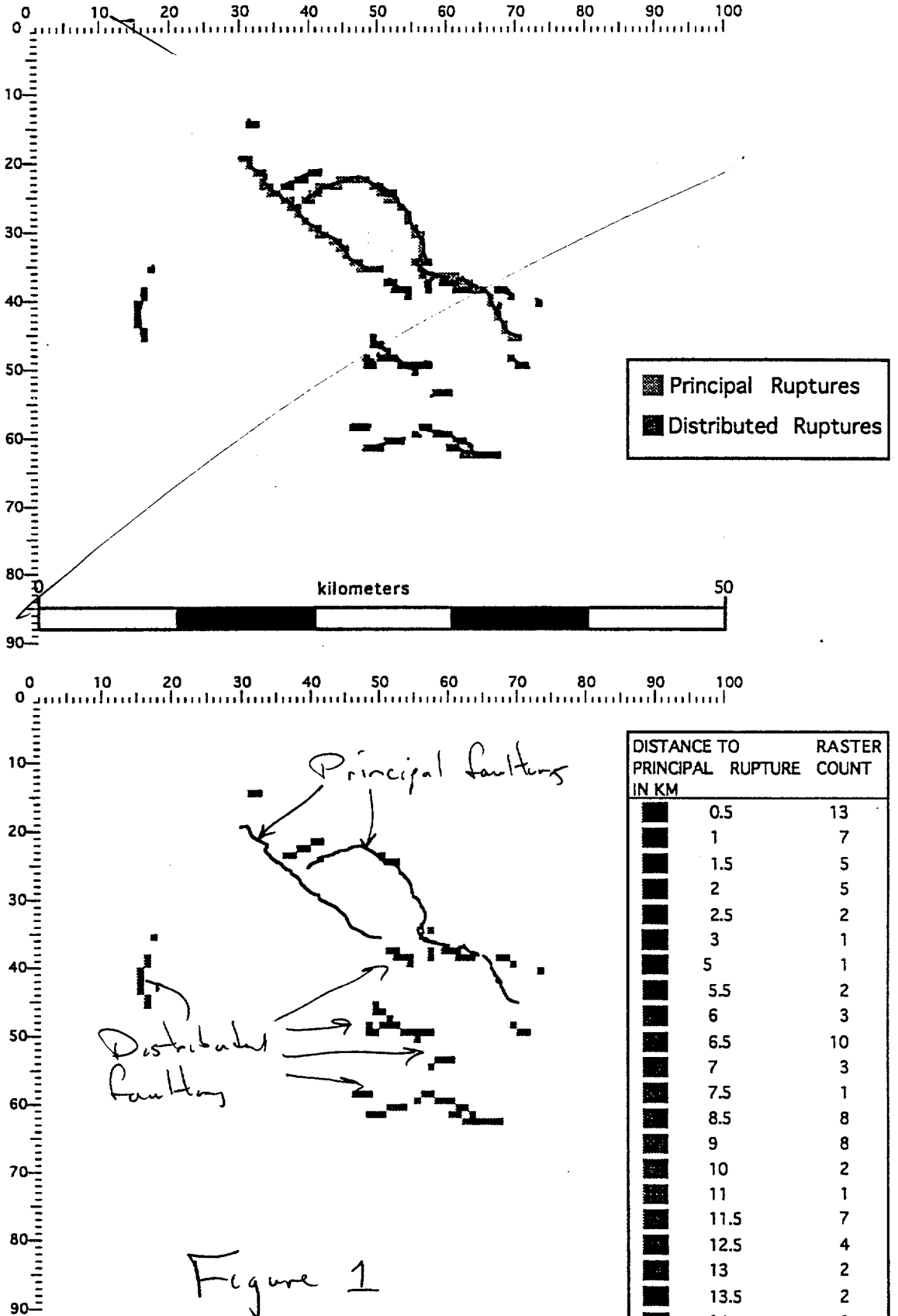

DISTANCE TO PRINCIPAL RUPTURE IN KM	RASTER COUNT
0.5	13
1	7
1.5	5
2	5
2.5	2
3	1
5	1
5.5	2
6	3
6.5	10
7	3
7.5	1
8.5	8
9	8
10	2
11	1
11.5	7
12.5	4
13	2
13.5	2
14	1

Figure 1

USGS-YMP Pezzopane Nov 96

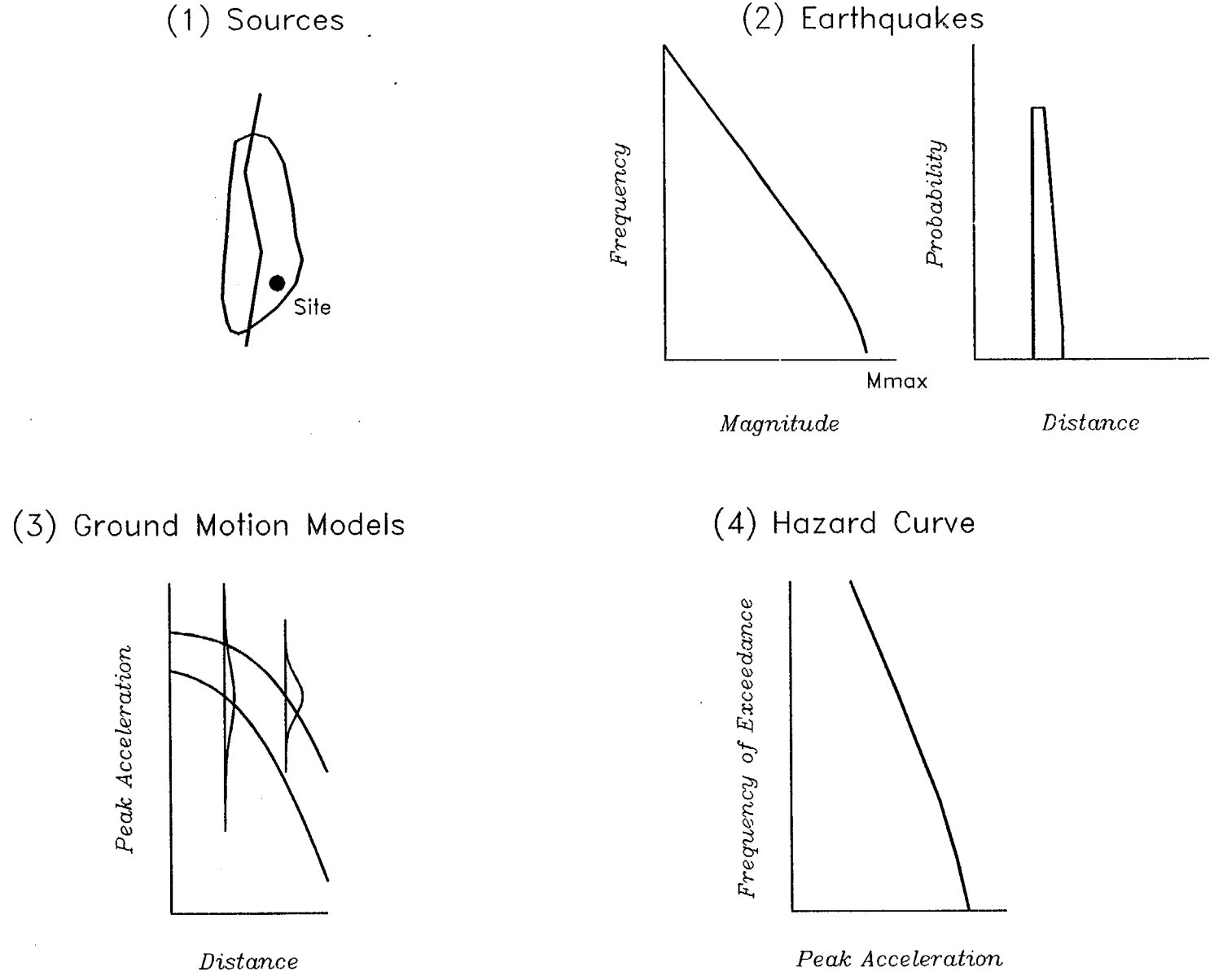

Figure 3 Schematic diagram of the components of PSHA for Ground Motion

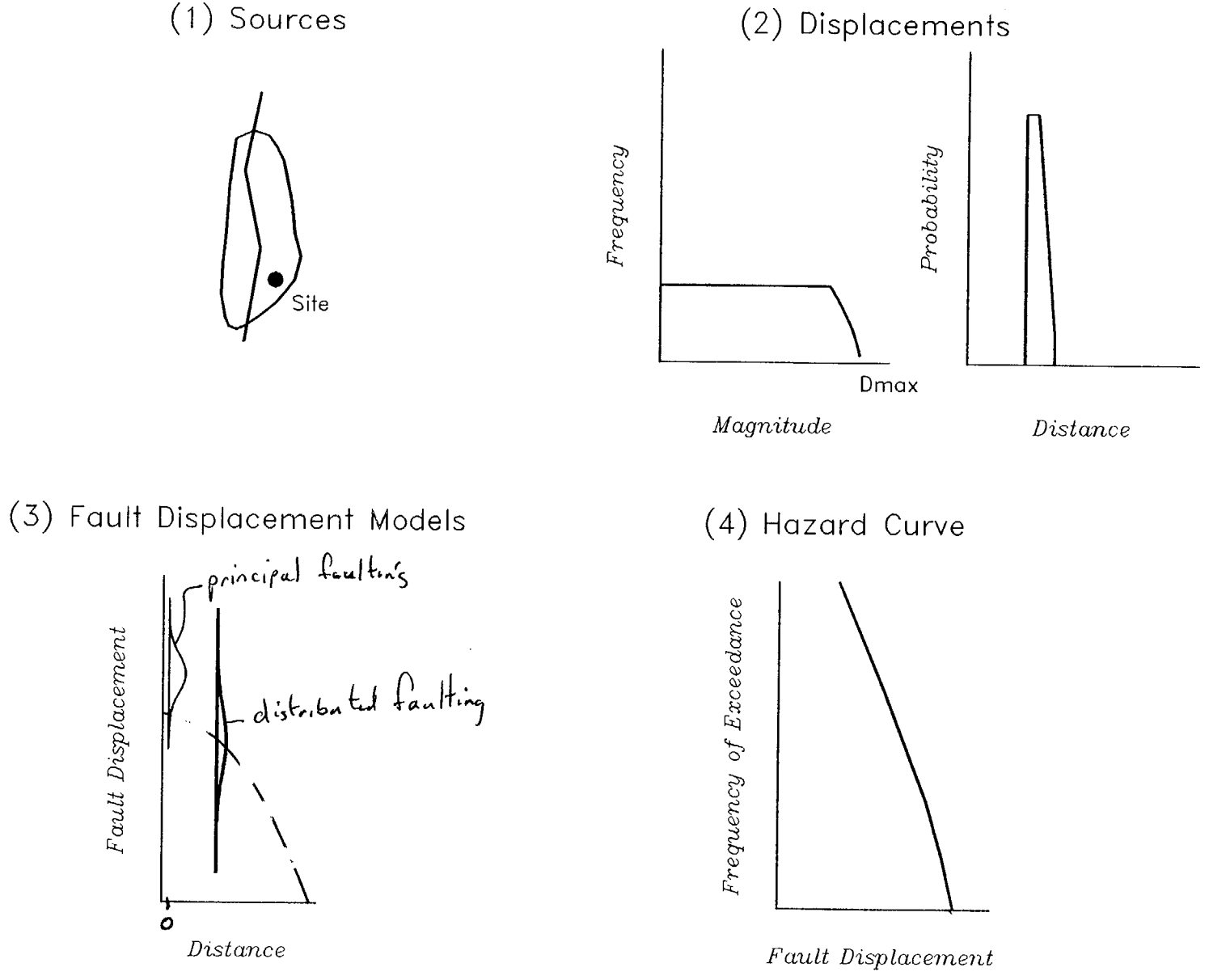

Figure 4 Schematic diagram of the components of PSHA for Fault Rupture

DISTRIBUTED RUPTURES FROM HISTORICAL BASIN AND RANGE EARTHQUAKES

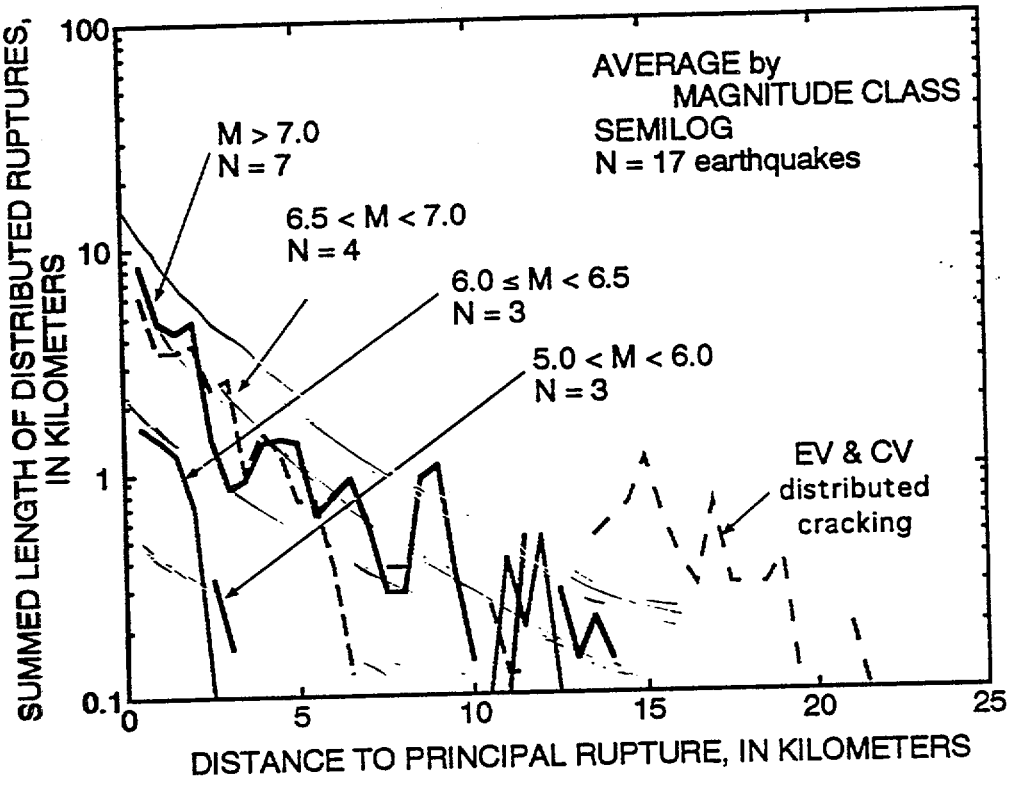

Figure 8

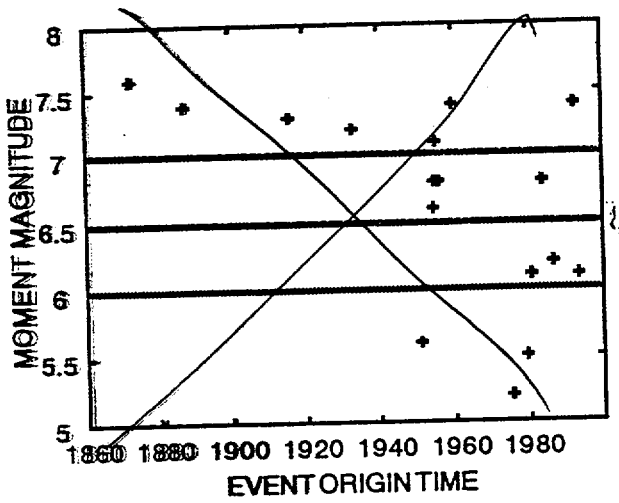

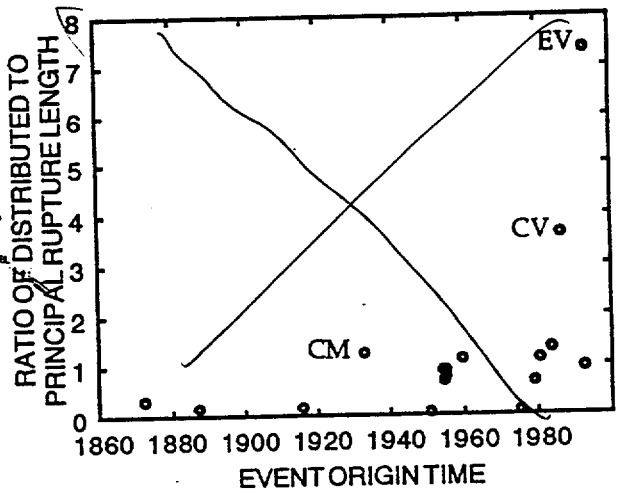

Bulletin of the Seismological Society of America, Vol. 86, No. 5, pp. 1487–1506, October 1996

Earthquake Magnitude Potential of the Intermountain Seismic Belt, USA, from Surface-Parameter Scaling of Late Quaternary Faults

by David B. Mason*

Abstract Two of the largest historical earthquakes documented for the United States occurred within the past four decades in a zone of anomalous seismicity in the western interior of the country known as the Intermountain Seismic Belt (ISB). Paleoseismology has revealed the presence of major active faults throughout this region, some of them extending through densely populated areas. This study presents mean-value estimates of the maximum earthquake magnitudes that can be expected from 65 of the most prominent late Quaternary fault segments of the ISB using surface rupture parameters. Linear, least-squares regressions of magnitude on surface rupture length, L, maximum surface displacement, D, and DL, respectively, were computed for an updated worldwide set of historical, normal-slip earthquakes. These were compared with similar regressions from other publications, and it was found that a DL-based formula restricted to normal-faulting mechanisms has a relatively high correlation, low standard deviation, and tends to yield magnitudes between those given by D and L alone. This last property is useful for applications to the ISB prehistoric data, where the record of historical, ground-rupturing earthquakes is too sparse to estimate the proportions in which D and L are likely to contribute to seismic energy release of a fault. Application of regressions to published paleoseismic displacements and estimated earthquake segment lengths for the ISB faults shows that D consistently scales a larger magnitude than the corresponding single-segment L by an average of 0.2 to 0.3 magnitude unit, after accounting for bias from the regressions. Considerations of uncertainties in paleoseismic displacements suggest that they cannot fully explain the discrepancy. Since it is known that large earthquakes often encompass multiple segments of a fault, these observations indicate that longer rupture lengths should be used to estimate maximum magnitudes for ISB faults. A dual-segment rupture scenario produces better agreement between D- and L-based magnitudes and is supported by historical and paleoseismic earthquake data from the region. Magnitudes scaled by the DL-based regression for dual-segment rupture range from M_s 6.8 to 7.5 ($\sigma_m = \pm 0.20$), and the largest are associated with the central segments of the Wasatch fault and the Swan/Grand Valley, Teton, Madison, and East Bear Lake faults.

Introduction

In the western part of the United States, a prominent zone of seismicity known as the Intermountain Seismic Belt (ISB) extends about 1400 km from southern Nevada and northwestern Arizona northward through central Utah and western Wyoming, with branches into southeastern Idaho and most of western Montana (Fig. 1). The area enclosing the ISB as defined in Figure 1 has been referred to as the Intermountain region by Smith and Arabasz (1991) and limits the area of this study. Most of the earthquakes occur within a zone 100 to 200 km wide and originate within the first 20-km depth. The ISB has experienced two severe ($M \geqq 7.3$) earthquakes since its settlement in the mid- to late 1800s, and growing evidence from the paleoseismic record compiled over the past two decades indicates that similar large earthquakes have repeatedly struck throughout the region during the Holocene.

This study evaluates the mean-value maximum magnitudes that can be expected from large earthquakes on prom-

*Present address: Science Applications International Corporation, Center for Monitoring Research, 1300 N. 17th Street, Suite 1450, Arlington, Virginia 22209.

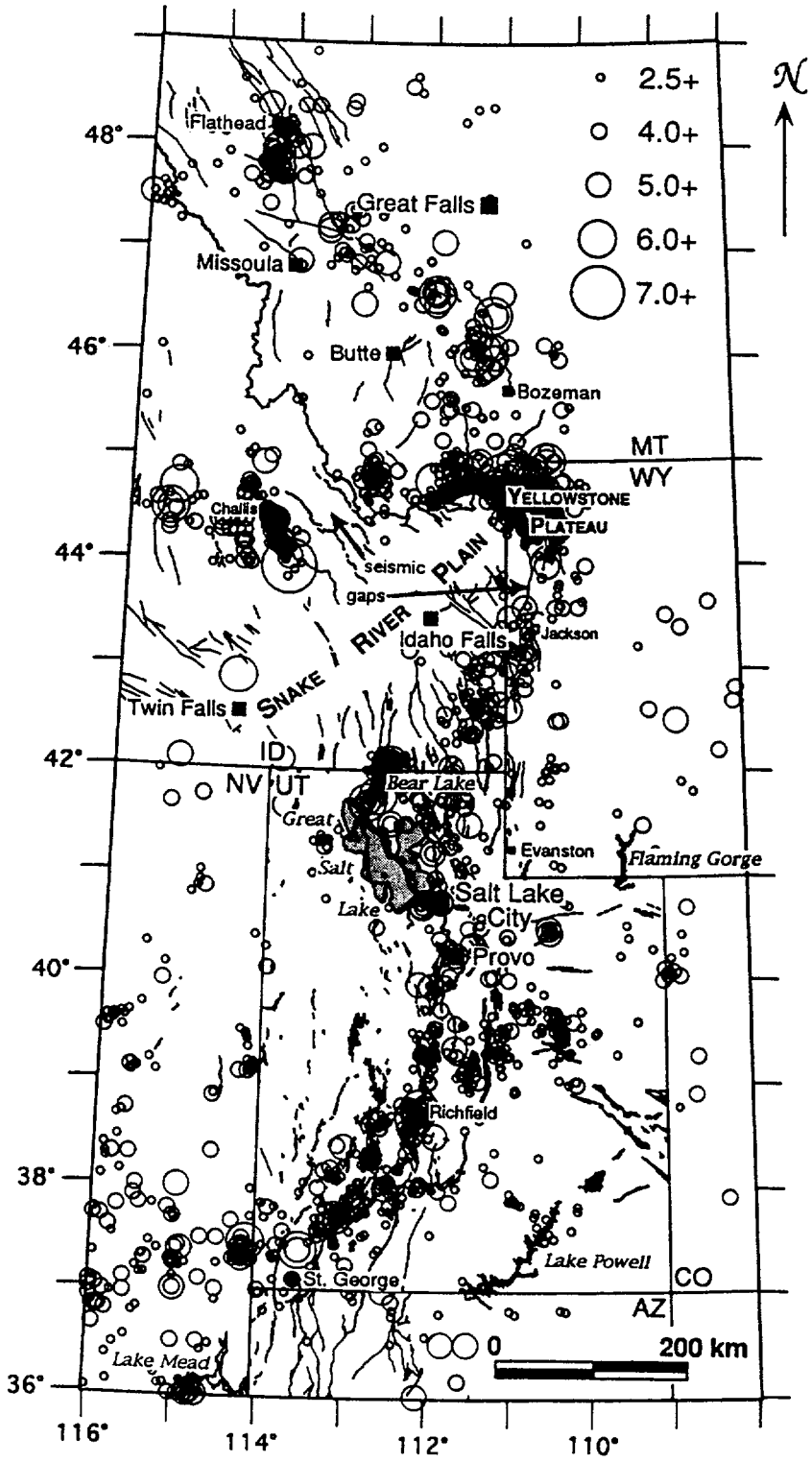

Figure 1. Earthquakes of the Intermountain Seismic Belt (ISB) with $M \geqq 2.5$, from 1900 through 1985 (from Engdahl and Rinehart, 1991) in relation to Quaternary faults and prominent geographic features.

inent active faults of the ISB by applying regressions of magnitude on surface rupture data from historical earthquakes having instrumentally computed magnitudes to paleoseismic data from ISB faults. It concludes preliminary work by Smith *et al.* (1990) and Mason (1992). Most of the faults included (highlighted in Fig. 2) lie within the central ISB, where the most reliable and best-preserved evidence for latest Quaternary earthquakes has been found to date. It includes the urban corridor along the Wasatch front of Utah, one of the largest population centers in the Intermountain region.

Intraplate extension dominates contemporary tectonics

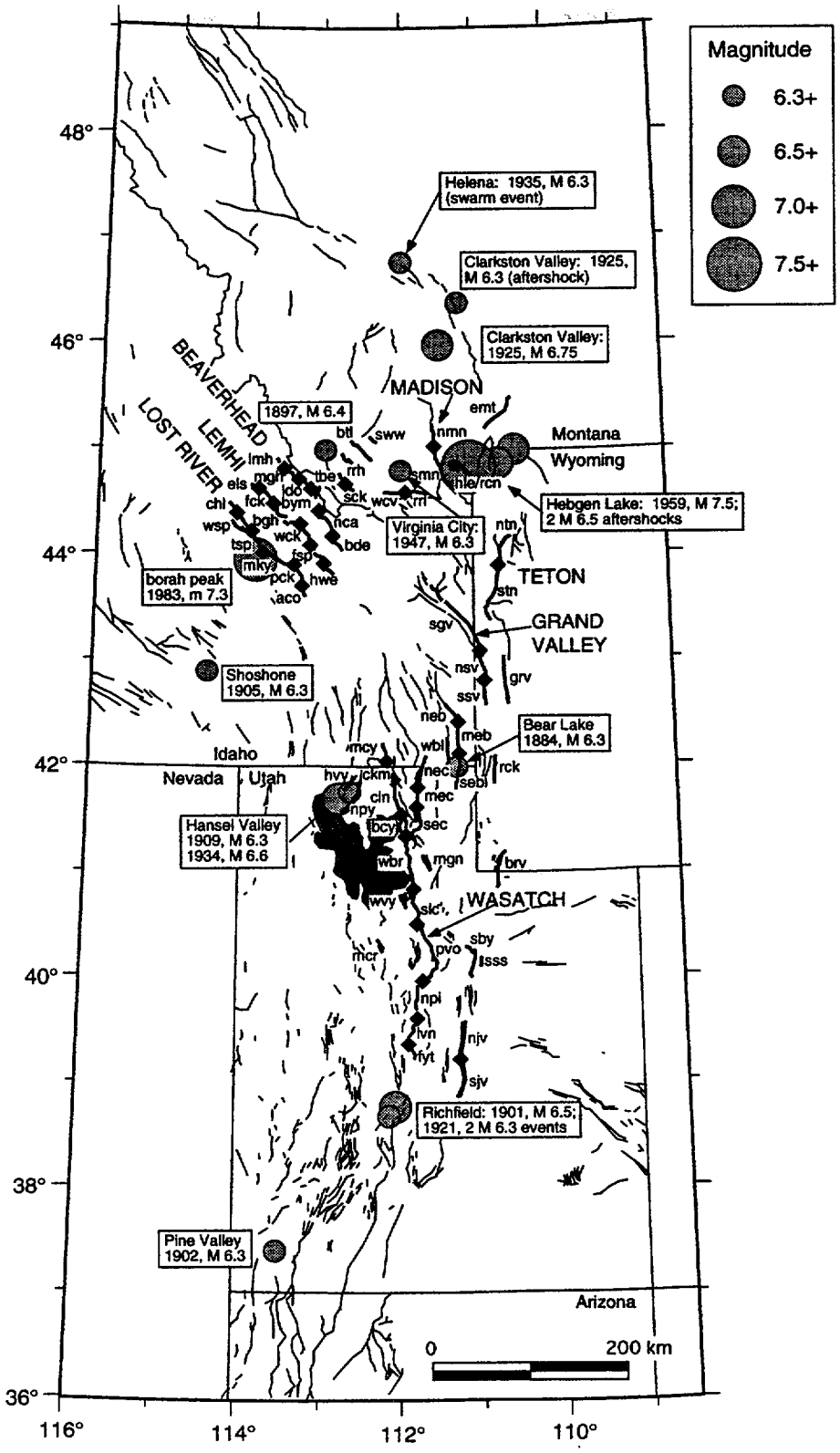

Figure 2. Quaternary faults of the ISB and historical earthquakes at or above the threshold magnitude for surface rupture ($M \geqq \sim 6.3$, from Engdahl and Rinehart, 1991; Smith and Arabasz, 1991). Faults selected for magnitude scaling in this study are shown in bold. Diamond symbols mark the ends of estimated earthquake segments as proposed in the literature. The three-letter segment labels correspond to entries in Table 2.

of the ISB. In tracing out the margin between the Basin and Range province to the west and the stable continental craton to the east, the ISB exhibits most of the structural and morphologic features of the former. Faulting is typically characterized by normal to normal-oblique slip, with σ_3 ranging from east-northeast to east-southeast (Savage *et al.*, 1985).

Two major tectonic events have markedly influenced the present shape of the ISB. The eastward thrusting Sevier orogen of the late Cretaceous left generally north–south structural fabrics against the west margin of the resilient preexisting Colorado Plateau and may have provided a locus for evolution of the ISB through much of central Utah (e.g., Smith and Bruhn, 1984). Farther north along the Snake River Plain of southern Idaho, migration of the continent over the Yellowstone hotspot has distorted the central ISB into a northeastward-vergent parabolic pattern focused on the present location of the caldera in northwestern Wyoming. The limbs of the parabola extend westward through central Idaho and south- to southwestward to the area just north of the Great Salt Lake (Fig. 1), bounding the relatively aseismic eastern Snake River Plain in southern Idaho. This volcanic basin developed in response to the east to northeast passage of the hotspot through the region since late Tertiary time (Smith *et al.*, 1982; Sparlin *et al.*, 1982).

Several aspects of the historical earthquake record for the ISB suggest that it presents a significant seismic risk. High rates of microseismicity in the ISB were recognized as early as the 1930s by Heck (1938) and later described by Woolard (1958), Ryall *et al.* (1966), Sbar *et al.* (1972), and Smith and Sbar (1974). All 16 historical earthquakes with magnitudes believed to have been at or above the threshold for surface rupture ($M \geqq \sim 6.3$) documented for the Intermountain region since its settlement in the last century occurred within the ISB (Fig. 2). The earthquakes at Hebgen Lake, Montana, in 1959 (mainshock M_S 7.5; Witkind, 1964) and Borah Peak in the central Lost River range of east-central Idaho in 1983 (M_S 7.3; special collection of articles in *Bull. Seism. Soc. Am.*, 1987, Vol. 77, no. 3, 694–876) were the largest and caused major surface deformation. The M_S 6.6 Hansel Valley, Utah, event of 1934 is the only other historical earthquake in the ISB known to have been associated with surface rupture (~12 km, possibly secondary; Shenon, 1936). The high seismic risk of the region is also suggested by the presence of two seismic gaps within the Yellowstone parabolic arc (Fig. 1). One coincides with the Teton fault of west-central Wyoming (Smith, 1978) and the other with the Beaverhead, Lemhi, and southern Lost River ranges of east-central Idaho (Smith and Arabasz, 1991). These seismic gaps are considered to represent areas with relatively high probability for the occurrence of large earthquakes (e.g., Mogi, 1985). The ISB gaps coincide with four of the most active fault systems in the region. For a more detailed review of the present tectonic setting and earthquake record of the ISB, see Smith and Arabasz (1991).

In addition to the historical earthquake record, paleoseismic investigations of the most prominent, well-preserved fault scarps throughout the ISB indicate that many active faults throughout the region show evidence for repeated ground-breaking earthquakes, with recurrence intervals of hundreds to tens of thousands of years (e.g., Machette *et al.*, 1992; Hecker, 1993; McCalpin, 1993; Scott *et al.*, 1985). Based on these investigations, "active" is used here to refer to faults that still exhibit evidence of geologically abrupt ground breakage and, therefore, rarely includes structures for which the last such event is more than a few tens of millennia old. The best example—the ~370-km-long Wasatch fault through central and northern Utah (Fig. 2)—is the longest continuously active normal fault in the United States (Machette *et al.*, 1991). Because of its high late Quaternary slip rates, well-preserved scarps, and coincidence with the region's most populated area (~1.7 million people), it has been the subject of numerous paleoseismic investigations [see Machette *et al.* (1992) for review]. The Wasatch was largely responsible for leading Schwartz and Coppersmith (1984) to their "characteristic earthquake" hypothesis, which proposes that a fault or fault segment tends to produce earthquakes of similar size.

The rationale of scaling magnitude from surface rupture parameters comes from the assumption that the logarithms of the same physical quantities that define seismic moment—fault rupture area, average displacement, and rigidity—should also vary in proportion to magnitude, a log-based empirical measure of earthquake size. A one-to-one correspondence has been demonstrated by Kanamori (1983) to exist between traditional and moment magnitude (Hanks and Kanamori, 1979) scales over limited ranges of values, the limiting factor being the frequency dependence of the former (Kanamori, 1977). The following articles develop the physical and statistical theory behind source parameter scaling and discuss factors affecting its reliability: Tocher (1958), Iida (1965), Bonilla and Buchanan (1970), Wesson *et al.* (1974), Mark (1977), Slemmons (1977), Bolt (1978), Acharya (1979), Mark (1979), Wyss (1979), Bonilla and Wyss (1980), Slemmons (1982), Bonilla *et al.* (1984), and Wells and Coppersmith (1994). The discussions beginning with Bolt (1978) have particular relevance to methods involving surface data.

Data Selection

The data involved in this study included maximum single-event surface displacements, D, surface rupture lengths, L, and surface-wave or moment magnitudes. They fall into two categories: (1) historical, instrumentally recorded earthquakes used in the regressions and (2) prehistoric, scarp-forming earthquakes in the ISB of late Quaternary age. Because many of the factors affecting the assessment of the surface parameters are common to both the historical and prehistoric data sets, the following discussion applies to both categories, except where noted. Data used for the regressions computed by the author and ISB paleoseismic data were ob-

tained from comparisons of as many relevant publications of original field work as could be acquired.

Parameters for the historical earthquakes used in the regressions computed for this study are given in Table 1. Because extension has characterized Quaternary and current modes of tectonism in the ISB, the data were limited to earthquakes with normal- to normal-oblique modes of faulting. Earthquakes were included from worldwide sources to strengthen statistics. Out of 33 events considered, the following 13 were rejected either because of large uncertainties in the source parameters or magnitudes, or because of large components of strike-slip motion: Owens Valley, California (1872); Pitaycachi, Mexico (1887); Locris, Greece (1894); N. Taupo, New Zealand (1922); Cedar Mountain, Nevada (1932); Excelsior, Nevada (1934); Hansel Valley, Utah (1934); Fort Sage Mountains, California (1950); Oroville, California (1975); Thessaloniki, Greece (1978); Corinth, Greece (two events in 1981); and Guinea, W. Africa (1983).

The final set of ISB faults selected for estimation of magnitude potential (Fig. 2) are listed along with their various surface parameters in Table 2. These faults show evidence for one or more geologically abrupt surface-rupturing events (inferred earthquakes) within the latest Pleistocene through Holocene ($< \sim 100$ ka) and have some of the best-preserved scarps in the region. Most of them strike north–south, as expected for the east-northeast to east-southeast σ_3 of the present crustal stress field derived from historical seismicity and well-bore data (Zoback, 1989). Based on these factors, they are regarded here as potentially active structures. Some fault systems were excluded from the data base, because their scarps were either too poorly preserved or too fragmented and distributed for reliable estimation of single-event surface parameters. Others were excluded, because they failed to meet the selection criteria discussed below.

Surface Rupture Length

Weathering and geometric complexity affect the reliability of surface rupture length estimates. For historical earthquakes, careful field work can often identify most of the area in which scarp formation took place, so assessment of L is primarily complicated by spatial distribution and continuity of scarps within the zone. For paleoearthquakes,

Table 1
Surface-Faulting Parameters of Historical, Normal-Faulting Earthquakes*

Event Name	Date (y m d)	M_S	L (km)	D (m)	ds (m)	ss (m)	References‡
Avezzano, Italy	15 01 13	6.95 ± 0.05	25 ± 5	2.0 + 0, − ?	2.0	—	16, 23, 27, 31, 39
Pleasant Val., Nevada	15 10 03	7.61 ± 0.30	70 ± 10	5.8 ± 0.2	5.8	2.0	9, 34, 36
Sabukia, Kenya	28 01 06	6.96 ± 0.26	31 ± 2	2.9 ± 0.5	2.9	0.3	9, 28, 40
Chirpan, Bulgaria	28 04 14	6.57 ± 0.26	36.5 ± 1.5	0.5 ± 0.1	0.4	—	8, 9, 28
Papazli, Bulgaria	28 04 18	6.94 ± 0.21	32.5 ± 2	3.5 ± 0.5	3.5	—	8, 9, 28
Salmas, Iran	30 05 06	7.4 ± 0.19	30 + 0, − 10	6.4 ± 0.2	6.0	4.0	2, 3, 9
Ancash, Peru	46 11 10	6.8 ± 0.50	21.5 ± 0.5	3.5 ± 0.1	3.5	—	1, 7, 14, 16, 32
Rainbow Mtn., Nevada	54 07 06	6.34 ± 0.26	18 ± 1	0.3 ± 0.05	0.3	—	6, 9, 35
Stillwater, Nevada	54 08 24	6.95 ± 0.28	46 + 0, − 12	0.76 ± 0.05	0.76	—	9, 35
Fairview Peak, Nevada	54 12 16	7.24 ± 0.22	48 ± 5	4.75 ± 0.15†	3.7†	3.7†	6, 9, 33, 34
Dixie Valley, Nevada	54 12 16	6.75 ± 0.28	47.5 ± 2	2.4 ± 0.3	2.4	—	6, 9, 37, 42
Hebgen Lake, Montana	59 08 18	7.5 ± 0.40	38 ± 2	5.5 ± 0.1	5.5	—	1, 9, 13, 18, 21, 41
Alasehir, Turkey	69 03 28	6.5	33 ± 3	0.8 ± 0.1	0.8	0.2	2, 15, 43
Gediz, Turkey	70 03 28	7.07 ± 0.17	48 ± 8	2.2 ± 0.05	2.2	—	4, 9, 15
Camp.-Luciana, Italy	80 11 23	6.9	28 ± 3	1.0 ± 0.05	1.0	—	10, 24, 38
Corinth, Greece	81 02 25	6.4	17 ± 0.7	1.50 ± 0.1	1.50	—	17, 19
Dhamer, N. Yemen	82 12 13	6.0	15 ± 1	0.04 ± 0.02	0.04	—	22, 26
Borah Peak, Idaho	83 10 28	7.3	43 ± 7	2.6 ± 0.1	2.6	0.4	11, 12, 18, 29, 30
Kalamata, Greece	86 09 13	6.2	16.5 ± 1.5	0.10 ± 0.01	0.10	0.03	20, 25
Edgecumbe, New Zeal.	87 03 02	6.6	18 ± 2.5	2.5 ± 0.1	2.5	—	5

*Abbreviations: M_S, surface-wave magnitude. Uncertainties represent sample standard deviations from multiple stations or the spread from different published values. L, surface rupture length averaged from trace and straight-line measurements, with the difference in the error bars. D, maximum surface displacement at a single location; ds, dip or vertical component; ss, strike-slip component. The components may have come from different locations.

†Slemmons (1957) reported a maximum lateral surface offset of 12 ft (3.7 m) at Fairview Peak, a maximum vertical slip of 12 ft at Bell Flat, and maximum oblique displacement of 15 to 16 ft (4.75 ± 0.15 m) at Fairview Peak.

‡References: 1 Abe (1981), 2 Ambraseys (1988), 3 Ambraseys and Melville (1982), 4 Ambraseys and Tchalenko (1972), 5 Beanland *et al.* (1990), 6 Bell *et al.* (1984), 7 Bellier *et al.* (1991), 8 Jankof (1945), 9 Bonilla *et al.* (1984), 10 Boschi *et al.* (1990), 11 Crone and Machette (1984), 12 Crone *et al.* (1987), 13 Doser (1985), 14 Doser (1987), 15 Eyidogan and Jackson (1985), 16 Gutenberg and Richter (1954), 17 Jackson *et al.* (1982), 18 Kanamori and Allen (1986), 19 King *et al.* (1985), 20 Lyon-Caen *et al.* (1988), 21 Myers *et al.* (1964), 22 National Earthquake Information Service, USA, 23 Pantosti and Valensise (1990), 24 Pantosti *et al.* (1989), 25 Papazachos *et al.* (1988), 26 Plafker *et al.* (1987), 27 Progetto Finalizzato Geodinamica (1986), 28 Richter (1958), 29 Salyards (1985), 30 Scott *et al.* (1985), 31 Serva *et al.* (1986), 32 Silgado (1951), 33 Slemmons (1957), 34 Slemmons *et al.* (1965), 35 Tocher (1956), 36 Wallace (1984), 37 Wallace and Whitney (1984), 38 Westaway and Jackson (1987), 39 Westaway *et al.* (1989), 40 Willis (1936), 41 Witkind (1964), 42 Slemmons (1977), 43 Ambraseys (1975).

Table 2

Prehistoric Surface Rupture Data and Associated Scaled Magnitudes from the Best Documented ISB Faults of Latest Pleistocene/Holocene Age*

Fault Segment	Map Label (Fig. 2)	L (km)	D (m)†	Last Slip Event (kya)	M from: L (1 segment)	M from: D (1 segment)	M from: DL (1 segment)	M from: DL (2‡)	References‖
Lost River									
Challis	chl	29 ± ?	?	?	6.8	?	?	7.1	44
Warm Spgs.	wsp	17 ± 2	2.7 ± 0.1	0.011	6.5	7.1	6.9	7.1	7, 44
Thousand Spgs.	tsp	25 ± 3	2.6 ± 0.1	0.011	6.7	7.1	6.9	7.1	7, 41, 44, 57
Mackay	mky	19 ± 1	2.6?	4.3 ± 0.2	6.6	7.1	6.9	7.1	7, 41, 44, 57
Pass Crk.	pck	31 ± ?	1.5 ± 0.5	40 ± 10	6.8	6.9	6.9	7.2	44
Arco	aco	20 ± 1	3 ± ?	27 ± 4	6.6	7.2	6.9	^	5, 38, 44
Lehmi									
Ellis	els	11 ± 2	2.9?	≧60	—§	7.2	—§	7.1	6, 18, 53
Falls Crk	fck	28 ± 4	3.0(0.7–1.3)	10.5 ± 3.5	6.8	7.2	7.0	7.2	6, 18, 53
Big Gulch	bgh	38 ± 10	3.3 ± 0.3	8 ± 1	6.9	7.2	7.1	7.2	6, 18, 53
Warm Crk	wck	22 ± 2	3.2 ± 0.2	2 ± 1.5	6.6	7.2	7.0	7.2	6, 18, 53
Fallert Spgs.	fsp	28 ± 8	2 ± ?	22 ± 3	6.8	7.0	6.9	7.1	18, 53
Howe	hwe	21 ± 2	3.0 ± 0.5	17 ± 2	6.6	7.2	6.9	^	6, 18, 29, 53
Beaverhead									
Lemhi	lmh	20 ± ?	?	100 ± ?	6.6	?	?	?	6, 11
Mollie Gulch	mgh	20 ± ?	?	L. Pleist.	6.6	?	?	7.1	6, 11
Leadore	ldo	23 ± ?	3.1 ± ?	5 ± −2	6.7	7.2	7.0	7.1	6, 11
Baldy Mtn	bym	21 ± ?	?	65 ± 35	6.6	?	?	7.2	6, 11
Nicholia	nca	42 ± ?	2.9	15 +0, −?	7.0	7.2	7.1	7.2	6, 11
Blue Dome	bde	25 ± ?	?	pre Quatern.	6.7	?	?	^	6, 11
Red Rock									
Timber Butte	tbe	16 ± 1	3 + 0, −1	15 ± 3	6.5	7.2	6.9	7.0	6, 14, 35, 47
Sheep Creeks	sck	11 ± 1	3 + 0, −1	4 ± 1	—§	7.2	—§	^	6, 14, 35, 47
Red Rock Hills	rrh	11 ± 1	2 ± ?	15 ± 3	—§	7.0	—§	—§	2, 35, 55
Blacktail	btl	24 ± ?	5+0, −2.5	22 ± 8	6.7	7.3	7.1	—	47
Sweetwater	sww	12 ± 1	2+0, −1	15+?, −3	—§	7.0	—§	—§	47
Centennial									
W. Centennial Val.	wcv	23 ± ?	3 ?	7 ± 3	6.7	7.2	7.0	7.1	47
Red Rocks Lake	rrl	25 ± ?	3 ?	65 ± 45	6.7	7.2	7.0	^	47
Madison									
North	nmn	19 ± 2	?	22 ± 3	6.6	?	?	7.4	47
South	smn	42 ± 2	6(1–2)	< 10	7.0	7.4	7.3	^	47
Hebgen Lake	hle	23 ± ?	5.5 ± 0.1	0.035	6.7	7.4	7.1	7.3	30, 47, 58
Red Canyon	rcn	20 ± 2	4.6 ± 0.1	0.035	6.6	7.3	7.0	^	30, 58
Emigrant	emt	25 ± ?	?	12 ± 1	6.7	?	?	—	36, 47
Teton									
North	ntn	13 ± 1	?	?	—§	?	?	7.4	4, 49
South	stn	50 ± 3	6(2.7–2.9)	5.2 ± 1.1	7.1	7.4	7.3	^	3, 4, 49
Grand Valley									
Swan/Grand Val.	sgv	72 ± 2	?	23 ± 8	7.2	?	?	7.5	1, 39
North Star Val.	nsv	28 ± 2	5.8 ± 0.5	9 to 70	6.8	7.4	7.2	7.3	1, 39
South Star Val.	ssv	25 ± 2	5.4 ± 0, −2	5.5 ± 0.1	6.7	7.4	7.1	^	1, 20, 39
Grey's River	grv	54 ± 2	5+0, −0.7	2 ± 0.2	7.1	7.3	7.3	—	15, 16
W. Bear Lake¶	wbl	23 ± 3	5.2(1.5–2.0)	6.2 ± 0.4	6.7	7.3	7.1	—	20, 21
E. Bear Lake									
North	neb	≧20	?	M.–L. Pleist.	≧6.6	?	?	≧7.3	20, 21
Middle	meb	26 ± ?	6+0, −?	5 +5, −0	6.7	7.4	7.2	7.3	20, 21
South	seb	32 ± ?	6(1.3–2.8)	2.1 ± 0.1	6.8	7.4	7.2	^	20, 21
Rock Creek	rck	29 ± 4	6−2, +1	3.6 ± 0.4	6.8	7.4	7.2	—	35
Hansel Valley	hvy	9 ± 1	2.6 + 0, −1.1	0.060	—§	7.1	—§	—	8, 24, 40, 45
N. Promontory	npy	29 ± 3	2.5+0, −0.5	<15	6.8	7.1	7.0	—	12, 24, 40
Mercur	mcr	35 ± 5	3.0+0, −2	32 +170, −16	6.9	7.2	7.1	—	12, 46, 59
West Valley¶									
Granger	ggr	16 ± 1	?	≦12	6.5	?	?	6.8	12, 17
Taylorsville	tvl	8 ± 2	1.5 + 0, −0.3	≦12	—§	6.9	—§		12, 17

(continued)

Table 2
Continued

Fault Segment	Map Label (Fig. 2)	*L* (km)	*D* (m)†	Last Slip Event (kya)	*M* from: *L* (1 segment)	*M* from: *D* (1 segment)	*M* from: *DL* (1 segment)	*M* from: *DL* (2‡)	References‖
Wasatch									
Malad City	mcy	17 ± 1	?	>14	6.5	?	?	?	26–28, 42, 57
Clarkston Mtn.	ckm	18 ± 1	?	>14	6.5	?	?	?	27, 28, 42, 57
Collinston	cln	30 ± 1	?	>14	6.8	?	?	7.4	27, 28, 42, 57
Brigham City	bcy	38 ± 3	6(1.7–2.0)	3.6 ± 0.5	6.9	7.4	7.2	7.5	12, 27, 28, 37, 42, 57
Weber	wbr	59 ± 3	6(0.7–4.2)	0.5? ± 0.3	7.1	7.4	7.4	7.5	27, 28, 42, 50, 57
Salt Lake City	slc	43 ± 4	6(2–5)	1.50 ± 0.30	7.0	7.4	7.3	7.5	27, 28, 42, 43, 52, 57
Provo	pvo	64 ± 5	6(0.8–2.9)	0.50 ± 0.20	7.2	7.4	7.4	7.5	10, 19, 25, 27, 28, 42, 50, 57
Nephi	npi	40 ± 3	6(1.7–2.6)	0.4 + 0.1, −0	6.9	7.4	7.3	7.4	13, 27, 28, 34, 42, 57
Levan	lvn	28 ± 3	5.2(1.6–3.0)	1.00 + 1.1, −?	6.8	7.3	7.1	7.2	13, 27, 28, 42, 57
Fayette	fyt	11 ± 1	?	12 ± 3	—§	?	?	^	27, 28, 42, 57
E. Cache Val.									
North	nec	33 ± 2	?	13.4 + ?, −0	6.8	?	?	7.1	22
Middle	mec	20 ± 0.5	2.4	5 ± 2	6.6	7.1	6.9	7.1	22, 51
South + James Pk.	sec	29 ± 5	?	36 ± 10	6.8	?	?	^	22, 32
Morgan	mgn	19 ± 2	1.0	≦9	6.6	6.8	6.7	—	12, 48
Bear River	brv	37 ± 3	5.3	−2.4	6.9	7.3	7.2	—	12, 56
Strawberry	sby	35 ± 3	3.6	8 ± 2	6.9	7.2	7.1	7.2	12, 31, 33
Stinking Spgs.	sss	11 ± 1	?	≦10	—§	?	?	^	12, 31, 54
Joes Valley									
West (mid. segm.)	wjv	42 ± ?	5.5	6.5 to 23	7.0	7.4	7.2	—	9, 12
East (mid. segm.)	ejv	42 ± ?	2	1.5	7.0	7.0	7.0	—	9, 12

*Latest Pleistocene is defined here as < ~100 ka, roughly the greatest age for which prehistoric earthquakes can be individually identified from surface morphology and trenching data. Faults and segments are listed from west to east and north to south. Abbreviations: *L*, simple average of straight-line and trace measurements from published maps and figures of distance between segment boundaries, with the difference taken as uncertainty; *D*, maximum single-event vertical surface displacement estimated from published measurements (tectonic values used when available); *M*, magnitude scaled from regressions (4), (5), and (6) in text. A question mark (?) indicates an unknown or inferred value.

†Entries that include numbers in parentheses reflect cases for which data was available from restricted locations along strike. Such numbers were considered in this study as more likely to approximate average than maximum displacement for the fault segment. The number left of the parentheses was used as *D* and was obtained by multiplying the optimum measured value in the range by 3, with an empirically constrained maximum of 6 m (see text for discussion).

‡Two segments. Each magnitude was scaled from the sum of the length of the respective segment and the one below it in the table. Where confusion might occur, an arrow (^) points toward the magnitude to which the segment contributed. The *D* used was the greater of the values for the segments that were combined.

§Based on empirical and theoretical considerations, surface-parameter scaling is not expected to give reliable results for cases in which $L < \sim 15$ km (see text for discussion).

¶This fault may rupture in a subsidiary sense with another fault, because of its antithetic orientation, smaller size, proximity to the other fault, *etc.* For the West Bear Lake fault, the probable primary structure is the East Bear Lake fault (McCalpin, 1990), and, for the West Valley faults, it is the Salt Lake City segment of the Wasatch.

‖References: 1 Anders *et al.* (1989), 2 Bucknam and Anderson (1979), 3 Byrd (1992), 4 Byrd and Smith (1991), 5 Coppersmith *et al.* (1991), 6 Crone and Haller (1991), 7 Crone *et al.* (1987), 8 Doser (1989), 9 Foley *et al.* (1986), 10 Forman *et al.* (1989), 11 Haller (1990), 12 Hecker (1993), 13 Jackson (1991), 14 Johnson (1981), 15 Jones (1992), 16 Jones and McCalpin (1992), 17 Keaton and Currey (1989), 18 Knuepfer *et al.* (1989), 19 Lund *et al.* (1991), 20 McCalpin (1990), 21 McCalpin (1993), 22 McCalpin and Forman (1991), 23 McCalpin and Warren (1992), 24 McCalpin *et al.* (1987), 25 Machette (1988), 26 Machette *et al.* (1987), 27 Machette *et al.* (1992), 28 Machette *et al.* (1991), 29 Malde (1987), 30 Myers *et al.* (1964), 31 Nelson and Martin (1982), 32 Nelson and Sullivan (1992), 33 Nelson and van Arsdale (1986), 34 Ostenaa (1990), 35 Ostenaa and Wood (1990), 36 Personius (1982), 37 Personius (1991a, b), 38 Pierce (1985), 39 Piety *et al.* (1986), 40 Richins (1979), 41 Salyards (1985), 42 Schwartz and Coppersmith (1984), 43 Schwartz and Lund (1988), 44 Scott *et al.* (1985), 45 Shenon (1936), 46 Solomon *et al.* (1992), 47 Stickney and Bartholomew (1987), 48 Sullivan and Nelson (1992), 49 Susong *et al.* (1987), 50 Swan *et al.* (1980), 51 Swan *et al.* (1983), 52 Swan *et al.* (1981), 53 Turko and Knuepfer (1991), 54 van Arsdale (1979), 55 Wallace (1977), 56 West (1988), 57 Wheeler and Krystinik (1992), 58 Witkind (1964), 59 Wu (1994).

weathering can cause underestimation of *L* by erasing the ends of earthquake segments where surface rupture was diminutive at the time of formation. The historical record has shown that an earthquake rarely affects the entire extent of a well-developed fault, i.e., one that has hundreds of meters of net tectonic offset and for which overall length exceeds a few tens of kilometers (e.g., Ambraseys, 1970; Schwartz and Coppersmith, 1984, 1986; dePolo *et al.*, 1991). Consequently, before scarp length of a fault in the ISB could be used to scale earthquake magnitude, it was necessary to estimate sections along it—called "earthquake segments" (Schwartz and Coppersmith, 1984; dePolo and Slemmons,

1990; dePolo *et al.*, 1991)—each of which could be expected to fail as a unit in an earthquake.

Several types of discontinuities have been proposed to constrain the ends of earthquake segments, including geometric (King and Nabelek, 1985), paleoseismic (Crone and Haller, 1991), geophysical (Haller, 1990; Crone and Haller, 1991; Richins *et al.*, 1987; Crone *et al.*, 1987), and structural (Turko and Knuepfer, 1991; Susong *et al.*, 1990). Machette *et al.* (1991) emphasized that any persistent discontinuity in earthquake faulting must ultimately be correlated with structural barriers (e.g., Fonseca, 1988). As a rule of thumb, discontinuities should have dimensions on the order of kilometers to be used as evidence for persistent impediments to earthquake rupture (Sibson, 1989; Crone and Haller, 1991). Studies of historical earthquakes (Knuepfer, 1989; dePolo *et al.*, 1991) show that ruptures may extend across certain discontinuities, affecting multiple fault segments. Evidence for transbarrier rupture has also been identified in the paleoseismic record. Examples from the ISB include the boundaries between the following segments: north and south segments (nec and sec in Fig. 2) of Star Valley (Anders *et al.*, 1989), south East Cache Valley and James Peak (combined as sec in Fig. 2) (McCalpin and Forman, 1991), Provo and Nephi (pvo and npi) on the Wasatch (Ostenaa, 1990), Thousand Springs and Warm Springs (tsp and wsp) on the Lost River (Crone *et al.*, 1987), and Leadore and Baldy Mountain (ldo and bym) on the Beaverhead (Crone and Haller, 1991). ISB segment lengths in this study were taken as those assigned by the authors referenced in Table 2 who performed the field investigations. Where disagreement existed, the most recent results were normally accepted.

Comparisons of short-term aftershock patterns with mainshock surface deformation (e.g., Kanamori and Allen, 1986) show that L below some threshold value fails to reliably scale earthquake magnitude. This threshold length probably varies with tectonic setting, but here might be a way to approximate it. Roberts and Jackson (1991) used the observation that normal-faulting earthquakes originate within the brittle upper crust to define large faults as those with dimensions exceeding the seismogenic depth. If there is no constraint on the depth to which faulting can extend, width cannot be considered invariant in magnitude scaling. However, Scholz (1982) showed that a crustal faulting model where width is fixed and length remains unconstrained supports empirical evidence for constant stress drop among certain categories of earthquakes, intraplate events being one, whereas the reverse model (width free, length fixed) does not. Thus, one could argue that, for intraplate earthquakes such as in the ISB, much of the seismic energy may be expressed in the width direction, until average fault dimension approaches the seismogenic thickness. Beyond that value, the width contribution may saturate, leaving the remaining mechanical energy to be more effectively expressed in length and displacement. The average seismogenic depth for the Intermountain region has been estimated at about 15 km (Smith and Bruhn, 1984). Based on these considerations, L-based regressions evaluated in this study and their application to ISB faults were restricted to cases for which $L \geqq 15$ km.

Rupture length was taken as the simple average of straight-line and trace measures of scarp zones for each earthquake. For surface ruptures with highly arcuate surface traces used in this study, such as the Gediz, Turkey, and Hebgen Lake (USA) earthquakes in Table 1, trace and straight-line lengths varied from the average by as much as $\pm 17\%$.

An effort was made to identify and exclude nonseismogenic (secondary) surface ruptures from length assessment in geometrically complex fault zones. Scarps less than 10% of overall rupture zone distance (segment length for prehistoric faults) and isolated from the main area of deformation by at least a few kilometers were generally regarded as secondary structures. This was particularly true where the sense of offset on the isolated scarp was discordant from that in the main zone or had much less slip. Examples include scarps from postevent slumping or spreading and antithetic faulting. Gaps in surface faulting well within the zone of deformation were generally included in length assessment on the assumption that they do not persist at depth. Overlap length from two *en-echelon* scarp traces was included when they were sufficiently separated (at least a few kilometers) to be on distinctly different seismogenic surfaces.

Maximum Surface Displacement

Displacements recorded in Tables 1 and 2 represent estimates of maximum single-event surface offset, with estimated nonseismogenic contributions removed when available. Maximum displacements were used, because they are less arbitrary than averages and because the latter are rarely available in the literature. Strike slip is rarely observed for ISB paleoearthquakes, which is to be expected from the prevailing strike directions, stress field data, and earthquake focal solutions (Smith and Sbar, 1974; Zoback *et al.*, 1981; Doser and Smith, 1982; Smith and Bruhn, 1984; Zoback, 1989). Also, the difference between vertical and dip slip is small, because trenching and shallow seismic data typically reveal near-vertical fault dip within a few meters of the surface.

The presence of aseismic slip can rarely be ruled out, although evidence suggests it may not seriously corrupt the data. Correlation between magnitude and $\log(D)$ tend to be fairly strong, suggesting that aseismic contributions to the historical data are modest. Beanland *et al.*, (1990) monitored a geodetic network across the main fault of the 1987 M_S 6.6 Edgecumbe, New Zealand, earthquake for 14 months, starting the day after the mainshock. Their data showed an exponential decay of slip during this time to a maximum relative elevation change across the scarp of 0.50 ± 0.1 m over a lateral distance of about 50 m. This represented 20% of D and affects scaled magnitude by $< \pm 0.1$, which lies well within the best standard errors for published regressions.

Estimates of single-event surface displacement from

very restricted locations along strike of a scarp, such as in trenching, will tend to underestimate maximum displacement. This is due partly to scarp degradation but also to the high variability along strike that typifies surface displacement and the short distance over which the maximum occurs (Crone and Machette, 1984; Schwartz *et al.*, 1984; Youngs *et al.*, 1987; Pantosti and Valensise, 1990; Beanland *et al.*, 1990). Bonilla (unpublished data referenced in Bonilla *et al.*, 1984) found, from earthquakes of various slip types, that average surface displacement averages about 30% of the maximum. Pechmann (1987a, b), who independently noted this ratio for the two largest historical ISB earthquakes—Hebgen Lake and Borah Peak (Table 1), proposed a method for estimating maximum single-event surface displacement, where restricted sampling along strike was expected to have missed the maximum value. This involved multiplying the average single-event offset derived from trench measurements along the Wasatch fault (Fig. 2) by 3 as estimates of D for that fault.

Validity of the 3:1 relationship does not at first appear to agree with recent results of Wells and Coppersmith (1994), who evaluated ratios of maximum- to average-surface displacement, D/d, for 57 historical earthquakes of all slip types. They found that the ratio varies from 1.2 to 5.0, averages 2, and has no dependence on magnitude. However, if one takes only the 15 predominantly normal-faulting earthquakes from their data set, excluding events that they considered unreliable, one obtains an average D/d of 2.4 with values ranging between 1.2 and 4.7. This average remains the same, when the data are limited further to the six earthquakes of the Basin and Range, including the ISB. However, it seems significant to note that the three largest historically documented earthquakes of the Basin and Range—Pleasant Valley, Hebgen Lake, and Borah Peak (Table 1)—have values of 2.9, 2.8, and 3.4 (data from Wells and Coppersmith, 1994), respectively, placing them all closer to 3:1 than 2:1. This suggests that there may be some dependence of D/d on faulting style or tectonic province and that earthquakes of the Basin and Range may be characterized by a slightly larger-than-average value.

Scarp profile data parallel to strike from several well-documented historical faults (Witkind, 1964; Myers *et al.*, 1964; Ambraseys and Tchalenko, 1972; Wallace, 1984; Crone and Machette, 1984; Beanland *et al.*, 1990; Clark, 1972) indicate that the measurement of displacement at an arbitrary point along strike is likely to be closer to the average value than to the maximum. One could argue that scarp measurements are likely to be made where the scarp is geomorphically well expressed. However, access to the optimum geomorphic locations are often prevented, particularly in urban areas and national parks, by development or land ownership. Also, site-dependent geologic conditions, such as composition of the scarp, surrounding topography, soil, *etc.*, can strongly influence how a scarp profile—and hence the apparent location of maximum offset—evolves through time. Thus, if a typical trench displacement for an ISB fault is assumed to approximate the average scarp offset, then multiplying it by 3, in accordance with Pechmann's (1987a and b) approach and observations of the preceding paragraph, provides a reasonable estimate of D. Situations where this method may overestimate D are hinted at, when it gives values that exceed the largest vertical offset documented for a historical normal-faulting earthquake (6.0 ± 0.4 m in Table 1). Examples of where this occurs in the ISB include the Blacktail, South Star Valley, and South East Bear Lake faults (btl, ssv, and seb in Fig. 2). If 6 m can be taken as an upper limit on primary, co-seismic surface offset for normal-faulting earthquakes in the Basin and Range and the approximate 3:1 relationship holds for the ISB, then a single-event offset measurement greater than about 2 m can be expected to exceed the average for an ISB fault.

In summary, the following approach was applied to estimate D in Table 2 for the ISB fault segments. In cases where single-event offset on a segment was represented only from trenching or otherwise very localized measurements, D was taken as the measured value multiplied by 3, unless the measurement was ≥2 m, in which case it was taken as 6 m. For displacements based only on scarp analysis or both trenching and scarp measurements, unless the field source indicated that all data came from a local portion of the scarp zone, it was assumed that quoted numbers represented maxima. Where measurements for more than one event were available on a segment, the largest value was normally selected for application of the above analysis. Preference was given to data corrected for nontectonic contributions, such as antithetic faulting, back-tilting, or graben formation.

Magnitude

Only surface-wave magnitudes, M_S, were used for the author's regressions, because reliable estimates of the more universally applicable moment magnitude, M_w, are unavailable for some of the older earthquakes in Table 1. A close one-to-one correspondence between the M_S and M_w has been repeatedly demonstrated for the range $6.0 \leqq M \leqq 8.0$ within which most surface-rupturing normal-faulting earthquakes occur (e.g., Kanamori, 1977; Hanks and Kanamori, 1979; Wells and Coppersmith, 1994). Whenever possible, well-sampled, multi-station averages of M_S were used to minimize azimuthal bias.

Regression Analysis

The many published regressions for magnitude on surface rupture data differ by up to several tenths in the magnitudes they give for values of D and L. The author needed an objective means for comparing the regressions computed in this study with others already in the literature and for choosing an appropriate solution from among them for use with the ISB data. This section describes the statistical analysis that was used to reduce the number of regressions to consider. First, regressions of magnitude on the logarithms of L, D, and DL were computed for the data in Table 1 and

then ranked together with similar regressions from two other studies using a statistical algorithm. Based on results from this algorithm, a preferred regression was then chosen from among each of the three formula types for application to the ISB fault data of Table 2 in the next section.

The regressions computed from the data of Table 1 are shown in Table 3 along with similar solutions taken from the widely referenced work on surface parameter scaling relationships by Bonilla *et al.* (1984) and a more recent update of global fault scaling relationships by Wells and Coppersmith (1994). From here on, these articles will be referred to as BML and WC, respectively. The solutions are grouped by formula and were all obtained by linear least-squares with no weighting of data values. BML showed that weighting of data values in surface parameter scaling is inappropriate, since stochastic variance dominates estimated measurement uncertainties. Regressions were chosen that included only normal faulting mechanisms because of relevance to the ISB as well as all faulting types. BML did not compute a length regression using only normal-faulting earthquakes, so their results for western North America are presented instead. WC presented no *DL*-based regressions, and BML presented none for normal-faulting data, so the author computed them using the data given by these authors and excluding events they regarded as having unreliable source parameters. All regressions were based on either surface-wave or moment magnitude scales.

Statistical ranking of the regressions was based on three attributes: number of data points, N, estimated minimum standard deviation, σ_m, and adjusted coefficient of determination:

$$r_v^2 = \frac{(N-1)r^2 - m + 1}{N - m}, \tag{1}$$

where r is the correlation coefficient and m is the number of regression coefficients (always 2 in this study). As a means of identifying a preferred regression for each of the three formula types, rankings were grouped by formula.

The ranking algorithm was derived as follows. Consider a set of regressions $\{1, \ldots, i, \ldots, k\}$ of a given formulation f. For each regression, we have a set of $\{1, \ldots, j, \ldots, n\}$ statistics S that we would like to use to rank the regressions based on degree of determinism in the members of S. "Determinism" means the degree to which a statistic helps to resolve a functional relationship between two variables, if one exists. A simple ranking, ρ, of regression i for statistic s_j, with respect to the other regressions, can be expressed as

Table 3
Regressions of Magnitude on Surface Rupture Parameters*

Regression Formula Slip Type	*M* Type	*a*	*b*	*N*	σ_m	r_v^2	R_f (%)	*M* Scaled for: AS, SM, EC (6.5, 7.4, 6.6)	References†
$M = b^*\log(L) + a$									
all	**W**	**5.08**	**1.16**	**77**	**0.28**	**0.79**	**100**	**6.8, 6.8, 6.5**	**WC**
normal	S	4.23	1.77	20	0.29	0.57	45	6.9, 6.8, 6.5	M
all	S	6.04	0.71	45	0.31	0.43	34	7.1, 7.1, 6.9	BML
Western N. Amer.	S	5.17	1.24	12	0.32	0.67	33	7.1, 7.0, 6.7	BML
normal	W	4.86	1.32	15	0.34	0.63	20	6.9, 6.8, 6.5	WC
$M = b^*\log(D) + a$									
normal	**S**	**6.81**	**0.74**	**9**	**0.19**	**0.79**	**67**	**6.7, 7.4, 7.1**	**BML**
normal	S	6.75	0.62	20	0.24	0.69	56	6.7, 7.2, 7.0	M
all	W	6.69	0.74	80	0.40	0.60	51	6.6, 7.3, 7.0	WC
normal	W	6.61	0.71	16	0.34	0.61	32	6.5, 7.2, 6.9	WC
all	S	6.95	0.72	39	0.32	0.38	27	6.9, 7.5, 7.2	BML
$M = b^*\log(DL) + a$									
normal	**S**	**5.95**	**0.55**	**20**	**0.20**	**0.79**	**72**	**6.7, 7.2, 6.9**	**M**
all	W	5.88	0.57	68	0.27	0.80	67	6.7, 7.2, 6.8	WC, M
normal	S	5.91	0.60	9	0.22	0.71	45	6.8, 7.3, 6.9	BML, M
normal	W	6.01	0.48	13	0.26	0.68	24	6.7, 7.1, 6.8	WC, M
all ($M \geqq 6$)	S	6.22	0.49	37	0.27	0.55	16	6.9, 7.3, 7.0	BML

*All regressions were derived by unweighted least squares. Variables are as follows: M, earthquake magnitude (S, surface-wave; W, moment); D, maximum vertical tectonic surface displacement (meters); L, surface rupture length (km); "normal," normal or normal-oblique slip; "all," all types of slip; N, number of data points; σ_m, minimum estimated standard deviation; r_v^2, adjusted coefficient of determination [coefficients of determination from Bonilla *et al.* (1984) and Wells and Coppersmith (1994) were adjusted to r_v^2 using equation (1) in the text]. R_f is the ranking of the regression with respect to the other regressions of the same formula in the table based on N, σ_m, and r_v^2 (see text). AS, SM, and EC are magnitudes given by the regressions for the Alasehir, Salmas, and Edgecumbe earthquakes using the values of D and L given in Table 1. Their instrumental magnitudes are shown in parentheses in the table header. Regressions selected for application to the ISB data in Table 2 appear in bold type.

†References: BML, Bonilla *et al.* (1984); WC, Wells and Coppersmith (1994); M, Table 1, this article. Regressions referenced as "BML, M" and "WC, M" were obtained by the author on data from BML or WC, respectively. For the case of WC, the data came from a March 1993 preprint. Earthquakes with unreliable parameters, as specified by those authors, were excluded.

the ratio of the difference between the value of s_j for the regression and the minimum observed value for s_j to the spread in observed values for s_j:

$$\rho_i(s_j) \equiv \begin{cases} \dfrac{s_j(i) - m}{M - m}, & M \text{ more deterministic than } m \\ 1 - \left(\dfrac{s_j(i) - m}{M - m}\right) = \dfrac{M - s_j(i)}{M - m}, & m \text{ more deterministic than } M, \end{cases} \tag{2}$$

where M is the maximum value of s_j for the k regressions and m is the minimum. Then, the net rank of i among all the regressions of formula f would be

$$R_f(i) \equiv \frac{1}{n} \sum_{j=1}^{n} \rho_i(s_j). \tag{3}$$

Notice that both ρ and R_f range from 0 to 1 and can therefore be expressed as percentages. For example, suppose we wish to rank five regressions of type $M_S = b^*\log(D) + a$ and that the minimum and maximum numbers of data points are 7 and 32, respectively. Since more data points potentially yield greater determinism to the data (versus say σ_m, for which smaller values are more deterministic), then, for a regression having 16 data points, $\rho = (16 - 7)/(32 - 7) = 0.36 = 36\%$. Finding values of 0.64 and 0.52 in the same way for σ_m and r_v^2, we would obtain $R_f = (0.36 + 0.64 + 0.52)/3 = 0.51 = 51\%$ as a ranking for this particular regression among the five D-based solutions.

Computed R_f values are shown in Table 3 in order of decreasing rank for each formula type. Note that comparisons among R_f values must be restricted to regressions of the same formula type. For each formula, the regression with the highest R_f was selected for application to the ISB data. For the L-based regression, the choice was obvious, since the first solution,

$$M_w = 1.16 \log(L) + 5.08, \quad \sigma_m = 0.28, \tag{4}$$

had the most deterministic values for all statistics. For the D-based formula, the choice of

$$M_S = 0.74 \log(D) + 6.81, \quad \sigma_m = 0.19 \tag{5}$$

was more difficult due to its small number of data points. However, it was accepted because of its relatively good values for the other two statistics and because eliminating it would have undermined the objectivity of the selection process. Strong correlation and low standard deviation resulted in

$$M_S = 0.55 \log(DL) + 5.95, \quad \sigma_m = 0.20, \tag{6}$$

having the highest R_f among the DL-based regressions, despite two other solutions with more data points. Plots of the data for (4) and (5) are provided in WC (Fig. 9) and BML (Fig. 2, NML), respectively. A plot of (6) and associated data are presented in Figure 3. Regression (6) has the same level of correlation as the highest ranking solutions for the other two regression formulas and the second lowest minimum standard deviation among all the regressions evaluated. Note that the selection of (4), (5), and (6) supports the findings by WC that displacement-based magnitude regressions can display some dependence on faulting style, whereas regressions based only on length do not. The next section compares these three regressions with each other in light of application to the ISB fault data.

Magnitude Estimation for ISB Paleoearthquakes

Surface rupture length and displacement have often been applied independently to scale earthquake size, despite findings by BML that magnitude regressions based on the product of these parameters have greater correlation and smaller standard errors. Yet a product-based regression requires estimates of both rupture length and displacement, a luxury that is often difficult to achieve for prehistoric faults. If L- and D-based regressions yield similar magnitudes for a given earthquake fault segment, then, practically speaking, one can estimate magnitudes with knowledge of just one of these parameters. In the remainder of this article, the three regressions selected in the previous section are applied to the ISB paleoseismic data of Table 2. The results are then

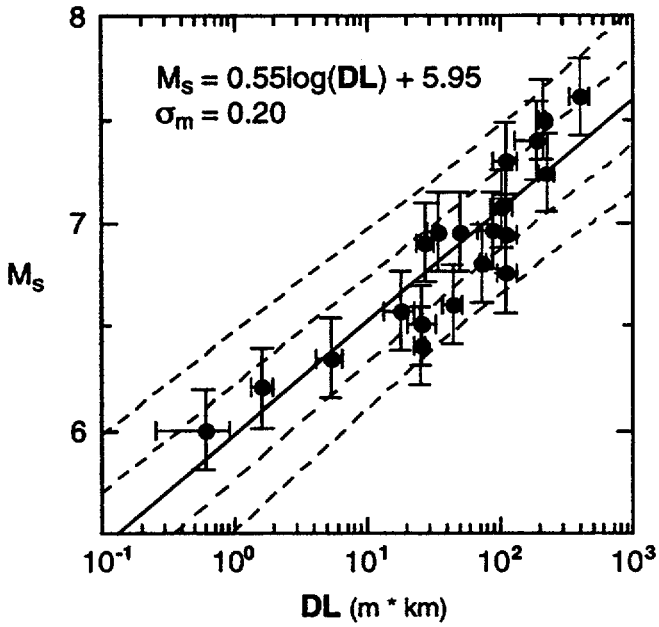

Figure 3. Data and preferred least-squares regression of M_S on $\log(DL)$ for earthquakes with normal to normal-oblique slip from worldwide sources (Table 3). The dashed curves indicate one and two estimated standard deviations.

used to arrive at a single preferred regression and a model for estimating maximum magnitude potential of ISB faults.

Length and Displacement as Independent Scalars of Magnitude

Figure 4 and Table 2 show the most likely (mean-value) maximum magnitudes estimated for the ISB paleoseismic fault data of Table 2 using (4) and (5). Diagonal lines indicate magnitudes based on data from restricted locations along strike, where maximum displacement was estimated as three times the measured value. The results show that maximum surface displacement consistently scales a larger magnitude than the estimated surface rupture length for the associated fault segment. There are four possible explanations for this—including (1) bias in the regression data, (2) overestimation of maximum paleoseismic displacements, (3) underestimation of paleoseismic surface rupture lengths, and/or (4) the expression of physical factors in the ISB—in addition to these two parameters, that cause ISB earthquakes to deviate from the global average scaling relationships.

In order to determine whether any of the negative bias in $M(L) - M(D)$ may have originated from the regressions, a histogram of $M(L) - M(D)$ was plotted for the earthquake data in Table 1 and for the normal faulting earthquakes presented by WC, where $M(L)$ was computed from (4) and $M(D)$ from (5) (Fig. 5). Only normal faulting earthquakes were plotted to allow for possible dependence of $M(D)$ on fault slip type. The data of WC were shown as a cross-check against the data presented in this study. Results indicate negative bias in $M(L) - M(D)$ for both data sets, averaging -0.1 and -0.2 magnitude unit for the data of Table 1 and WC, respectively. Thus, for the L- and D-based regressions selected for this study, the former tends to scale slightly smaller magnitudes than the latter for data from the same faults. This likely reflects a combination of factors, such as the relatively low number of data points upon which (5) is based, slight differences between the M_w and M_S scales used by the two regressions, the lack of a minimum cutoff for L in the data used for regression 1, *etc.*

In order to assess the influence of regression error on the magnitudes estimated for the ISB fault segments, the paleomagnitudes of Fig. 4 were plotted as a histogram of $M(L) - M(D)$ for each segment having both L and D estimates and with the -0.2 M average regression bias subtracted out (Fig. 6a). All cases for which D was based on measurements from restricted locations along strike were ex-

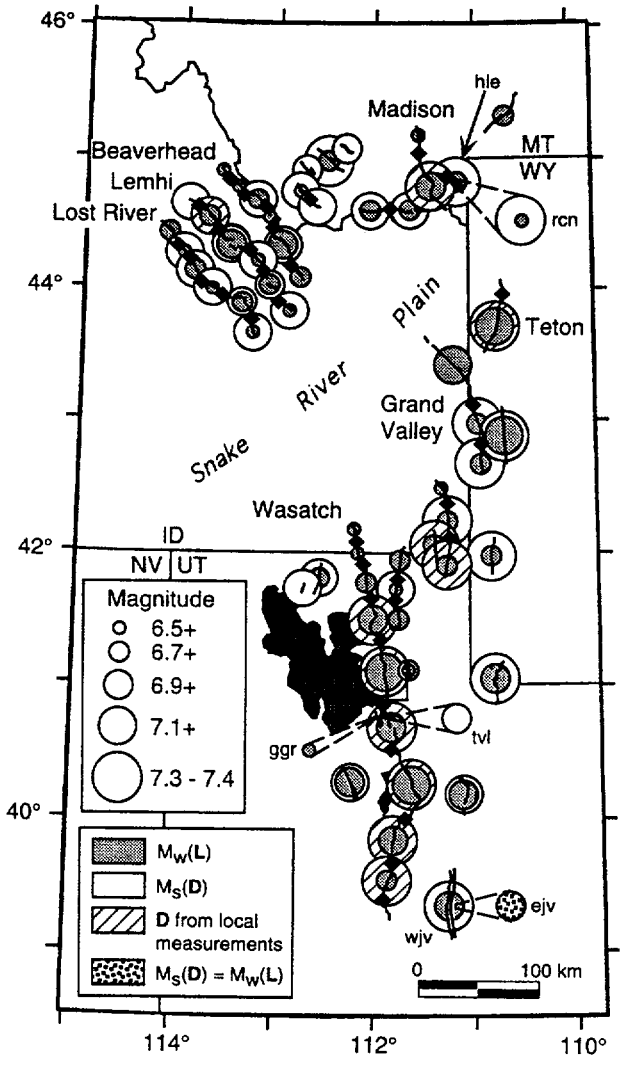

Figure 4. Paleomagnitudes scaled from surface rupture length (gray) and maximum surface displacement (white) for individual earthquake segments of late Quaternary ISB faults. No displacement-based magnitudes are shown for segments lacking sufficiently reliable estimates of single-event displacement.

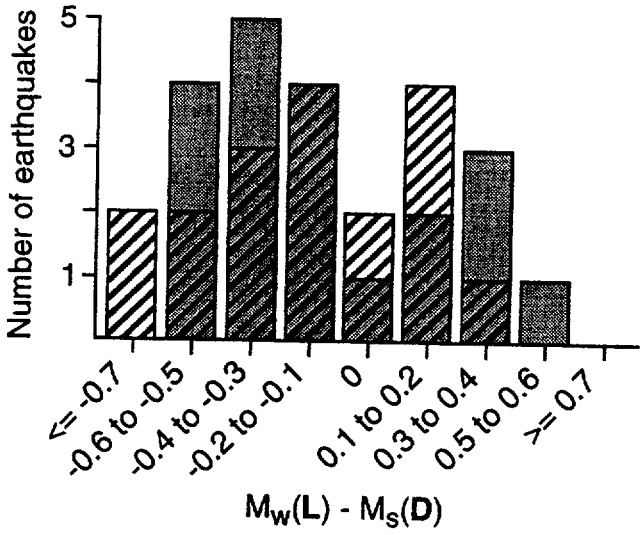

Figure 5. Distributions of the differences between magnitude scaled from surface rupture length versus maximum surface displacement for the normal faulting historical earthquake data sets of Table 1 (gray) and Wells and Coppersmith (1994) (hachured).

cluded because of the uncertainty that they represent the whole extents of those segments. The results show that, even with these factors removed, a distinct negative bias of -0.2 to -0.3 persists in $M(L) - M(D)$ for the ISB. This illuminates the level of inaccuracy that can be expected in estimating magnitude potential of a fault from either L or D without reference to the other parameter and suggests a systematic bias either in the ISB paleoseismic data or in the assumptions used to scale magnitudes from them.

The negative bias in $M(L) - M(D)$ for ISB faults may be caused by overestimation of D. This could result from mistakenly attributing a multiple-event offset to a single event, or from unrecognized nonseismic contributions such as creep, fault block tilting, or antithetic faulting. Yet in many trenching studies, multiple events can be identified to at least estimate an average single-event D value. Nontectonic contributions to slip are most likely to be overlooked at sites lacking trench data. Along the Wasatch fault, trenching has revealed that back-tilting, graben formation, and/or antithetic faulting can account for as much as 55% of the total offset at a given location (*e.g.*, Schwartz and Coppersmith, 1984). However, there is evidence that nontectonic slip cannot account for all of the bias in $M(L) - M(D)$ for the ISB faults. The three major fault systems—Lost River, Lemhi, and Beaverhead—in east-central Idaho (Fig. 2) have similar tectonic characteristics in terms of their close proximity to each other, strike, overall lengths, and morphological features. Table 2 indicates that they also have similar paleoseismic estimates of D, with a mean value and standard deviation of 2.9 ± 0.42 m; this is consistent with the observed maximum tectonic displacement of 2.6 m measured from the 1983 Borah Peak earthquake scarp on the Lost River fault. Yet, even the estimated single-event values of D for these fault systems that were less than the mean, including the Borah Peak value, scaled larger magnitudes than their corresponding single-segment lengths. These observations suggest that the tendency for D to scale larger magnitudes than the corresponding single-segment L cannot be fully attributed to overestimation of D.

The discrepancy between D- and L-scaled magnitudes for the ISB faults may, in some cases, be caused by mistakenly assuming single-segment rupture. Crone and Haller (1991) pointed out that no barrier can completely impede rupture all the time due to the continuity of range topography. DePolo *et al.* (1991) showed that 9 out of 11 ground-breaking historical earthquakes in the Basin and Range induced failure on multiple structural or geometric segments. They included the normal-faulting example of the M_S 7.6 Pleasant Valley, Nevada, earthquake of 1915, which crossed gaps as much as 6 to 10 km wide and broke parts of as many as five segments. In the ISB, the Hebgen Lake earthquake caused failure along two distinct faults (Witkind, 1964), and the Borah Peak event ruptured all of the Thousand Springs segment and about half of the adjacent Warm Springs segment (Richins *et al.*, 1987; Crone *et al.*, 1987). Figure 6b shows $M(L) - M(D)$ for the multi-segmented ISB faults in Fig. 4, using the sum of lengths from each pair of adjacent segments. Each value was computed using the larger of the two D estimates for cases in which values were available from both segments. As before, regressions (4) and (5) were used, and the -0.2 M regression bias was removed. This time, the results show no bias to one decimal place, a reasonable level of accuracy for the data. This suggests that a dual-segment rupture scenario may represent a good first approximation to the average rupture pattern for ISB faults.

Properties of the crustal rheology in the ISB may cause its surface parameter scaling relationships to deviate from the global averages represented by the regressions of this study. As noted above, the three largest historical earthquakes of the Basin and Range all had larger ratios of D/d than the global average. Based on comparisons of displacements from trench studies on several faults in the central ISB with associated segment lengths and the surface parameter regressions of BML, McCalpin (1993) proposed that surface displacements hypothesized for latest Quaternary earthquakes along some fault systems in that region, such as Star Valley, Rock Creek, and Greys River faults (nsv, ssv, rck, and grv in Fig. 2), may be larger than the worldwide average for events with comparable rupture lengths. The ISB Hebgen Lake earthquake of 1959 (Table 1) had a well-documented surface rupture (Myers *et al.*, 1964; Witkind, 1964) that was significantly shorter than the global average (98 km; WC, Table 2A) for earthquakes of comparable magnitude and displacement. It is of interest to note that paleoseismic data from other documented faults in its vicinity of the ISB also show unexpectedly short scarp zones for their estimated single-event displacements (faults in southwest Montana, Fig. 2 and Table 2). However, 220 km west, surface parameters for the Borah Peak earthquake (Table 1) were less anomalous compared to global averages. Thus, as our knowledge of seismic behavior in the ISB progresses, it may be found necessary to delineate zones in which different faulting models apply for estimation of earthquake magnitude.

Length Times Displacement as a Scaler

Use of the product of length with displacement to scale earthquake magnitude tends to yield an average value between the magnitudes given by either of these parameters alone. The definition of seismic moment indicates that appropriate trade-offs between D and L can yield the same fault strength and, presumably, similar seismic energy release. This would partly explain why some earthquakes are outliers in regressions of magnitude on one or the other of these parameters. The sizes of such earthquakes may be more effectively represented by the other rupture variable. Examples are shown in Table 3. There, the magnitudes given by each of the regressions analyzed in this study for three representative earthquakes from Table 1—Alasehir, Turkey; Salmas, Iran; and Edgecumbe, New Zealand—are shown, with their instrumentally computed M_S values parenthesized in the header for comparison. The essentially identical rupture

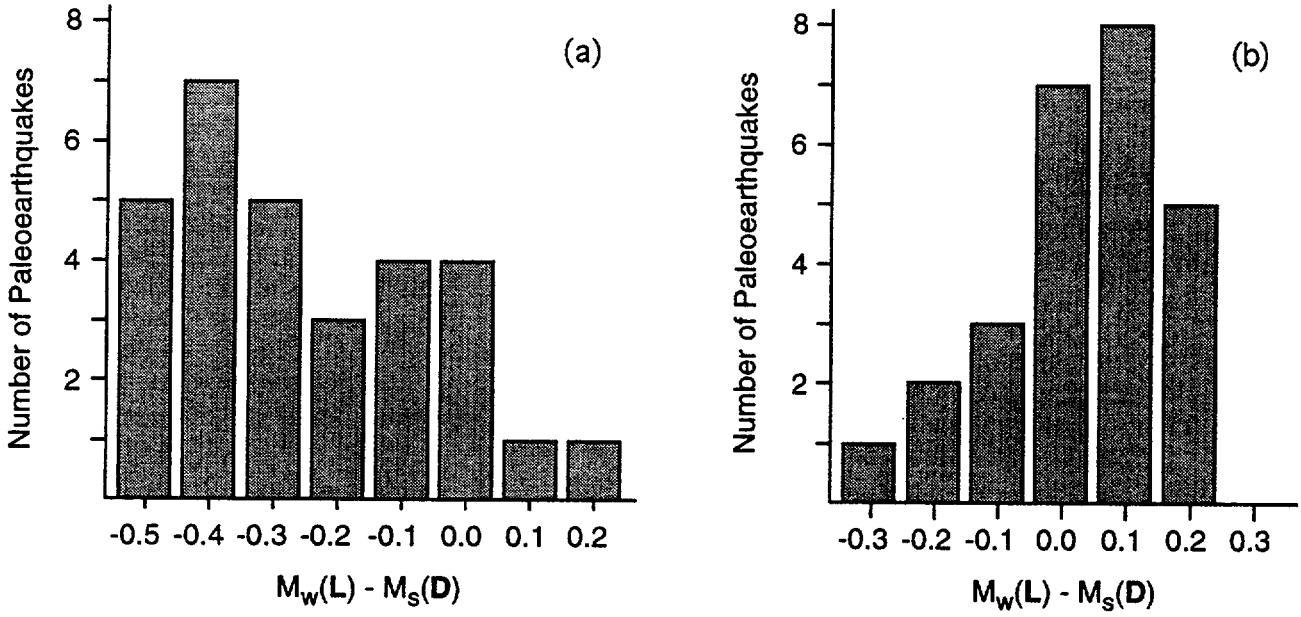

Figure 6. Distributions of $M_w(L) - M_s(D)$ for the ISB paleoseismic data for (a) single- and (b) double-segment rupture scenarios.

lengths of the Alasehir and Salmas events imply identical magnitudes, but the instrumental magnitudes differ by almost a full unit. On the other hand, displacement does a noticeably better job of predicting the measured magnitudes for these two events. In the case of the Edgecumbe earthquake, displacement was anomalous, with rupture length giving a magnitude closer to the measured value. The Hebgen Lake earthquake (Table 1) is an example of an event with an unusually short rupture length for its seismically measured size but which is made up for by its large displacement. A *DL*-based regression helps moderate the risk of over- or underestimating a paleomagnitude, where it is uncertain whether displacement or rupture length may have more accurately expressed the actual seismic energy release.

Because of this moderating tendency of *DL*-based regressions, (6) was chosen as the preferred regression for estimating magnitude capability for ISB faults in this study. However, it should be kept in mind that this approach requires reasonable estimates of two parameters, D and L, rather than just one and on whether the two values resulted from the same earthquake. These factors can be difficult to confidently assess for some prehistoric faults. Figure 7 and Table 2 show the magnitudes scaled by (6) for individual fault segments of the ISB for which published estimates of both D and L were available. Values range from M_S 6.7 to 7.4 $\pm$ 0.20 σ_m and lie between the values predicted by D and L independently, but they are generally closer to the former than to the latter.

A Multi-Segment Rupture Model

No basis has yet been proposed for quantifying the fractions of segments that can be expected to fail in multi-segment earthquakes. However, a few lines of evidence support two-segment rupture as a reasonable first approximation for a multi-segment rupture model in assessing maximum magnitude potential of ISB earthquakes. As shown in the previous section, dual-segment rupture, with the larger D value used from each segment pair, can explain the discrepancy between L- and D-based magnitudes from individual segments. The two historical ISB earthquakes that resulted in known primary surface rupture, Hebgen Lake and Borah Peak, produced surface offset along two fault segments. Recurrence intervals for the Wasatch fault during the past 6 ka allow for the possibility of as many as six or seven paleoearthquakes that could have involved two segments, one which may have included three segments, and none that affected more than three (Fig. 4 in Machette *et al.*, 1991).

Table 2 and Figure 8 show the magnitudes given by (6) for each pair of adjacent fault segments among the multi-segmented ISB faults for which at least one D estimate was available. As before, when D values were available from both segments, the larger of the two was used. The magnitudes range from M_S 6.8 to 7.5 $\pm$ 0.20 σ_m, and the largest magnitudes are associated with some of the longest fault systems, including the Madison, Teton, and Swan/Grand Valley faults and the central sections of the Wasatch fault.

Summary and Conclusions

What are the largest earthquakes that can be expected to occur in the ISB, and where are they likely to occur? Surface parameter scaling provides a practical statistical basis from which to begin answering these questions, because it takes advantage of both the growing amount of paleoseis-

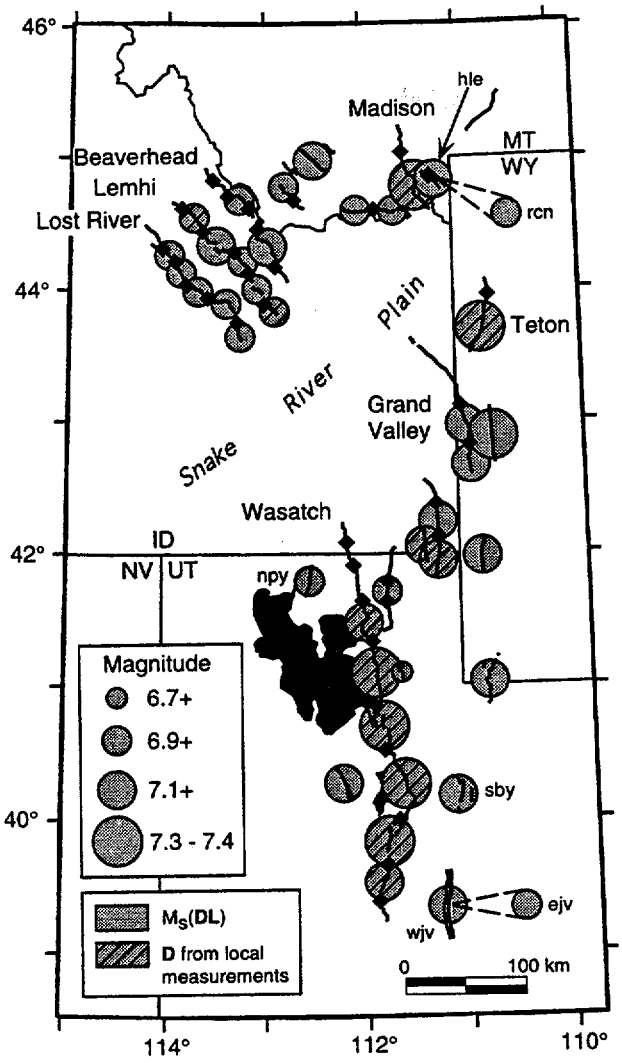

Figure 7. Paleomagnitudes scaled from *DL* for individual ISB fault segments.

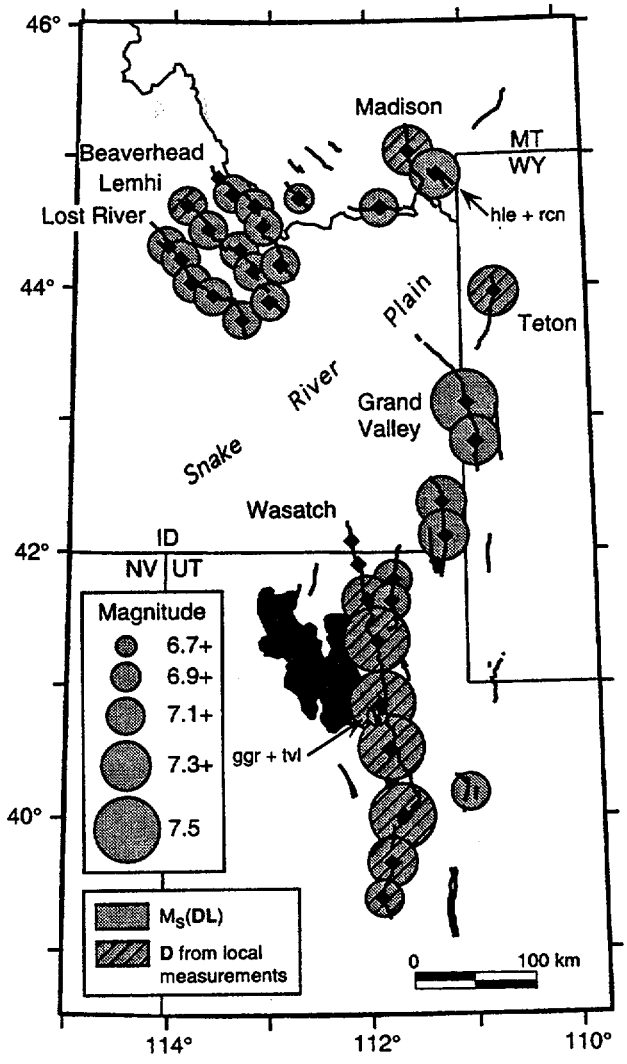

Figure 8. Paleomagnitudes scaled from *DL* for multi-segmented faults, assuming rupture in pairs of adjacent segments. Each magnitude symbol is centered over the boundary between the two segments from which it was derived.

mological data now available from faults throughout the ISB as well as historical earthquake data from around the world.

In order to obtain an appropriate magnitude scaling relationship for use with the ISB paleoseismic data, the author computed unweighted, linear, least-squares regressions of magnitude on the logarithms of surface rupture length *L*, maximum surface displacement *D*, and *DL*, respectively, for an updated set of 20 historical, normal-slip earthquakes from worldwide sources. These were compared with 12 similar regressions from two other published studies. Two categories of faulting were represented: normal slip, because of its relevance to the ISB, and all slip types. Statistical ranking showed that the *L*-based formula including all slip types (4) had high correlation with a large number of data points, but the highest ranking regressions for the normal slip *D*- and *DL*-based formulas, (5) and (6), had comparable correlation and 0.1 *M* unit lower standard deviation. Some earthquakes express a disproportionate amount of seismic energy in one surface rupture parameter versus the other, resulting in significant disparity between magnitudes scaled independently by the two parameters. A *DL*-based regression tends to average these magnitudes. For this reason and because it is uncertain whether *D* or *L* may more accurately scale earthquake size for ISB faults, (6) was chosen as the preferred regression for application to the ISB faults with estimates of both length and displacement.

Application of magnitude regressions to 65 late Quaternary fault segments throughout a large portion of the ISB reveals that maximum surface displacements scale larger magnitudes by 0.2 to 0.3 *M* unit on average than the estimated surface rupture lengths of the single earthquake segments from which they are measured. This includes a correction for disparities between the regressions, which implies a problem either in the paleoseismic data or in the

assumptions made in using it. Considerations of the expected uncertainties associated with measurements of paleoseismic D suggest that overestimation of D is generally insufficient to explain the negative bias in $M(L) - M(D)$. However, the ratio of maximum-to-average displacements for the largest historical earthquakes in the Basin and Range support observations by McCalpin (1993) that some ISB faults may produce larger-than-average displacements for the rupture lengths associated with them. Examples may include faults in southwestern Montana.

Since it is now known that large earthquakes often rupture multiple segments of a fault, any attempt to assess maximum magnitude potential for the ISB must include multi-segment failure. There is presently no standard basis for quantifying the fractions of segments that may fail in an earthquake, but a dual-segment rupture model for multi-segmented faults effectively removes the discrepancy between $M(L)$ and $M(D)$ to 0.1 M unit. A dual-segment model represents a good first approximation to maximum magnitude estimation for ISB earthquakes, based on the surface deformation of the Hebgen Lake and Borah Peak earthquakes and evidence from previously published timing estimates for prehistoric faulting of adjacent segments in the Wasatch fault zone in the central ISB.

Mean-value estimates of maximum magnitude were computed for the ISB faults of this study using (6) and a dual-segment rupture scenario. Values range from M_S 6.8 to 7.5 ($\sigma_m = \pm 0.20$) and, with one σ_m, encompass all of the largest magnitudes documented in the worldwide historical record for normal-faulting earthquakes (M_S 7.6, Pleasant Valley, USA). The largest magnitudes are associated with the longest fault systems and include the Brigham City, Weber, Salt Lake City, and Provo segments of the Wasatch fault and the Grand Valley, Teton, North Madison, and middle East Bear Lake faults. The inclusion of the Teton fault in this list is significant in light of the fact that it spans a noticeable seismic gap in the ISB (Smith, 1978) and that such gaps have, in some cases, been associated with the locations of large damaging earthquakes (*e.g.*, Mogi, 1985).

Acknowledgments

This work was supported by the U.S. Geological Survey, National Earthquake Hazards Program, Grants 14-08-0001-G1762 and 1434-93-G-2348. The author would like to thank Robert B. Smith at the University of Utah for helping to guide this research. Thanks are also extended to Donald Wells, Craig dePolo, James C. Pechmann, and Ronald Bruhn for many constructive comments and corrections. Jim McCalpin, Peter Knuepfer, Donald Wells, Kevin Coppersmith, David West, and John O. Byrd provided valuable fault data and preprints.

References

Abe, K. (1981). Magnitudes of large shallow earthquakes from 1904 to 1980, *Phys. Earth Planet. Interiors* **27**, 72–92.

Acharya, H. K. (1979). Regional variations in the rupture-length magnitude relationships and their dynamical significance, *Bull. Seism. Soc. Am.* **69**, no. 6, 2085–2099.

Ambraseys, N. N. (1970). Some characteristic features of the Anatolian fault zone, *Tectonophysics* **9**, 143–165.

Ambraseys, N. N. (1975). Studies in historical seismicity and tectonics, in *Geodynamics Today*, The Royal Society, London, 7–16.

Ambraseys, N. N. (1988). Engineering seismology, *Earthquake Eng. Struct. Dynam.* **17**, 1–105.

Ambraseys, N. N. and C. P. Melville (1982). *A History of Persian Earthquakes*, Cambridge U Press, Cambridge, 219 pp.

Ambraseys, N. N. and J. S. Tchalenko (1972). Seismotectonic aspects of the Gediz, Turkey, earthquake of March 1970, *Roy. Astr. Soc. Geophys. J.* **30**, 229–252.

Anders, M. H., J. W. Geissman, L. A. Piety, and J. T. Sullivan (1989). Parabolic distribution of circumeastern Snake River Plain seismicity and latest Quaternary faulting: migratory pattern and association with the Yellowstone hotspot, *J. Geophys. Res.* **94**, no. B2, 1589–1621.

Beanland, S., G. H. Blick, and D. J. Darby (1990). Normal faulting in a back arc basin: geological and geodetic characteristics of the 1987 Edgecumbe earthquake, New Zealand, *J. Geophys. Res.* **95**, no. B4, 4693–4707.

Bell, J. W., D. B. Slemmons, and R. E. Wallace (1984). Reno to Dixie Valley-Fairview Peak earthquake areas [roadlog] in *Western Geological Excursions*, Vol. 4, J. Lintz (Editor), prepared for Annual meetings *Geol. Soc. Am.* and Affil. Socs. at Reno, Nevada, 388–402 and 425–472.

Bellier, O., J. F. Dumont, M. Sebrier, and J. L. Mercier (1991). Geological constraints on the kinematics and fault-plane solution of the Quiches fault zone reactivated during the 10 November 1946 Ancash earthquake, Northern Peru, *Bull. Seism. Soc. Am.* **81**, no. 2, 468–490.

Bolt, B. A. (1978). Incomplete formulations of the regression of earthquake magnitude with surface fault rupture length, *Geology* **6**, 233–235.

Bonilla, M. G. and J. M. Buchanan (1970). Interim report on world-wide historic surface faulting, *U.S. Geol. Surv. Open-File Rept.*, 32 pp.

Bonilla, M. G. and M. Wyss (1980). Comment and Reply on "Estimating maximum expectable magnitudes of earthquakes from fault dimensions," *Geology* **8**, no. 4, 162–164.

Bonilla, M. G., R. K. Mark, and J. J. Lienkaemper (1984). Statistical relations among earthquake magnitude, surface rupture length, and surface fault displacement, *Bull. Seism. Soc. Am.* **74**, no. 6, 2379–2411.

Boschi, E., D. Pantosti, and G. Valensise (1990). Paradoxes of Italian seismicity: the Irpinia earthquake of November 23, 1980, *EOS* **71**, no. 46, 1787–1788.

Bucknam, R. C. and R. E. Anderson (1979). Estimation of fault scarp ages from a scarp height-slope angle relationship, *Geology* **7**, 11–14.

Byrd, J. O. (1992). Personal communication, Dept. of Geology and Geophysics, Univ. of Utah, Salt Lake City, Utah.

Byrd, J. O. and R. B. Smith (1991). Paleoseismicity, near-surface fault geometry, and segmentation of Teton normal fault, Wyoming, *EOS* **72**, 316.

Clark, M. M. (1972). Surface rupture along the Coyote Creek fault, in *The Borrego Mountain Earthquake of April 9, 1968, U.S. Geol. Surv. Profess. Pap. 787*, 55–86.

Coppersmith, K., R. Youngs, I. Wong, M. Hemphill-Haley, T. Sawyer, P. Knuepfer, R. Bruhn, D. Smith, B. Hackett, and S. Jackson (1991). Probabilistic ground motion evaluation for the proposed new production reactor at the Idaho National Engineering Laboratory, *Geomatrix Consultants, Woodward-Clyde Consultants, and EG&G Idaho, Inc.*

Crone, A. J. and K. M. Haller (1991). Segmentation and the coseismic behavior of Basin and Range normal faults: examples from east-central Idaho and southwestern Montana, U.S.A., *J. Struct. Geol.* **13**, no. 2, 151–164.

Crone, A. J. and M. N. Machette (1984). Surface faulting associated with the Borah Peak earthquake, central Idaho, *Geology* **12**, 664–667.

Crone, A. J., M. N. Machette, M. G. Bonilla, J. J. Lienkaemper, K. L. Pierce, W. E. Scott, and R. C. Bucknam (1987). Surface faulting accompanying the Borah Peak earthquake and segmentation of the Lost River fault, central Idaho, *Bull. Seism. Soc. Am.* **77**, 739–770.

dePolo, C. M. and D. B. Slemmons (1990). Estimation of earthquake size

for seismic hazards, in *Neotectonics in Earthquake Evaluation,* E. L. Krinitzsky and D. B. Slemmons (Editors), Boulder, Colorado, *Geol. Soc. Am. Rev. Eng. Geol.,* Vol. VIII, 1–28.

dePolo, C. M., D. G. Clark, D. B. Slemmons, and A. R. Ramelli (1991). Historical surface faulting in the Basin and Range province, western North America: implications for fault segmentation, *J. Struct. Geol.* **13,** no. 2, 123–136.

Doser, D. I. (1985). Source parameters and faulting processes of the 1959 Hebgen Lake, Montana earthquake sequence, *J. Geophys. Res.* **90,** 4537–4555.

Doser, D. I. (1987). The Ancash, Peru, earthquake of 1946 November 10: evidence for low-angle normal faulting in the high Andes of northern Peru, *Geophys. J. R. Astr. Soc.* **91,** 57–71.

Doser, D. I. (1989). Extensional tectonics in northern Utah–southern Idaho, U.S.A., and the 1934 Hansel Valley sequence, *Phys. Earth Planet. Interiors* **48,** 64–72.

Doser, D. I. and R. B. Smith (1982). Seismic moment rates in the Utah region, *Bull. Seism. Soc. Am.* **72,** 525–551.

Engdahl, E. R. and W. A. Rinehart (1991). Seismicity Map of North America Project, in *Neotectonics of North America,* D. B. Slemmons, E. R. Engdahl, M. D. Zoback, and D. D. Blackwell (Editors), *Geol. Soc. Am.,* Decade Map Vol. I, Boulder, Colorado.

Eyidogan, H. and J. Jackson (1985). A seismological study of normal faulting in the Demirci, Alasehir and Gediz earthquakes of 1969–70 in western Turkey: implications for the nature and geometry of deformation in the continental crust, *Geophys. J. R. Astr. Soc.* **81,** 569–607.

Foley, L. L., R. A. Martin, Jr., and J. T. Sullivan (1986). Seismotectonic study for Joes Valley, Scofield and Huntington North Dams, Emery County and Scofield Projects, Utah, *U.S. Bureau of Reclamation Seismotectonic Rept. No. 86-7,* 132 pp.

Fonseca, J. (1988). The Sou Hills, a barrier to faulting in the central Nevada seismic belt, *J. Geophys. Res.* **93,** 475–489.

Forman, S. L., M. N. Machette, M. E. Jackson, and P. Mott (1989). An evaluation of thermoluminescence dating of paleoearthquakes on the American Fork segment, Wasatch fault zone, Utah, *J. Geophys. Res.* **94,** 1622–1630.

Gutenberg, B. and C. F. Richter (1954). *Seismicity of the Earth and Associated Phenomena,* 2nd ed., Princeton University Press, Princeton, New Jersey, 310 pp.

Haller, K. M. (1990). Late Quaternary movement on basin-bounding normal faults north of the Snake River plain, east-central Idaho, in *Geologic Field Tours of Western Wyoming,* S. Roberts (Editor), *Geol. Surv. Wyom.,* 191 pp.

Hanks, T. C. and H. Kanamori (1979). A moment magnitude scale, *J. Geophys. Res.* **84,** no. B5, 2348–2350.

Heck, N. H. (1938). Earthquakes and the western mountain region, *Geol. Soc. Am. Bull.* **49,** 1–22.

Hecker, S. (1993). Quaternary tectonics of Utah with emphasis on earthquake hazard characterization, *Utah Geol. Surv. Bull.* **127,** 157.

Iida, N. (1965). Earthquake magnitude, earthquake fault and source dimensions, *Nagoya Univ. J. Earth Sci.* **13,** 115–132.

Jackson, J. A., J. Gagnepain, G. Houseman, G. C. P. King, P. Papadimitriou, C. Soufleris, and J. Virieux (1982). Seismicity, normal faulting, and the geomorphological development of the Gulf of Corinth (Greece): the Corinth earthquakes of February and March 1981, *Earth Planet. Sci. Lett.* **57,** 377–397.

Jackson, M. E. (1991). Paleoseismology of Utah, Vol. 3—The number and timing of Holocene paleoseismic events on the Nephi and Levan segments, Wasatch fault zone, Utah, *Utah Geol. Min. Surv. Spec. Studies 78,* 23 pp.

Jankof, K. (1945). Changes in ground level produced by the earthquakes of April 14 and 18, 1928, in southern Bulgaria, in *Tremblements de Terre en Bulgarie 29–31,* Institute Meterologique Central de Bulgarie, 131–136.

Johnson, P. P. (1981). Geology along the Red Rock fault and adjacent Red Rock basin, Beaverhead County, Montana, in southwest Montana, Special Publication, *1981 Field Conference Guidebook, Montana Geological Society,* 245–251.

Jones, L. C. A. (1992). Personal communication, Dept. of Geol., Utah State Univ., Logan, Utah.

Jones, L. C. A. and J. McCalpin (1992). Quaternary faulting on the Grey's River fault, a listric normal fault in the overthrust belt of Wyoming, in preparation for 1992 regional spring meeting of the *Geol. Soc. Am.,* Utah State Univ., Logan, Utah.

Kanamori, H. (1977). The energy release in great earthquakes, *J. Geoph. Res.* **82,** no. 20, 2981–2987.

Kanamori, H. (1983). Magnitude scale and quantification of earthquakes. *Tectonophysics* **93,** 185–199.

Kanamori, H. and C. R. Allen (1986). Earthquake repeat time and average stress drop, in *Earthquake Source Mechanics,* Vol. 6, S. Das, J. Boatwright, and C. Scholz (Editors), Geophysical Monograph 37, 341 pp.

Keaton, J. R. and D. R. Currey (1989). Earthquake hazards evaluation of the West Valley fault zone, Salt Lake City urban area, Utah (rept.), *U.S. Geol. Surv.,* Contract 14-08-0001-G1397, September 15, 1989, Salt Lake City, Utah, Dames and Moore, 68 pp.

King, G. and J. Nabelek (1985). Role of fault bends in the initiation and termination of earthquake rupture, *Science* **228,** 984–987.

King, G. C. P., Z. X. Ouyang, P. Papadimitriou, A. Deschamps, J. Gagnepain, G. Houseman, J. A. Jackson, C. Soufleris, and J. Virieux (1985). The evolution of the Gulf of Corinth (Greece): an aftershock study of the 1981 earthquakes, *Geophys. J. R. Astr. Soc.* **80,** 677–693.

Knuepfer, P. L. K. (1989). Implications of the characteristics of endpoints of historical surface fault ruptures for the nature of fault segmentation, in *Proc. of Conf. XLV, Fault Segmentation and Controls of Rupture Initiation and Termination,* D. P. Schwartz and R. H. Sibson (Editors), *U.S. Geol. Surv. Open-File Rept. 89-315,* 193–228.

Knuepfer, P. K., E. M. Baltzer, and J. M. Turko (1989). Repeatability of fault rupture segments and earthquake potential, *U.S. Geol. Surv. Final Tech. Rept.,* Contract 14-08-0001-G1527, 45 pp.

Lund, W. R., D. P. Schwartz, W. E. Mulvey, K. E. Budding, and B. D. Black (1991). Paleoseismology of Utah, Vol. 1—Fault behavior and earthquake recurrence on the Provo segment of the Wasatch fault zone at Mapleton, Utah County, Utah, *Utah Geol. Min. Surv. Spec. Studies 75,* 41 pp.

Lyon-Caen, H., R. Armijo, J. Drakopaulos, J. Baskoutass, N. Delibassis, R. Gaulon, V. Kouskouna, J. Latoussakis, K. Makropopoulos, P. Papadimitriou, D. Papanastassiou, and G. Pedotti (1988). The 1986 Kalamata (South Peloponnesus) earthquake: detailed study of a normal fault, evidences for East–West extension in the Hellenic Arc, *J. Geophys. Res.* **93,** no. B12, 14967–15000.

McCalpin, J. (1990). Latest Quaternary faulting in the Northern Wasatch-to-Teton Corridor (NWTC), *U.S. Geol. Surv. Final Tech. Rept.,* Contract No. 14-08-001-G1396, 42 pp.

McCalpin, J. (1993). Neotectonics of the northeastern Basin and Range margin, western USA, *Zeitschrift Geomorph. N. E.,* Suppl.-Bd. **94,** 137–157.

McCalpin, J. and S. L. Forman (1991). Late Quaternary faulting and thermoluminescence dating of the East Cache fault zone, north-central Utah, *Bull. Seism. Soc. Am.* **81,** no. 1, 139–161.

McCalpin, J. and G. A. Warren (1992). Quaternary faulting on the Rock Creek Fault, overthrust belt, Western Wyoming, *Geol. Soc. Am. Abstr. Progr.* **24,** 51.

McCalpin, J., R. M. Robison, and J. D. Garr (1987). Neotectonics of the Hansel Valley–Pocatello Valley corridor, northern Utah and southern Idaho, in *Assessing Regional Earthquake Hazards and Risk Along the Wasatch Front, Utah,* P. L. Gori and W. W. Hays (Editors), *U.S. Geol. Surv. Profess. Paper 1500-A,* G-1-28.

Machette, M. N. (1988). American Fork Canyon—Holocene faulting, the Bonneville fan-delta complex, and evidence for the Keg Mountain oscillation, in *In the Footsteps of G. K. Gilbert—Lake Bonneville and Neotectonics of the Eastern Basin and Range Province,* M. N. Mach-

ette (Editor), Geological Society of America Guidebook to Field Trip 12, *Utah Geol. Min. Surv. Misc. Publ. 88-1,* 89–95.

Machette, M. N., S. F. Personius, and A. R. Nelson (1987). Quaternary geology along the Wasatch fault zone: segmentation, recent investigations, and preliminary conclusions, *U.S. Geol. Surv. Open-File Rept. 87-585,* A1–A72.

Machette, M. N., S. F. Personius, and A. R. Nelson (1992). Paleoseismology of the Wasatch fault zone: a summary of recent investigations, interpretations, and conclusions, in *Assessment of Regional Earthquake Hazards and Risk Along the Wasatch Front, Utah,* P. L. Gori and W. W. Hays (Editors), *U.S. Geol. Surv. Profess. Paper* 1500-A-J.

Machette, M. N., S. F. Personius, A. R. Nelson, D. P. Schwartz, and W. R. Lund (1991). The Wasatch fault zone, Utah: segmentation and history of Holocene earthquakes, *J. Struct. Geol.* **13,** no. 2, 137–149.

Malde, H. E. (1987). Quaternary faulting near Arco and Howe, Idaho, *Seism. Soc. Am. Bull.* **77,** 847–867.

Mark, R. K. (1977). Application of linear statistical models of earthquake magnitude versus fault length in estimating maximum expectable earthquakes, *Geology* **5,** 464–466.

Mark, R. K. (1979). Comment on "Incomplete formulations of the regression of earthquake magnitude with surface fault rupture length," *Geology* **7,** no. 1, 6.

Mason, D. B. (1992). Earthquake magnitude potential of active faults in the Intermountain Seismic Belt from surface parameter scaling, *Master's Thesis,* University of Utah, Salt Lake City, Utah, 110 pp.

Mogi, K. (1985). *Earthquake Prediction,* Academic Press, Tokyo, 355 pp.

Myers, W., W. Hamilton, W. H. Hays, I. J. Witkind, J. B. Epstein, J. B. Hadley, and F. A. Swenson (1964). Map of Hebgen Lake–West Yellowstone area showing surficial features and ground deformation that resulted from the Hebgen Lake earthquake, in *The Hebgen Lake, Montana Earthquake of August 17, 1959, U.S. Geol. Surv. Profess. Paper 435,* 242 pp. scale 1:62,500.

Nelson, A. R. and R. A. Martin, Jr. (1982). Seismotectonic study for Soldier Creek Dam, Central Utah Project, *U.S. Bureau of Reclamation Seismotectonic Report 82-1,* 115 pp.

Nelson, A. R. and J. T. Sullivan (1992). Late Quaternary history of the James Peak fault, southernmost Cache Valley, North-Central Utah, in *Assessment of Regional Earthquake Hazards and Risk Along the Wasatch Front, Utah,* P. L. Gori and W. W. Hays (Editors), *U.S. Geol. Surv. Profess. Paper* 1500-A-J.

Nelson, A. R. and R. B. van Arsdale (1986). Recurrent late Quaternary movement on the Strawberry normal fault, Basin and Range—Colorado Plateau transition zone, Utah, *Neotectonics* **1,** 7–37.

Ostenaa, D. A. (1990). Late Holocene displacement history, Water Canyon site, Wasatch fault, Utah, *Geol. Soc. Am. Abs. Prog.* **22,** no. 6, 42.

Ostenaa, D. and C. Wood (1990). Seismotectonic Study for Clark Canyon Dam Pick-Sloan Missouri Basin Program, Montana, Seismotectonic Rept. 90-4, *U.S. Bureau of Reclamation,* Denver, Colorado, 78 pp. also plate.

Pantosti, D. and G. Valensise (1990). Faulting mechanism and complexity of the November 23, 1980, Campania-Lucania earthquake, inferred from surface observations, *J. Geophys. Res.* **95,** no. B10, 15319–15341.

Pantosti, D., D. P. Schwartz, and G. Valensise (1989). Paleoseismologic and geomorphic observations along the 1980 Irpinia surface fault rupture, southern Apennines (Italy), *EOS* **70,** 1349.

Papazachos, B., A. Kiratzi, B. Karacostas, D. Panagiotopoulos, E. Scordilis, and D. M. Mountrakis (1988). Surface fault traces, fault plane solution and spatial distribution of the aftershocks of the September 13, 1986 earthquake of Kalamata (Southern Greece), *Pure Appl. Geophys.* **126,** no. 1, 55–68.

Pechmann, J. C. (1987a). Earthquake design considerations for the interisland diking project, Great Salt Lake, Utah, Technical Rept. submitted to Rollins, Brown, and Gunnell, Inc., Provo, Utah, 60 pp.

Pechmann, J. C. (1987b). Personal communication, Department of Geology and Geophysics, University of Utah, Salt Lake City, Utah.

Personius, S. F. (1982). Geomorphic analysis of the Deep Creek fault, upper Yellowstone Valley, south-central Montana, Thirty-third Annual Field Conference, *1982 Wyoming Geological Association Guidebook,* 203–212.

Personius, S. F. (1991a). Paleoseismic analysis of the Wasatch fault zone at the Brigham City trench site, Brigham City, Utah, in *Paleoseismology of Utah,* Vol. II, W. R. Lund (Editor), *Utah Geol. and Min. Surv. Spec. Publ. 76,* 1–18.

Personius, S. F. (1991b). Paleoseismic analysis of the Wasatch fault zone at the Pole Patch trench site, Pleasant View, Utah, in *Paleoseismology of Utah,* Vol. II, *Utah Geol. Min. Surv. Special Studies 76,* 19–39.

Pierce, K. L. (1985). Quaternary history of faulting on the Arco segment of the Lost River fault, central Idaho, *Proceedings of Workshop XXVIII on the Borah Peak, Idaho Earthquake,* R. S. Stein and R. C. Bucknam (Editors), *U.S. Geol. Surv. Open-File Rept. 85-290,* 195–206.

Piety, L. A., C. K. Wood, J. D. Gilbert, J. T. Sullivan, and M. H. Anders (1986). Seismotectonic study for Palisades Dam and Reservoir, Palisades Project, Seismotectonic Report No. 86-3, U.S. Bureau of Reclamation, Denver, Colorado, and *Bureau of Reclamation,* Boise, Idaho, 190 pp.

Plafker, G., R. Agar, A. H. Asker, and M. Hanif (1987). Surface effects and tectonic setting of the 13 December 1982 North Yemen earthquake, *Bull. Seism. Soc. Am.* **77,** no. 6, 2018–2037.

Progetto Finalizzato Geodinamica (1986). Catalogo dei terromoti italiani dal 1000 al 1980, *Italian National Research Council.*

Richens, W. D. (1979). The Hansel Valley, Utah, earthquake sequence of November 1976, in *Earthquake Studies in Utah, 1850 to 1978,* W. J. Arabasz, R. B. Smith, and W. D. Richens (Editors), Special Publication, University of Utah Seismograph Stations, Salt Lake City, Utah, 409–421.

Richens, W. D., J. C. Pechmann, R. B. Smith, C. J. Langer, S. K. Goter, J. E. Zollweg, and J. J. King (1987). The 1983 Borah Peak, Idaho, earthquake and its aftershocks, *Bull. Seism. Soc. Am.* **77,** 694–723.

Richter, C. F. (1958). *Elementary Seismology,* W. H. Freeman and Co., San Francisco, California, 768 pp.

Roberts, S. and J. Jackson (1991). Active faulting in central Greece: an overview, in *The Geometry of Normal Faults,* Spec. Publ. *Geol. Soc. Lond.* **56,** 125–142.

Ryall, A., D. B. Slemmons, and L. S. Gedney (1966). Seismicity, tectonism, and surface faulting in the western United States during historic time, *Bull. Seism. Soc. Am.* **56,** 1105–1135.

Salyards, S. L. (1985). Patterns of offset associated with the 1983 Borah Peak earthquake and previous events, in *Proc. of Workshop XXVIII, On the Borah Peak, Idaho, Earthquakes,* R. S. Stein and R. C. Bucknam (Editors), *U.S. Geol. Surv. Open-File Rept. 85-290,* 59–75.

Savage, J. C., M. Lisowski, and W. H. Prescott (1985). Strain accumulation in the Rocky Mountain states, *J. Geophys. Res.* **90,** 10310–10320.

Sbar, M. L., M. Barazangi, J. Dorman, C. H. Scholz, and R. B. Smith (1972). Tectonics of the Intermountain seismic belt, western United States: microearthquake seismicity and composite fault plane solutions, *Geol. Soc. Am. Bull.* **83,** 13–28.

Scholz, C. H. (1982). Scaling laws for large earthquakes: consequences for physical models, *Bull. Seism. Soc. Am.* **72,** no. 1, 1–14.

Schwartz, D. P. and K. J. Coppersmith (1984). Fault behavior and characteristic earthquakes: examples from the Wasatch and San Andreas fault zones, *J. Geophys. Res.* **89,** no. B7, 5681–5698.

Schwartz, D. P. and K. J. Coppersmith (1986). Seismic hazards: new trends in analysis using geologic data, in *Active Tectonics, Studies in Geophysics,* National Academy Press, Washington, D.C., 215–230.

Schwartz, D. P. and W. R. Lund (1988). Paleoseismicity and earthquake recurrence at Little Cottonwood canyon, Wasatch fault zone, Utah, in *In the Footsteps of G. K. Gilbert—Lake Bonneville and Neotectonics of the Eastern Basin and Range Province, Utah Geol. Min. Surv. Misc. Publ. 88-1,* 89–99.

Schwartz, D. P., F. H. Swan, and L. S. Cluff (1984). Fault behavior and earthquake recurrence along the Wasatch fault zone, in *Proc. of Con-*

ference XXVI: A Workshop on Evaluation of Regional and Urban Earthquake Hazards and Risk in Utah, U.S. Geol. Surv. Open-File Rept. 84-763, 113–125.

Scott, W. E., K. L. Pierce, and M. H. Hait, Jr. (1985). Quaternary tectonic setting of the 1983 Borah peak earthquake, Central Idaho, *Bull. Seism. Soc. Am.* **75,** no. 4, 1053–1066.

Serva, L., A. M. Blumetti, and A. M. Michetti (1986). Gli effetti sul terreno del grande terremoto del Fucino (13 gennaio 1915): tentativo di interpretazione della evoluzione tettonica recent di alcune strutture, *Mem. Soc. Geol. It.* **35.**

Shenon, P. J. (1936). The Utah earthquake of March 12, 1934 (extracts from unpublished report), in *United States Earthquakes, 1934,* F. Neuman (Editor), *U.S. Dept. Commerce, Coast and Geodetic Survey, Ser. 593,* 43–48.

Sibson, R. H. (1989). Earthquake faulting as a structural process, *J. Struct. Geol.* **11,** 1–14.

Silgado, E. (1951). The Ancash, Peru, earthquake of November 10, 1946, *Bull. Seism. Soc. Am.* **41,** no. 2, 83–100.

Slemmons, D. B. (1957). Geological effects of the Dixie Valley–Fairview Peak, Nevada, earthquakes of December 16, 1954, *Bull. Seism. Soc. Am.* **47,** 353–375.

Slemmons, D. B. (1977). Faults and earthquake magnitude, *U.S. Army Corps of Engineers, Misc. Paper S-73-1, Rept. 6,* Waterways Experiment Station, Vicksburg, Mississippi, 1–129.

Slemmons, D. B. (1982). Determination of design earthquake magnitudes for microzonation, *Proc. Third International Earthquake Microzonation Conf. Vol. 1,* U.S. National Science Foundation, Washington, D.C., 119–130.

Slemmons, D. B., A. E. Jones, and J. I. Gimlet (1965). Catalog of Nevada earthquakes 1852–1960, *Bull. Seism. Soc. Am.* **55,** 537–583.

Smith, R. B. (1978). Seismicity, crustal structure, and intraplate tectonics of the Western Cordillera, in *Cenozoic Tectonics and Regional Geophysics of the Western Cordillera, Memoir 152,* R. B. Smith and G. P. Eaton (Editors), *Geol. Soc. Amer.,* 111–144.

Smith, R. B. and W. J. Arabasz (1991). Seismicity of the Intermountain seismic belt, in *Neotectonics of North America,* D. B. Slemmons, E. R. Engdahl, M. D. Zoback, and D. D. Blackwell (Editors), *Geol. Soc. Am. Decade of N. Am. Geol.,* 498 pp.

Smith, R. B. and R. L. Bruhn (1984). Intraplate extensional tectonics of the eastern Basin-Range: inferences on structural style from seismic reflection data, regional tectonics, and thermal-mechanical models of brittle-ductile deformation, *J. Geophys. Res.* **89,** 5733–5762.

Smith, R. B. and M. L. Sbar (1974). Contemporary tectonics and seismicity of the western United States with emphasis on the Intermountain seismic belt, *Geol. Soc. Am. Bull.* **85,** 1205–1218.

Smith, R. B., J. O. D. Byrd, A. A. Sylvester, and D. D. Susong (1990). Neotectonics and earthquake hazards of the Teton fault, *Geol. Soc. Am. Abstr. Progr.,* 43rd Annual Meeting, Rocky Mountain Section, 45.

Smith, R. B. *et al.* (1982). The Yellowstone-eastern Snake River Plain seismic profiling experiment: crustal structure of Yellowstone, *J. Geoph. Res.* **84,** 2583–2596.

Solomon, B. J., B. L. Everitt, D. R. Currey, J. S. Paulick, D. Wu, S. Olig, and T. N. Burr (1992, preprint). Quaternary geology and geologic hazards of Tooele and northern Rush valleys, Utah, *Geol. Soc. Am. Field Guide,* Rocky Mtn. Sectn., 47–52.

Sparlin, M. A., L. W. Braile, and R. B. Smith (1982). Crustal structure of the Eastern Snake River Plain determined from ray trace modeling of seismic refraction data, *J. Geophys. Res.* **87,** 2619–2633.

Stickney, M. C. and M. J. Bartholomew (1987). Seismicity and late Quaternary faulting of the northern Basin and Range province, Montana and Idaho, *Bull. Seism. Soc. Am.* **77,** no. 5, 1602–1625.

Sullivan, J. T. and A. R. Nelson (1992). Late Quaternary displacement on the Morgan fault, a back-valley fault in the Wasatch Range of Northeastern Utah, in *Assessment of Regional Earthquake Hazards and Risk along the Wasatch Front, Utah,* Vol. I, P. L. Gori and W. W. Hays (Editors), *U.S. Geol. Surv. Prof. Paper 1500-A-J.*

Susong, D. D., S. U. Janecke, and R. L. Bruhn (1990). Structure of a fault segment boundary in the Lost River fault zone, Idaho, and possible effect on the 1983 Borah Peak earthquake rupture, *Bull. Seism. Soc. Am.* **80,** no. 1, 57–68.

Susong, D., R. B. Smith, and R. L. Bruhn (1987). Quaternary faulting and segmentation of the Teton fault zone, Grand Teton National Park, Wyoming, *EOS* **68,** no. 44, 1244.

Swan, F. H., III, D. P. Schwartz, and L. S. Cluff (1980). Recurrence of moderate to large magnitude earthquakes produced by surface faulting on the Wasatch fault zone, Utah, *Bull. Seism. Soc. Am.* **70,** no. 5, 1431–1462.

Swan, F. H., III, K. L. Hanson, D. P. Schwartz, and J. H. Black (1983). Study of earthquake recurrence intervals on the Wasatch fault, Utah, *U.S. Geol. Surv. Eighth Semi-Annual Tech. Rept.,* Contract No. 14-08-0001-19842, 20 pp.

Swan, F. H., III, K. L. Hanson, D. P. Schwartz, and P. L. Knuepfer (1981). Study of earthquake recurrence intervals on the Wasatch fault at the Little Cottonwood Canyon site, Utah, *U.S. Geol. Surv. Open-File Rept. 81-450,* 30 pp.

Tocher, D. (1956). Movement on the Rainbow mountain fault, *Bull. Seism. Soc. Am.* **46,** 10–14.

Tocher, D. (1958). Earthquake energy and ground breakage, *Bull. Seism. Soc. Am.* **48,** 147–153.

Turko, J. M. and P. L. K. Knuepfer (1991). Late Quaternary fault segmentation from analysis of scarp morphology, *Geology* **19,** 718–721.

van Arsdale, R. B. (1979). Geology of Strawberry Valley and regional implications, *unpublished Ph.D. Dissertation,* Univ. of Utah, Salt Lake City, 65 pp.

Wallace, R. E. (1977). Profiles and ages of young fault scarps, north-central Nevada, *Geol. Soc. Am. Bull.* **88,** 1267–1281.

Wallace, R. E. (1984). Fault scarps formed during the earthquakes of October 2, 1915, Pleasant Valley, Nevada, and some tectonic implications, *U.S. Geol. Surv. Profess Paper 1274-A,* 33 pp.

Wallace, R. E. and R. A. Whitney (1984). Late Quaternary history of the Stillwater seismic gap, *Seism. Soc. Am. Bull.* **74,** no. 1, 301–314.

Wells, D. L. and K. J. Coppersmith (1994). New empirical relationships among magnitude, rupture length, rupture width, rupture area, and surface displacement, *Bull. Seism. Soc. Am.* **84,** 974–1002.

Wesson, R. L., R. A. Page, D. M. Boore, and R. F. Yerkes (1974). Expectable earthquakes in the van Norman Reservoirs area, *U.S. Geol. Surv. Circ. 691-B,* 9 pp.

West, M. W. (1988). Geologic and tectonic studies in the vicinity of Meeds Cabin and Stateline dams, in *Seismotectonic Study for Meeks Cabin and Stateline Dams,* Lyman Project, Wyoming, *U.S. Bureau of Reclamation Seismotectonic Report 88-11,* 121 pp.

Westaway, R. and J. A. Jackson (1987). The earthquake of 1980 November 23 in Campania-Basilicata (southern Italy), *Geophys. J. Res. Astr. Soc.* **90,** 375–443.

Westaway, R., R. Gawthorpe, and M. Tozzi (1989). Seismological and field observations of the 1984 Lazio-Abruzzo earthquakes: implications for the active tectonics of Italy, *Geophys. J. Int.* **98,** no. 3, 489–514.

Wheeler, R. L. and K. B. Krystinik (1992). Persistent and nonpersistent segmentation of the Wasatch fault zone, Utah: statistical analysis for evaluation of seismic hazard, in *Assessment of Regional Earthquake Hazards and Risk along the Wasatch Front, Utah,* P. L. Gori and W. W. Hays (Editors), *U.S. Geol. Surv. Profess. Paper 1500-A-J.*

Willis, B. (1936). Studies in comparative seismology: East African plateaus and rift valleys, Washington, D.C., *Carnegie Inst. Wash. Publ. 470,* 358 pp.

Witkind, I. J. (1964). Reactivated faults north of Hebgen Lake, in *The Hebgen Lake, Montana Earthquake of August 17, 1959, U.S. Geol. Surv. Profess. Paper 435,* 3750.

Woolard, G. P. (1958). Areas of tectonic activity in the United States as indicated by earthquake epicenters, *EOS* **39,** 1135–1150.

Wu, Daning (1994). Personal communication, University of Utah, Department of Geology and Geophysics, Salt Lake City, Utah.

Wyss, M. (1979). Estimating maximum expectable magnitude of earthquakes from fault dimensions, *Geology* **7,** 336–340.

Youngs, R. R., F. H. Swan, M. S. Power, D. P. Schwartz, and R. K. Green (1987). Probabilistic analysis of earthquake ground shaking hazard along the Wasatch front, Utah, in *Assessment of Regional Earthquake Hazards and Risk along the Wasatch Front, Utah,* Vol. 2, *U.S. Geol. Surv. Profess. Paper 87-585,* 110 pp.

Zoback, M. L. (1989). State of stress and modern deformation of the northern Basin and Range province, *J. Geophys. Res.* **94,** 7105–7128.

Zoback, M., R. Anderson, and G. Thompson (1981). Cenozoic evolution of the Basin and Range Province of the western United States, *Philos. Trans. R. Soc. London Ser. A* **300,** 407–434.

Department of Geology and Geophysics
University of Utah
Salt Lake City, Utah 84112

Manuscript received 10 August 1995.

WHERE WE GO FROM HERE?

PRELIMINARY INTERPRETATIONS WORKSHOP
SEISMIC SOURCE CHARACTERIZATION
YUCCA MOUNTAIN SEISMIC HAZARD ANALYSIS

JANUARY 6-8, 1996
SALT LAKE CITY, UTAH

STEPS TO COME

Leave this workshop prepared, with some more homework, to provide your interpretations

ELICITATION INTERVIEWS

- **1-day sessions for each team**
- **Open book**
- **Will step through overall framework for SSC, including logic structure**
- **Will address all issues**
- **Will document evaluations, data, and uncertainties**
- **Plan to get about 80% of total assessment**
- **Will result in "Draft Elicitation Summary"**

FOLLOWING ELICITATION INTERVIEW

- **Follow-up to assessments left open**
- **Calculations will be conducted using your assessments**
- **Sensitivity to identify significance of issues to results**
- **Importance of uncertainties (contributions to total uncertainty)**

STEPS TO COME (cont'd.)

WORKSHOP #5 FEEDBACK

- Preliminary results presented (by team and across teams)
- Sensitivities identified
- Focused discussion on key issues: technical basis for evaluations and uncertainties
- Opportunity to re-evaluate your positions

FINALIZATION OF ELICITATION SUMMARY

- Full documentation of evaluations, data used, and uncertainties

PROBABILITY ASSESSMENT WORKSHOP

Peter A. Morris
Applied Decision Analysis, Inc.

Yucca Mountain Seismic Hazard Project
Salt Lake City, Utah
January, 1997

SDG Policy on Client Confidentiality

SDG considers all client-proprietary material highly confidential. Thus, SDG does not divulge its clients' names or the nature of its work for its clients without their explicit permission. The corporate illustrations we use in our seminars are drawn from companies whose experience is already in the public domain, either because publications exist describing the experience or because company personnel have made reference to it in public presentations.

SDG Copyright Notice

Workshop Outline

- Using probability to quantify uncertainty
- Representing and manipulating probabilities
- Assessing probabilities

PROBABILITY

Workshop outline

- **Using probability to quantify uncertainty**
- Representing and manipulating probabilities
- Assessing probabilities

Probabilities for hazard analyses are obtained from experts

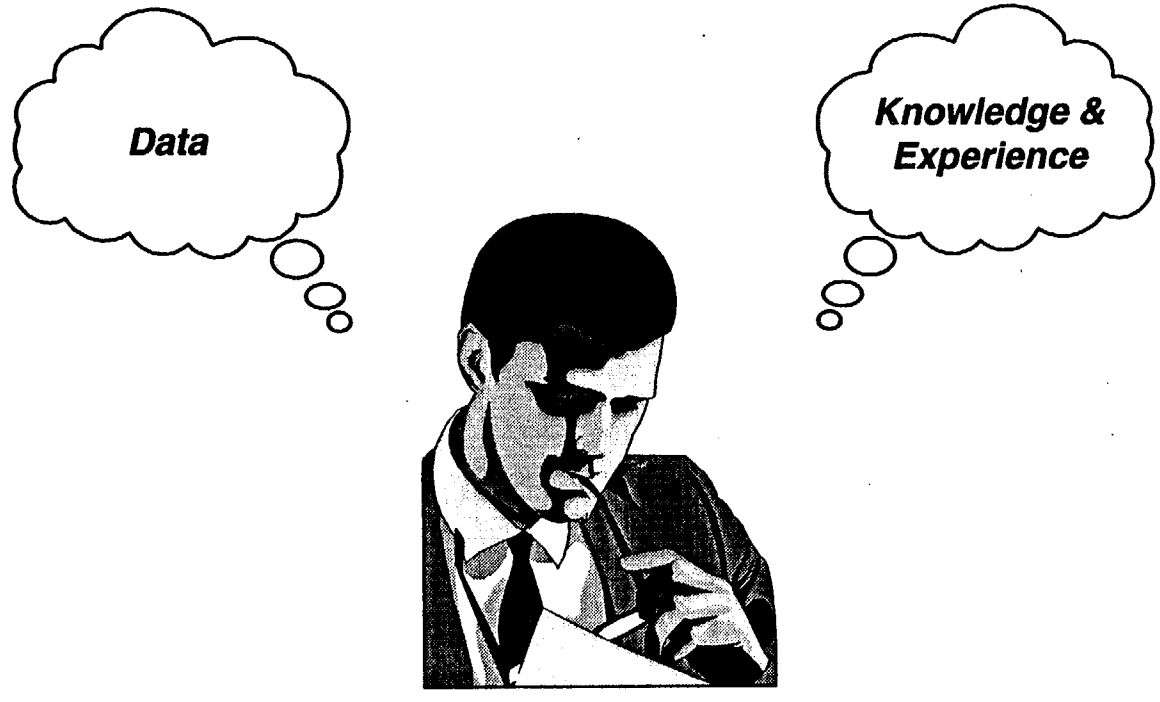

They may be based on data, judgment, or both.

PROBABILITY

Probability is a formal quantification of uncertainty

- Probabilities are numbers between 0 and 1 (e.g., p = .2)
- Probability is sometimes expressed as a percentage (e.g., 20% chance)
- A "probability distribution" assigns probabilities to the states of an uncertainty

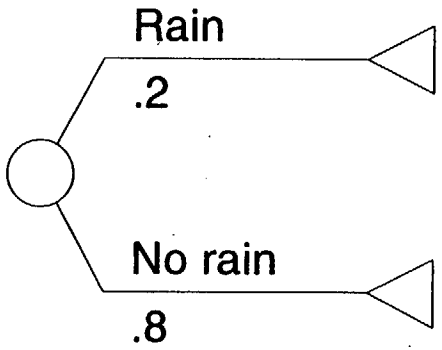

- Probabilities of all states must sum to 1.

Procedures for assessing probabilities can be characterized as either:

Objective

- Uncertainty is a ***property*** of the physical world
- Uncertainty is relevant only for repetitive events
- Probabilities are obtained from historical data

Subjective

- Uncertainty is a degree of ***belief*** about the real world
- Uncertainty is relevant for any type of event
- Probabilities are obtained from expert judgment

Probability assessments can be viewed as a quantitative representation of a person's knowledge

"To know that we know what we know, and that we do not know what we do not know, that is true knowledge."

—Confucius

A pointed decision problem: the thumbtack toss

Uncertainty

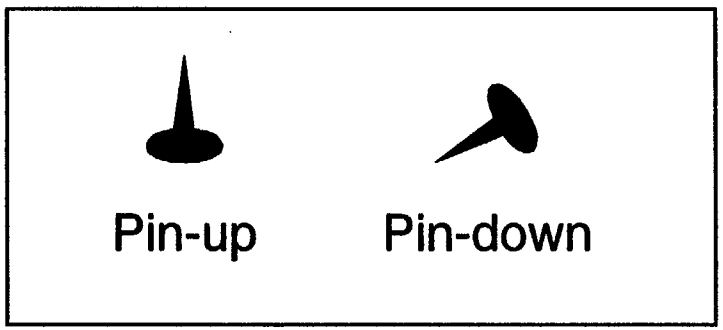

Outcomes

Win	$100	
Lose	$0	

Play just once!

Thumbtack sweepstakes rules

1. The player will specify the direction of a winning toss.
2. The cost to play is $20.
3. I only collect from one person.
4. Payment is cash or check; no refunds.
5. I will "toss" a thumbtack.
6. If the toss is in the winning direction, the player wins $100; otherwise, nothing.
7. I keep the $20 paid to play, regardless of the outcome.
8. No collusion (syndicates) and no old pros.

Pin-up

Pin-down

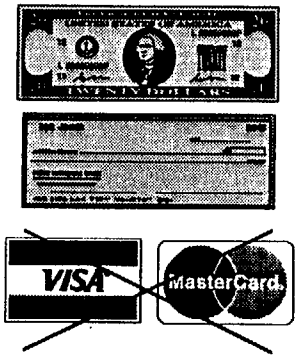

We define a decision as an "irrevocable" allocation of resources

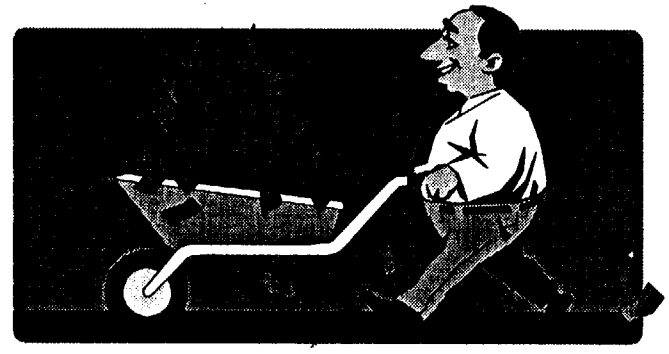

It is not a "worry" or an "issue."

Probabilities quantify the player's likelihood of calling the toss correctly

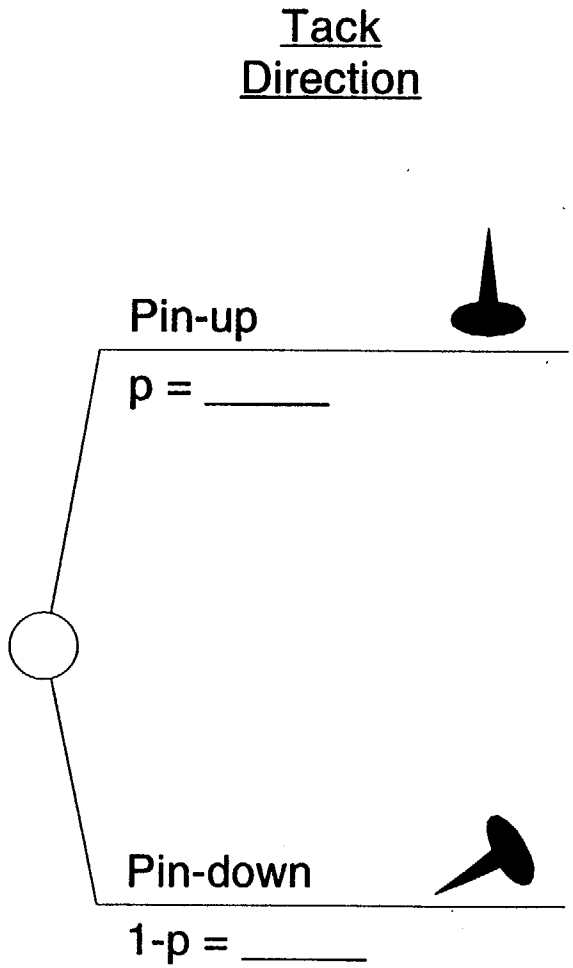

Probabilities may change with new information

- Weather forecast says 30% chance of rain today

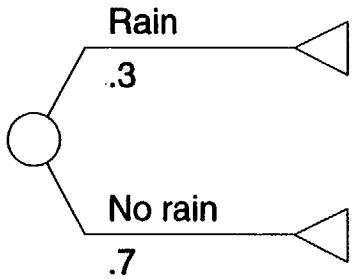

- You look out the window and see storm clouds

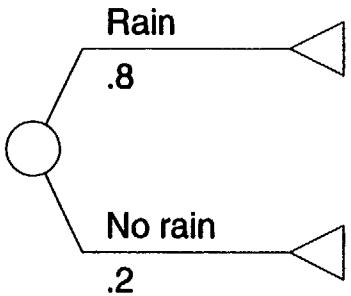

Probabilities represent your state of information.

FUNDAMENTALS

Information is usually not perfect

Sources of imperfect information:

- Experiments (5 trial tosses of the thumbtack)
- Surveys
- Experts
- Models

PROBABILITY

A psychologist's view of uncertainty

Let us pause to examine this quest for certainty. By "certainty" I mean the opposite of contingency. Having survived a disastrous fire in our neighborhood and being concerned about my home, I decide to investigate the likelihood that I would not be so fortunate again. I find my odds are 1000 to 1 against the likelihood that my house will burn, but I am not content and so I have the brush cleared back some distance. Now the odds are 1,500 to 1, I find. Still concerned, I have an automatic sprinkling system installed. Now I'm told my odds are 3,500 to 1. However I try, though, I must recognize always that I cannot achieve certainty that the house will not burn. I may do much, but I can't be sure but that the earth might be drawn closer to the sun and the whole world thus be ignited.

Now these are ridiculous extremes, of course, but the point remains: There is no true certainty to be had. So it is with any issue. Nevertheless, we seek that certainty constantly. We buy insurance, seat belts, medicines, locks, education, and much else to try to protect ourselves against tragedy, to secure good outcomes. So long as we recognize we are dealing in probabilities, such choices can be useful. But every therapist has seen the pathology of seeking for certainty instead of better probabilities.

Excerpt from *The Search of Authenticity,* James F.T. Bugental, Holt

PROBABILITY

Workshop Outline

- Using probability to quantify uncertainty
- **Representing and manipulating probabilities**
- Assessing probabilities

We will review terminology and probability calculations used in probabilistic analysis.

Probability Trees

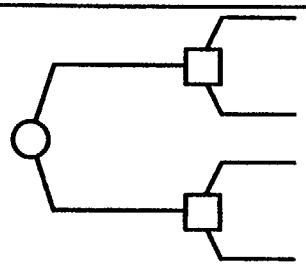

Cumulative Probability Distributions

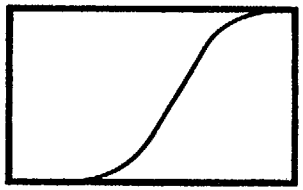

Expected Values

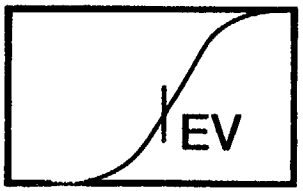

We will work with probabilities associated with discrete events and continuous variables.

Discrete Event

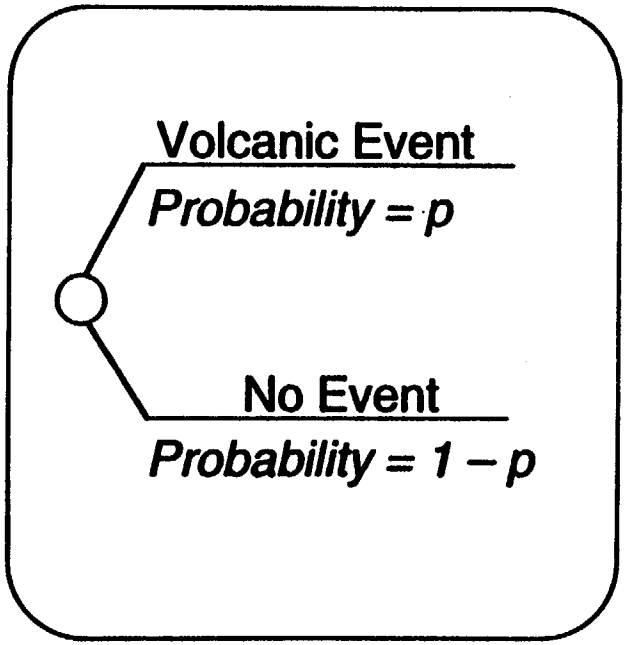

Continuous Variable

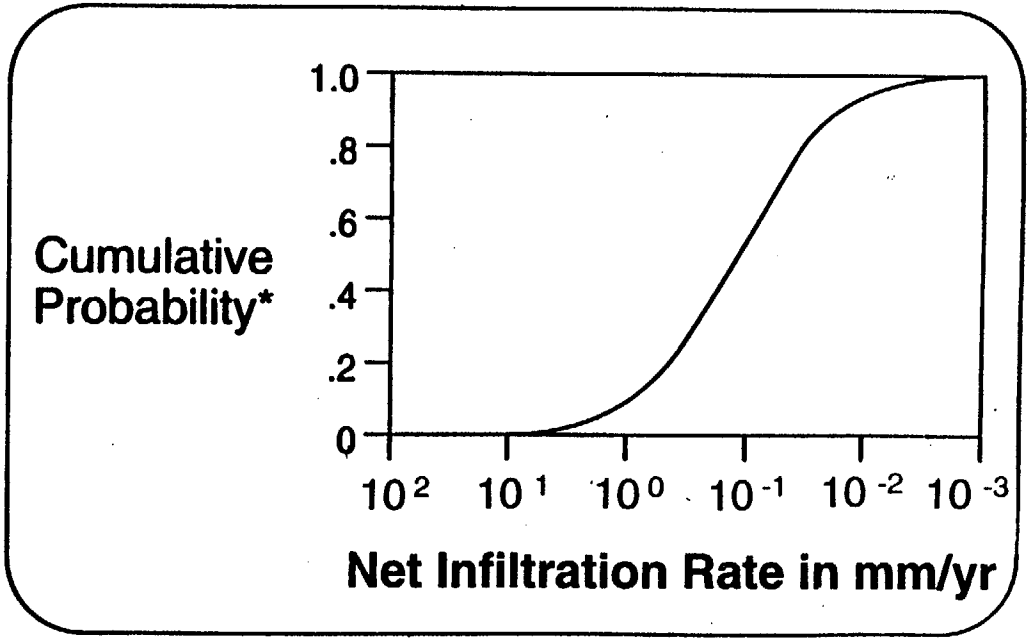

* Probability of rate less than or equal to any given value

Probability nodes represent discrete, uncertain events in probability and decision trees.

Anatomy of a Single Probability Node

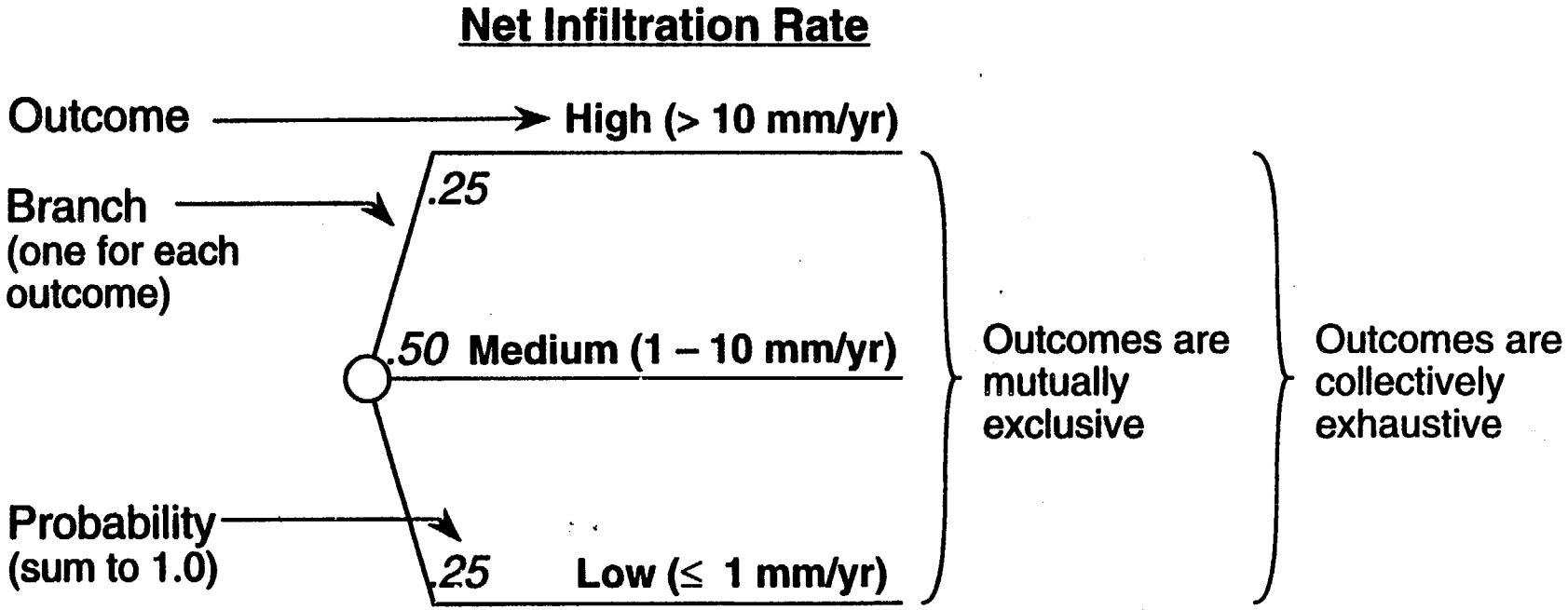

Uncertainty associated with continuous variables can be represented in a tree using a discrete approximation.

Two events may be probabilistically independent or dependent.

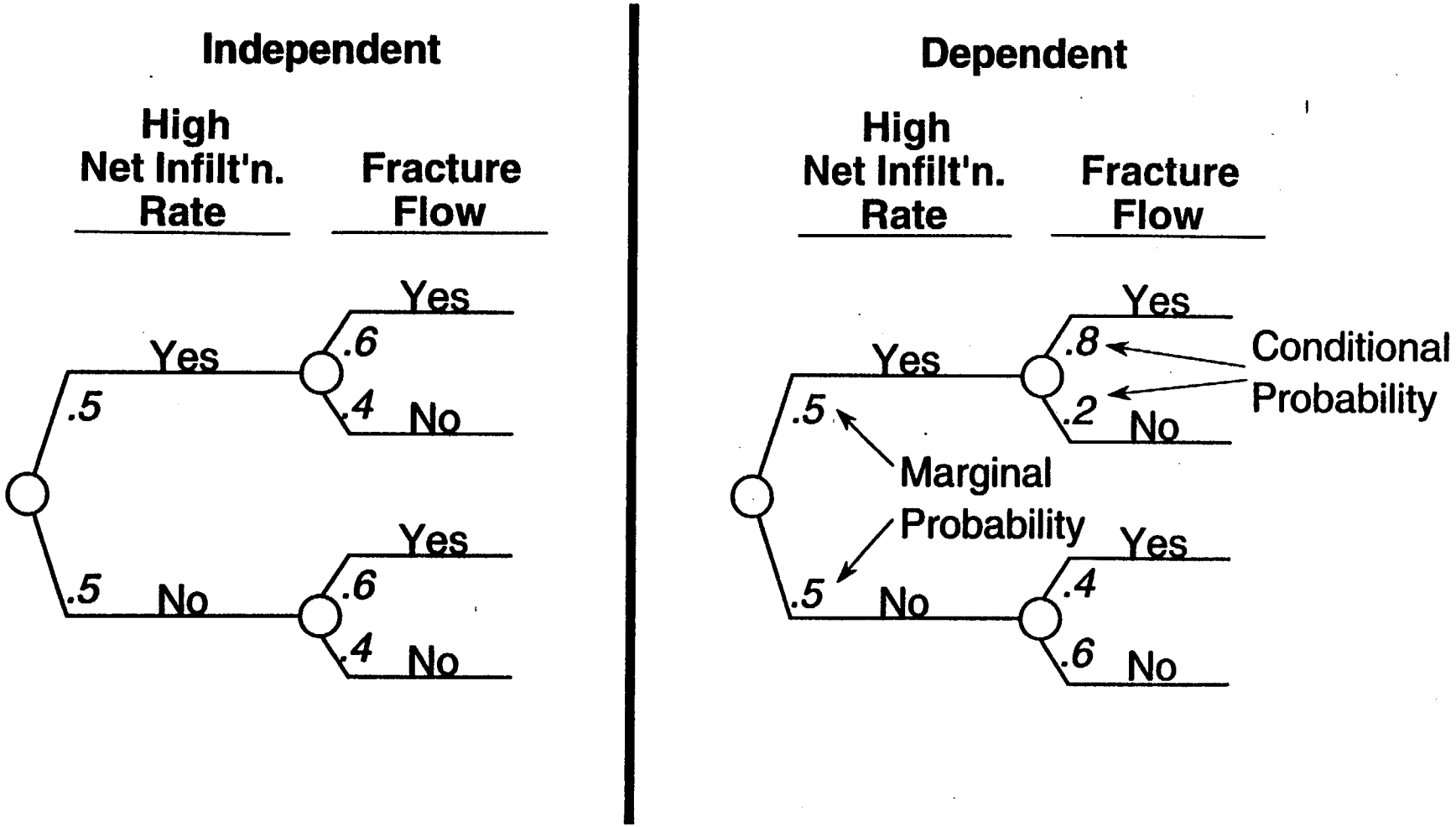

The order of adjacent probability nodes can be reversed.

A "joint probability distribution" can be computed from data in the probability tree.

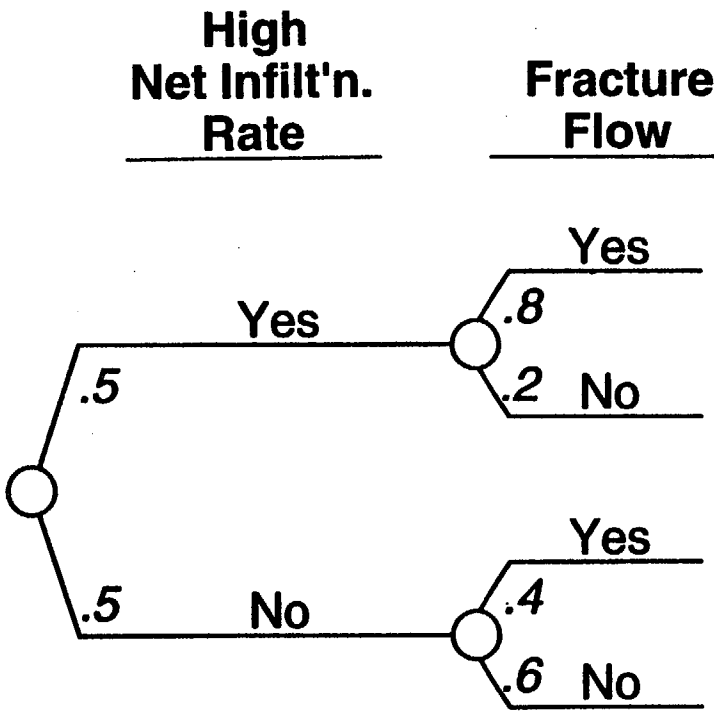

Joint Probability
.4*
.1
.2
.3
1.0

* .5 x .8 = .4

Sometimes it is necessary to switch the conditioning variable.

The information is available in this order.

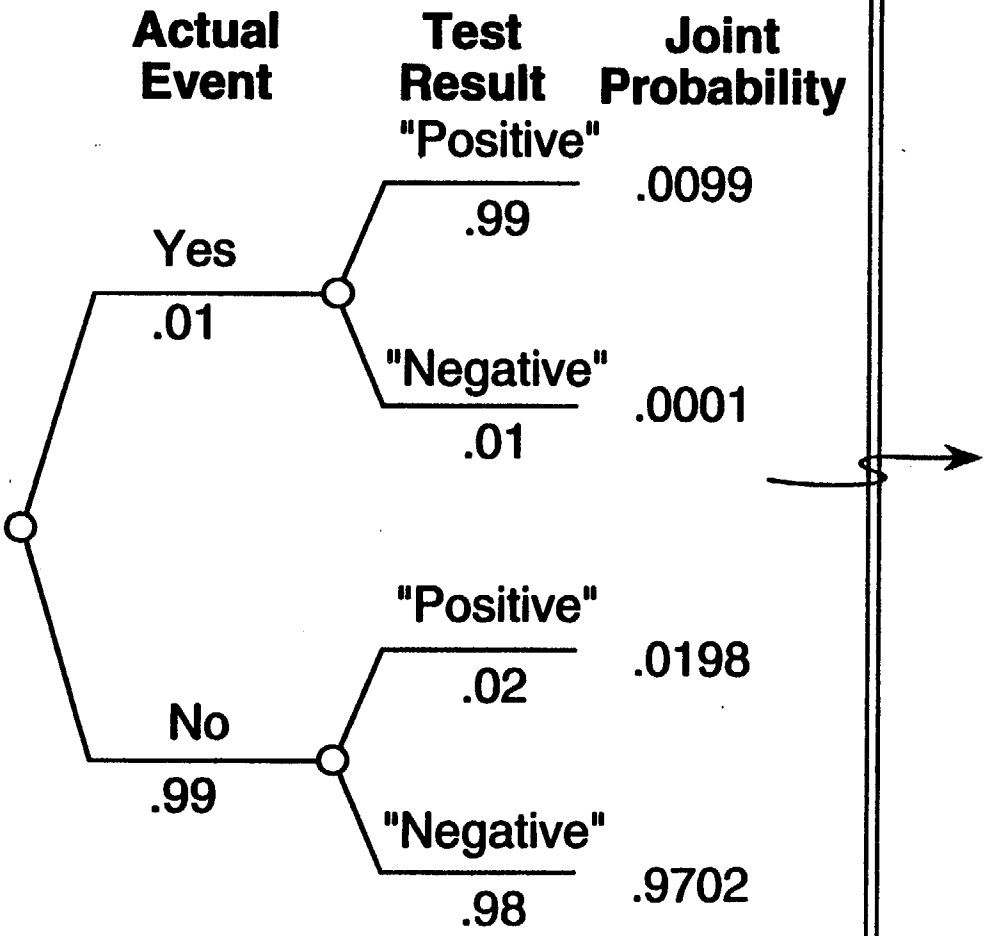

But we want to use the information in this order.

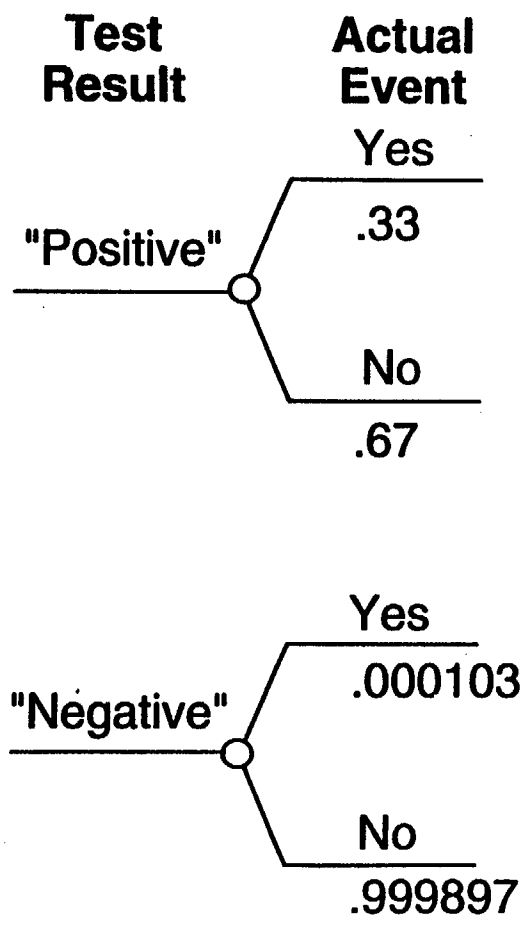

Illustrative Example

Actual Event (A) — A volcanic event occurred within a region during the Holocene

$P(A) = .01$

Test: Age dating technique:

2 results: "Positive"
"Negative"

"Positive:" Estimated age ≤ 10,000 years
"Negative:" Estimated age > 10,000 years

P("Positive" / A) = .99
P("Negative" / Not A) = .98

Cumulative probability distributions are a convenient way to display an uncertain quantity.

Probability Trees

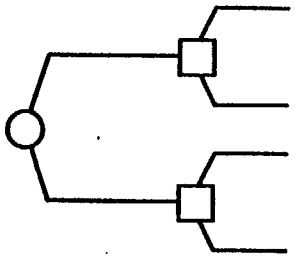

Cumulative Probability Distributions

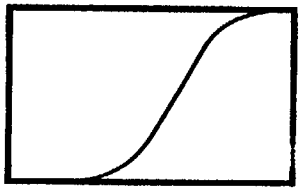

Histograms

Expected Values

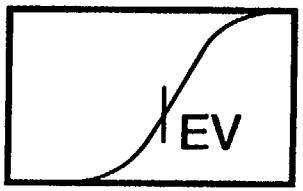

What is a cumulative probability distribution?

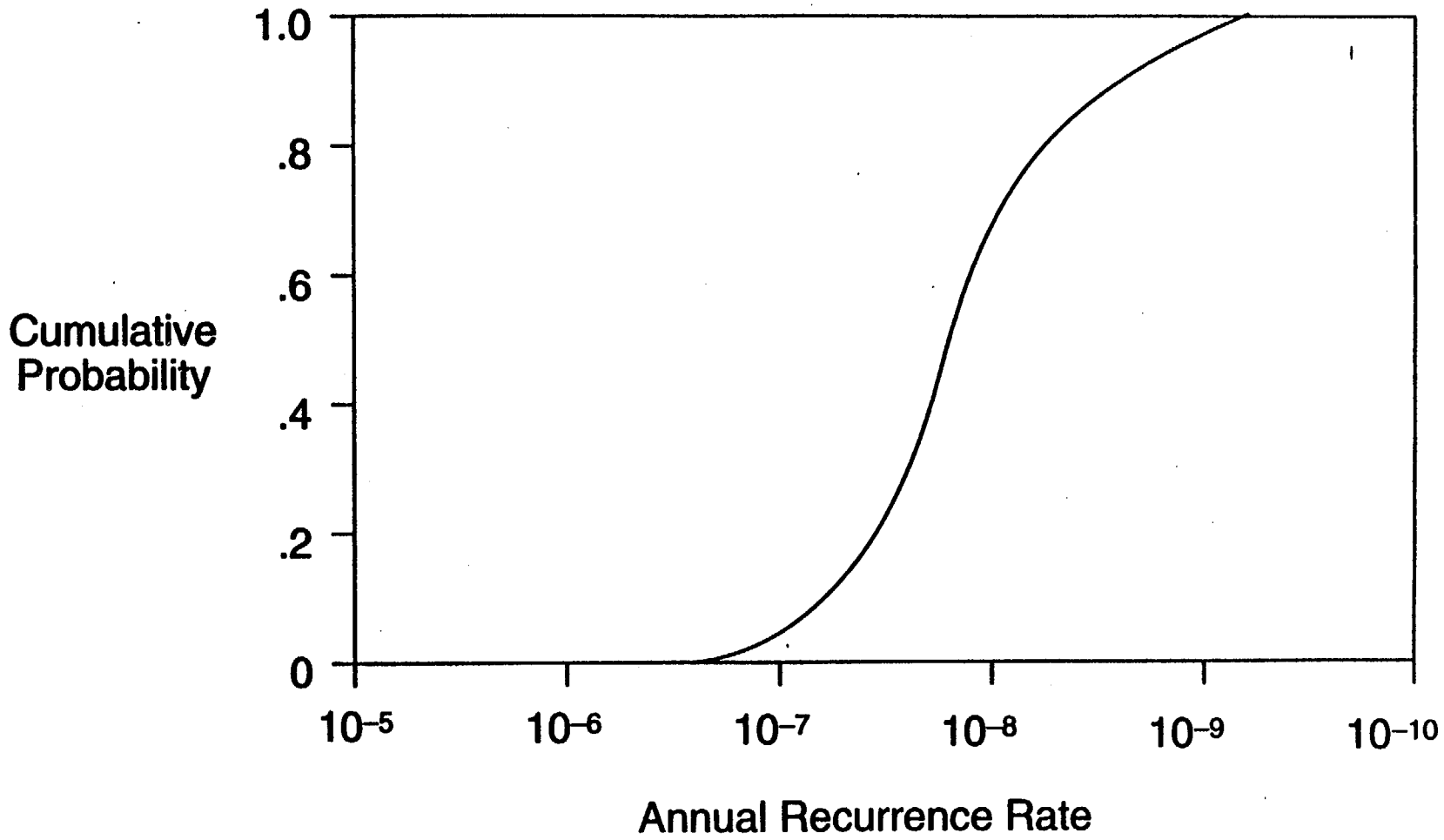

The cumulative probability distribution displays information decision-makers need.

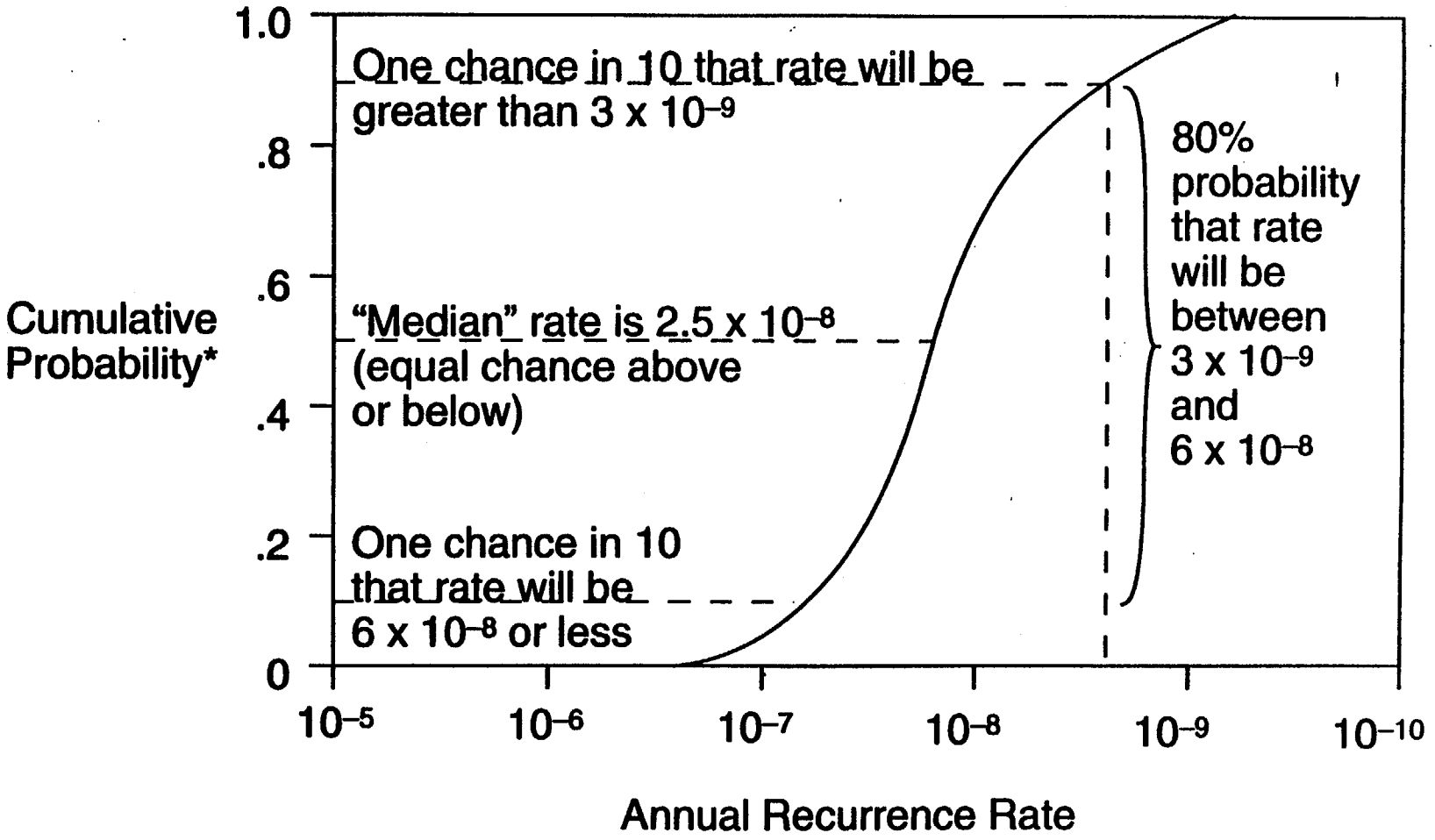

* Probability that rate is less than or equal to a given value

Continuous variables also can be plotted as "probability density functions."

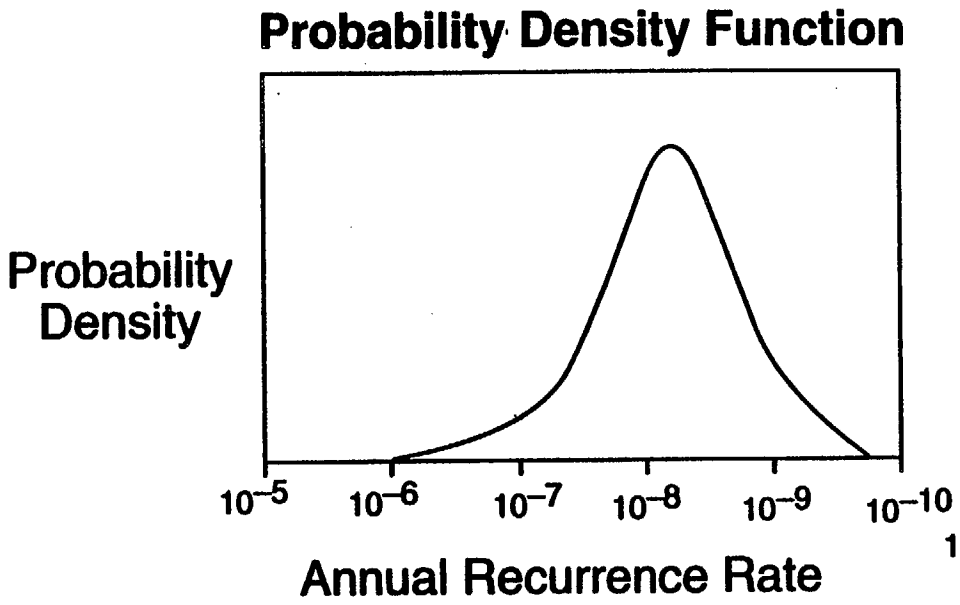

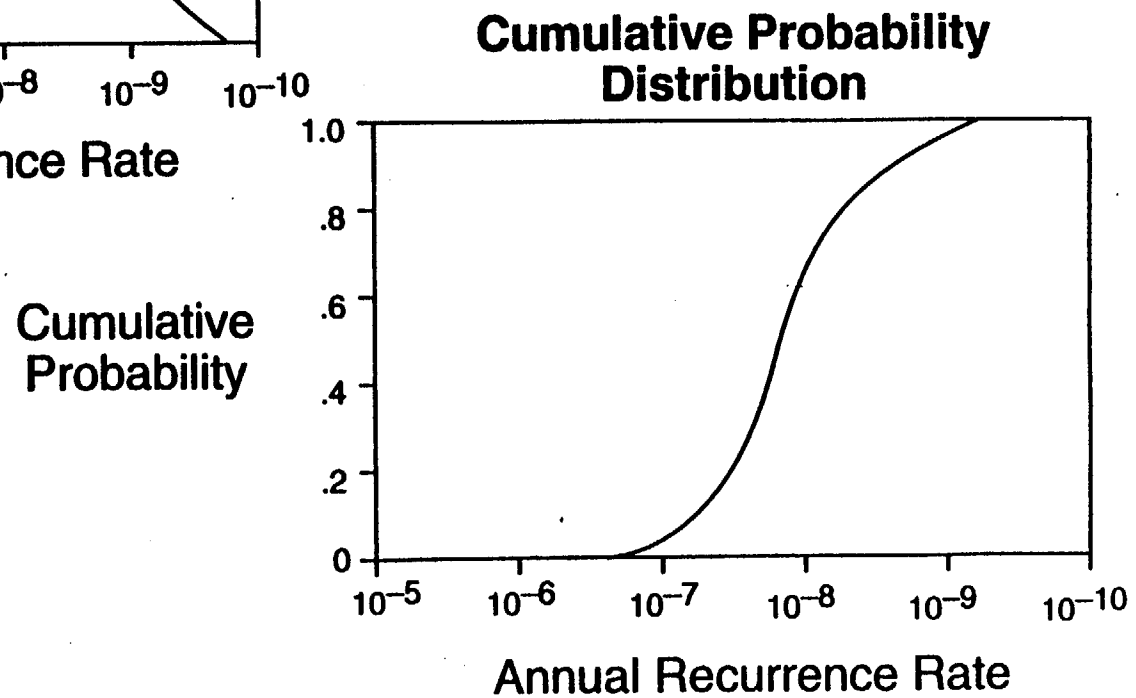

The cumulative form is easier to use for assessing and making calculations with probabilities.

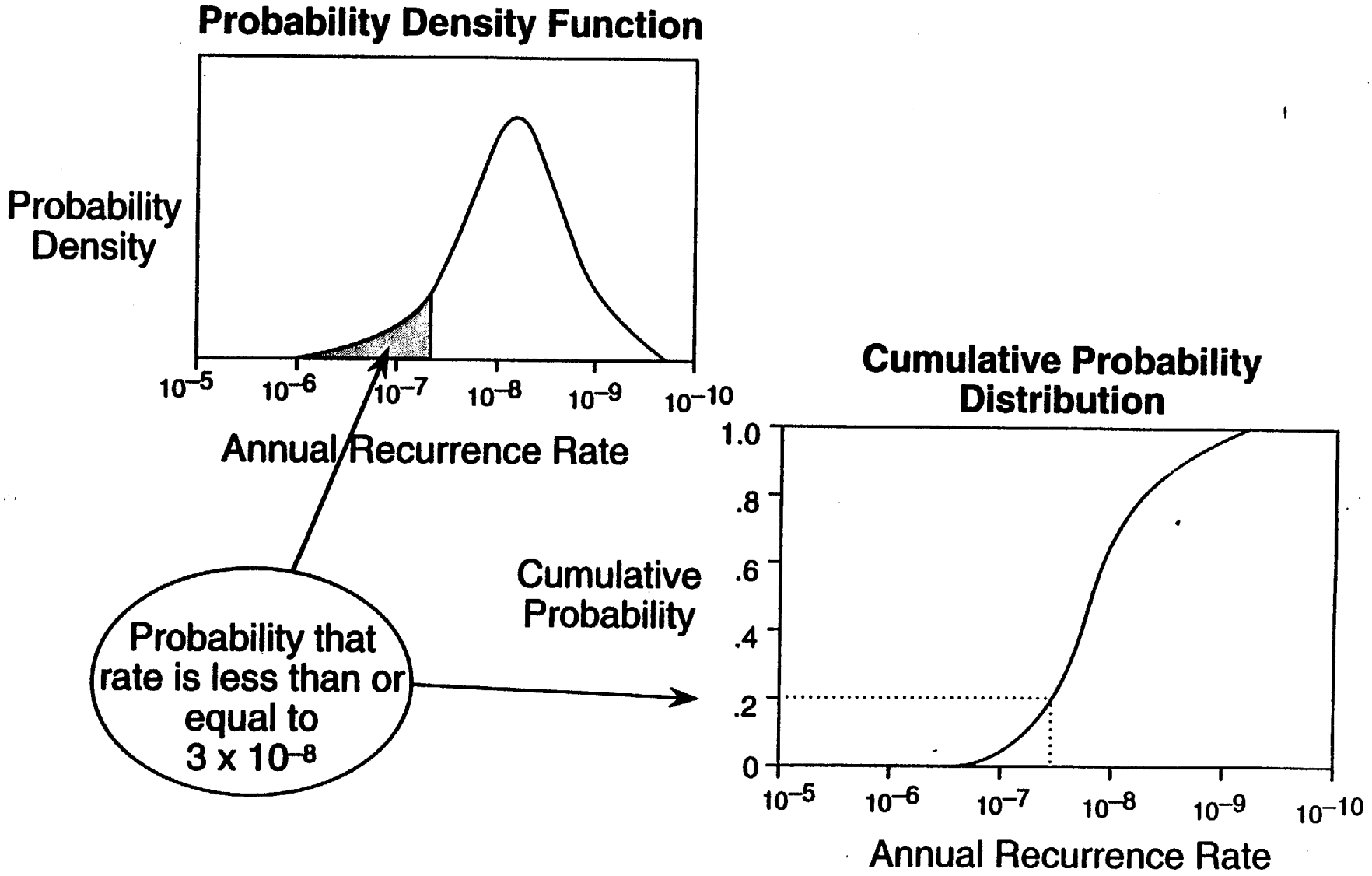

The expected values of probability distributions are used extensively in probabilistic analysis.

Probability Trees

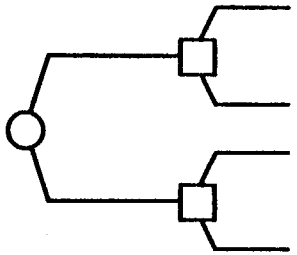

Cumulative Probability Distributions

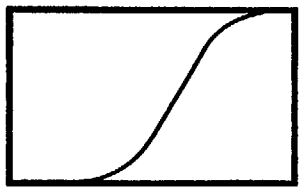

Expected Values

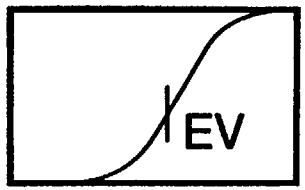

The expected value (EV) is a single number that can represent an entire probability distribution.

Discrete Variable

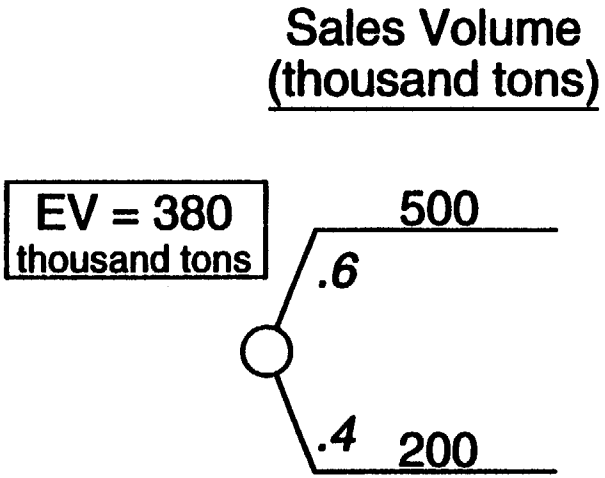

Cumulative Probability Distribution

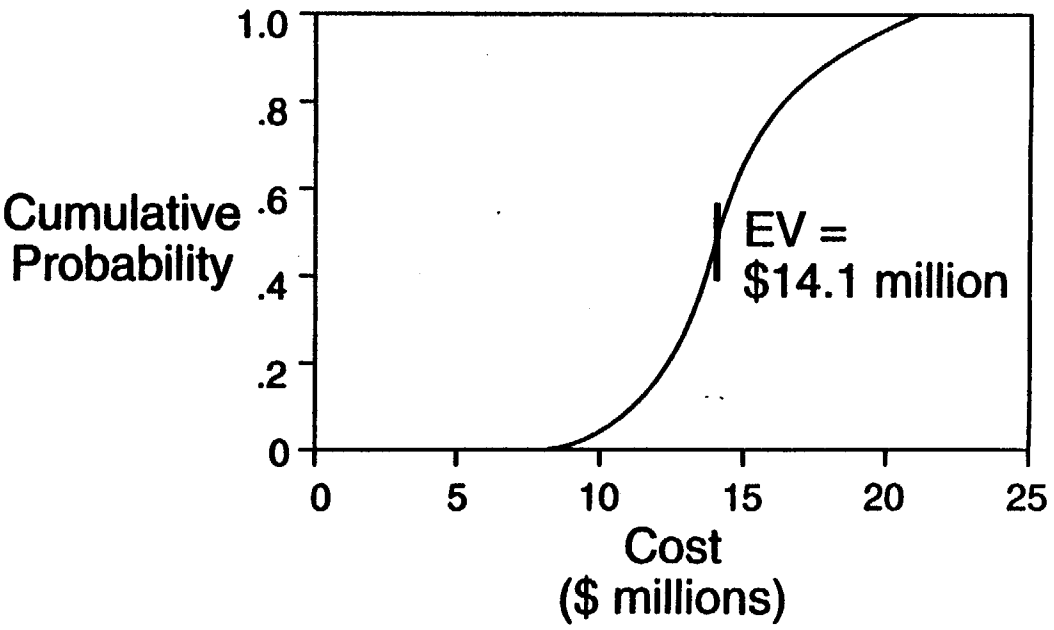

The expected value is a "probability-weighted average."
"Mean" is synonymous with expected value.

Three different parameters can be used to describe distributions.

Probability Density Function

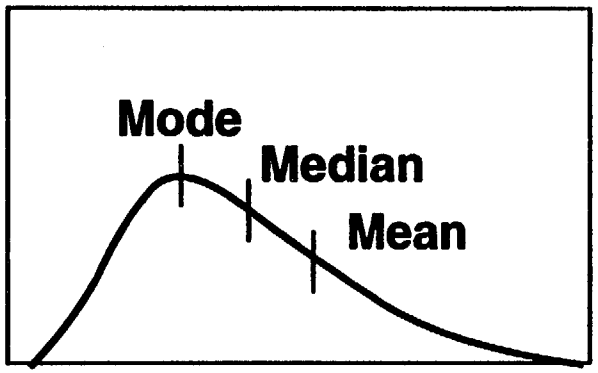

Cumulative Probability Distribution

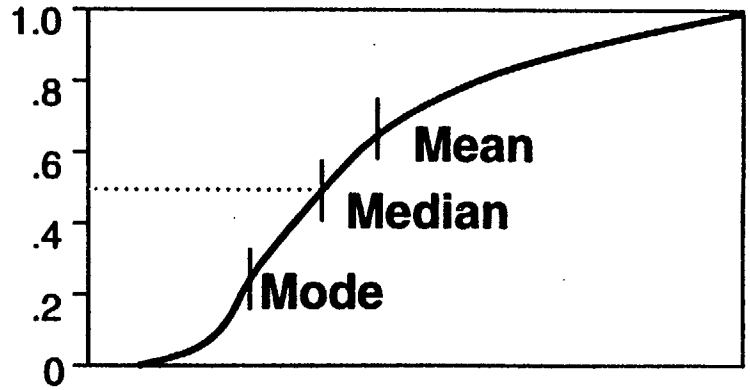

Parameter	Meaning
Mean	Expected value; probability-weighted average
Median	50th percentile
Mode	Most likely value

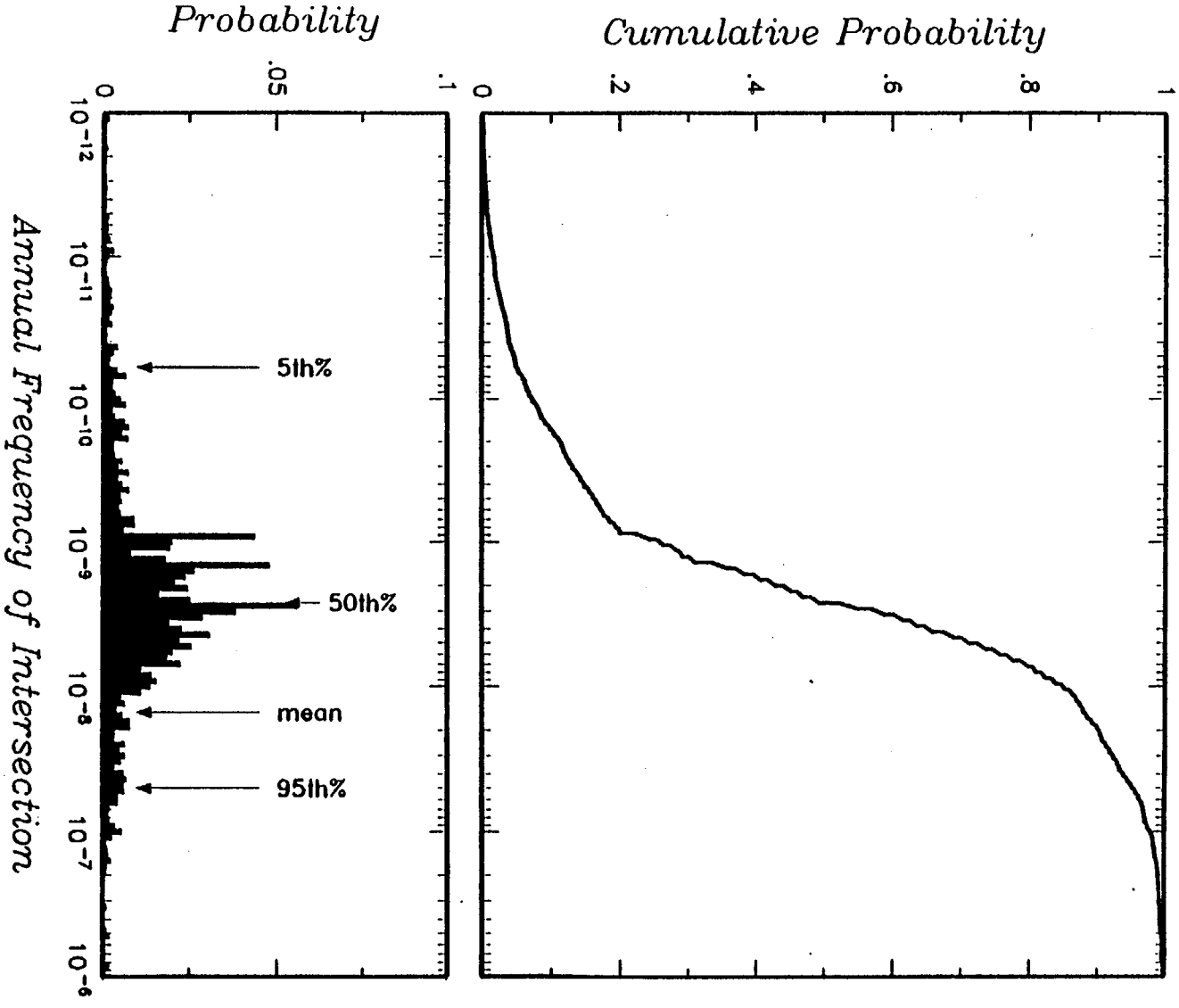
Probability
Cumulative Probability
Annual Frequency of Intersection
0
.05
.1
0
.2
.4
.6
.8
1
10^{-12}
10^{-11}
10^{-10}
10^{-9}
10^{-8}
10^{-7}
10^{-6}
5th%
50th%
mean
95th%

We have discussed the probabilistic analysis phase and reviewed basic probability tools.

Probability Trees

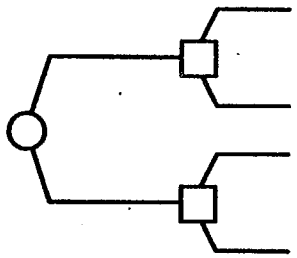

Cumulative Probability Distributions

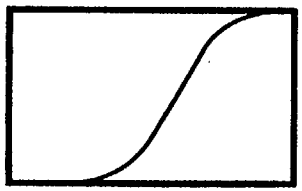

Expected Values

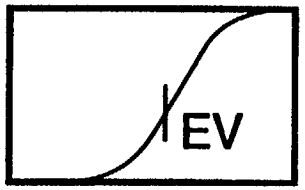

This phase produces trees, distributions, and insights!

Probability Assessment

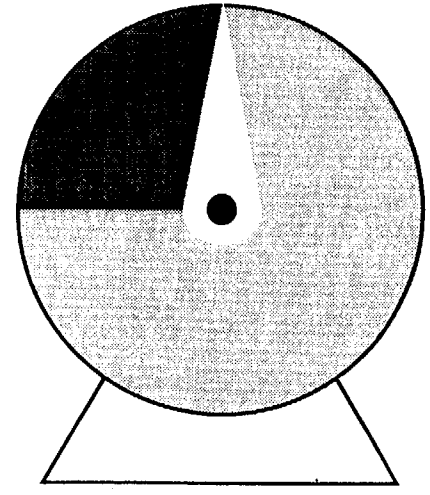

We will discuss quantifying uncertainty with probabilities.

Using Probabilities to Communicate

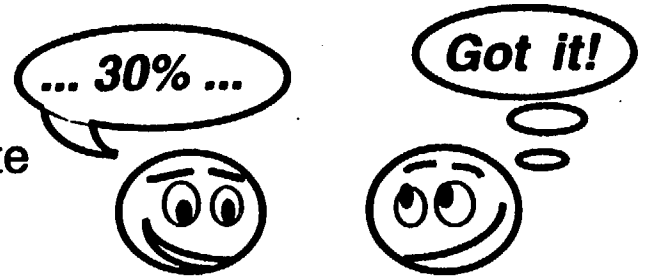

Avoiding Biases

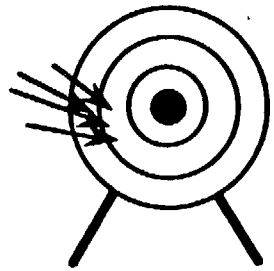

Assessing Probabilities

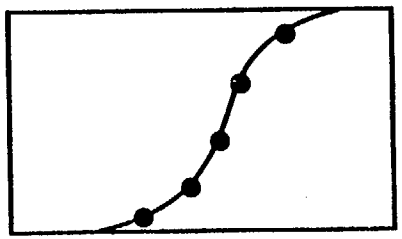

Probability assessment allows us to measure differences among experts and, perphaps, to resolve them.

- Experts may dispute point estimates but accept probability distributions.
- Specifying probability distributions can avoid artificial focus on whose point estimates are "right" or "wrong".
- Sharing information may foster consensus.
- Sensitivity analysis tests the importance of disagreements.

Probabilities serve two purposes in decision-making

- They provide a common language to describe uncertainty.
  - Ordinary language is ambiguous and imprecise:
    "The operation will probably succeed."
    "Costs are likely to rise."
- They facilitate the analysis of decisions involving uncertainty

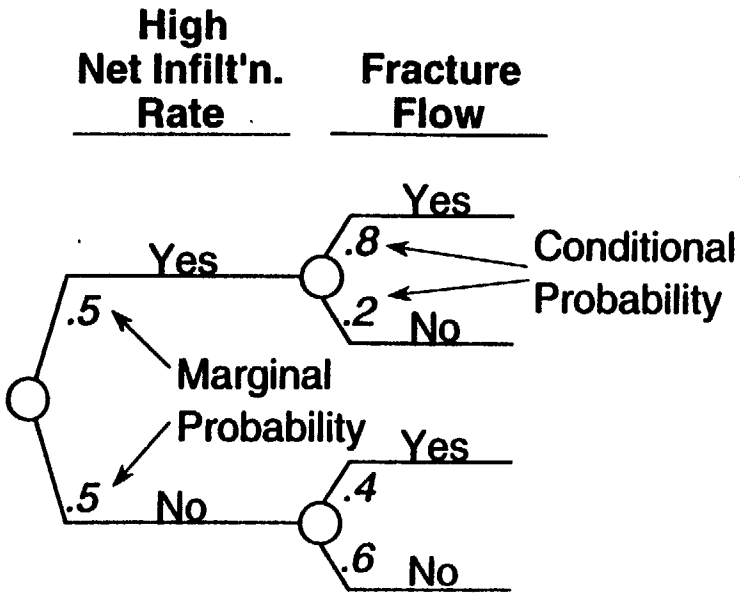

Exercise: Using words to describe uncertainty

Common Expression	Your Probability										
	0	.1	.2	.3	.4	.5	.6	.7	.8	.9	1.0

We will discuss quantifying uncertainty with probabilities.

Using Probabilities to Communicate

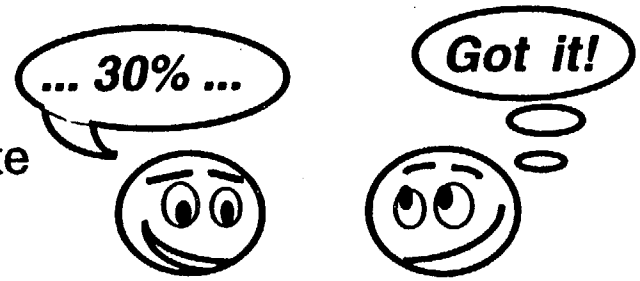

Avoiding Biases

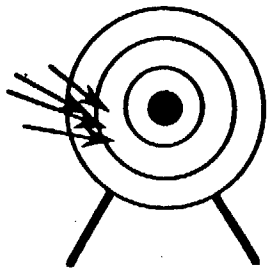

Assessing Probabilities

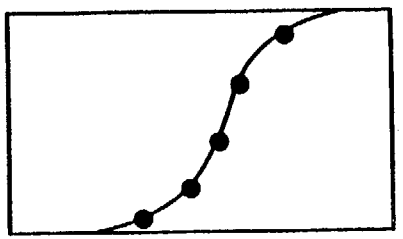

PROBABILITY

Probability language is unambiguous and precise, but we still need a formal assessment method

- Assigning probabilities is not natural for most people
- There are biases in the way we quantify uncertainty
  - Motivational biases: Expert's answers don't reflect his/her beliefs
  - Cognitive biases: Expert's beliefs don't reflect his/her information

We must recognize types of biases and minimize or compensate for them.

- Many biases are systematic.

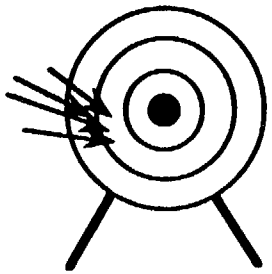

- Biases occur in both qualitative and quantitative assessments.

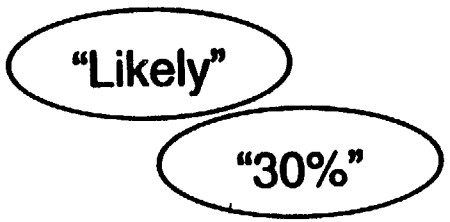

There are two classes of biases: motivational and cognitive.

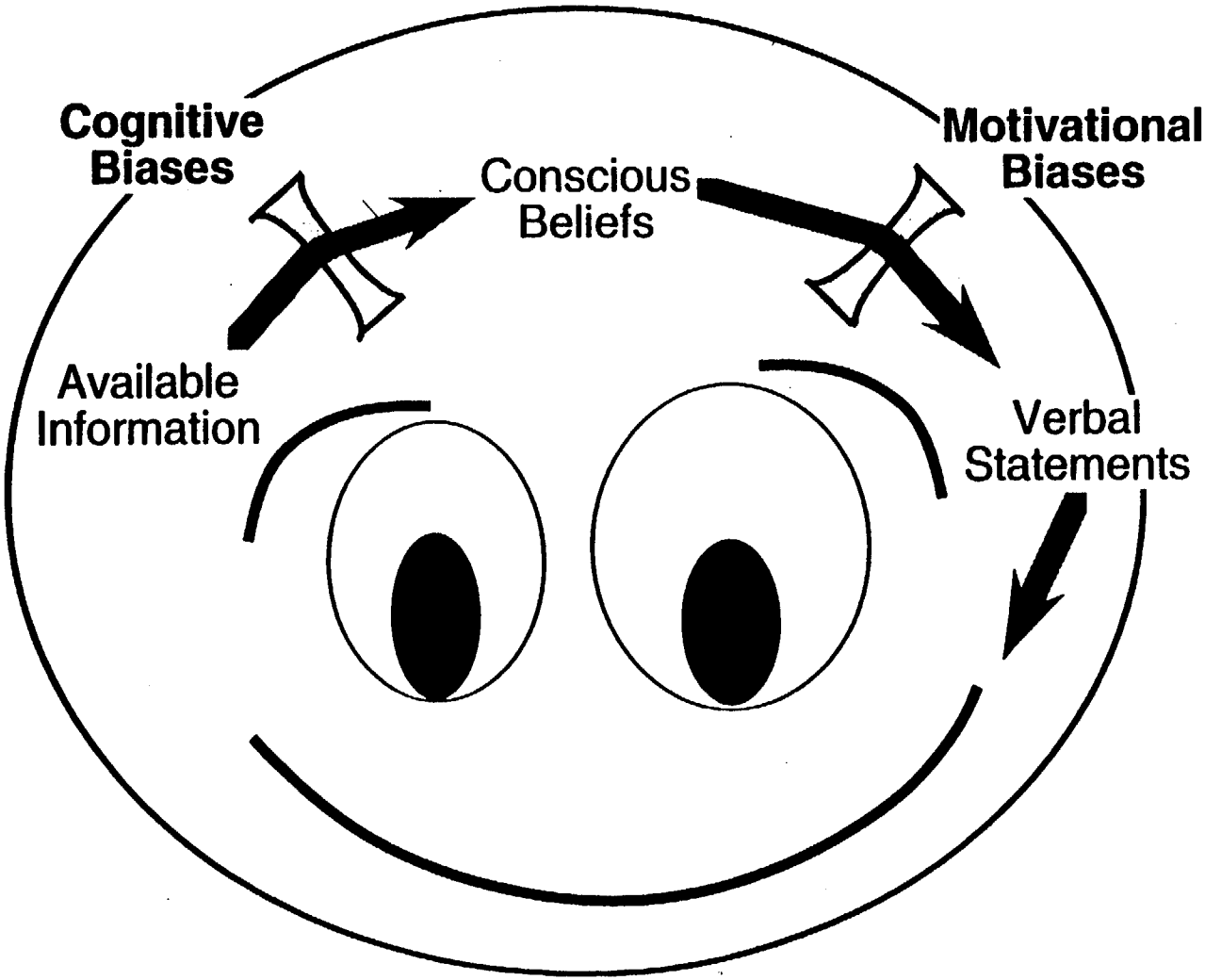

Motivational bias is motivated by personal involvement

Examples include:

- Suppression of uncertainty to appear more "expert"
- High estimate of probability of success by project manager
- Reluctance to use anything but numbers "approved" by management
- Being conservative in fear of later being accused of underperformance

Motivational bias can be mitigated.

- Change rewards.
- Stress "communication," not "predictions" or "targets."
- Decompose the assessment.

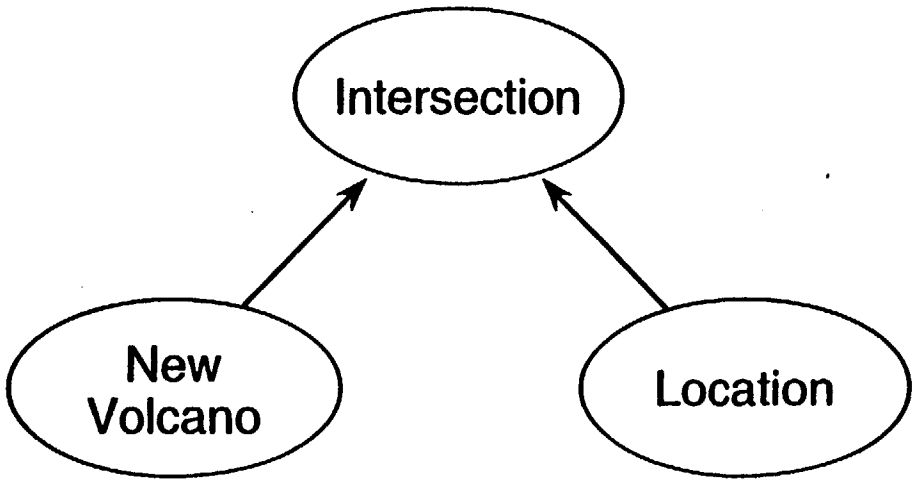

Cognitive biases are analogous to optical illusions

Example:

- A clear day makes things look closer

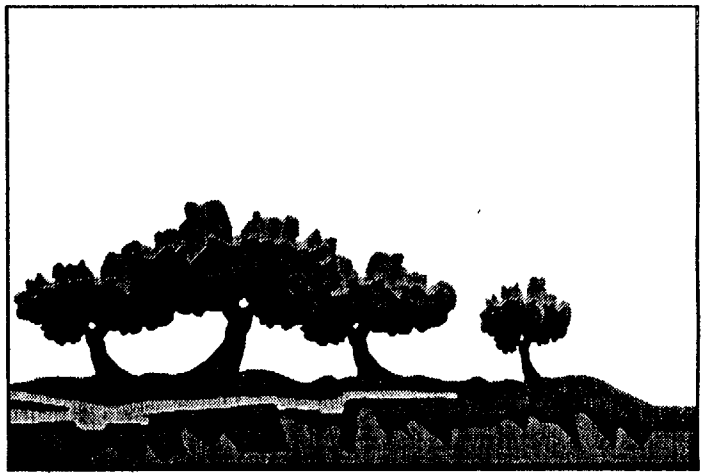

The illusion occurs because the heuristic used to estimate distance is imperfect

- Heuristic: The clarity of an object is an indicator of its distance
- Clarity has some reliability because it decreases with distance
- But there are systematic and predictable errors
  - Underestimate when visibility is good
  - Overestimate when visibility is bad

Similar heuristics generate biases in expert judgment

Be aware of the most common cognitive biases

- Anchoring: focusing on a specific number
- Availability: focusing on a dramatic/recent event
- Overconfidence: overestimating what is known
- Coherence: overestimating the likelihood of an event because there is a good supporting story
- Hidden assumptions: conditioning estimates on unstated assumptions about the outcome of influencing events

Anchoring & Adjustment

Experts can "anchor" on an initial estimate and then "adjust" inadequately for uncertainty.

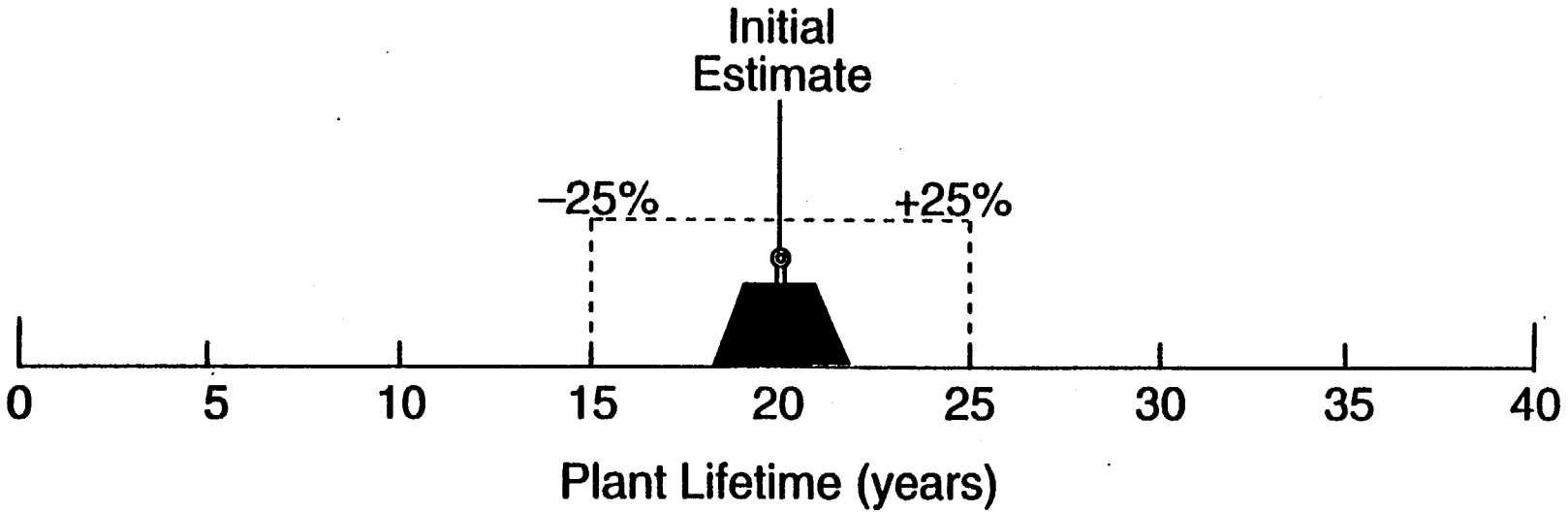

They believed it*

* Source: C. Cerf and V. Navasky, *The Experts Speak* (New York: Pantheon Books, 1984)

- "Heavier-than-air flying machines are impossible."
  (Lord Kelvin, British mathematician, physicist, and president of the British Royal Society, c. 1895)
- "With over fifty foreign cars already on sale here, the Japanese auto industry isn't likely to carve out a big slice of the U.S. market for itself."
  (*Business Week*, 2 August 1968)
- "A severe depression like that of 1920-1921 is outside the range of probability."
  (The Harvard Economic Society, 16 November 1929)
- "I think there is a world market for about five computers."
  (Thomas J. Watson, chairman of IBM, 1943)
- "There is no reason for any individual to have a computer in their home."
  (Ken Olson, president, Digital Equipment Corporation, 1977)
- "We don't like their sound. Groups of guitars are on the way out."
  (Decca Recording Co. executive, turning down the Beatles in 1962)
- "The phonograph... is not of any commercial value."
  (Thomas Alva Edison, inventor of the phonograph, c. 1880)
- "No matter what happens, the U.S. Navy is not going to be caught napping."
  (Frank Knox, Secretary of the Navy, 4 December 1941, just before the Japanese attack on Pearl Harbor)
- "They couldn't hit an elephant at this dist..."
  (General John B. Sedgwick, last words, Battle of Spotsylvania, 1864)

Availability

Experts can "anchor" on an initial estimate and then "adjust" inadequately for uncertainty.

Characteristics That Make Information Available

Recent

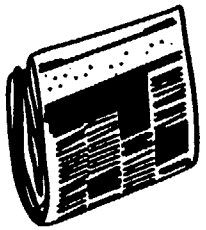

Certified

Dramatic

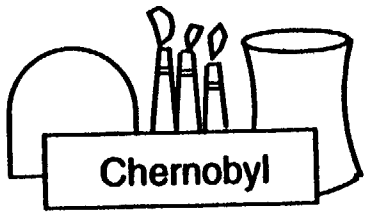

Imaginable

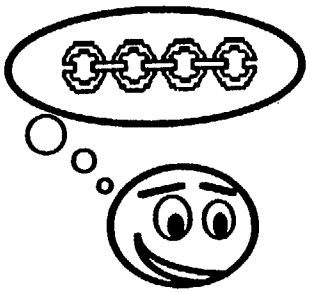

Ordered "R"

Write down your .1 and .9 cumulative probabilities for these uncertain quantities.

	Uncertain Quantity	Cumulative Probabilities* .1	.9
1	Year in which Attila the Hun died		
2	Number of auto thefts in the U.S. in 1991		
3	U.S. consumption of beef in 1991		
4	Planned date to select waste package emplacement orientation (page 8.3.2.2–89)		
5	Expected water content of host rock (TSW2 unit), expressed as percent saturation (page 8.3.2.3–30)		
6	Expected annual cloud-to ground lighting strikes at facility (magnitude unspecified; page 8.3.2.3–33)		

* Probability that the quantity listed in The World Almanac and Book of Facts 1993 will be less than or equal to the value you write down for questions 1, 2 and 3. For questions 4, 5 and 6, the answers are found in Volume VI, "Yucca Mountain Site Characterization Plan.".

Implicit Conditioning

Implicit conditioning occurs when the expert makes unstated assumptions.

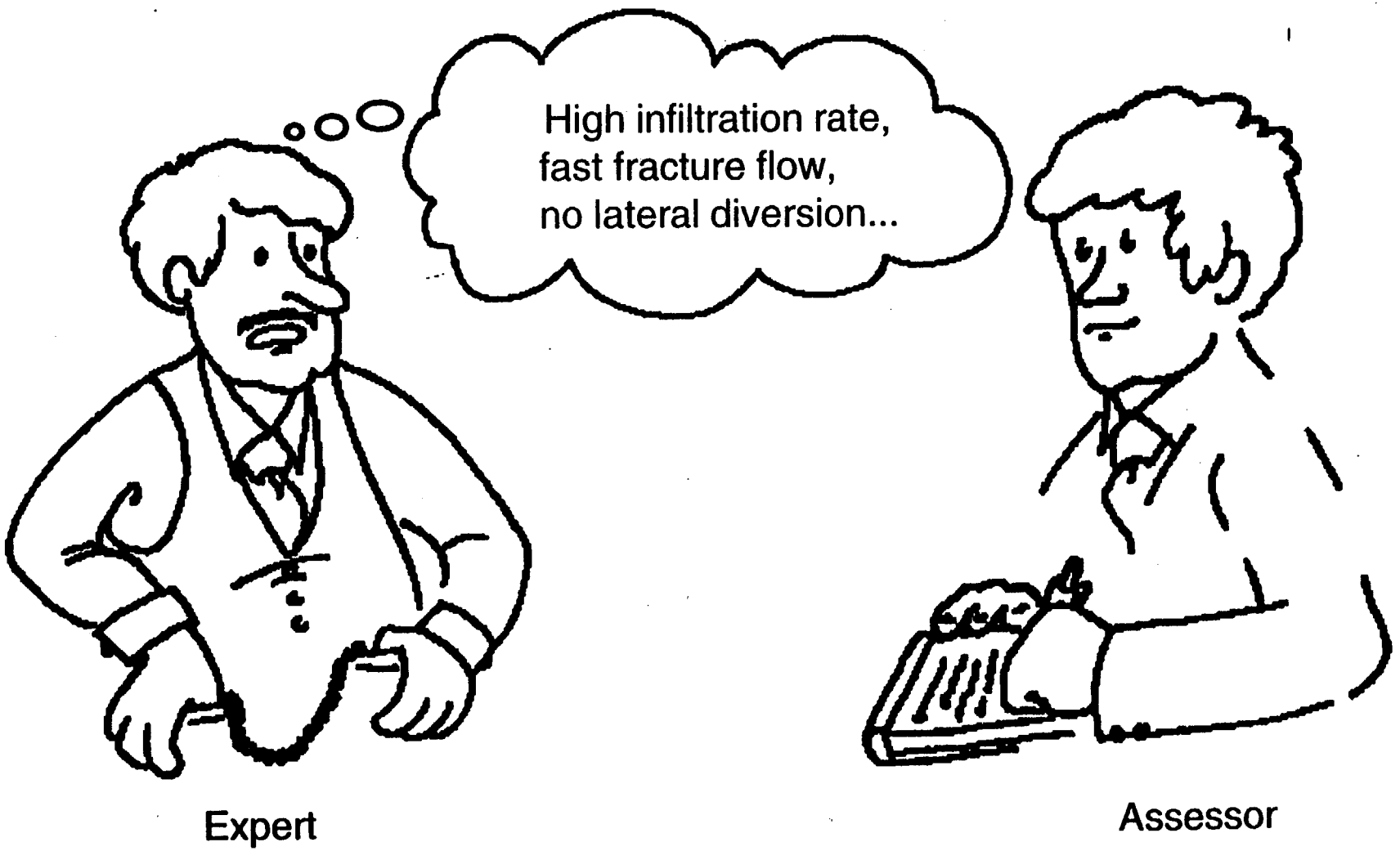

We will discuss quantifying uncertainty with probabilities.

Using Probabilities to Communicate

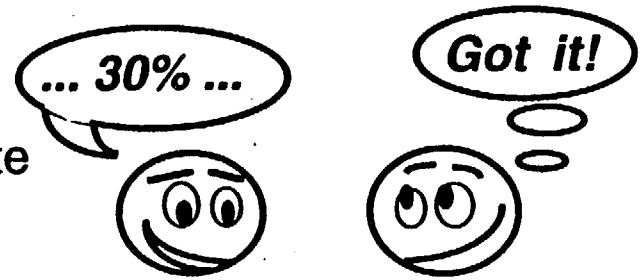

Avoiding Biases

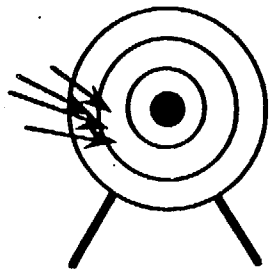

Assessing Probabilities

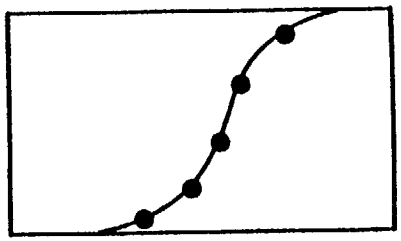

To ensure that assessed probabilities are authentic, decision analysis has developed formal procedures

- Interview techniques to control biases
- Encoding devices to simplify quantitative assessment of uncertainty
- Methods to assess multiple experts and resolve differences in opinion

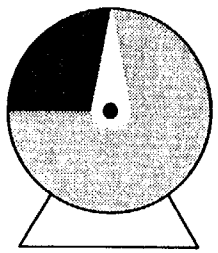

The six-phase probability assessment process

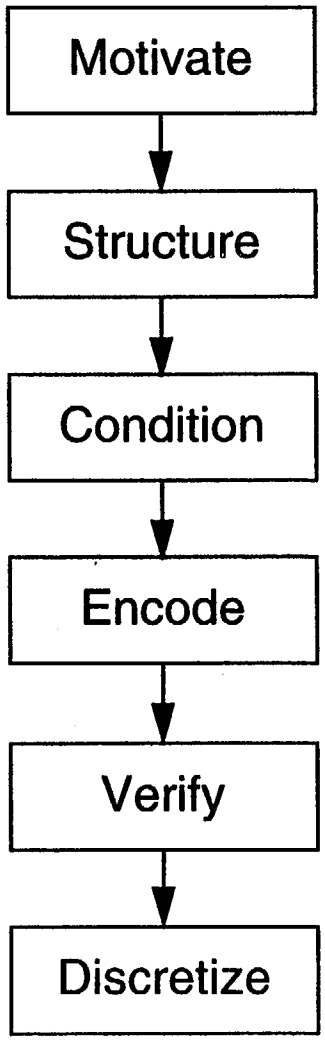

Introduce task and identify biases

Establish definition of variable, assumptions and measurement scales

Counteract biases

Develop probability distribution(s)

Verify that distribution accurately reflects beliefs

Select discrete points to represent continuous distributions

Phase 1—Motivating

Step 1: Explain purpose of the analysis and how the assessment fits in

Step 2: Introduce encoding task

- Explain importance of achieving an accurate assessment
- "Not seeking a commitment or a prediction, only a representation of uncertainty"

Step 3: Identify potential for motivational biases

- Start taking notes as a measure to try to counteract biases

Phase 2—Structuring

Step 1: Define variable precisely

- Does it pass the "clairvoyance test?"
- Select an appropriate measurement scale

Step 2: Create an influence diagram to explore underlying events

Step 3: Make a list of assumptions

Do you agree with the following statement?

It is reasonably likely that a moderate to large earthquake will strike the San Franciso Bay Area in the near future.

☐ Yes ☐ No

This experiment was created by Dr. Ralph Keeney.

Probability elicitation cycle

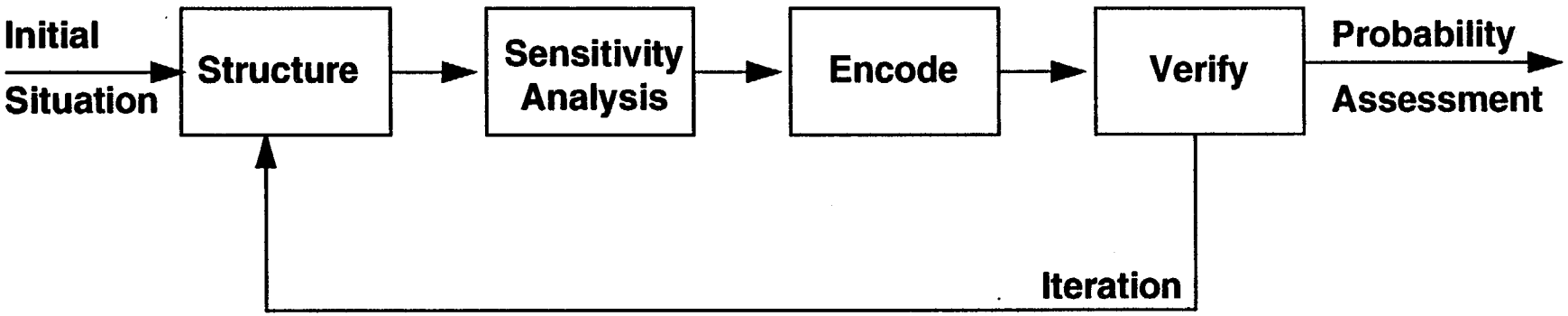

The influence diagram is built from right to left

- What do I need to know to estimate profits?
- If I couldn't find out profits, what would I ask for next?

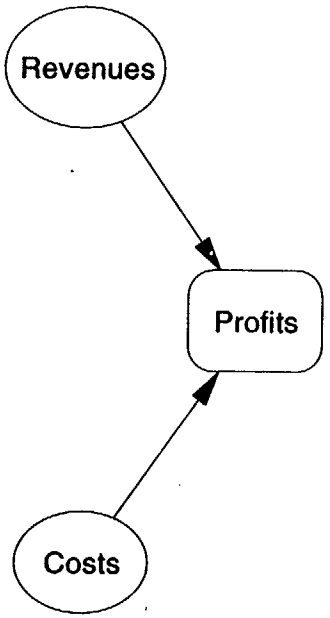

Next we turn to revenues

- What do I need to know to estimate revenues?

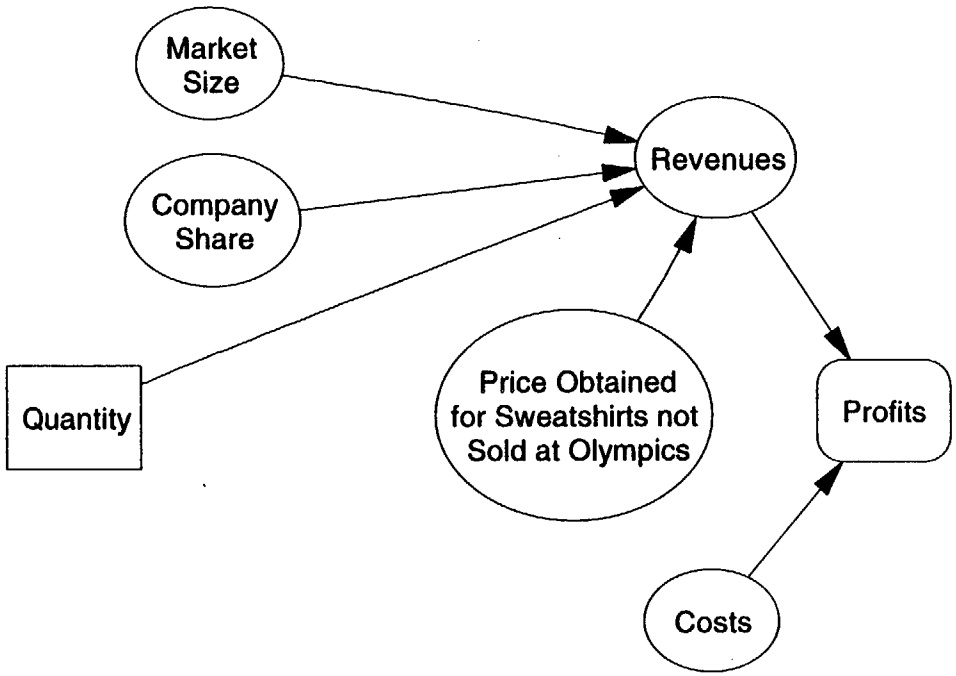

Lastly, we turn to market size and costs

- What do I need to know to estimate market size and costs?

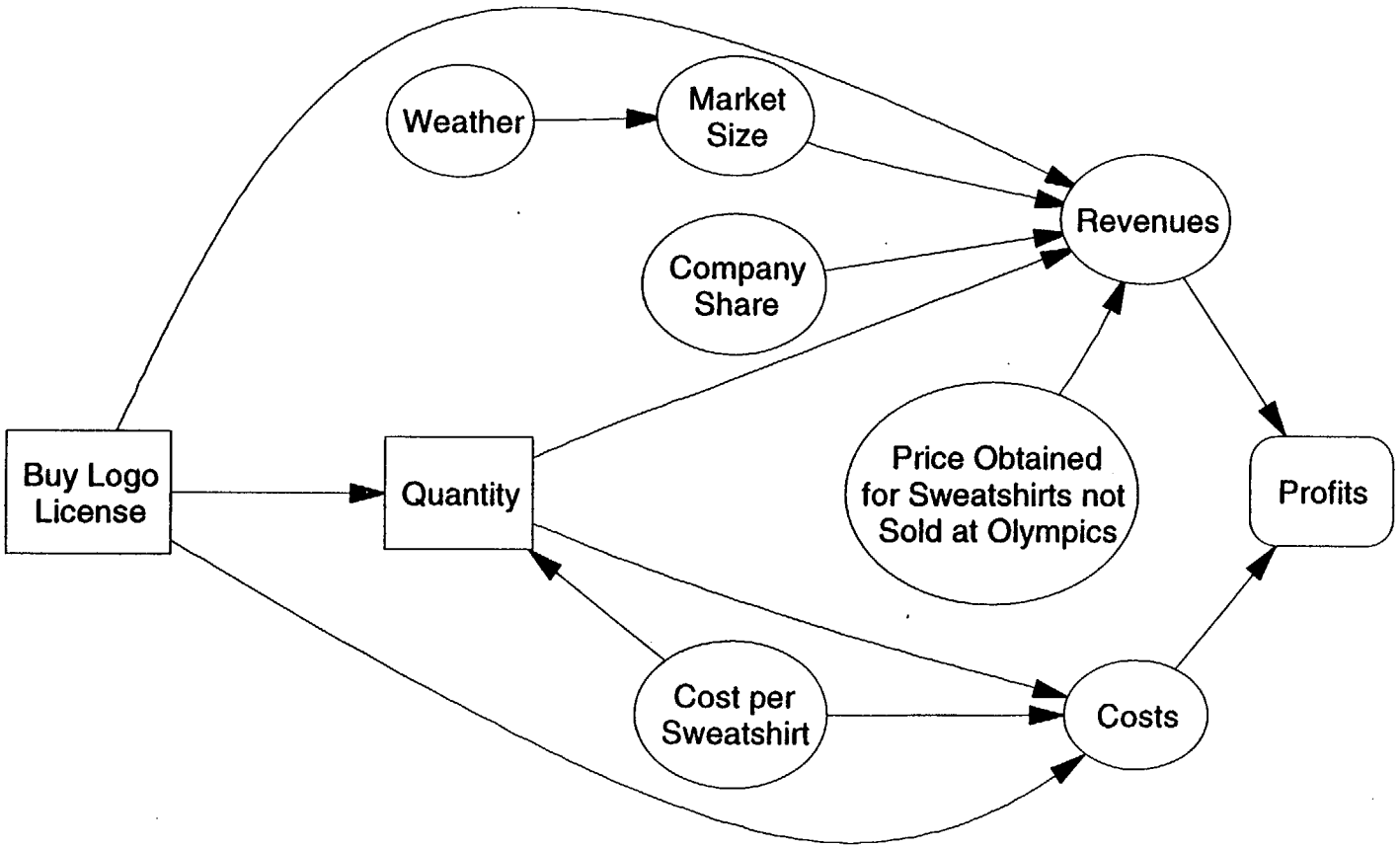

"Conditional" probability distributions are assessed for dependent variables

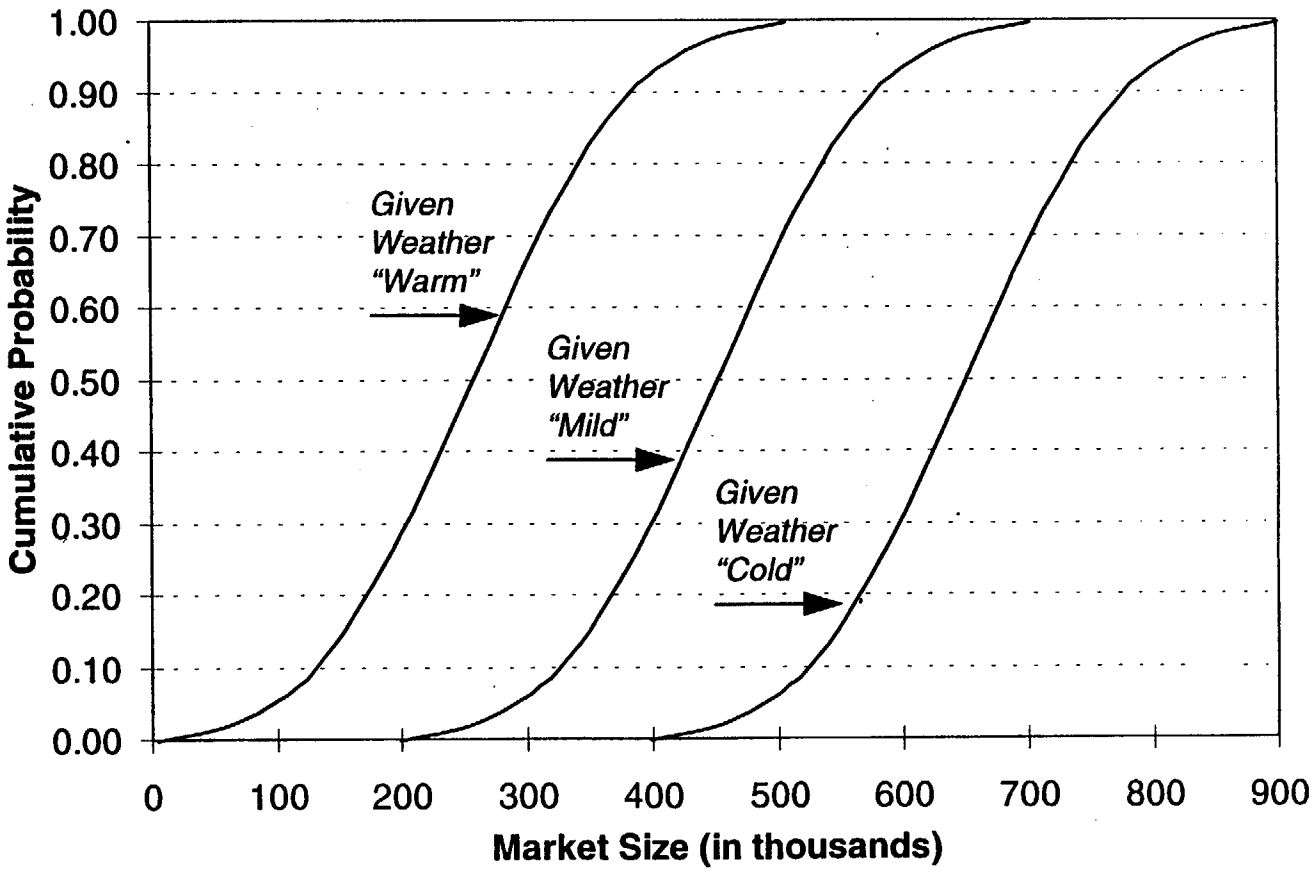

Phase 3—Conditioning

Step 1: Educate expert about cognitive biases

- Explain tendency to underestimate uncertainty
- Explain tendency to focus on recent/dramatic events

Step 2: Identify and encourage expert to use all relevant information and experience

Step 3: Elicit extreme scenarios

- "If years from now I tell you the worst (best) possible outcome occurred, what would have happened to cause it?"

Phase 4—Encoding: full distributions

Step 1: Assess from "outside-in"

- 1 and 99 percentiles
- then 10 and 90 percentiles
- then 50 percentile

Step 2: Assess values for 6-10 points in between the extremes using at least 2 different techniques

- Probability wheel
- Familiar reference events (e.g., poker hands, dice)
- Interval technique
- Numerical assignments
- Graphing

Step 3: Plot the points on a cumulative distribution

- Keep the plot hidden

Step 4: Fit a curve through the points

- Resolve inconsistencies

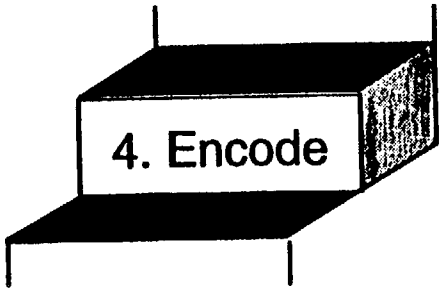

Assess additional points if the expert gives inconsistent responses or if a refined assessment is needed.

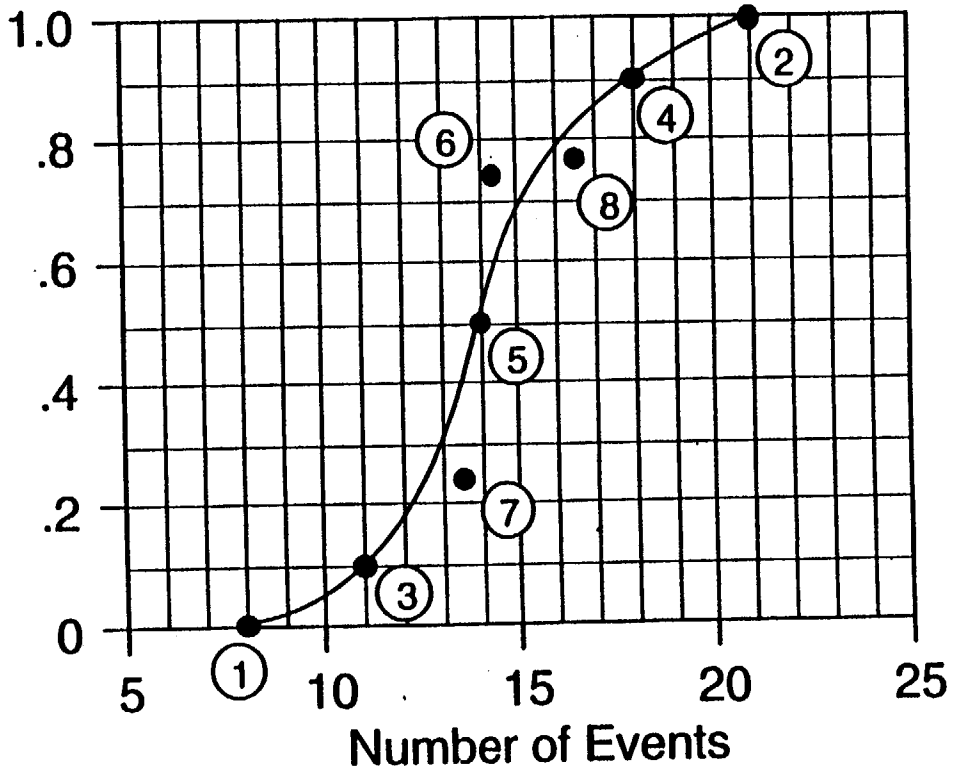

Assess additional points using probability questions.

Q: What is the probability that the number of events will be less than or equal to 11?

Phase 5—Verifying (full distributions)

Step 1: Re-assess outlying points on cumulative. Re-draw, if necessary.

Step 2: Verify 3-4 points on the curve with expert

Step 3: Show expert the distribution and allow adjustments

Step 4: Would the subject bet his or her own money according to the results?

Probability assessment worksheet

Subject: _____ **Variable:** _____

Interviewer: _____ _____

Date: _____ _____

Value	Outcome Probability		Value	Outcome Probability	
	less than value	greater than value		less than value	greater than value
_____	_____	_____	_____	_____	_____
_____	_____	_____	_____	_____	_____
_____	_____	_____	_____	_____	_____
_____	_____	_____	_____	_____	_____
_____	_____	_____	_____	_____	_____
_____	_____	_____	_____	_____	_____
_____	_____	_____	_____	_____	_____
_____	_____	_____	_____	_____	_____

Probability encoding worksheet

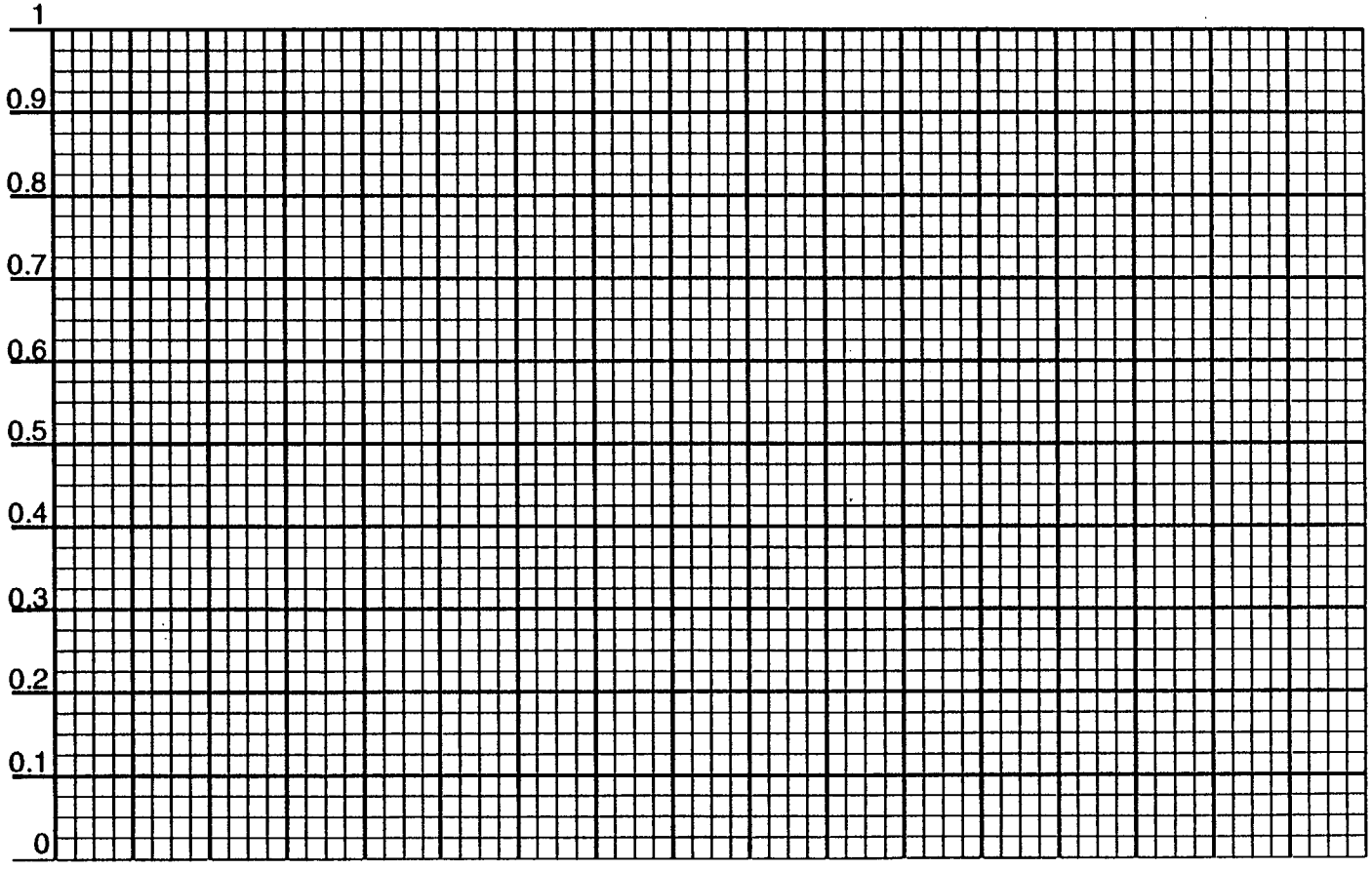

VARIABLE _____ UNITS _____ DATE _____

EXPERT _____ INTERVIEWER _____ COMMENTS _____

We have discussed quantifying uncertainty with probabilities.

Using Probabilities to Communicate

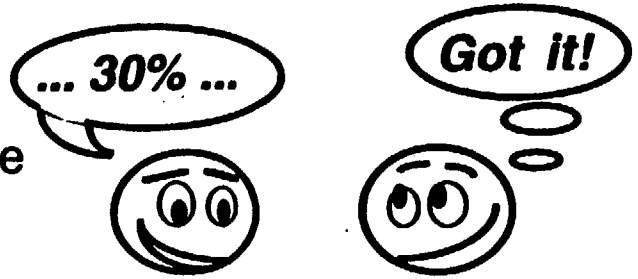

Avoiding Biases

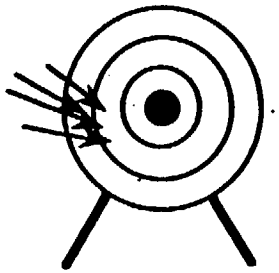

Assessing Probabilities

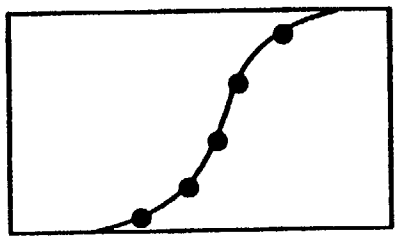

Write down your .1 and .9 cumulative probabilities for these uncertain quantities.

	Uncertain Quantity	
1	Year in which Attila the Hun died	453 A.D.
2	Number of auto thefts in the U.S. in 1991	1,661,738
3	U.S. consumption of beef in 1991	1.1Billion Kg 24.113 Billion lbs.
4	Planned date to select waste package emplacement orientation (page 8.3.2.2–89)	September, 1989
5	Expected water content of host rock (TSW2 unit), expressed as percent saturation (page 8.3.2.3–30)	Topopah Springs Welded Unit 65%
6	Expected annual cloud-to ground lighting strikes at facility (magnitude unspecified; page 8.3.2.3–33)	18
		① ② ③

* Probability that the quantity listed in The World Almanac and Book of Facts 1993 will be less than or equal to the value you write down for questions 1, 2 and 3. For questions 4, 5 and 6, the answers are found in Volume VI, "Yucca Mountain Site Characterization Plan.".

GROUND MOTION CHARACTERIZATION
FINAL AGENDA

WORKSHOP #2:
METHODS AND MODELS,
PRELIMINARY INTERPRETATIONS

January 8 to 10, 1997
Doubletree Hotel, Salt Lake City, UT

GOAL OF THE WORKSHOP:

The primary goal of this Workshop is to present available models for characterizing ground motions and discuss ways in which elements inherent to the models may differ from conditions at Yucca Mountain. The experts will also participate in a preliminary ground motion modeling exercise which will be discussed in the Workshop. Additionally, the range of the magnitude and distance modeling which must be covered by their interpretations will be specified.

APPROACH:

Several models directly applicable to ground motion modeling at Yucca Mountain have been developed or revised since the Workshop #1. These "proponent models" represent the spectrum of methods used to model ground motion. The Workshop will be used as a forum first to present the proponent models. Because many of the empirical models are generic for the western U.S. and not specific to Yucca Mountain, the elements which differ for the two regions will also be presented. These will include source, path, and site characteristics typical of normal faulting earthquakes in the Yucca Mountain region. As a preface to the discussion of the models and methods, the experts will also be presented with the explicit limits in earthquake magnitude, source distance, faulting style, and fault geometry for their interpretations. This discussion is necessary to facilitate identifying both deficiencies and positive attributes of the proponent models during the Workshop. In advance of the Workshop, the experts will be asked to evaluate ground motions for a postulated earthquake. This exercise is intended to focus the Workshop discussions on modeling techniques and illuminate the issues which should be resolved in the Workshop.

WEDNESDAY, JANUARY 8

1:00 - 4:30	**EXPERT ELICITATION TECHNIQUES**	
1:00 - 4:30	Elicitation Training	Morris

THURSDAY, JANUARY 9

7:30 - 8:00	**CONTINENTAL BREAKFAST**	
8:00 - 9:45	**INTRODUCTION**	
8:00 - 8:15	Welcome	Sullivan, Stepp
8:15 - 8:30	Overview of Workshop	Abrahamson
8:30 - 9:00	Experts' Scope of Work	Abrahamson
9:00 - 9:15	QA Issues	Chaney
9:15 - 9:45	Uncertainty	Toro

9:45 - 4:15	**YUCCA MOUNTAIN- AND SITE-SPECIFIC ISSUES**	
9:45 - 10:00	Introduction	Abrahamson
10:00 - 10:30	Foam Rubber Modeling of Normal Faults	Brune
10:30 - 11:00	Break	
11:00 - 11:30	Extensional Regime Data Base	Spudich
11:30 - 11:45	Stress Drops for Extensional Regime Earthquakes	Becker
11:45 - 12:45	Various Stress Drops in Context of the Composite Source Model	Anderson
12:45 - 1:45	Lunch	
1:45 - 2:15	Nonlinear Properties of Yucca Mountain Tuff	Stokoe
2:15 - 3:15	Scaling Relations (YM/CA) Based on Point Source Model	Campbell
3:15 - 3:45	Break	
3:45 - 4:15	2-D Effects at Yucca Mountain from Blast Data	Somerville
4:15 - 5:00	**PROPONENT MODELS**	
4:15 - 5:00	Evaluation of Empirical Attenuation Relations for Extensional Regime Earthquakes	Spudich
5:00 - 5:30	**COMMENTS FROM OBSERVERS**	

FRIDAY, JANUARY 10

7:30 - 8:00	**CONTINENTAL BREAKFAST**	
8:00 - 1:30	**PROPONENT MODELS, continued**	
8:00 - 8:15	Empirical Attenuation Model for Normal Faults	Abrahamson
8:15 - 9:00	Point Source RVT Model	Silva
9:00 - 9:30	Hybrid Empirical Model	Campbell
9:30 - 10:00	Attenuation Relations Based on Blast Data	Bennett
10:00 - 10:30	Break	
10:30 - 11:30	Numerical Simulations from Scenario Earthquake Study	Abrahamson
11:30 - 12:00	Numerical Simulations for the Bare Mtn. Fault	Stamatakos
12:00 - 12:30	Constraints on Attenuation from Precarious Rocks	Brune
12:30 - 1:30	Lunch	
1:30 - 4:45	**PRELIMINARY INTERPRETATIONS**	
1:30 - 3:00	Magnitude 6.5 Modeling Exercise	Abrahamson
3:00 - 3:30	Break	
3:30 - 4:45	Exercise, cont.	Abrahamson
4:45 - 5:00	**WHERE DO WE GO FROM HERE**	Abrahamson
5:00 - 5:30	**COMMENTS FROM OBSERVERS**	

YUCCA MOUNTAIN GROUND MOTION CHARACTERIZATION
WORKSHOP #2: METHODS AND MODELS, PRELIMINARY INTERPRETATIONS

Registration List
JANUARY 8 to 10, 1997

Name	Signature	Affiliation
1. Abrahamson, Norm		Consultant
2. Anderson, John		UNR
3. Becker, Ann		WCFS
4. Bennett, Joe		Maxwell Technologies
5. Boore, David		USGS
6. Brune, James		UNR
7. Campbell, Ken		EQE
8. Cornell, Allin		Consultant
9. Ferrill, David		CNWRA
10. Hanks, Tom		USGS
11. Ibrahim, Bakr		NRC
12. King, Jerry		M&O/SAIC
13. Lui, Christiana		NRC
14. McGarr, Art		USGS
15. McGuire, Robin		Risk Engineering
16. Parizek, Richard	DID NOT COME	NWTRB
17. Parks, Bruce		USGS
18. Penn, Sue		WCFS
19. Pomeroy, Paul		Advisory Committee on Nuclear Waste
20. Quittmeyer, Rich		WCFS
21. Reiter, Leon		NWTRB
22. Savino, John		DOE
23. Savy, Jean	DID NOT COME	LLNL
24. Sheaffer, Patricia		USGS
25. Silva, Walt		Pacific Engineering & Analysis
26. Soeder, Daniel	DID NOT COME	USGS
27. Somerville, Paul		WCFS
28. Spudich, Paul		USGS
29. Stamatakos, John		CNWRA
30. Stepp, Carl		WCFS
31. Stokoe, Ken		University of Texas
32. Sullivan, Tim		DOE

Attachment 6

YUCCA MOUNTAIN GROUND MOTION CHARACTERIZATION
WORKSHOP #2: METHODS AND MODELS, PRELIMINARY INTERPRETATIONS

Registration List
JANUARY 8 to 10, 1997

Name	Signature	Affiliation
33. Toro, Gabe		Risk Engineering
34. Walck, Marianne	Marianne C Walck	Sandia National Labs
35. Whitney, John		USGS
36. Wong, Ivan	IGWong	WCFS
37. Tom Charley	Tom Charley	USGS
38. Justus, Phil	Philip Justus	NRC
39.		
40.		
41.		
42.		
43.		
44.		
45.		

MODEL OF STRONG GROUND MOTIONS FROM EARTHQUAKES IN CENTRAL AND EASTERN NORTH AMERICA: BEST ESTIMATES AND UNCERTAINTIES

Gabriel R. Toro
Risk Engineering, Inc., 4155 Darley Ave., Suite A, Boulder, CO 80303

Norman A. Abrahamson
Pacific Gas and Electric Co., 245 Market St., San Francisco, CA 94111

John F. Schneider
Impact Forecasting, L.L.C., 230 W. Monroe Street, Chicago, IL 60606

Submitted to
Seismological Research Letters
September 5, 1996

Version 3

September 24, 1996

To appear in Seismological Research Letters, vol. 68, No. 1, 1997

ABSTRACT

Ground-motion attenuation equations for rock sites in central and eastern North America are derived, based on the predictions of a stochastic ground-motion model. Four sets of attenuation equations are developed (i.e., 2 crustal regions × 2 magnitude scales). The associated uncertainties are derived by considering the uncertainties in parameter values, as well as those uncertainties associated with the ground-motion model itself. Comparison to data shows a reasonable agreement. Comparison to other attenuation functions for the region shows consistency with most attenuation functions in current use.

INTRODUCTION

This paper presents a set of attenuation equations for spectral acceleration (SA) and peak ground acceleration (PGA) in the central and eastern North America (CENA), based on a stochastic model of source excitation and a model of path effects that considers multiple rays in a horizontally layered model of the crust. These models and the values of their parameters were developed following an extensive analysis of ground-motion data and other relevant data. This effort is documented in EPRI (1993) and in a series of upcoming papers (Schneider et al., 1996; Abrahamson et al., 1996a, 1996b). The objective in the EPRI study was to obtain both the best-estimate value and the associated uncertainty in each parameter, and to carry these uncertainties through to the final results. This paper presents the best estimates and uncertainties in the ground motions predicted by the stochastic model, in a functional form that is amenable to use in probabilistic hazard analysis and other earthquake-engineering applications, as well as some insights developed from these results and comparisons to other attenuation equations that have been proposed for CENA. Additional information about the derivation of these attenuation equations is provided in EPRI (1993) and Toro et al. (1996).

The frequency band, distance range, and magnitude range of interest for this study are 1 to 35 Hz, 1 to 500 km (with emphasis on distances of 1 to 100 km), and moment magnitude 5 to 8. Separate attenuation equations are obtained for two crustal regions found to be typical of CENA, for each of six frequencies and for peak ground acceleration, and for two different magnitude scales (i.e., moment magnitude M and Lg-wave magnitude m_{Lg}). The results presented here are directly applicable to hard rock (defined as having average shear-wave velocities of 6000 feet/s at the surface). Results for soil sites may be obtained from these results by using the amplification factors in EPRI (1993) and Silva et al. (1996).

Other studies (e.g. , Atkinson, 1984; Boore and Atkinson, 1987; Toro and McGuire, 1987; McGuire et al., 1988; Atkinson and Boore, 1995) have used a similar stochastic model to derive attenuation equations for CENA. This study is the first to develop a comprehensive quantification of the uncertainties in model parameters for CENA ground motions and to propagate these uncertainties to obtain the total uncertainty in ground-motion amplitude.

This paper begins with a summary of the stochastic ground-motion model, the parameters used to represent source and path effects in the study region, and the uncertainties in these parameters. This summary is not exhaustive and the reader is referred to EPRI (1993), Schneider et al. (1996), and Abrahamson et al. (1996a, 1996b) for further details on the model or its justification. This summary is followed by the tables and equations that describe attenuation functions and associated measures of uncertainty. Next, this paper presents comparisons to data and to other attenuation

equations proposed for CENA. Finally, this paper describes the procedure for estimating ground-motion at soil sites.

SUMMARY OF MODEL, PARAMETERS, AND UNCERTAINTIES

The stochastic model of earthquake ground motions uses simplified, yet physically based, representations of seismic energy release and wave propagation to obtain predictions of ground-motion amplitude for given values of earthquake size and depth, distance to the site, and model parameters. The source excitation is characterized by means of Brune's ω-squared model (Brune, 1970, 1971). The model for geometric attenuation considers the effect of crustal structure by using the formulation of Ou and Herrmann (1991; refinements to this formulation are documented in EPRI, 1993). The model for anelastic attenuation considers both crustal and near-surface attenuation (by means of parameters Q(f) and kappa, respectively). A comprehensive test of the stochastic model against recorded motions for several large magnitude events is contained in EPRI (1993) and Schneider et al. (1996). This test shows that the stochastic model is consistent with the recorded ground motions for the frequency, distance, and magnitude range of interest (i.e., the bias in the model predictions is essentially zero for most frequencies, considering its statistical uncertainty).

The key parameters for the stochastic model are stress-drop, crustal velocity structure, crustal anelastic attenuation (Q), near-site anelastic attenuation (κ or kappa), and focal depth. The selected values and associated uncertainties for these parameters are described below, after the definition of some terms related to uncertainty.

Types of Uncertainties

It is customary in seismic hazard studies to distinguish between two types of uncertainty, as follows:

Epistemic Uncertainty. Uncertainty that is due to incomplete knowledge and data about the physics of the earthquake process. In principle, epistemic uncertainty can be reduced by the collection of additional information.

Aleatory Uncertainty. Uncertainty that is inherent to the unpredictable nature of future events. It represents unique details of source, path, and site response that cannot be quantified before the earthquake occurs. Aleatory uncertainty cannot be reduced by collection of additional information. One may be able, however, to obtain better estimates of the aleatory uncertainty by using additional data.

This paper will refer to the combined epistemic and aleatory uncertainty as total uncertainty (or simply uncertainty). Epistemic and aleatory uncertainty are sometimes called "Uncertainty" and "Randomness" respectively.

To bring these concepts into the context of ground-motion prediction, consider that ground-motion models give estimates of the probability distribution of ground-motion amplitude for a given event. For most ground-motion models, including the one presented here, this distribution is assumed to be lognormal and is characterized by a median (μ) and a logarithmic standard deviation (σ). The scatter quantified by σ is the aleatory uncertainty.

Due to the limited data available, there is epistemic uncertainty in the values of μ and σ for a given magnitude and distance. This epistemic uncertainty is denoted σ_μ and σ_σ. The values of these quantities may be magnitude- and distance-dependent.

From the point of view of the ground-motion analyst or modeler, the total uncertainty in predicted ground motions is often partitioned in a manner that may be considered orthogonal to the above partition (see Abrahamson et al., 1990), as follows:

Modeling Uncertainty. Represents differences between the actual physical process that generates the strong earthquake ground motions and the simplified model used to predict ground motions (Abrahamson et al., 1990 call this modeling+random uncertainty). Modeling uncertainty is estimated by comparing model predictions to actual, observed ground motions. Because it is computed from comparisons to data, the modeling uncertainty captures all shortcomings of the model (provided that a sufficient number of earthquakes with a wide distribution of magnitudes and distances are used to estimate the modeling uncertainty).

Parametric Uncertainty. Represents uncertainty in the values of the model's event, path, and site-specific parameters (e.g., stress drop) for future earthquakes. Parametric uncertainty is quantified by observing the variation in parameters inferred (usually in an indirect manner) for several earthquakes and/or several recordings.

It is important to recognize that the distinction between modeling and parametric uncertainty is model-dependent. For instance, one may reduce the scatter in the predictions by making the model more complete, thereby introducing new parameters in the model. Unless these new parameters are known a-priori for future earthquakes and for

the site of interest, there will be additional parametric uncertainty, thereby transferring some modeling uncertainty into parametric uncertainty, without varying the total uncertainty (at least for the types of events and sites that are well represented in the data).

Both the modeling and parametric uncertainties contain epistemic and aleatory uncertainty. For instance, observed scatter that is not accounted for by the model and varies from event to event is aleatory modeling uncertainty, whereas statistical uncertainty about the bias of the model's median estimate (due to limited data) is epistemic modeling uncertainty. Similarly, the event-to event variation in stress drop is aleatory parametric uncertainty, whereas the imperfect knowledge about the probability distribution of stress drops from future earthquakes (e.g., what is the median stress drop for M 7 earthquakes?)

is epistemic parametric uncertainty. Table 1 illustrates this two-way partition of total uncertainty.

		Seismic-Hazard Analyst	
		Epistemic (σ_μ,σ_σ)	Aleatory (σ)
Ground-Motion Analyst	Modeling	σ_μ: Uncertainty in the true bias of model σ_σ: Uncertainty in estimate of $\sigma_{modeling}$	$\sigma_{modeling}$: Unexplained scatter due to physical processes not included in the model
	Parametric	σ_μ: Uncertainty in median values of source, path, and site parameters σ_σ: Uncertainty in probability distributions of source, path, and site parameters	σ_{param}: Event-to-event variation in source, path, and site-specific parameters of the model

Table 1. Partition of Uncertainty in Ground-Motion Prediction

The distinctions among the various types of uncertainty are subtle, but important in practice. They determine whether a particular component of uncertainty affects the median hazard curve or the associated uncertainty band. They also affect how the observed squared

residuals are partitioned. The most important reason for these distinctions is, however, to make sure that all uncertainties in the various pieces of the ground-motion model are considered, in order to obtain a realistic estimate of the total uncertainty.

Model Parameters and their Uncertainties

Stress Drop. The stress drop is a key parameter in the Brune model of source excitation: it determines how the corner frequency, the Fourier amplitude at high frequencies, and the source duration vary as a function of seismic moment. The median stress drop (120 bars) and its uncertainty were determined from the CENA stress-drop compilation of Atkinson (1993), adjusted to make the stress-drop values consistent with the crustal shear-wave velocity used in the EPRI study (see Figure 1a). Stress drops obtained in the EPRI study by inversion of seismograph data from CENA (see EPRI, 1993, or Abrahamson, 1996a) yield similar results.

The data for large magnitudes is sparse, but it suggests a reduction in the median stress drop and in the scatter with increasing magnitude (Figure 1a). This study conservatively ignored this possible reduction in median for large magnitudes, but increased the epistemic uncertainty in the median stress drop (i.e., increasing σ_{μ}) for large magnitudes.

The aleatory uncertainty in stress drop was assumed to be smaller for larger magnitudes. This is consistent with empirical studies that show a reduction in σ (i.e., the total aleatory uncertainty in ground-motion amplitude) for larger magnitudes (e.g., Youngs et al., 1995). The resulting model for the epistemic and aleatory uncertainties in stress drop is shown in Figure 1b. Note that the total uncertainty in stress drop is assumed to be constant, but its partition into epistemic and aleatory is magnitude-dependent.

Focal Depth. Initially, separate probability distributions were constructed for rifted and non-rifted CENA areas, but these differences do not lead to statistically significant differences in predicted ground motions. Thus, we use a single probability distribution of focal depth for all of CENA (see EPRI, 1993, and Abrahamson et al., 1996b). Uncertainty in focal depth is treated as being all aleatory; epistemic uncertainty in depth is not considered.

Crustal Velocity Structure. Sixteen crustal velocity models were compiled for the various tectonic domains in CENA (see Figure 2), and the effects of these velocity models on ground-motion amplitude were evaluated. We determined that--for the purposes of ground-motion calculations for the depth, distance, and frequency range of interest--15 of the 16 crustal models predicted similar ground motions and could be grouped into one (see EPRI, 1993, or Abrahamson et al., 1996b). Based on this result, the CENA is partitioned into two attenuation regions, namely the Gulf Coastal Plain (region 4) and everything else (represented by the crustal structure in region 12: the Midcontinent region). These representative crustal structures are then used in separate simulations that we use to derive the engineering model for each region. Uncertainty in crustal structure (within each attenuation region) is not modeled explicitly as parametric uncertainty. This uncertainty is, however, included in the modeling uncertainty obtained from comparisons of data to predictions (EPRI, 1993; Schneider et al., 1996).

Near-Site Anelastic Attenuation, Kappa. The analysis of data on kappa for CENA and the western United States (WUS) is described in EPRI (1993) and Abrahamson et al. (1996b). A kappa of 0.006 provides an adequate match to the spectral shape of CENA hard rock ground motions. Uncertainty in the larger dataset of WUS kappa values for rock is described as log-normally distributed with a logarithmic standard deviation of 0.4. This study used

three equally weighted values of 0.003, 0.006, and 0.012, which correspond to a logarithmic standard deviation of 0.7.

Epistemic uncertainty in kappa was neglected in this study. It should be noted, however, that to the extent that kappa is a property of each individual site (for which one can obtain better estimates using site-specific geophysical measurements or recordings), some of its uncertainty should be considered epistemic. The same is true for variations in near-surface shear-wave velocities among rock sites.. This study treats variations within a region as aleatory uncertainty, as is common practice.

Crustal Anelastic Attenuation, Q. The data on Q for the two attenuation regions are described in EPRI (1993) and Abrahamson et al. (1996b). The uncertainty in Q for each region is characterized by three models that are given equal weights based on the EPRI (1993) analyses and on earlier studies. This uncertainty is considered all aleatory, as it is thought that most of this uncertainty is due to regional variations in crustal properties. Again, if one considers a smaller region around a specific site, some of the uncertainty in Q should be treated as epistemic.

Modeling Uncertainty

The modeling uncertainty is determined from the misfit of modeled ground motion data with recorded data, as described in EPRI (1993) and Schneider et al. (1996). The epistemic modeling uncertainty is made up of the site-correction terms (called D terms in the above references) and the model bias. The aleatory modeling uncertainty is made up of the remaining misfit or scatter (allowing the D terms to be different from 1). The resulting modeling uncertainties are approximated by

$$\sigma_{a,\,\text{modeling}} = \begin{cases} 0.32 & f>9 \text{ Hz} \\ 0.63-0.14\ \ln(f) & 2<f\leq 9 \text{ Hz} \\ 0.53 & f\leq 2 \text{ Hz} \end{cases} \quad (1)$$

$$\sigma_{e,\,\text{modeling}} = 0.27 \quad (2)$$

where σ represents standard deviation in natural log units.

Total Uncertainty

In summary, aleatory uncertainty in the predicted ground motions comes from parametric uncertainty in stress drop, focal depth, kappa and Q, and from aleatory modeling uncertainty. Epistemic uncertainty in the predicted ground motions comes from epistemic parametric uncertainty in stress drop and from epistemic modeling uncertainty.

FUNCTIONAL FORM OF PREDICTIVE EQUATIONS

Practical considerations dictate that the ground-motion predictions for engineering applications must be in the form of relatively simple equations in terms of magnitude and distance (we will call this set of attenuation functions the Engineering Model). The functional form and number of terms in these equations must, however, be sufficient to match the main features of the ground motions predicted by the stochastic ground-motion model described earlier, over the entire range of magnitudes, distances, and frequencies of engineering interest.

The functional form adopted here is the following:

$$\ln Y = C_1 + C_2(M-6) + C_3(M-6)^2 - C_4 \ln R_M - (C_5 - C_4) \max\left[\ln\left(\frac{R_M}{100}\right), 0\right] - C_6 R_M + \varepsilon_e + \varepsilon_a \quad (3)$$

$$R_M = \sqrt{R_{jb}^2 + C_7^2} \quad (4)$$

where Y is spectral acceleration or peak ground acceleration (in units of g), C_1 through C_7 are constants to be determined from the modeling results (see next section), M is either Lg magnitude (m_{Lg}) or moment magnitude (M), and R_{jb} is the closest horizontal distance (or Joyner-Boore distance) to the earthquake rupture (km).

The quadratic magnitude term is needed in order to provide a better fit to the model predictions for low-frequency ground motions (it is not required for frequencies of 5 Hz or higher). The magnitude terms are of the form $(M-6)^n$ for the sake of numerical stability in the values of C_2 and C_3. The terms in C_4 and C_5 represent geometrical spreading with slopes (in log-log space) C_4 ($R_M < 100$ km) and C_5 ($R_M > 100$ km). The model with two slopes provides a better fit to the crustal effects predicted by the ground-motion model in Schneider et al. (1996).

Uncertainty in ground-motion amplitude is represented by the quantities ε_a (aleatory) and ε_e (epistemic), which are assumed to follow normal distributions with mean zero. The standard deviations of ε_a and ε_e are, in general, dependent on magnitude and distance.

Table 2 list the values of coefficients C_1 through C_7. Separate sets of coefficients are provided for the Midcontinent[1] and Gulf crustal models and for the two choices of magnitude variable.

[1]We refer to the Midcontinent as a "region", although it is a group of crustal regions.

TABLE 2
Coefficients of Attenuation Equations

Freq.	Median		Weight=0.046		Weight=0.454		Weight=0.454		Weight=0.046		Median and all cases				
(Hz)	C1	C2	C1	C2	C1	C2	C1	C2	C1	C2	C3	C4	C5	C6	C7
	Midcontinent, equations using Moment Magnitude														
0.5	-0.74	1.86	-1.53	1.72	-0.99	1.82	-0.49	1.91	0.05	2.00	-0.31	0.92	0.46	0.0017	6.9
1.0	0.09	1.42	-0.75	1.25	-0.18	1.36	0.35	1.47	0.93	1.58	-0.20	0.90	0.49	0.0023	6.8
2.5	1.07	1.05	0.23	0.89	0.81	1.00	1.34	1.10	1.91	1.21	-0.10	0.93	0.56	0.0033	7.1
5.0	1.73	0.84	0.89	0.68	1.46	0.79	1.99	0.89	2.57	1.00	0.00	0.98	0.66	0.0042	7.5
10.0	2.37	0.81	1.53	0.65	2.10	0.76	2.64	0.86	3.21	0.97	0.00	1.10	1.02	0.0040	8.3
25.0	3.68	0.80	2.84	0.63	3.41	0.74	3.95	0.85	4.52	0.96	0.00	1.46	1.77	0.0013	10.5
35.0	4.00	0.79	3.16	0.63	3.74	0.74	4.27	0.85	4.84	0.96	0.00	1.57	1.83	0.0008	11.1
PGA	2.20	0.81	1.36	0.64	1.93	0.75	2.46	0.86	3.04	0.97	0.00	1.27	1.16	0.0021	9.3
	Midcontinent, equations using Lg Magnitude														
0.5	-0.97	2.52	-1.83	2.29	-1.24	2.45	-0.69	2.60	-0.10	2.76	-0.47	0.93	0.60	0.0012	7.0
1.0	-0.12	2.05	-0.94	1.86	-0.38	1.99	0.14	2.11	0.70	2.23	-0.34	0.90	0.59	0.0019	6.8
2.5	0.90	1.70	0.10	1.53	0.64	1.64	1.15	1.75	1.69	1.86	-0.26	0.94	0.65	0.0030	7.2
5.0	1.60	1.24	0.80	1.07	1.35	1.18	1.85	1.29	2.39	1.40	0.00	0.98	0.74	0.0039	7.5
10.0	2.36	1.23	1.57	1.07	2.11	1.18	2.62	1.28	3.16	1.39	0.00	1.12	1.05	0.0043	8.5
25.0	3.54	1.19	2.75	1.03	3.29	1.14	3.79	1.24	4.34	1.35	0.00	1.46	1.84	0.0010	10.5
35.0	3.87	1.19	3.08	1.03	3.62	1.14	4.12	1.24	4.66	1.35	0.00	1.58	1.90	0.0005	11.1
PGA	2.07	1.20	1.27	1.04	1.81	1.15	2.32	1.25	2.86	1.36	0.00	1.28	1.23	0.0018	9.3
	Gulf, equations using Moment Magnitude														
0.5	-0.81	1.72	-1.60	1.58	-1.06	1.67	-0.56	1.76	-0.02	1.86	-0.26	0.74	0.71	0.0025	6.6
1.0	0.24	1.31	-0.60	1.15	-0.03	1.26	0.51	1.36	1.08	1.48	-0.15	0.79	0.82	0.0034	7.2
2.5	1.64	1.06	0.80	0.90	1.38	1.01	1.91	1.12	2.48	1.23	-0.08	0.99	1.27	0.0036	8.9
5.0	3.10	0.92	2.26	0.76	2.83	0.87	3.36	0.97	3.94	1.08	0.00	1.34	1.95	0.0017	11.4
10.0	5.08	1.00	4.25	0.84	4.82	0.95	5.35	1.05	5.92	1.16	0.00	1.87	2.52	0.0002	14.1
25.0	5.19	0.91	4.35	0.74	4.92	0.86	5.46	0.96	6.03	1.07	0.00	1.96	1.96	0.0004	12.9
35.0	4.81	0.91	3.97	0.74	4.54	0.86	5.08	0.96	5.65	1.07	0.00	1.89	1.80	0.0008	11.9
PGA	2.91	0.92	2.07	0.75	2.64	0.86	3.18	0.97	3.75	1.08	0.00	1.49	1.61	0.0014	10.9
	Gulf, equations using Lg Magnitude														
0.5	-1.01	2.38	-1.87	2.14	-1.28	2.30	-0.73	2.45	-0.15	2.61	-0.42	0.75	0.83	0.0032	6.8
1.0	0.06	1.97	-0.76	1.78	-0.20	1.91	0.32	2.03	0.88	2.16	-0.32	0.80	0.92	0.0030	7.3
2.5	1.49	1.74	0.69	1.57	1.23	1.68	1.74	1.79	2.28	1.90	-0.26	1.00	1.36	0.0032	9.0
5.0	3.00	1.31	2.20	1.15	2.74	1.26	3.25	1.36	3.79	1.47	0.00	1.35	2.03	0.0014	11.4
10.0	4.65	1.30	3.86	1.14	4.40	1.25	4.91	1.35	5.45	1.46	0.00	1.78	2.41	0.0000	13.8
25.0	5.08	1.29	4.29	1.13	4.83	1.24	5.33	1.34	5.87	1.45	0.00	1.97	2.04	0.0000	12.9
35.0	4.68	1.30	3.88	1.13	4.42	1.24	4.93	1.35	5.47	1.46	0.00	1.89	1.88	0.0005	11.9
PGA	2.80	1.31	2.00	1.14	2.54	1.25	3.05	1.36	3.59	1.47	0.00	1.49	1.68	0.0017	10.9

Figures 3 and 4 show representative predictions by the Engineering Model for the two representative crustal regions and for the two magnitude representations considered in this study. Comparing the predictions for the two regions, we observe that ground motions at short distances are higher for the Gulf region, due to lower shear-wave velocities (which produce greater amplification) near the surface. At longer distance, this effect is counteracted by higher anelastic attenuation in the Gulf region, resulting in lower predictions.

Figures 3 and 4 indicate only a minor discontinuity in slope at 100 km as a result of crustal reflections. Discontinuities introduced by the layered crustal structure are smoothed out by the distribution of hypocentral depth. These discontinuities increase uncertainty near 100 km, as will be shown in Figure 5.

QUANTIFICATION OF UNCERTAINTY

The combined effect of all parametric uncertainties is obtained by performing statistics on the residuals from the least-squares fit to model predictions. The modeling uncertainty is added later.

Figure 5 (panels a and b) illustrates the various components of aleatory uncertainty and their dependence on distance for **M** 6.5 in the Midcontinent. This figure shows that depth is a very important contributor to aleatory uncertainty at short distances, stress drop and modeling error are important contributors at all distances, and Q is an important contributor at long distances (particularly for high frequencies). Figure 5 (panels c and d) shows the components of aleatory uncertainty and their dependence on moment magnitude for a distance of 20 km.

Figure 6 shows the components of epistemic uncertainty and their dependence on magnitude for a distance of 20 km, and for attenuation equations in terms of both **M** and m_{Lg} (Figure 6 also shows the total uncertainty). Epistemic uncertainty is higher, and aleatory uncertainty is slightly lower, for higher magnitudes. This is a consequence of our assumption about the magnitude dependence of the epistemic and aleatory uncertainties in stress drop (see Figure 1 and Equation 1). Aleatory uncertainty is higher for low-frequency ground motions due to higher aleatory modeling uncertainty.

The equations and tables that follow provide a simplified representation of how the aleatory and epistemic uncertainties vary as a function of magnitude and distance for the various ground-motion measures. The emphasis here is on the magnitude-distance-frequency combinations of engineering interest. Little attention is paid to unimportant combinations such as high frequencies at long distances.

The expressions for the total aleatory uncertainty in ground-motion amplitude for a given magnitude and distance can be decomposed into a magnitude-dependent term (aleatory modeling uncertainty plus aleatory uncertainty due to stress drop) and a distance-dependent term (aleatory uncertainty due to focal depth, Q, and kappa). Thus, the total aleatory uncertainty is given by the following equation:

$$\sigma_a(M,R) = \sqrt{\sigma^2_{a,\ \text{modeling}+\Delta\sigma}(M) \ + \ \sigma^2_{a,\ \text{depth}+Q+\kappa}(R_{jb})} \qquad (5)$$

The magnitude-dependent aleatory uncertainty $\sigma_{a,\ \text{modeling}+\Delta\sigma}$ is approximated by three linear segments, defined by its values for three magnitude (see Table 3). Values for other magnitudes are obtained by linear interpolation. The distance-dependent aleatory uncertainty

$\sigma_{a,depth+Q+\kappa}$ is approximated as constant for R_{jb} < 5 km, varies linearly between 5 and 20 km, and is constant for R_{jb} > 20 km (see Table 4 for values at 5 and 20 km).

TABLE 3

Values of Magnitude-Dependent Aleatory Uncertainty ($\sigma_{a,modeling+\Delta\sigma}$) for Critical Magnitudes

Freq	M-based equations			m_{Lg}-based equations		
(Hz)	M 5	M 5.5	M 8.0	m_{Lg} 5	m_{Lg} 6	m_{Lg} 7.5
0.5	0.61	0.62	0.66	0.63	0.81	0.61
1.0	0.63	0.64	0.67	0.62	0.81	0.61
2.5	0.63	0.68	0.64	0.58	0.70	0.59
5.0	0.60	0.64	0.56	0.54	0.63	0.51
10.0	0.59	0.61	0.50	0.54	0.57	0.44
25.0	0.62	0.63	0.50	0.57	0.58	0.44
35.0	0.62	0.63	0.50	0.57	0.58	0.44
PGA	0.55	0.59	0.50	0.58	0.58	0.44

TABLE 4

Values of Distance-Dependent Aleatory Uncertainty ($\sigma_{a,depth+Q+\kappa}$) at Critical Distances

Freq. (Hz)	Midcontinent		Gulf	
	<5 km	>20 km	<5 km	>20 km
0.5	0.45	0.12	0.54	0.39
1.0	0.45	0.12	0.51	0.39
2.5	0.45	0.12	0.50	0.34
5.0	0.45	0.12	0.50	0.33
10.0	0.50	0.17	0.53	0.38
25.0	0.57	0.29	0.63	0.47
35.0	0.62	0.35	0.68	0.47
PGA	0.54	0.20	0.48	0.30

The epistemic uncertainty is magnitude-dependent (as was seen in Figure 6) and is approximated as a linear function of magnitude of the form:

$$
\begin{aligned}
\sigma_e(M) &= 0.34+0.06(M-6) && M \text{ equations, f=0.5 Hz} \\
&\quad 0.36+0.07(M-6) && M \text{ equations, f}\geq 1 \text{ Hz and PGA} \\
&\quad 0.37+0.10(m_{Lg}-6) && m_{Lg} \text{ equations, f=0.5 Hz} \\
&\quad 0.35+0.08(m_{Lg}-6) && m_{Lg} \text{ equations, f=1 Hz} \\
&\quad 0.34+0.07(m_{Lg}-6) && m_{Lg} \text{ equations, f}\geq 2.5 \text{ Hz and PGA}
\end{aligned}
\qquad (6)
$$

DISCRETIZATION OF EPISTEMIC UNCERTAINTY FOR SEISMIC HAZARD ANALYSIS

In seismic hazard analysis, epistemic uncertainty is typically represented by considering multiple attenuation equations with weights related to their credibilities. This approach is natural when using attenuation equations developed by different authors or under a discrete set of alternative assumptions. This approach is also convenient because it lends itself to a logic-tree analysis and to the display of sensitivity. Aleatory uncertainty, on the other hand, is represented by a continuous random variable and is integrated over during the first step (i.e., the conditional analysis step) of the seismic-hazard calculations.

The median predictions by the Engineering Model (represented by Equation 3 and Table 2) and the uncertainty represented by σ_e are transformed into a discrete set of attenuation equations. This is accomplished by replacing the normal distribution of the uncertainty term ε_e in Equation 3 with a discrete probability distribution. The discrete distribution consists of n values

$$\varepsilon_{e,i}=U_i\sigma_e(M), \qquad i=1,n \tag{7}$$

and their associated weights W_i, where U_i represents a value from a discrete approximation to a standard normal distribution. For n=4, the values of U_i and W_i in Table 5 have been chosen so that the probabilistic moments up to order six of the four-point discrete distribution are equal to the corresponding moments of the standard normal distribution. By substituting Equations 7 and 6 in Equation 3, and using U_i values in Table 5, we obtain four alternative

attenuation equations with associated weights. These alternative attenuation equations (which differ from the median attenuation equation in their C_1 and C_2 coefficients only) are given in Table 2, along with the median attenuation equations.

TABLE 5

Discrete Approximation to Standard Normal Distribution (Used to Discretize the Epistemic Uncertainty)

i	Distance U_i	Weight W_i
1	-2.33	0.046
2	-0.74	0.454
3	0.74	0.454
4	2.33	0.046

COMPARISON TO ENA GROUND-MOTION DATA

The CENA ground-motion data (see EPRI, 1993) are used for comparison to the Engineering ground-motion model developed here. In order to remove complications such as site effects and to limit the comparison to magnitudes and distances not too removed from the range of engineering interest, the following criteria are used for the selection of records for this comparison: (1) magnitudes $M \geq 4$, (2) distances less than 200 km, (3) horizontal components, (4) rock site conditions, (5) instruments located in shelters or at the lower level of buildings at most four stories high, and (6) estimate of stress drop available in Abrahamson et al. (1996a). Table 6 lists the records that meet these criteria. Figure 7 compares the observed spectral accelerations at 1 and 10 Hz to the predictions by the Engineering Model (using both the attenuation equations for M). The data are partitioned into two groups ($M \leq 5$ and $M > 5$).

Table 6
Earthquake Records used in Comparisons

Event Name	Date	m_{Lg}	M	Site Name	R (km)	No. of Compo-nents	Code	Stress Drop (bars)
New Madrid, Mo	04/27/89	4.7	4.7	Old Appleton, Missouri	8.0	2	2	229
New Madrid, Mo	05/04/91	4.6	4.4	Old Appleton, Missouri	160	2	3	39
Saguenay, Can.	11/23/88	4.8	4.5	Dickey, Maine	198	2	4	53
New Brunswick (A)	03/31/82	4.8	4.0	Indian Brook II, N.B, (IB2)	0.8	2	1	96
New Brunswick (A)	03/31/82	4.8	4.0	Mitchell Lake Rd, N.B (ML, Temp.)	4.0	2	1	96
New Brunswick (A)	03/31/82	4.8	4.0	Hickey Lake, N.B, (HL, Temp.)	4.1	2	1	96
Nahanni, Can.	12/23/85	6.4	6.7	Nahanni, NWT, Station 2	7.4	2	5	86
Nahanni, Can.	12/23/85	6.4	6.7	Nahanni, NWT, Station 1	7.6	2	5	86
Nahanni, Can.	12/23/85	6.4	6.7	Nahanni, NWT, Station 3	22.6	2	5	86
Saguenay, Can.	11/25/88	6.5	5.9	GSC Site 17 - St-Andre-Du-Lac, Que	64.1	2	6	655
Saguenay, Can.	11/25/88	6.5	5.9	GSC Site 20 - Les Eboulements, Que	90.	2	6	655
Saguenay, Can.	11/25/88	6.5	5.9	GSC Site 8 - La Malbaie, Que	93.	2	6	655
Saguenay, Can.	11/25/88	6.5	5.9	GSC Site 14 - St. Lucie de Beaur., Que	101.	2	6	655
Saguenay, Can.	11/25/88	6.5	5.9	GSC Site 5 - Tadoussac, Que	113	1	6	655
Saguenay, Can.	11/25/88	6.5	5.9	GSC Site 10 - Riviere Quelle	118	2	6	655
Saguenay, Can.	11/25/88	6.5	5.9	GSC Site 1 - St. Ferreol, Que	117	2	6	655
Saguenay, Can.	11/25/88	6.5	5.9	GSC Site 9 - St. Pascal, Que	132	2	6	655
Saguenay, Can.	11/25/88	6.5	5.9	Dickey, Maine	197	2	6	655

Predictions are shown as median curve, median$\times\exp(\pm\sigma_r)$, and median$\times\exp[\pm(\sigma_a^2+\sigma_e^2)^{1/2}]$. The reference magnitudes for the two groups of data are M 4.5 and 5.9, and m_{Lg} 5.0 and 6.5 (the reference magnitude for the large-magnitude group is chosen as the magnitude of the 1988 Saguenay earthquake). All observations are scaled to the corresponding reference magnitude. Figure 7 shows that the ground-motion amplitudes predicted by the Engineering Model are generally consistent with observations. The only discrepancy relates to the 1988 Saguenay earthquake. The observed 10-Hz amplitudes for Saguenay lay, on average, two standard deviations above the median (1.5 standard deviations for the m_{Lg} attenuation equations). This discrepancy is explained by the higher stress drop of this event. This stress drop is high, but is not inconsistent with the stress-drop distribution obtained in Abrahamson et al. (1996a). Additional comparisons to this dataset are contained in EPRI (1993) and Toro et al. (1996).

COMPARISON TO OTHER MODELS

Figure 8 compares the predictions by the Engineering Model for the Midcontinent region, in terms of both M and m_{Lg} , to predictions by other attenuation functions and ground-motion models for ENA. Predictions in terms of m_{Lg} are compared to predictions by the attenuation equations of Boore and Atkinson (1987) and McGuire et al. (1988; labeled EPRI, 1988). Predictions in terms of M are compared to predictions by the attenuation equations of Boore and Atkinson (1987) and Atkinson and Boore (1995).

The differences between predictions by the Engineering Model developed here and by the earlier attenuation equations are comparable to the uncertainties obtained in the previous Section. This indicates general consistency between the new model and the earlier models.

The differences at high frequencies are due to differences in ground-motion duration. The larger differences at low frequencies are due to the combined effect of duration and spectral shape. The only significant difference is with the Atkinson and Boore (1995) ground-motion model at 1 Hz and is due to differences in the assumed shape of the power spectrum of large earthquakes at low frequencies.

GROUND-MOTION PREDICTIONS FOR SOIL SITES

Silva et al. (1996, see also EPRI, 1993) have calculated spectral acceleration and PGA amplification factors for five separate CENA soil categories and for various levels of shaking. Median ground-motion predictions for CENA soil sites are obtained by multiplying the spectral accelerations and PGA for rock, calculated using Equation 3 and Table 2, by the appropriate amplification factors from Silva et al. (1996).

Intuitively, the uncertainty in ground motion at soil sites would be estimated by adding the uncertainty in site response to the uncertainty in the input rock ground motion. The uncertainty in the input rock ground motion would be estimated by the uncertainty in the rock attenuation relation. Although intuitively appealing, this procedure would significantly overestimate the uncertainty in soil ground motions. In the discussion that follows, we show that the uncertainty in ground motions for a given soil site category is actually less than for rock sites. We recommend using the rock-site uncertainty as a conservative estimate of the soil-site uncertainty.

There are two main issues to consider in comparing the uncertainty of soil site and rock site ground motions. The first is the uncertainty in the site response for low to moderate

levels of shaking and the second is the uncertainty in non-linear site response for high levels of shaking.

For low to moderate levels of shaking, the uncertainty in ground motion on soil and rock sites can be compared using recordings from dense arrays of seismometers. Abrahamson and Sykora (1993) examined the spatial correlation of response spectra using data from nine dense arrays. Five of the arrays were located on rock and four were located on soil. The amplitude variation for each array was fit to the functional form:

$$\sigma(f,\xi) = c_1(f,M)[1-\exp(c_2(f))] \tag{8}$$

where σ is the standard deviation of the difference ln[Sa(f)] between two sites separated by a distance ξ, and $c_1(f,M)$, $c_2(f)$ are constants for each frequency and magnitude range that are estimated by maximum likelihood. The resulting response spectral variation models are shown in Figure 9. The uncertainty in ground response at rock sites is larger than or equal to the uncertainty at soil sites. The small-magnitude (M 4.1-4.7) rock-site standard deviation is larger than the small-magnitude (M 4.1-4.7) soil-site standard deviation at low and high frequencies, whereas the two are similar at intermediate frequencies (3-7 Hz). The large-magnitude rock-site curve comes from a single event (Coalinga aftershock) so it is not as robust as the other curves, but it also shows larger standard deviations than the M5 soil-site curve for frequencies of 1 to 7 Hz.

If the total aleatory uncertainty in spectral acceleration at soil sites is computed by simply adding the variance in soil amplification to the variance in the rock spectral acceleration, then

the uncertainty in spectral acceleration would be higher for soil sites than for rock sites. The dense-array data, however, suggest that the opposite is true. This suggests that either the soil has a homogenizing effect on ground motions or that the uncertainty in the bedrock motions is lower than the uncertainty in the outcrop motions.

A second concern is whether the uncertainty in the high-strain properties of soil sites should increase the total uncertainty of soil site ground motions for large ground motion levels. This issue was examined by modeling site response using a range of soil properties for site category 4 using the equivalent linear procedure described in Silva et al. (1996). The uncertainty in the resulting surface ground motion was computed for two sites from events with magnitudes ranging from 5.5 to 7.5. The results are shown in Figure 10. As the amplitude of shaking increases, the uncertainty in the ground motion decreases slightly. We conclude that the effect of nonlinear response is to reduce the uncertainty in surface ground motions such that it counteracts the additional uncertainty due to variations of the soil properties.

These results imply that the uncertainty computed for rock sites is an upper bound for the uncertainty on soil sites in a given site category. Therefore, we recommend using the uncertainty of ground motion given here for rock sites as a conservative estimate of the uncertainty of ground motion for soil sites.

DISCUSSION

The median attenuation equations and the associated models of aleatory and epistemic uncertainty presented here embody the ground motions predicted using the ground-motion models and parameters presented in EPRI (1993), Schneider et al. (1996), and Abrahamson et

al. (1996a, 1996b). Though slightly more complicated than most attenuation equations in current use, these attenuation equations are in a form suitable for the determination of design ground motions and for seismic hazard evaluations.

Predicted ground motions for the Midcontinent and Gulf crustal regions are comparable to predictions by earlier models that use omega-square representations of the source spectra and are generally consistent with available records from CENA. The associated aleatory and epistemic uncertainties are similar to the values in current use for some cases (i.e., high frequencies and moderate distances) and higher in other cases (i.e., low frequencies or short distances). The high aleatory uncertainty at low frequencies is due to high modeling uncertainty (an additional contributor in the relations for m_{Lg} is uncertainty in the relationship between m_{Lg} and seismic moment; see Abrahamson et al., 1996a). The higher uncertainty at shorter distances is due to the explicit consideration of aleatory uncertainty in focal depth.

What sets this study apart from the earlier studies of ground motions in CENA is the much larger amount of data that was collected and used to estimate model parameters, the more realistic modeling of crustal effects, and the rational, quantitative process used to derive the median predictions and associated uncertainties. These characteristics make the median predictions and measures of uncertainty presented here much more robust than earlier results.

It must be pointed out that these attenuation equations were derived using mainly point-source modeling assumptions (the only exception being the conversion of asperity depth to hypocentral depth, see EPRI, 1993). As a consequence, these results may overestimate ground motions at sites near the rupture of a large earthquake, because we have not included other geometric and potential source-scaling effects associated with extended ruptures. Therefore, caution should be exercised if these results are used to predict ground motions at

distances shorter than one or two source dimensions. This limitation is of little significance for most sites in the Central and Eastern United States.

ACKNOWLEDGEMENTS

This work was performed as part of the Early Site Permit Demonstration Project, under the direction of the EPRI, and sponsored by Southern Electric International, Commonwealth Research Corporation, Public Service Corporation of New Jersey, EPRI, the Nuclear Management and Research Council, the U.S. Department of Energy, and Sandia National Laboratories. We thank all project participants, particularly Gail Atkinson, Walt Silva, and Bob Youngs, for their inputs and comments.

REFERENCES

Abrahamson, N.A., P.G. Somerville, and C.A. Cornell (1990). Uncertainty in numerical strong motion predictions, *Proc. fourth U.S. Nat. Conf. Earth. Eng.*, Palm Springs, CA, **1**, 407-416.

Abrahamson, N.A., and D. Sykora (1993). Variation of ground motion across individual sites. *Proc., Fourth DOE Natural Phenomena Hazards Mitigation Conference*, LLNL CONF-9310102.

Abrahamson, N.A., G.M. Atkinson, and G.R. Toro (1996a). Quantification of seismic source parameters for eastern North America." submitted to *Earthquake Spectra.*

Abrahamson, N.A., G.M. Atkinson, and G.R. Toro (1996b). Effect of the propagation path on ground motion in eastern North America, submitted to *Earthquake Spectra.*

Atkinson, G.M. (1984). Attenuation of strong ground motion in Canada from a random vibrations approach. *Bulletin, Seismological Society of America,* 74 (5), 2629-2653.

Atkinson, G.M. 1993. Earthquake source spectra in eastern North America, *Bulletin, Seismological Society of America,* 83 (6):1778-1755.

Atkinson, G.M. and D.M. Boore (1995). Ground-motion relations for eastern North America, *Bulletin, Seismological Society of America,* 85 (1):17-30.

Boore, D.M., and G.M. Atkinson (1987). Stochastic prediction of ground motion and spectral response parameters at hard-rock sites in eastern North America, *Bulletin, Seismological Society of America,* 77 (2):440-467.

Brune, J. (1970). Tectonic stress and the spectra of seismic shear waves from earthquakes, *J. Geoph. Res.*, **75,** 4997-5009.

Brune, J. (1971). Correction, *J. Geoph. Res.*, **76,** 5002.

Electric Power Research Institute (EPRI) (1993). *Guidelines for Site Specific Ground Motions.* Palo Alto, California: Electric Power Research Institute, November. TR-102293.

McGuire, R.K., G.R. Toro, and W.J. Silva (1988). *Engineering Model of Earthquake Ground Motion for Eastern North America.* Palo Alto, California: Electric Power Research Institute, October. NP-6074.

Ou, G.B., and R.B. Herrmann (1990). A statistical model for ground motion produced by earthquakes at local and regional distances, *Bulletin, Seismological Society of America,* **80,** 1397-1417.

Schneider, J.F., W.I. Silva, and P. Somerville (1996). Validation of ground motion models and modeling variability, submitted to *Earthquake Spectra.*

Silva, W.I., R. Pyke, R.R. Youngs, and I.M. Idriss (1996). Development of generic site amplification factors, submitted to *Earthquake Spectra.*

Toro, G.R., and R.K. McGuire (1987). An investigation into earthquake ground motion characteristics in eastern North America, *Bulletin, Seismological Society of America,* 77, 467-489.

Toro, G.R., N.A. Abrahamson, and J.F. Schneider (1996). Engineering model of strong ground motions from earthquakes in the central and eastern United States, submitted to *Earthquake Spectra.*

Youngs, R.R., N.A. Abrahamson, F.I. Makdisi, and K. Sadigh (1995). magnitude-dependent variance of peak ground acceleration, *Bulletin, Seismological Society of America,* **85**(4), 1161-1176.

FIGURE CAPTIONS

Figure 1. a) Stress-drop data (adjusted from Atkinson, 1993). b) Model of stress-drop uncertainty. Note: the total uncertainty (expressed as a standard deviation) is equal to the square root of the sum of the squares of the epistemic and aleatory uncertainties.

Figure 2. Regionalization of crustal structure for CENA. Attenuation equations are developed for the Mid-continent and Gulf crustal regions (regions 12 and 4, respectively). The equations for the Mid-continent are applicable to regions 1 through 3 and 5 through 16.

Figure 3. Attenuation equations for the Mid-continent region; predictions for 1-Hz and PGA.

Figure 4. Attenuation equations for the Gulf region; predictions for 1-Hz and PGA.

Figure 5. Contributors to aleatory uncertainty in ground-motion predictions. Results shown as functions of both distance and magnitude.

Figure 6. Contributors to epistemic uncertainty in ground-motion prediction. Results shown for equations in terms of both M and m_{Lg}. Also shown is the total uncertainty.

Figure 7. Comparison of ground-motion predictions (in terms of M) to ENA data. Dashed lines: $\pm\sigma_{aleatory}$ bounds; dots: $\pm\sigma_{aleatory+epistemic}$ bounds. See Table 6 for earthquake symbols.

Figure 8. Comparisons of ground-motion predictions for Midcontinent region to other attenuation equations for ENA.

Figure 9. Models of spatial variation of spectral acceleration as a function of frequency for a separation distance of 100 m. The open symbols are for soil sites and the solid symbols are for rock sites. Source: Abrahamson and Sykora (1993).

Figure 10. Magnitude dependence of uncertainty in ground motion for two soil sites with 75 m depths to bedrock and horizontal distances of 10 and 25 km from the source. The computed uncertainty includes the effects of uncertainty in stress drop and in soil properties. The total uncertainty remains fairly constant as magnitude (and ground-motion amplitude) increases, even though the effect of site response becomes more important. After Silva et al. (1996).

Note to typesetter: Please reduce figures in size as appropriate. I (G.R. Toro) have EPS files available for all figures except 2 and 9 and for Table 2. Please contact me (ph. 303-499-3000, e-mail toro@riskeng.com) if you want these.

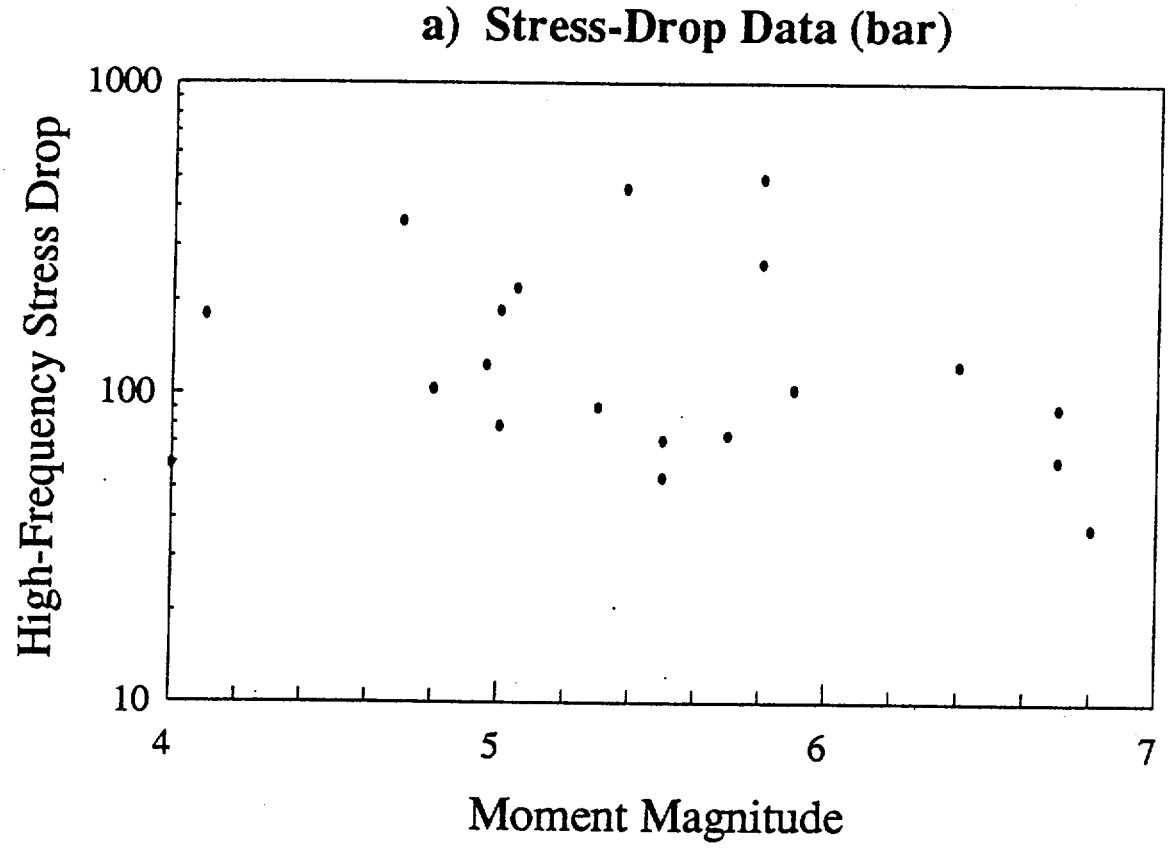
a) Stress-Drop Data (bar)
High-Frequency Stress Drop
1000
100
10
4
5
6
7
Moment Magnitude

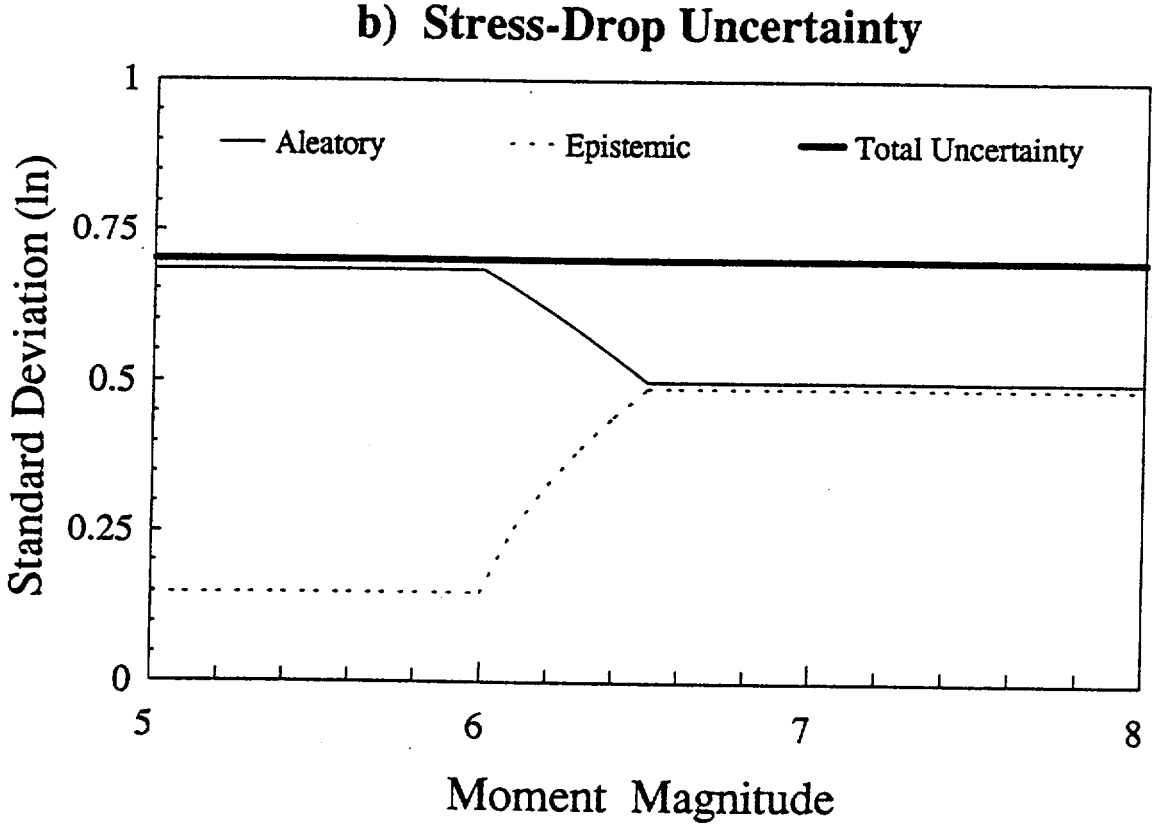
b) Stress-Drop Uncertainty
Standard Deviation (ln)
1
0.75
0.5
0.25
0
Aleatory
Epistemic
Total Uncertainty
5
6
7
8
Moment Magnitude

1

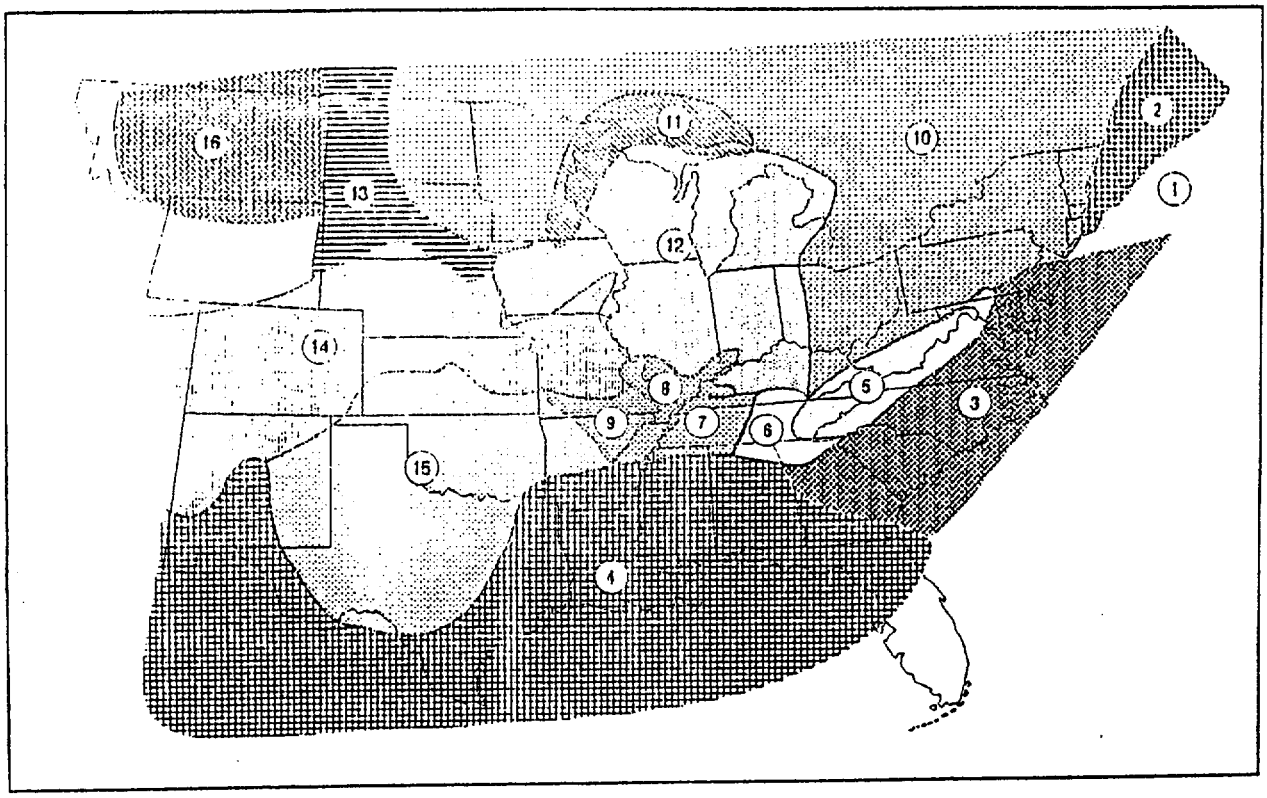
16
13
11
10
2
1
12
14
8
5
3
9
7
6
15
4

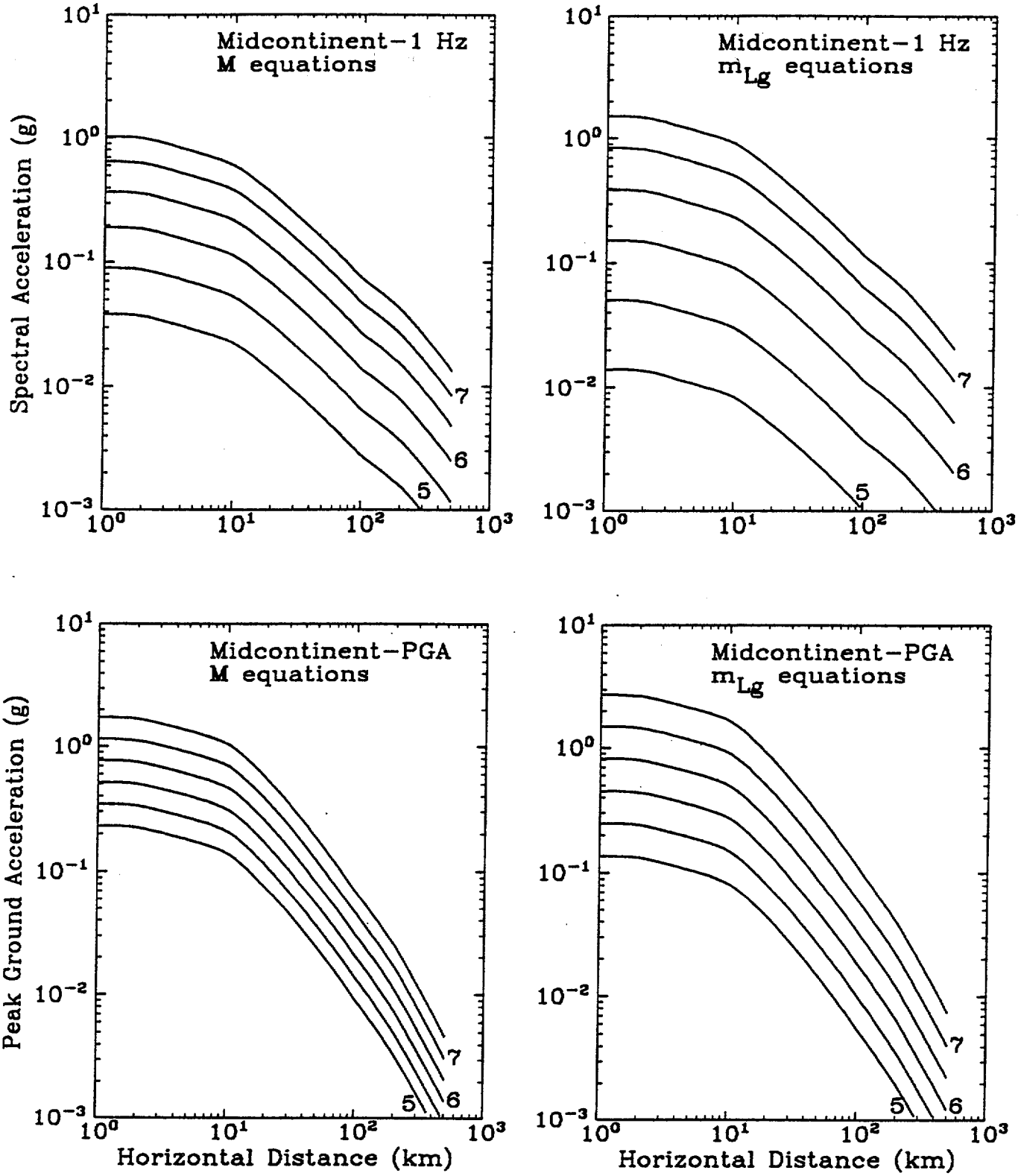
Midcontinent–1 Hz
M equations
Midcontinent–1 Hz
m_{Lg} equations
Midcontinent–PGA
M equations
Midcontinent–PGA
m_{Lg} equations
Spectral Acceleration (g)
Peak Ground Acceleration (g)
Horizontal Distance (km)
5
6
7

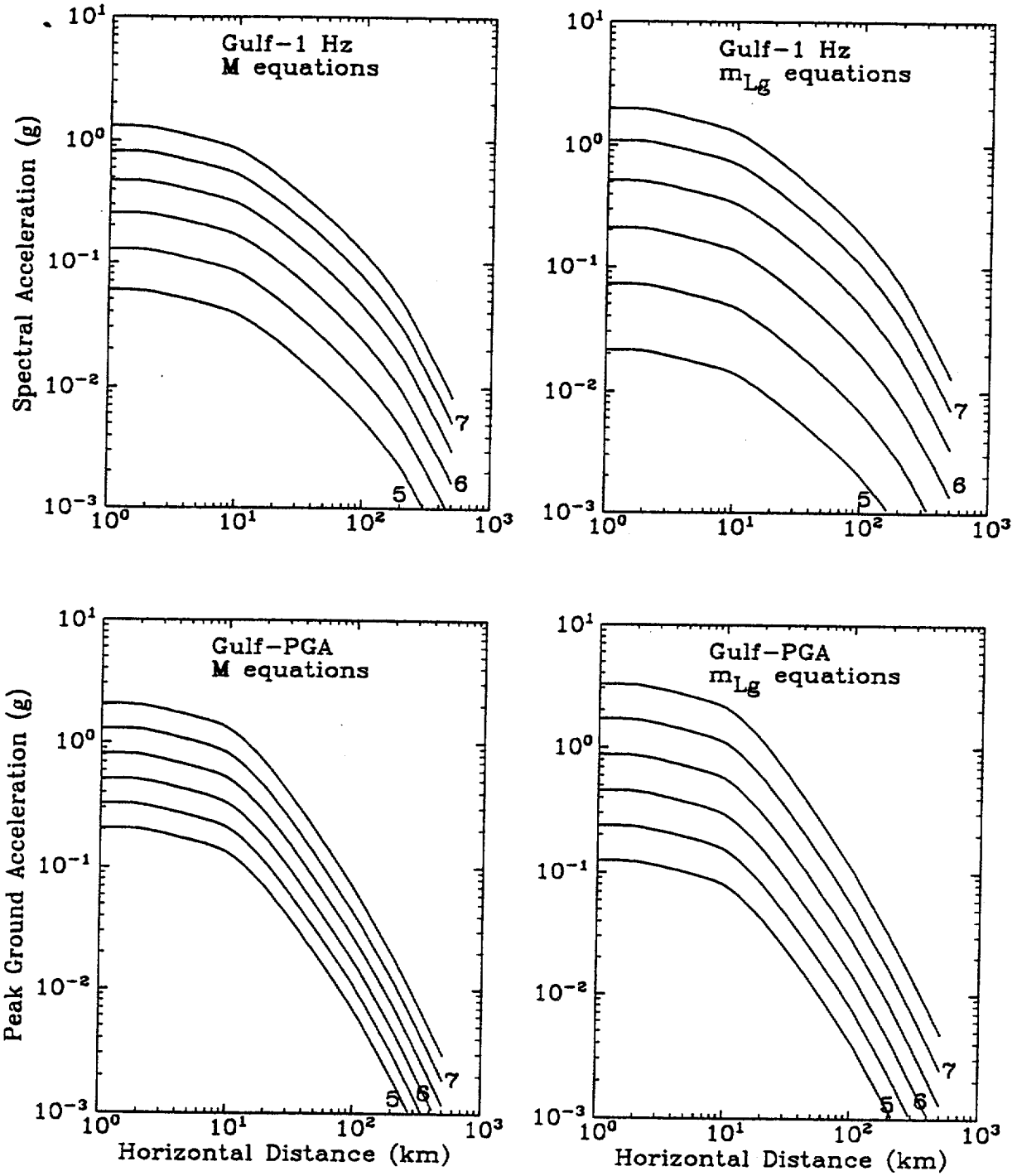
Gulf–1 Hz
M equations
Gulf–1 Hz
m_{Lg} equations
Gulf–PGA
M equations
Gulf–PGA
m_{Lg} equations
Spectral Acceleration (g)
Peak Ground Acceleration (g)
Horizontal Distance (km)
Horizontal Distance (km)
5
6
7

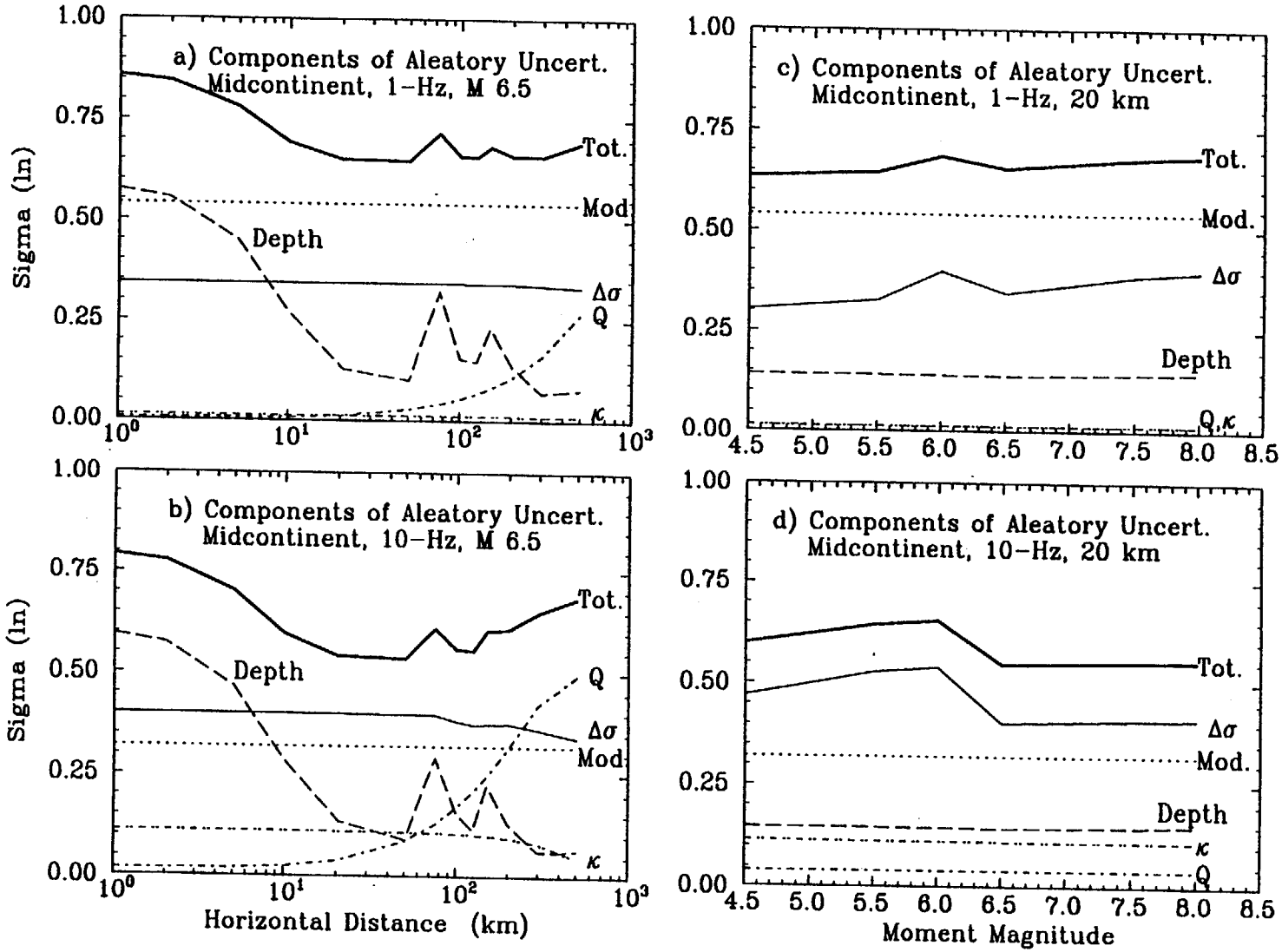
a) Components of Aleatory Uncert.
Midcontinent, 1-Hz, M 6.5
b) Components of Aleatory Uncert.
Midcontinent, 10-Hz, M 6.5
c) Components of Aleatory Uncert.
Midcontinent, 1-Hz, 20 km
d) Components of Aleatory Uncert.
Midcontinent, 10-Hz, 20 km
Sigma (ln)
Horizontal Distance (km)
Moment Magnitude
Tot.
Mod.
Depth
Δσ
Q
κ
Q,κ
1.00
0.75
0.50
0.25
0.00
10^0
10^1
10^2
10^3
4.5
5.0
5.5
6.0
6.5
7.0
7.5
8.0
8.5

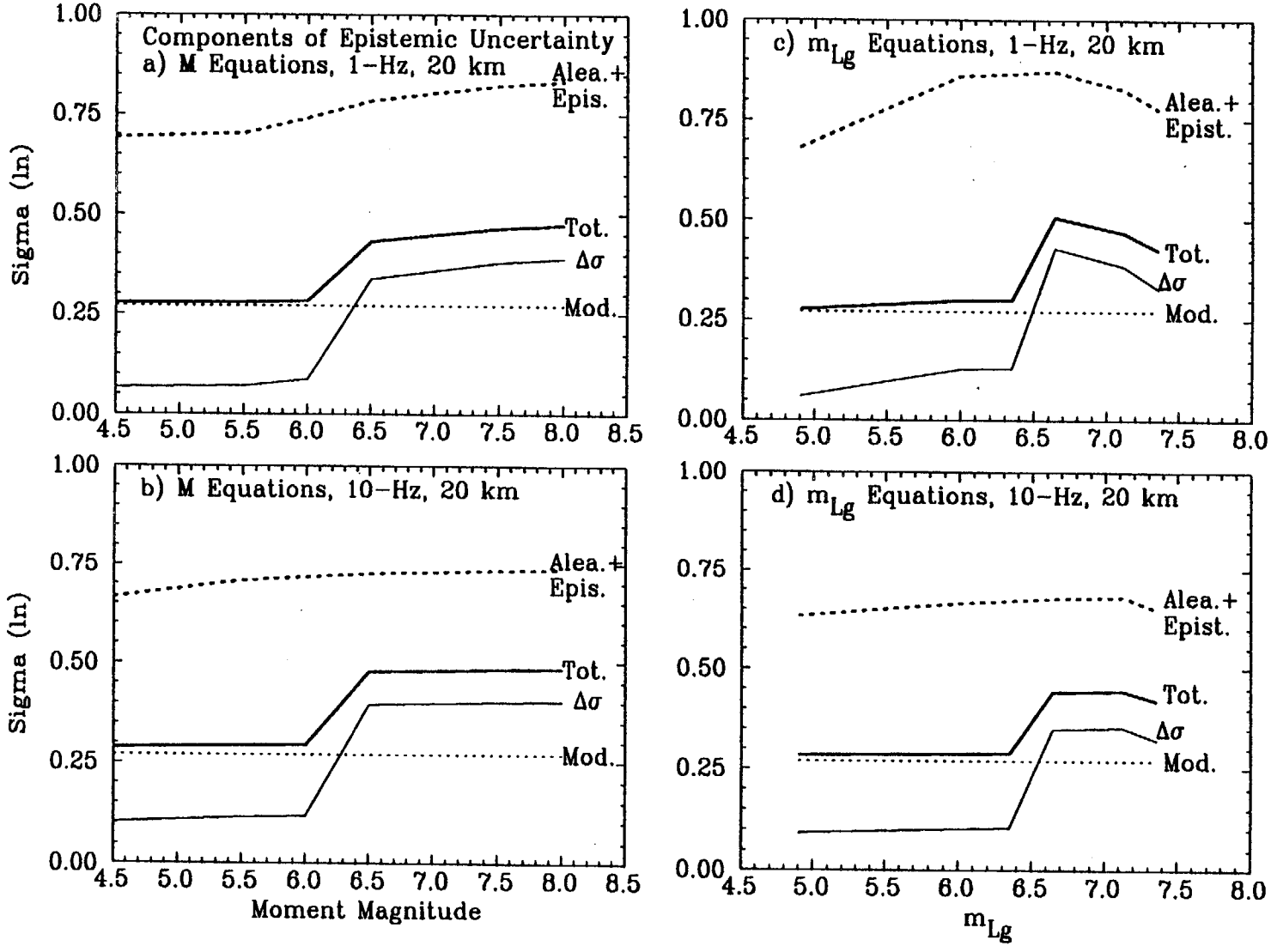
Components of Epistemic Uncertainty
a) M Equations, 1-Hz, 20 km
b) M Equations, 10-Hz, 20 km
c) m_{Lg} Equations, 1-Hz, 20 km
d) m_{Lg} Equations, 10-Hz, 20 km
Alea.+ Epis.
Alea.+ Epist.
Tot.
Δσ
Mod.
Sigma (ln)
Moment Magnitude
m_{Lg}
1.00
0.75
0.50
0.25
0.00
4.5
5.0
5.5
6.0
6.5
7.0
7.5
8.0
8.5

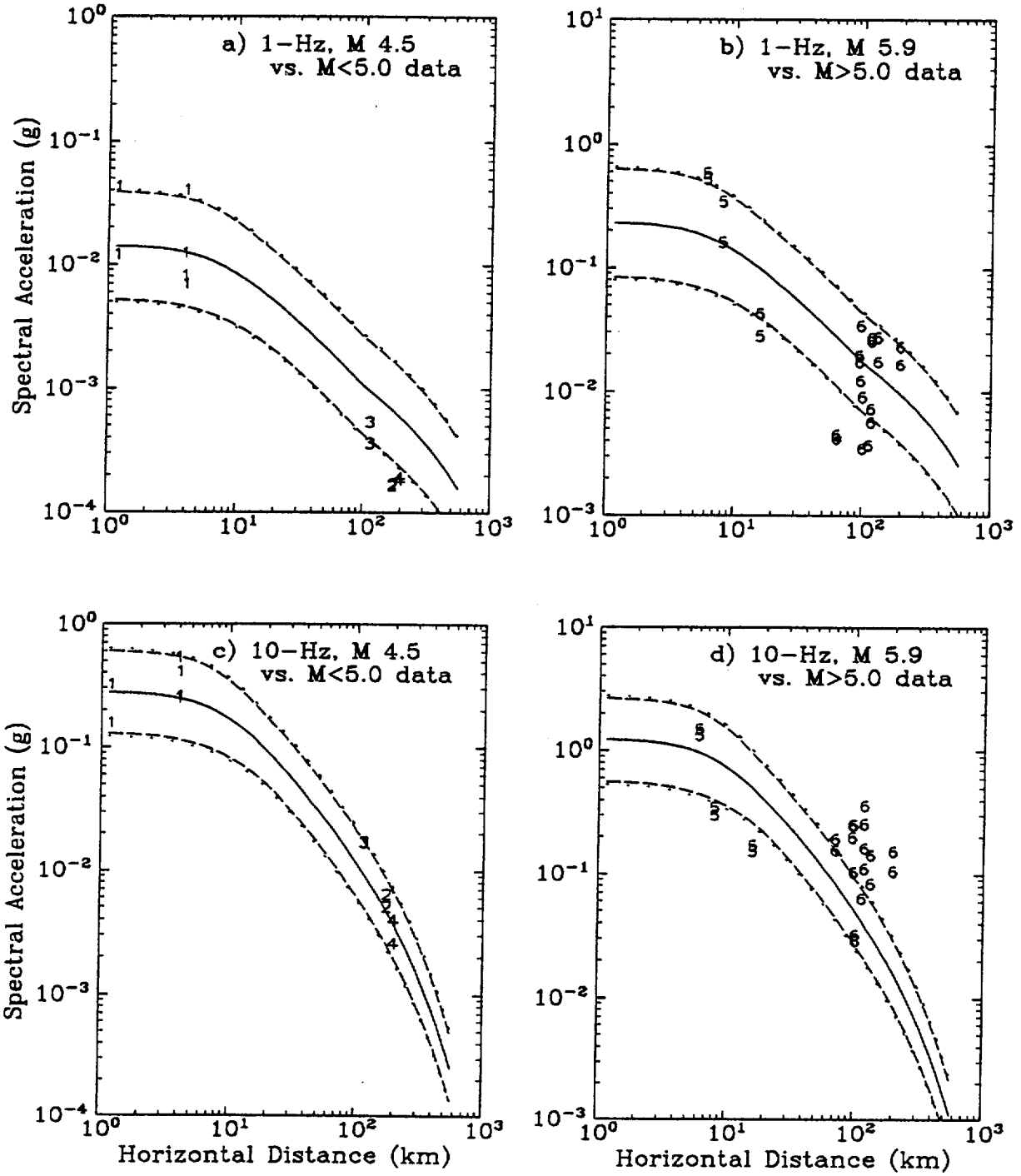
a) 1-Hz, M 4.5
vs. M<5.0 data
b) 1-Hz, M 5.9
vs. M>5.0 data
c) 10-Hz, M 4.5
vs. M<5.0 data
d) 10-Hz, M 5.9
vs. M>5.0 data
Spectral Acceleration (g)
Horizontal Distance (km)

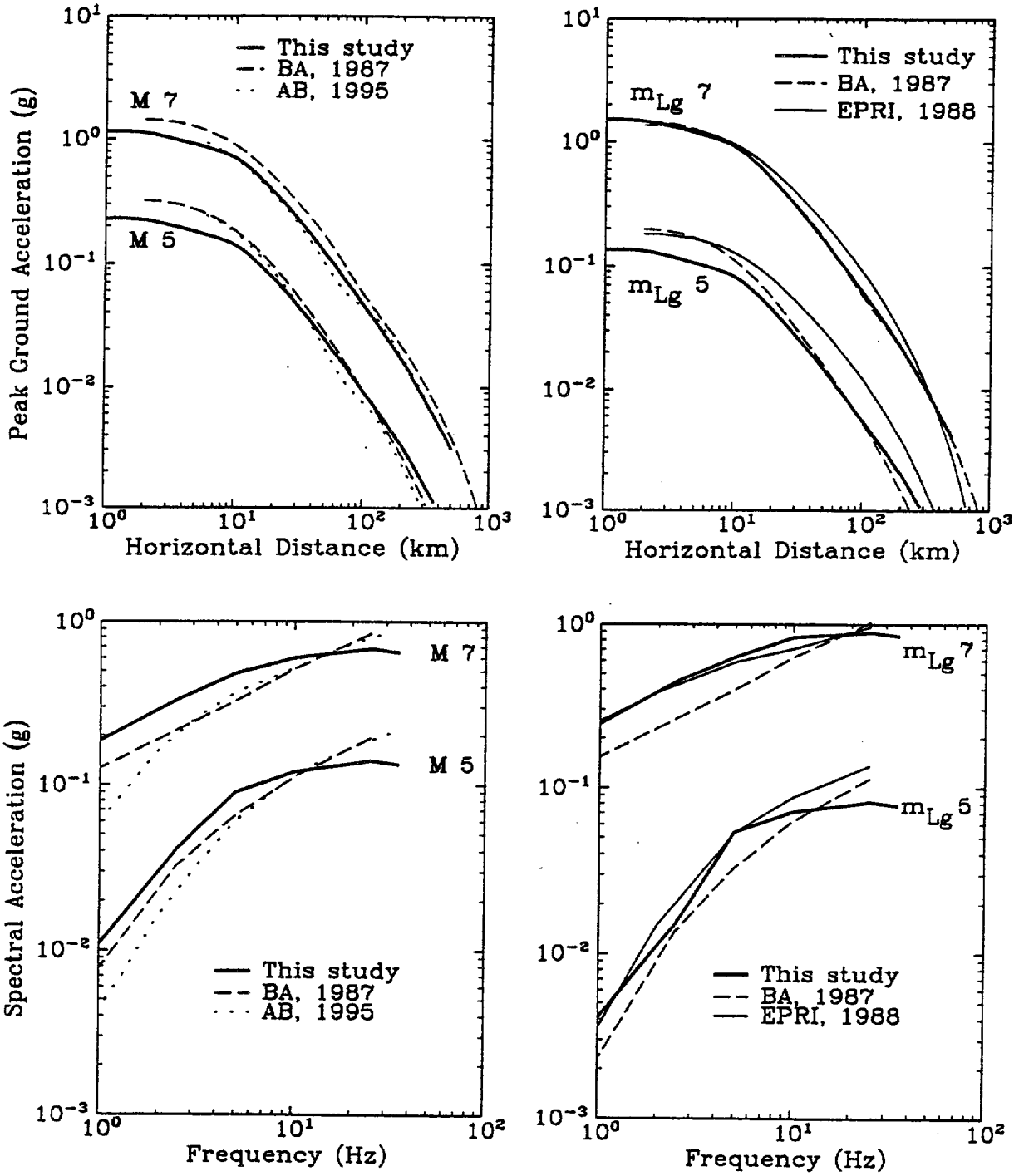
Peak Ground Acceleration (g)
Horizontal Distance (km)
This study
BA, 1987
AB, 1995
M 7
M 5
EPRI, 1988
m_{Lg} 7
m_{Lg} 5
Spectral Acceleration (g)
Frequency (Hz)

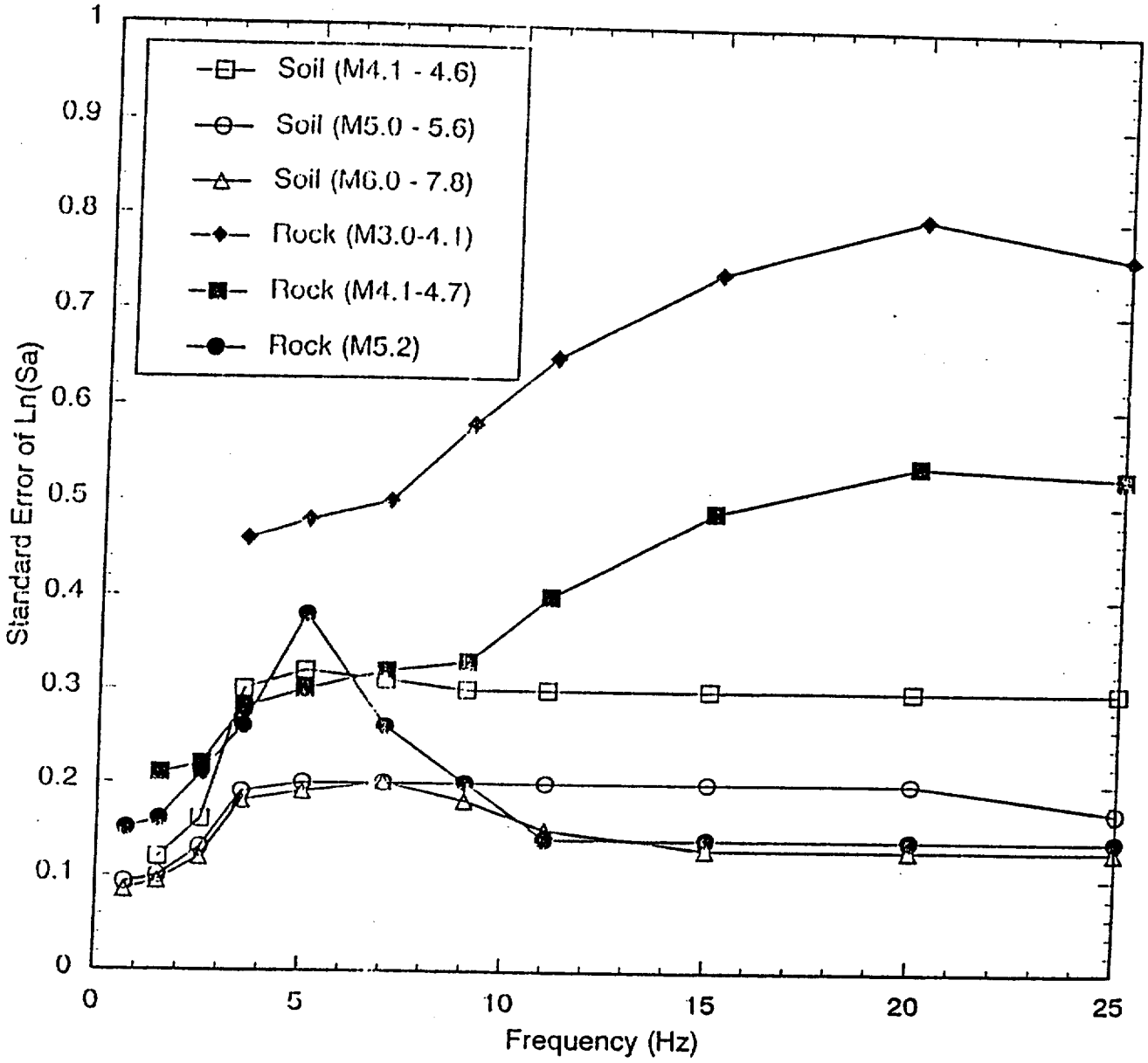
Soil (M4.1 - 4.6)
Soil (M5.0 - 5.6)
Soil (M6.0 - 7.8)
Rock (M3.0-4.1)
Rock (M4.1-4.7)
Rock (M5.2)
Standard Error of Ln(Sa)
Frequency (Hz)
0
0.1
0.2
0.3
0.4
0.5
0.6
0.7
0.8
0.9
1
0
5
10
15
20
25

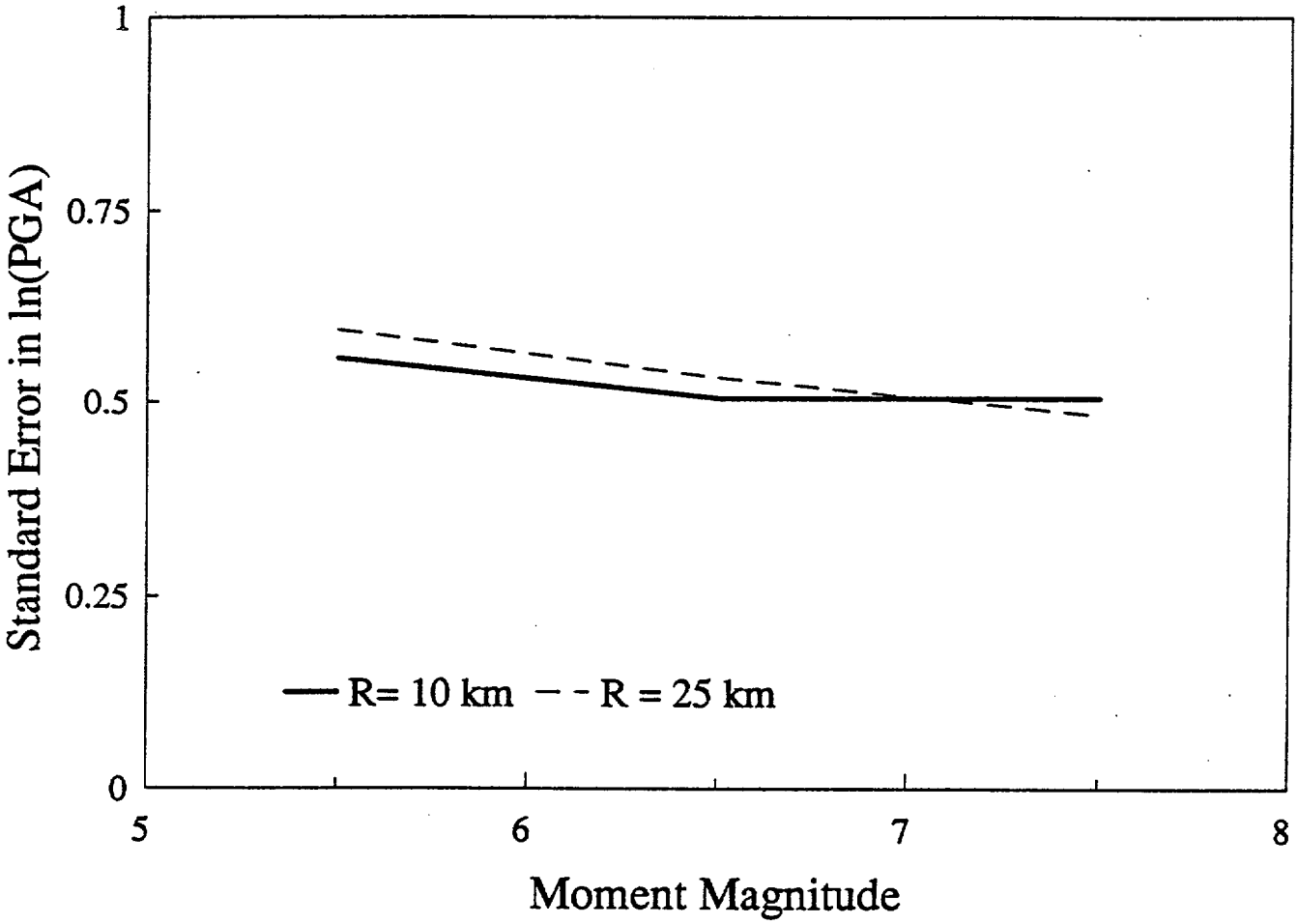
1
0.75
0.5
0.25
0
5
6
7
8
Standard Error in ln(PGA)
Moment Magnitude
R= 10 km
R = 25 km

GROUND MOTION CHARACTERIZATION WORKSHOP #2

Norm Abrahamson

9 January 1997

Ground Motion Characterization Approach

- Experts provide point estimates of ground motion for specified magnitudes and source-site geometries
  - Dipping normal (hanging wall and footwall)
  - Vertical strike slip

- Facilitation team fits equations to each experts estimates separately
  - Experts to define the distance measure to be used

- Experts to review fits to their point estimates
  - Fits to be revised if needed to gain experts approval

- 7 attenuation models provided to PSHA calculation team

Overview of Workshop #2

Describe what is required from each expert.
    Scope and schedule

Discuss the available ground motion models and scaling relations

Discuss sample application

Objectives:
By end of workshop, experts should have a clear understanding of what they need to provide, and a good idea of how they are going to make their estimates.

Experts Scope of Work

Point estimates of ground motions given:

- Magnitude
- Source-Site Geometry
  - Distance
  - Dip
  - Footwall / Hanging wall

4 Required Estimates:

- Median (m)
- Aleatory uncertainty (σ)
- Epistemic uncertainty in median (σ_m)
- Epistemic uncertainty in aleatory uncertainty (σ_s)

Site Condition

Hypothetical YM Rock Outcrop

- Velocity Profile: Repository outcrop (Vs=1900m/s at surface)

- Flat Topography

Ground Motion Parameters

Frequencies:	0.5, 1.0, 2.0, 5.0, 10.0, 20.0 Hz; PGA and PGV
Components:	Average Horizontal, Vertical
Sources:	60 degree Normal (hanging wall and footwall) vertical strike-slip

MAGNITUDE/DISTANCE POINT ESTIMATES

Distance[1]	Shallow Focus[2]		Deep Focus[2]					
(km)	M5.0	5.8	5.0	5.8	6.5	7.0	7.5	8.0
1	x	x	x	x	x	x	x	
3				x	x			
5	x				x	x		
10	x	x	x	x	x	x	x	
20	x				x			
50	x	x	x	x	x	x	x	x
100					x			x
160	x				x	x		x

[1] Horizontal distance from surface expression of fault (up-dip extension).
[2] Shallow focus is centered at 5 km depth, deep focus extends to 14 km depth.

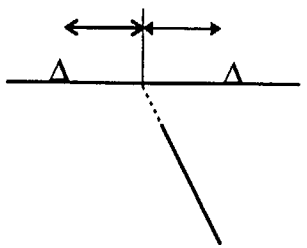

Suggestions for Keeping the Workload Manageable:

35 (M, Dist) pairs
x 3 source types (Normal HW, Normal FW, strike-slip)
x 8 Ground motion parameters
x 2 components
= 1680 combinations

Develop methods (rules) for estimating ground motions for a few magnitude/distance/frequency combinations

Estimate ground motions at other points following the rules

Adjust estimates for special cases (where particular models break down)

Documentation

Need to document reasoning behind development of estimates

Eliciation will help the documentation process.

Expert Elicitation

One-on-one elication for each expert

Subset of about 5 magnitude-distance pairs for elicitation
(3 freq, 2 comp, 2 sources) = 60 total combinations
- note any important differences in approach for other magnitude and distance pairs

Provides a starting point for the documentation

Checks for inconsistencies

Feedback Workshop

Experts to explain/defend their judgements

Faciliation Team will make comparisons of estimates

- Between experts
- Mag, Dist, Freq scaling for individual experts

Outliers will be identified for discussion at the Feedback Workshop

Schedule

Jan 8-10	Workshop #2: Methods and Models
Jan 31	Additonal proponent model calculations completed and sent to experts
Feb 28	Experts preliminary estimates of ground motions complete
Mar 10	Preliminary attenuation relations to PSHA Calc Team
Mar 10-28	Elicitations
Apr 14-15	Workshop #3: Feedback
May 2	Experts final estimates of ground motion complete
May 9	Attenuation relations sent to experts for review
May 16	Final attenuation relations sent to PSHA Calc Team
Jun 9	Expert's documentation due

Yucca Mtn Site Specific Issues

Source Issues

Are ground motions from normal faulting events different from typical CA strike-slip events?

- Foam rubber modeling
- Spudich extensional data base
- Stress drop estimates (from corner freq)
- Static stress drop dependence on slip rate

Effect of shallow slip for sites at short distances

Site Issues

Low kappa at YM

Non-linear response of YM tuff vs CA rock

Path Issues

Q

2-D Effects from Blast data

CHARACTERIZATION OF

UNCERTAINTY

IN GROUND-MOTION PREDICTIONS

Presentation to

Yucca Mountain Seismic Hazard Study
Ground Motion Workshop No. 2
Salt Lake City, Utah
January 9, 1996

by

Gabriel R. Toro
Risk Engineering, Inc.
4155 Darley Ave., Suite A
Boulder, Colorado 80303

BACKGROUND

- Natural tendency among analysts: concentrate on obtaining best estimates of ground motion amplitudes; quantification of uncertainty is often an afterthought.

- This tendency appears to be counter-intuitive, because a deterministic estimate has a higher information content (i.e., it implies we know more).

- Uncertainty estimates are required in PSHA because our knowledge of earthquakes is limited and the data we have shows significant scatter. Estimates of ground-motion amplitude (given magnitude and distance) for PSHA must also include quantification of the associated uncertainties.

DEFINITIONS (1)

Types of uncertainty from the point of view of seismic-hazard analyst:

Epistemic Uncertainty. Uncertainty that is due to incomplete knowledge and data about the physics of the earthquake process. In principle, epistemic uncertainty can be reduced by the collection of additional information.

Aleatory Uncertainty. Uncertainty that is inherent to the unpredictable nature of future events. It represents unique (small-scale) details of source, path, and site response that cannot be quantified before the earthquake occurs. Given a model, one cannot reduce the aleatory uncertainty by collection of additional information. One may be able, however, to better quantify the randomness by using additional data.

Notes:

1. Distinction is model dependent

2. $[\text{Epistemic}^2 + \text{Aleatory}^2]^{1/2} = \text{Uncertainty (or total uncertainty)}$

3. Alternative Terminology
   Epistemic Uncertainty: uncertainty
   Aleatory Uncertainty: randomness

RATIONALE/HISTORY FOR DISTINCTION

- Introduced in WASH-1400 Reactor Safety study and used in most advanced PSHA studies (especially those associated with PRA studies).

- Useful to know how much of the uncertainty can be reduced with additional study (money, time).

- Useful to know how much the perception of the hazard may change over a certain time period (e.g., design life of surface facilities)

- Aversion to epistemic uncertainty (a departure from classical decision theory): decision-makers prefer chance over ignorance

- Aleatory/Epistemic distinction is not clear-cut (it depends on the models adopted). One could argue that all uncertainty in ground motion and in seismic hazard is epistemic.

- Separate treatment of epistemic and aleatory uncertainties places additional burdens on the experts, increases the difficulty of PSHA calculations by at least one order of magnitude, and may lead to loss of transparency.

Personal perspective: Labeling of different sources of uncertainty is important so that we can identify and quantify all contributors to uncertainty.

EVOLUTION OF SEISMIC HAZARD OVER PROJECT'S DESIGN LIFE

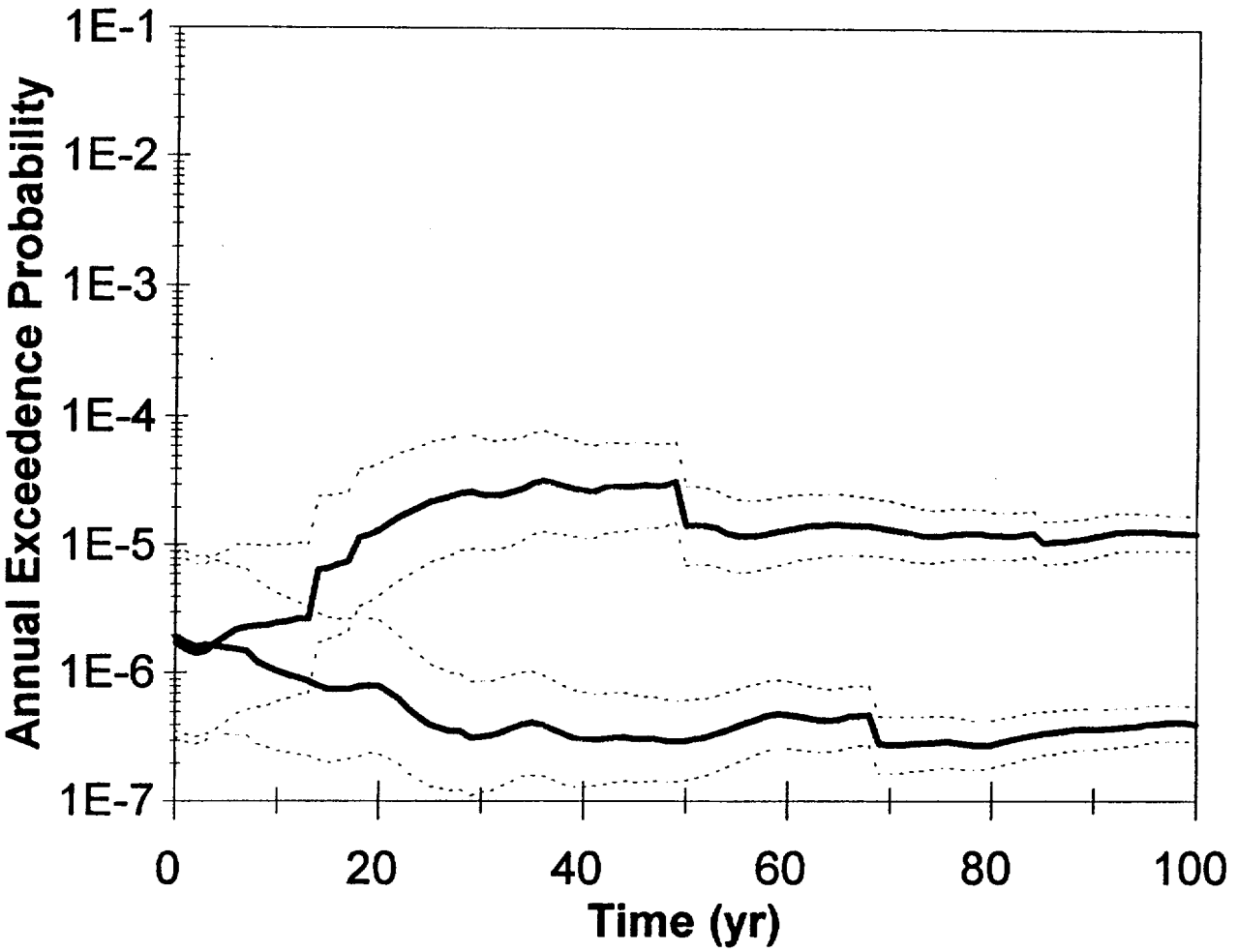

DEFINITIONS (2)

Partition of uncertainty from the point of view of ground-motions analyst

Parametric Uncertainty. Represents variability in the values of model parameters (e.g., stress drop, anelastic attenuation, slip distribution) of future earthquakes. Parametric uncertainty is quantified by observing the variation in parameters inferred (usually in an indirect manner) for several earthquakes and/or several recordings.

Modeling Uncertainty. Represents differences between the actual physical process that generates the strong earthquake ground motions and the simplified model used to predict ground motions. Modeling uncertainty is estimated by comparing model predictions to actual, observed ground motions.

Note: Parametric/Modeling partition is model-dependent.

DEFINITIONS (3)

Partitions are not different; they are orthogonal (or complementary):

		Seismic-Hazard Analyst	
		Epistemic	Aleatory
Ground-Motion Analyst	Modeling	Uncertainty about the true model bias (i.e, to what extent model has a tendency to over- or under-predict observations)	Unexplained scatter due to physical processes not included in the model (e.g., slip distribution, crustal heterogeneity)
	Parametric	Uncertainty about probability distributions of model parameters (e.g., what is the median stress drop for Basin and Range events)	Event-to-event variation in model parameters (e.g., stress drop or focal depth, etc)

EXAMPLES OF PARAMETRIC AND MODELING UNCERTAINTY

EMPIRICAL ATTENUATION EQUATIONS

Epistemic Uncertainty: traditionally quantified by using several attenuation equations developed empirically by different investigators (using different data sets, functional forms, fitting procedures, etc.).

Typical California application:

Boore, Joyner, and Fumal	1/4
Campbell	1/4
Idriss	1/4
Sadigh	1/4

Within-model epistemic uncertainty: represented by the standard errors of estimation of the regression coefficients (and their correlation matrix) [rarely considered in empirical models].

Aleatory Uncertainty. Quantified by the residual standard deviation σ from the regression calculations. It represents the scatter in observed ground motions for a given magnitude and distance. Typically, σ is assumed to be constant, but some recent studies find that σ depends on magnitude.

STOCHASTIC POINT-SOURCE MODEL

Physical Parameters that appear explicitly:

1. Moment magnitude and distance
2. Asperity depth (i.e., depth at which the equivalent point source is located)
3. Stress drop (or more generally, FA(f) given M_0)
4. Crustal s-wave velocity structure
5. Q
6. Site kappa

STOCHASTIC POINT-SOURCE MODEL (continued)

Options in Treatment of Physical Parameters

1. Parameter is treated as known

   PSHA - M, R are independent variables (PSHA integrates over them)

   Scenario earthquake: other quantities may be known (e.g., azimuth)

2. Parameter is treated as uncertain from event to event or site to site (e.g., stress drop)

   - Quantify aleatory uncertainty in parameter (distribution of parameter)

   - Quantify epistemic uncertainty about the probability distribution of parameter

3. Parameter is treated as fixed (e.g., crustal velocity structure)

   - Aleatory uncertainty is picked in modeling aleatory uncertainty

   - Epistemic uncertainty is picked in modeling epistemic uncertainty (additional epistemic uncertainty may arise if there are issues of regional transportability of the parameter).

STEPS IN THE CALCULATION OF VARIABILITY
(Example: EPRI, 1993)

Idealized Situation: One data set (from the region of interest) and one model are used to characterize all sources of uncertainty:

Invert data from many events:

Find optimal values of free parameters (stress drop, etc.), so that $\Sigma(\text{obs} - \text{predicted})^2$ is minimized.

$\Sigma(\text{obs} - \text{predicted})^2$ --> modeling uncertainty

values of optimal parameter values
from many events: --> distributions of parameters

STEPS IN THE CALCULATION OF UNCERTAINTY (cont'd)

MODELING UNCERTAINTY

Compare observations to model predictions; examine residuals

$$\varepsilon_{ij} = \ln[Amplitude(\text{event } i,\ \text{site } j)_{\text{observed}}] - \ln[Amplitude(M_i, R_{ij},\ \text{optimal params.})_{\text{predicted}}]$$

Model bias

$$\mu(f) = \frac{1}{n} \sum_{i\ (\text{events})} \sum_{j\ (\text{sites})} \varepsilon_{ij}(f)$$

bias-corrected variance

$$\sigma_\varepsilon(f) = \sqrt{\frac{1}{n-1} \sum_{i\ (\text{events})} \sum_{j\ (\text{sites})} \left(\varepsilon_{ij}(f) - \mu(f)\right)^2} = \text{modeling aleatory uncertainty}$$

Modeling epistemic uncertainty (i.e., how well we know the model bias):

$$\frac{\sigma_\varepsilon(f)}{\sqrt{n_{\text{independent observations}}}}$$

Another consideration: higher bias implies less confidence in model

STEPS IN THE CALCULATION OF UNCERTAINTY (cont'd)

PARAMETRIC UNCERTAINTIES

1. Quantification of the uncertainty (both aleatory and epistemic) in the model parameters.

   From inversion results or other datasets

   From other studies + subjective weights

2. Propagation of uncertainties in model parameters into uncertainty in ground-motion amplitude. Again, this must be done for both aleatory and epistemic uncertainty.

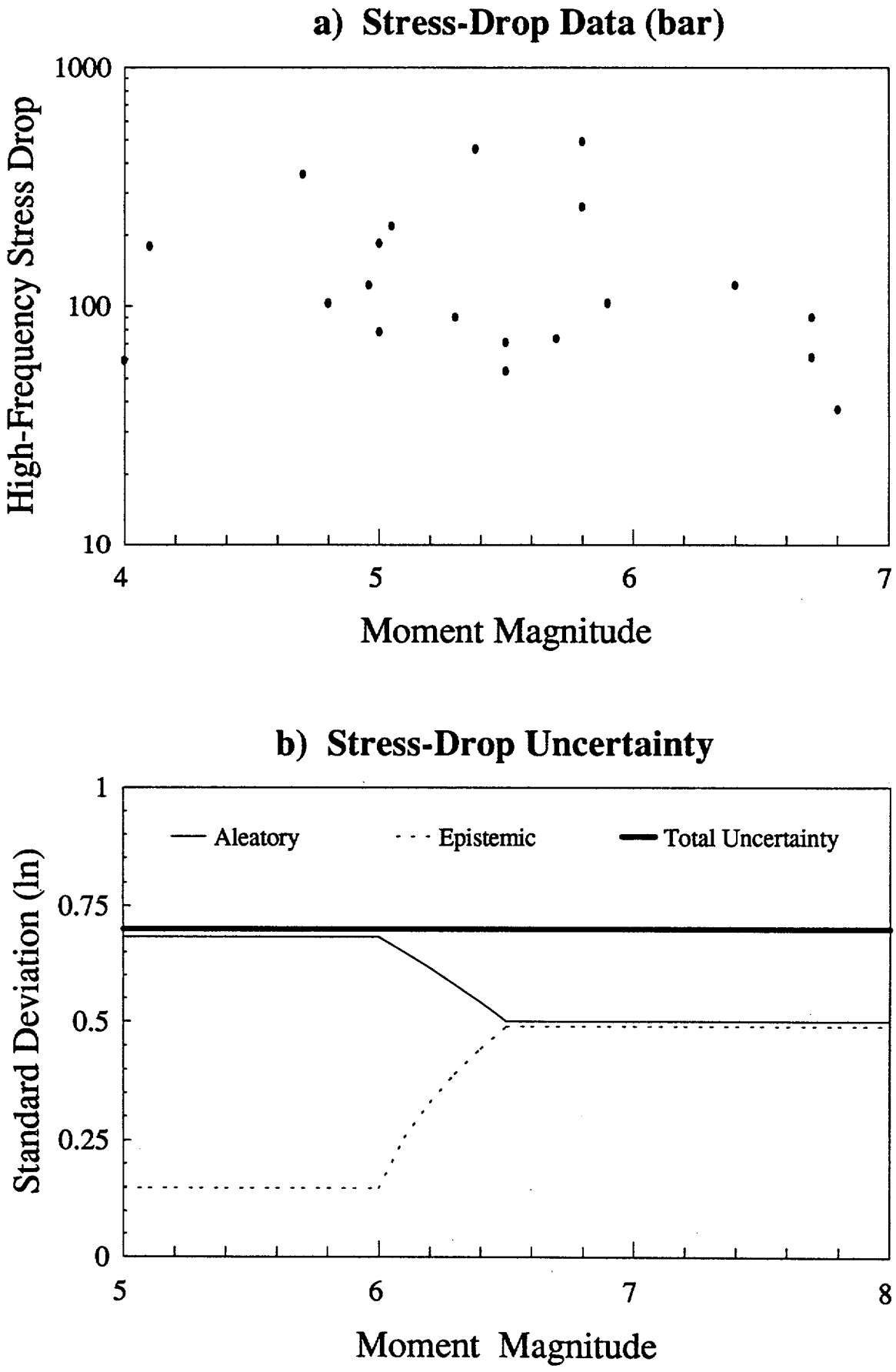
a) Stress-Drop Data (bar)
High-Frequency Stress Drop
1000
100
10
4
5
6
7
Moment Magnitude
b) Stress-Drop Uncertainty
Standard Deviation (ln)
1
0.75
0.5
0.25
0
Aleatory
Epistemic
Total Uncertainty
5
6
7
8
Moment Magnitude

PARAMETER DISTRIBUTION DETERMINED FROM OTHER DATA SETS

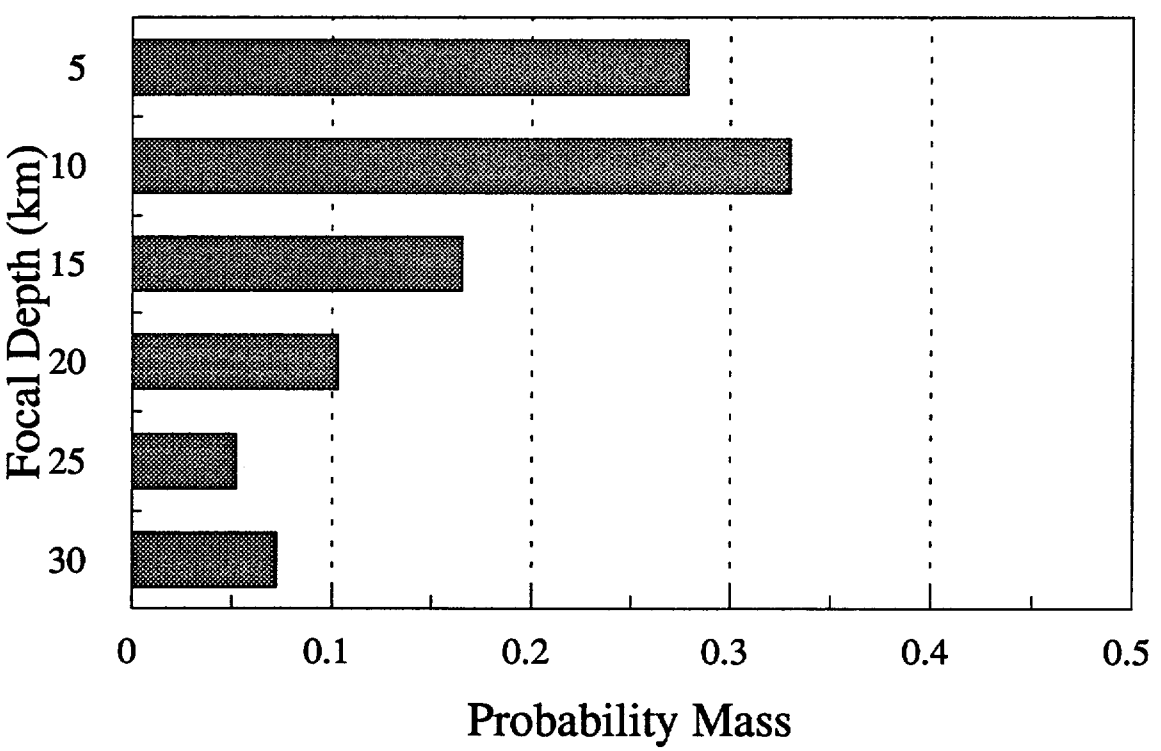

PARAMETER DISTRIBUTION BASED ON

OTHER STUDIES AND JUDGMENT

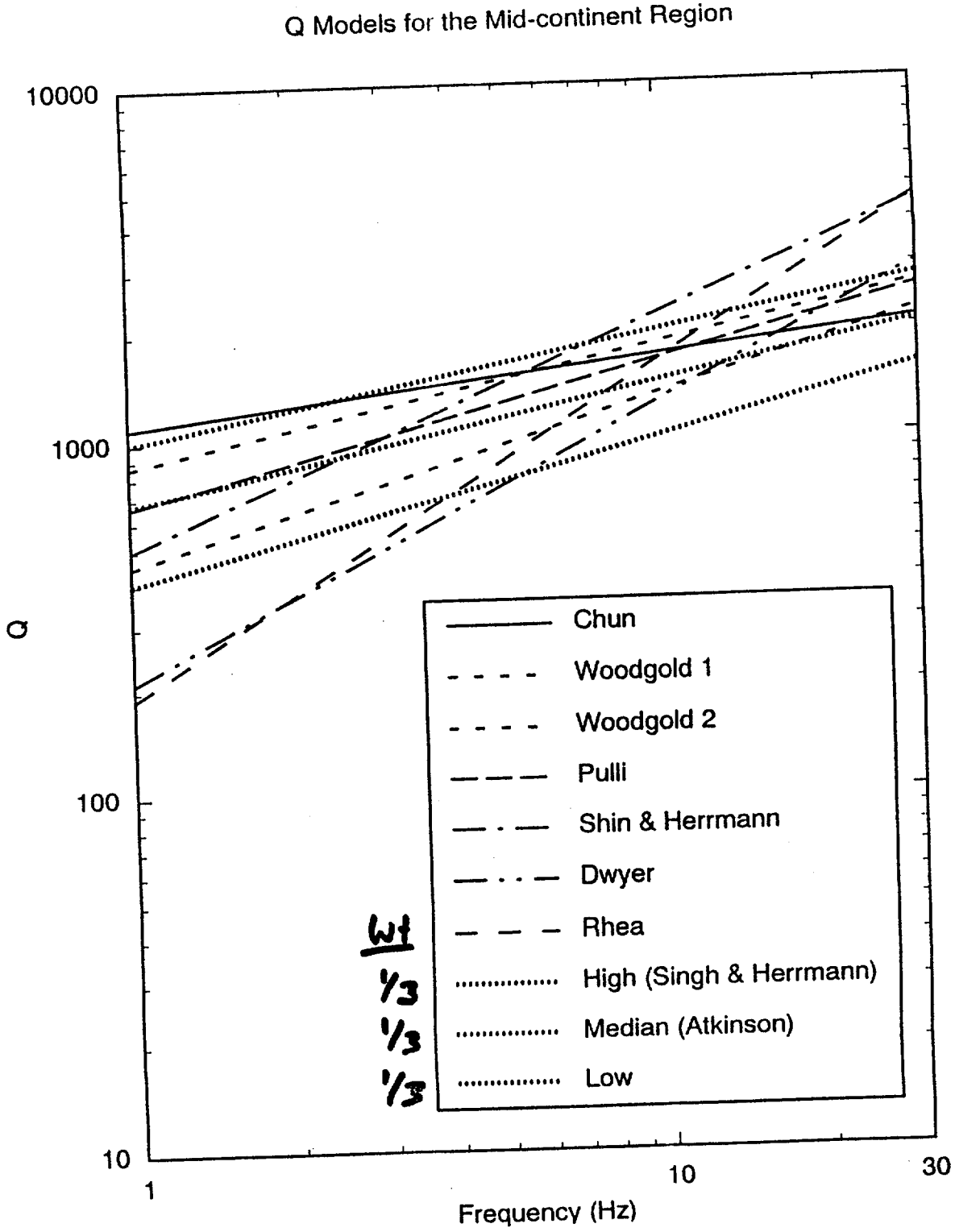

Figure 5-50. Q models for the Mid-continent region. The dashed lines are the median, high, and low Q models used to generate the ground motions analyzed in Section 9.

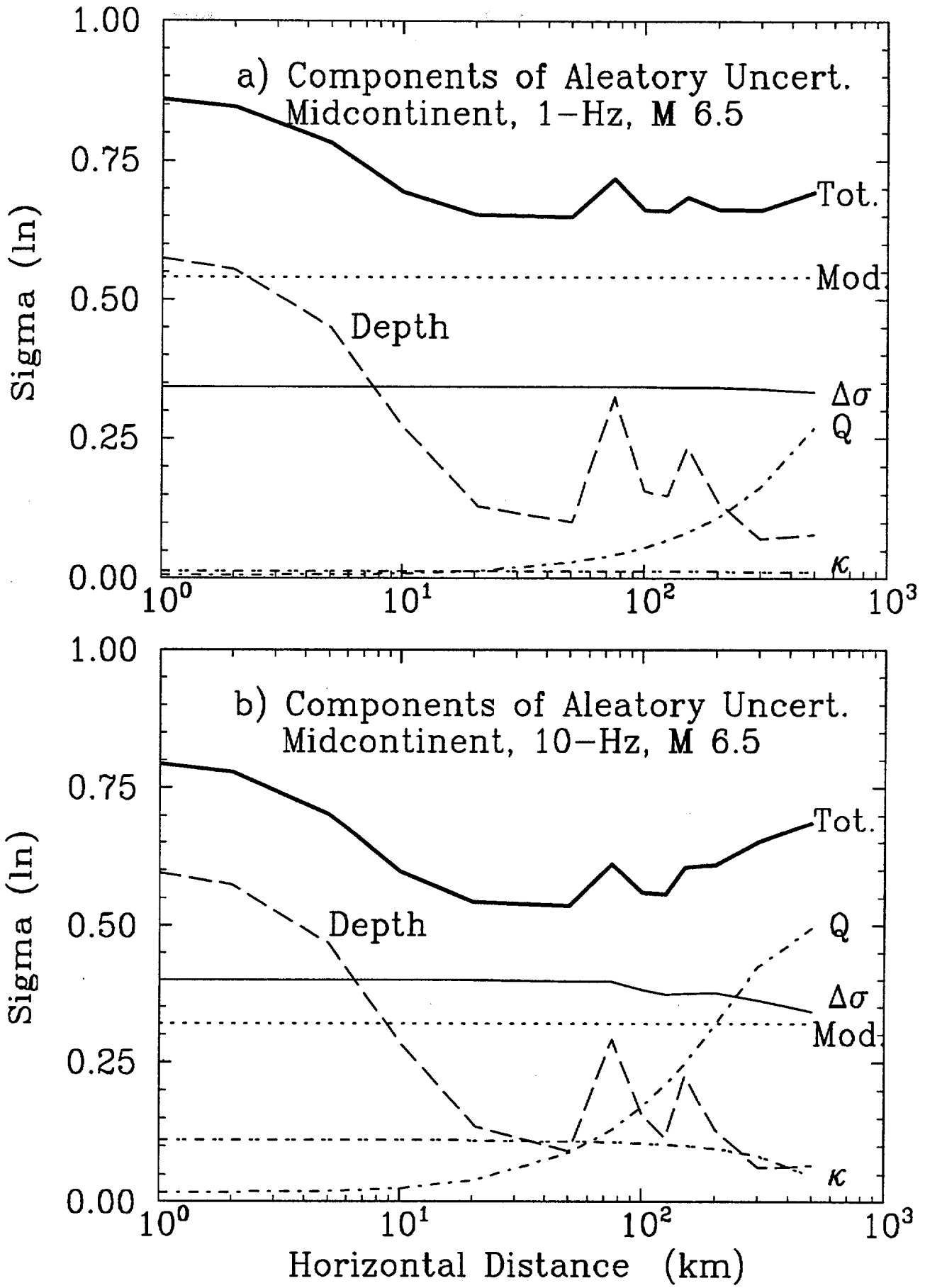
a) Components of Aleatory Uncert.
Midcontinent, 1−Hz, M 6.5
b) Components of Aleatory Uncert.
Midcontinent, 10−Hz, M 6.5
Sigma (ln)
1.00
0.75
0.50
0.25
0.00
Tot.
Mod.
Depth
Δσ
Q
κ
10^0
10^1
10^2
10^3
Horizontal Distance (km)

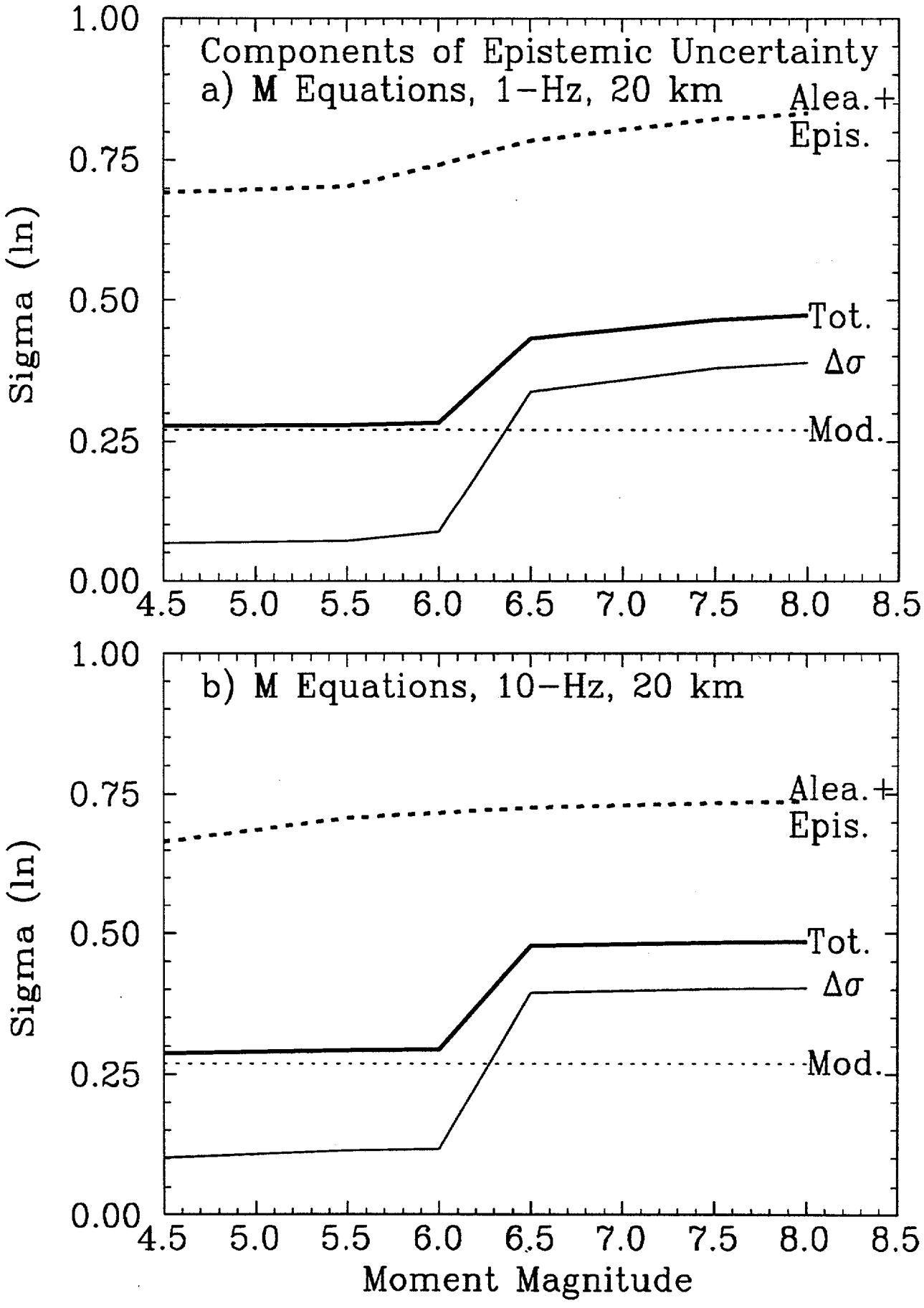
Components of Epistemic Uncertainty
a) M Equations, 1-Hz, 20 km
Alea.+ Epis.
Tot.
Δσ
Mod.
b) M Equations, 10-Hz, 20 km
Alea.+ Epis.
Tot.
Δσ
Mod.
Sigma (ln)
1.00
0.75
0.50
0.25
0.00
4.5
5.0
5.5
6.0
6.5
7.0
7.5
8.0
8.5
Moment Magnitude

SHALLOW FOCUS, M=5.0

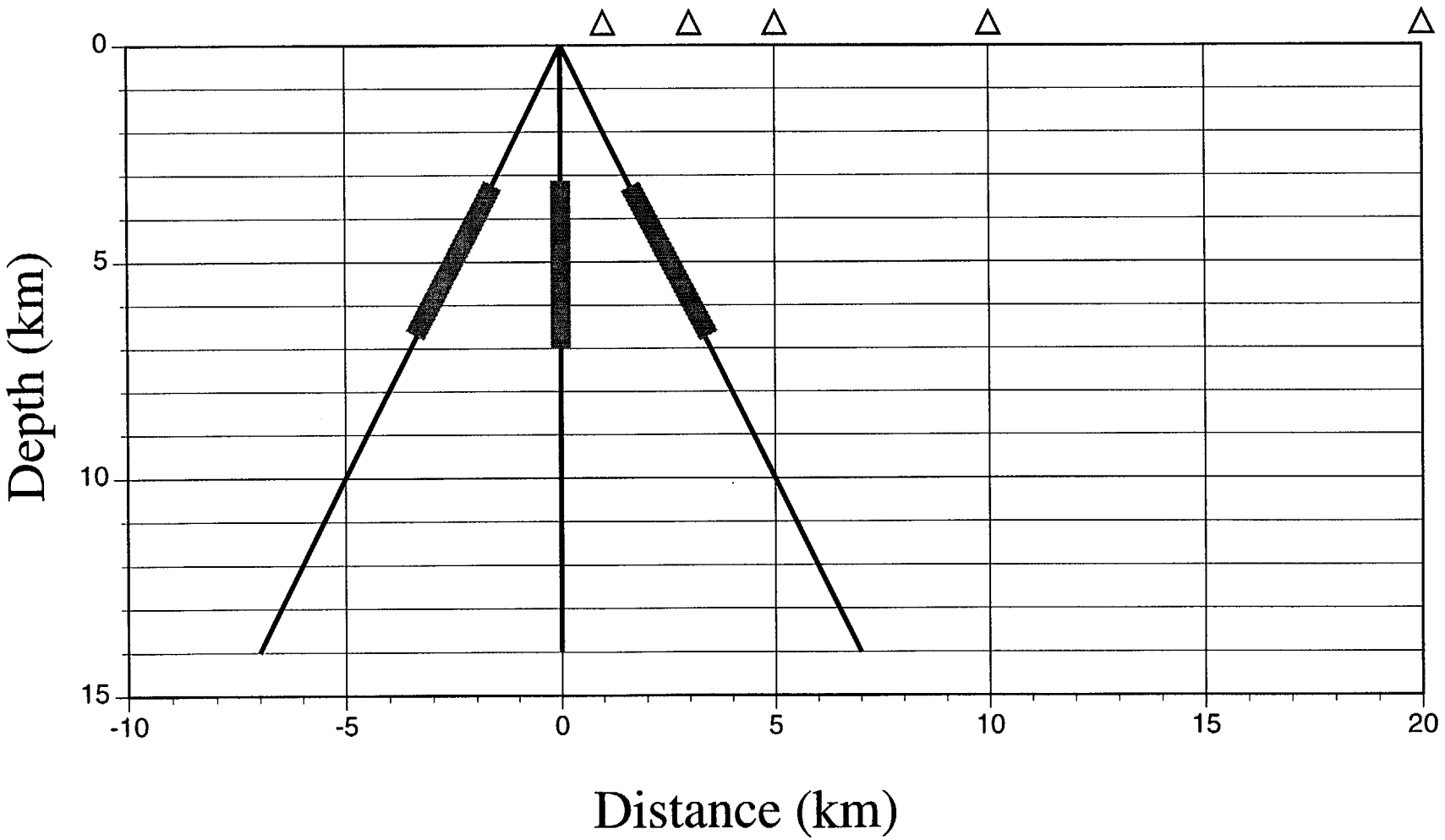

SHALLOW FOCUS, M=5.8

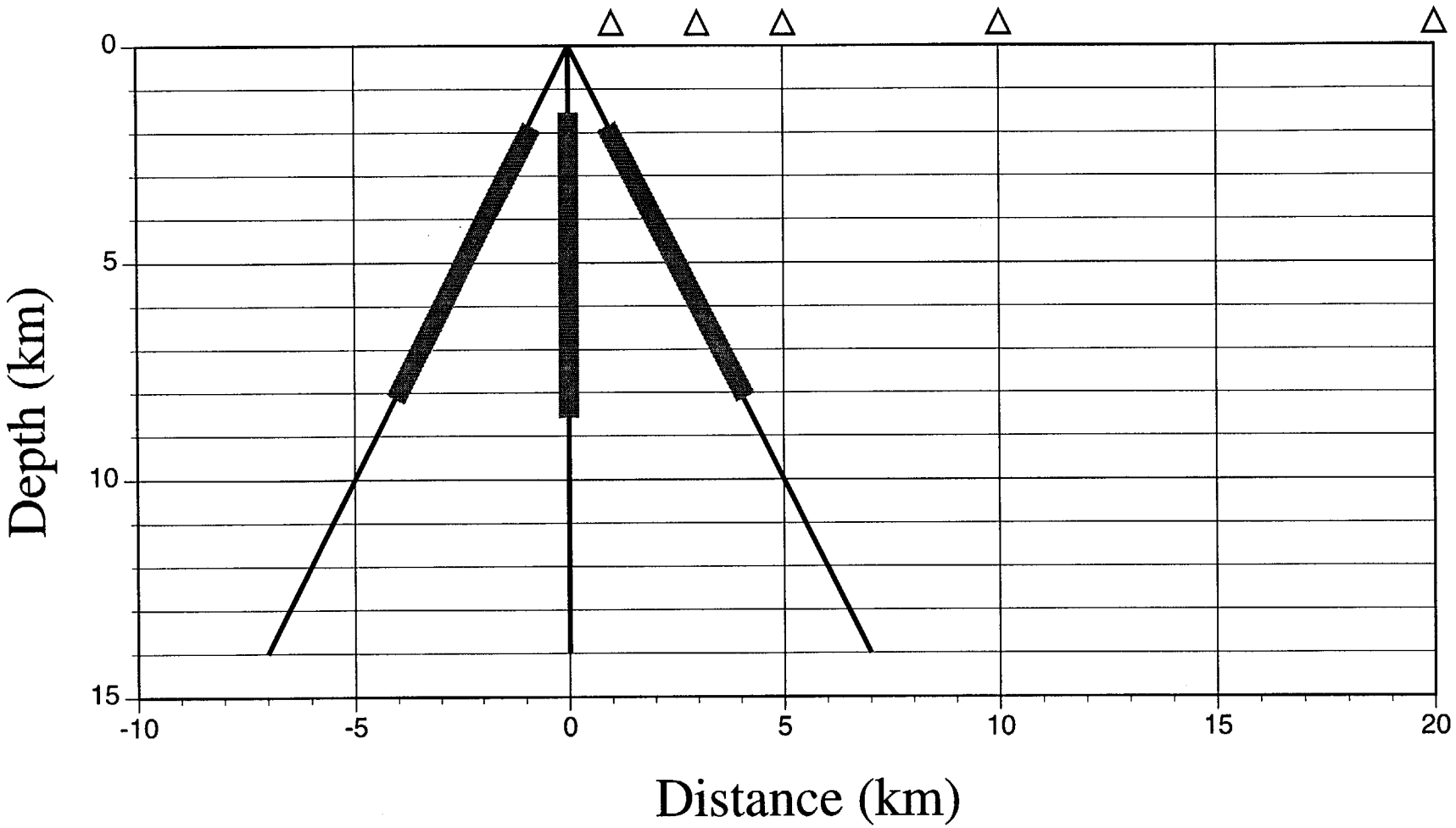

DEEP FOCUS, M=5.0

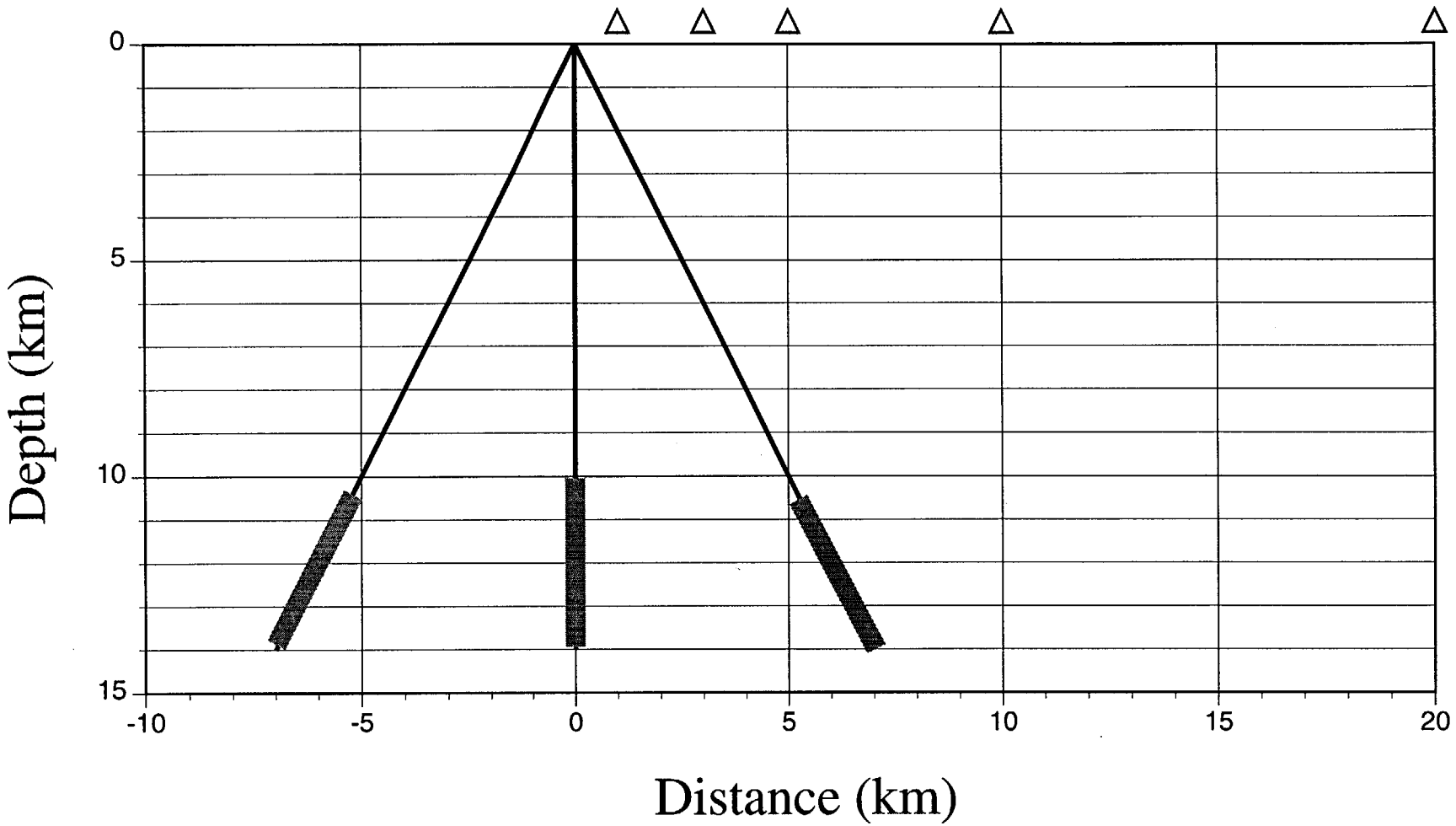

SHALLOW FOCUS, M=5.8

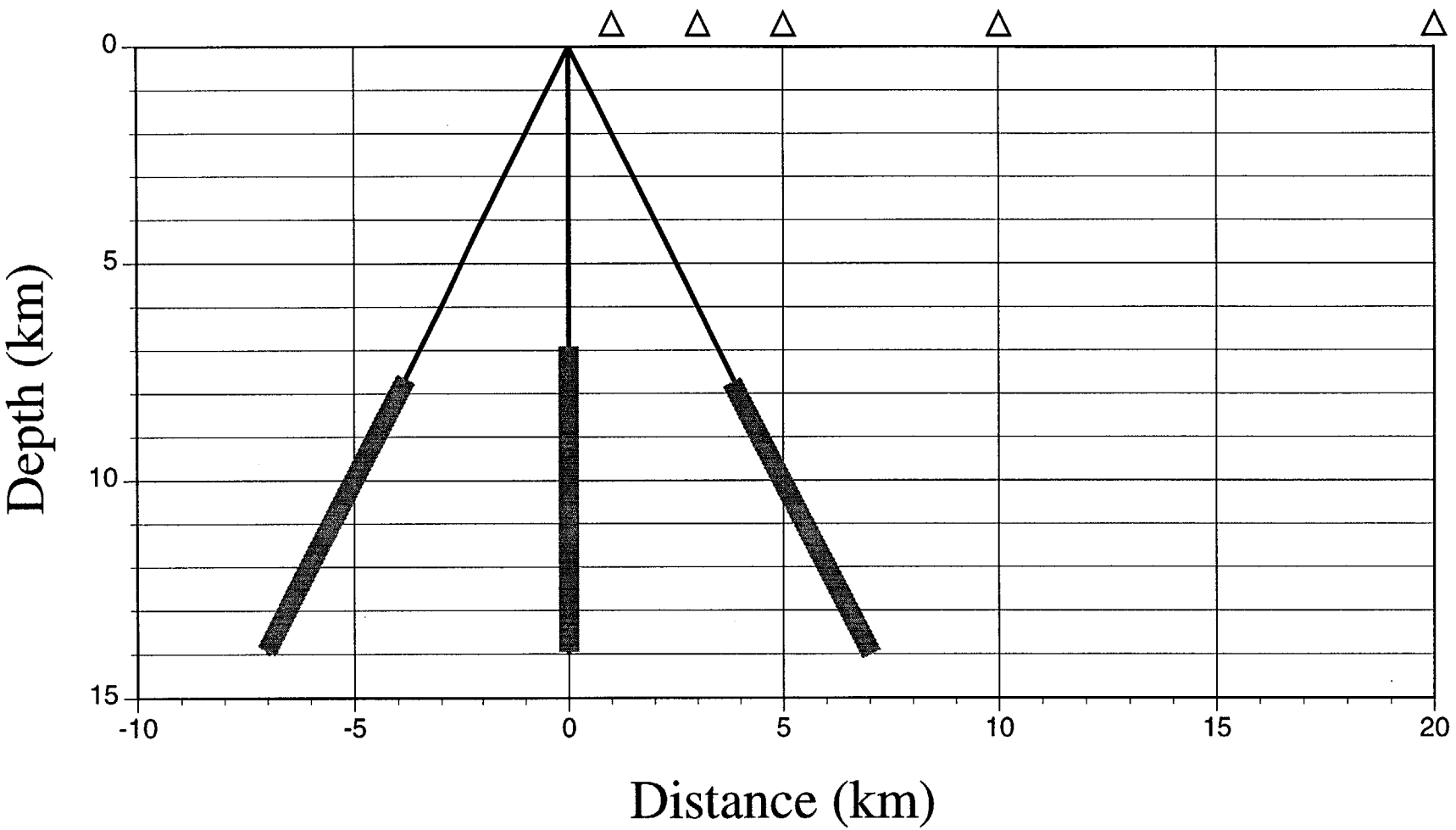

SHALLOW FOCUS, M=6.5

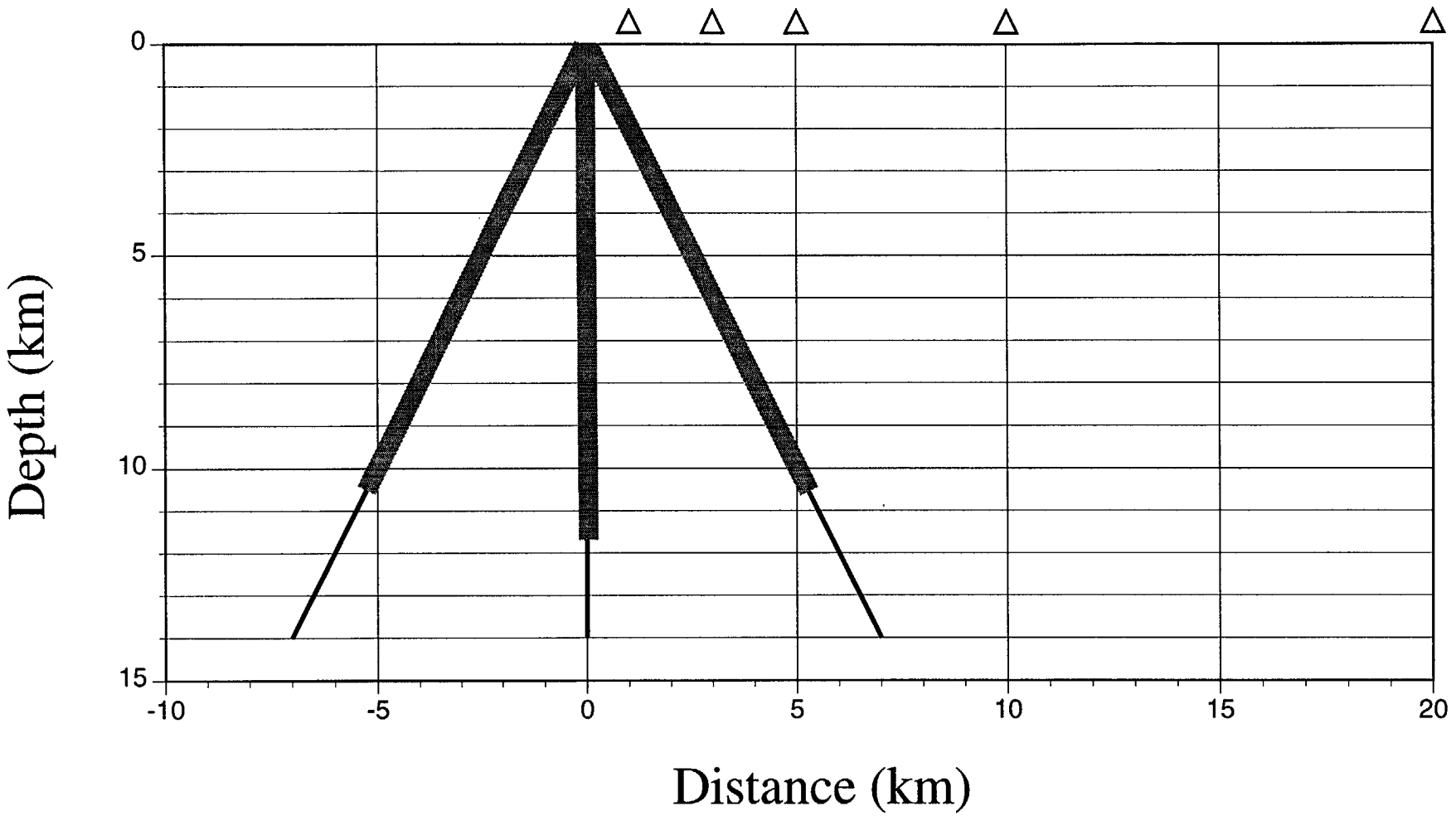

M=7.0, 7.5, 8.0

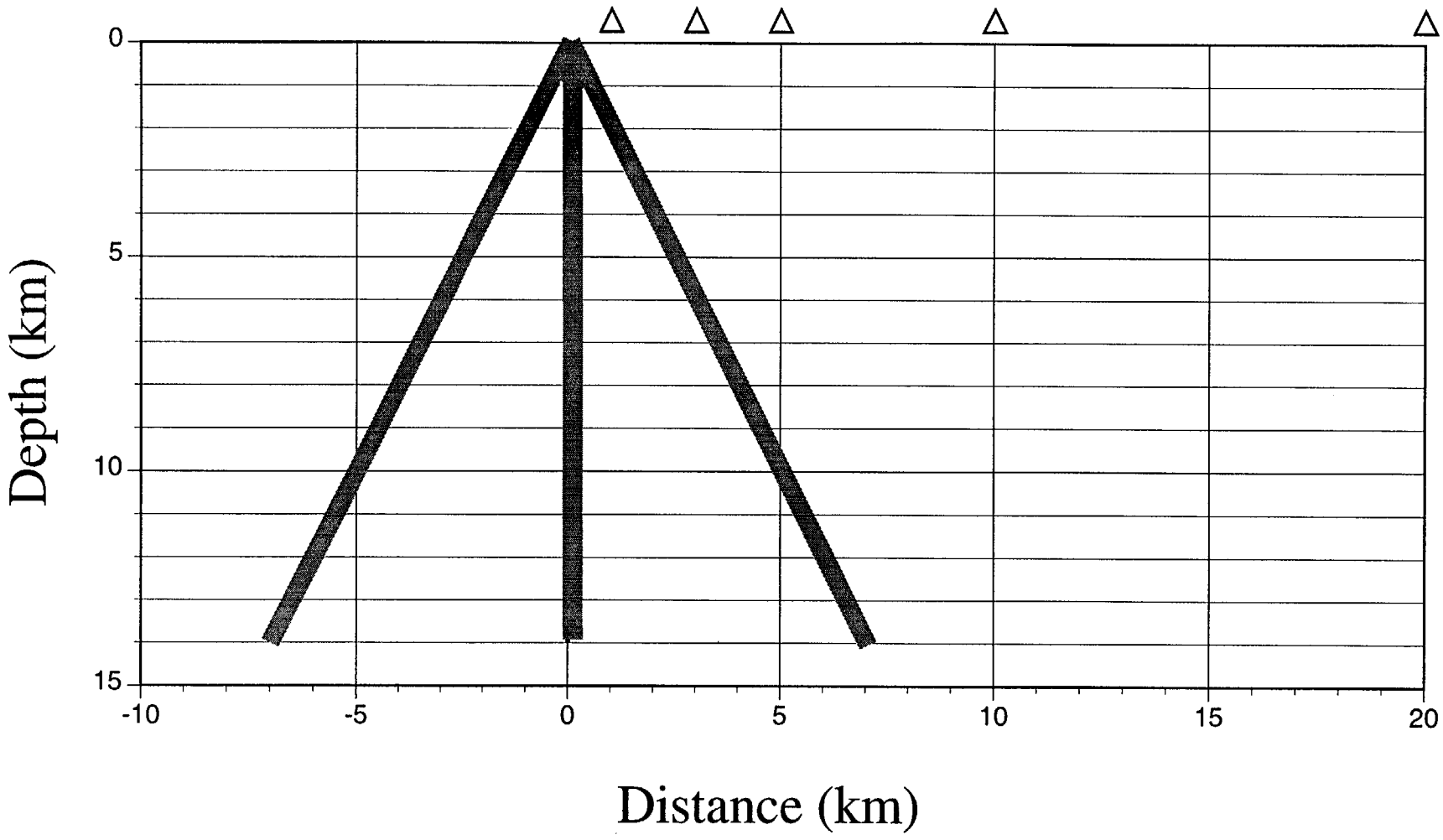

Yucca Mountain Rock Toppling acceleration

Mountain area and the location of these rocks. The quasi-static horizontal toppling acceleration, a, of a rock is defined as

$$a = \frac{f}{m},$$

where f and m are the quasi-static horizontal toppling force through the center of mass and the mass of the rock, respectively. In the field, each rock was subjected to a horizontal force (by either pulling or pushing) through the center of mass (or making a correction to make the force equivalent to a force through the center of mass). The force, monitored by a load cell, is quasi-statically increased until the rock begins rotating about a pivot. As the angular displacement increases quasi-statically, the force necessary to overturn the rock decreases; it approaches zero when the rock is on the verge of overturning. At this point the pulling (or pushing) is stopped to avoid the toppling of the rock. The toppling force, f, is the magnitude of the maximum horizontal force before overturning (fig. 3 shows a strip chart record of the load cell output during the toppling experiment on rock D). The mass, m, is determined either by weighing the rock in the field (for rocks weighing under 500 lb) or by determining the product of the volume (estimated from the dimensions of the rock) and density (~ 2.33 g/cm^3). The toppling accelerations for several rocks tested in the field are given in table 2. The parallelepiped shaped rock, D, was tip-tested in two different directions (fig. 4). Rock E weighs about 8000 lb; with the existing equipment it was not possible to tip-test it in the field.

Table 2: Field and laboratory toppling accelerations

Label	Rock ID#	Toppling Acceleration/g	
		Rock	Model
A	92 JB NC 01	0.14	0.10 – 0.16
B	93 RC SC 83	0.18	–
C	92 JB 8T 02	0.17	0.13
D[1]	92 JB 8T 01	0.34	0.32
D[2]	92 JB 8T 01	0.22	–
E	93 JB 8T 02	–	0.3

Laboratory Experiments

Among the rocks tested in the field, those with simpler shapes were selected for physical modeling. Scaled models were constructed out of styrofoam using field measurement of rock dimensions along with pictures taken from different angles (with the vertical line clearly shown). In order to simulate the resting position of the rocks in the field a styrofoam base, with the same surface inclination as that in the field was also constructed for each model.

[1]Corresponds to toppling force F_1 in fig. 4

[2]Corresponds to toppling force F_2 in fig. 4

DRAFT REPORT

DYNAMIC GEOMETRICAL EFFECTS ON STRONG GROUND MOTION IN A NORMAL FAULT MODEL

YMP WBS: 1.2.3.2.8.4.1, Task SPT 38PM4 (FY97)

James N. Brune and Rasool Anooshehpoor

Seismological Laboratory, University of Nevada, Reno

ABSTRACT

We report results of modeling particle motion in a foam-rubber model of normal faulting, and compare the results with similar results for a strike-slip geometry. Standard modeling of strong ground motion from normal fault earthquakes has used dislocation theory in which slip along the shallow part of the fault is prescribed by assuming particular time functions for fault slip. Unfortunately, in the case of normal faults, there are essentially no data from large earthquakes to constrain the modeling. In a normal faulting regime the static normal and shear stresses along the fault must approach zero at the surface, and thus the upper few km of the fault are inherently weaker than is the case for strike-slip faults. In addition there are dynamic effects from geometry and the fault surface physics which effect the fault motion.

Physical models of faulting, such as foam-rubber modeling (as distinct from numerical or mathematical models), are guaranteed to obey static and dynamic mechanical laws, and thus can be used to gain insight into the physical processes involved. In this study we compare surface accelerations from normal fault and strike-slip geometries. The data shows surface accelerations near the normal fault trace that are systematically lower, by an average factor of about 0.10, compared to the accelerations at the side sensors, which represent strike-slip motion. These results suggest that kinematic modeling of ground motion using classical dislocation theory should apply a significant adjustment of the fault slip time function on the shallow part of the fault. We conclude that estimates of accelerations for normal faults should be scaled down considerably from values based on current regression curves or simulations.

INTRODUCTION

Modeling of strong ground motion from normal fault earthquakes has generally used kinematic dislocation theory, in which the fault slip along the shallow part of the fault is prescribed by assuming particular time functions for fault slip (kinematic dislocation modeling). Since the time function and amplitude of fault slip is arbitrary as far as the theory is concerned, constraints on the fault slip must be determined from data. Unfortunately, in the case of normal faults there are essentially no data from large earthquakes, and for the modeling exercises described in the Georgetown report, the time functions were chosen based primarily on data for strike-slip earthquakes.

It is obvious that in a normal faulting regime the static normal and shear stresses along the fault must approach zero at the surface (since the tectonic forces are extensional, and the lithostatic forces are zero). Even at depth the stresses are limited if the fault gouge is weak or if the material on one side of the fault surface consists of incompetent sediments, since such materials could not maintain permanent stresses. Therefore normal faults are inherently weak along the upper few kilometers of the fault zone, and cannot maintain high levels of shear strain required for high dynamic energy release during earthquakes.

In addition to the effects of low stress on the shallow part of the fault, there are dynamic geometric effects resulting from the fault surface physics. During the rupture the fault surface will not be a transparent surface as assumed in dislocation modeling, and consequently energy trapped in the acute angle hanging wall wedge will be effected differently than energy trapped in the obtuse angle footwall wedge. The polarity of the P-waves in the hanging wall block of the fault also tends to stabilize the fault (Brune, 1996).

The object of this report is to present results of physical modeling using a normal fault geometry to demonstrate the dynamic effects resulting from both the normal fault geometry and the inherent low stress level on the shallow part of the fault.

Difficulties with Kinematic Dislocation Modeling

In kinematic modeling the time function for slip on the fault is prescribed, and the response of the layered medium is calculated. Unfortunately, there is no guarantee that the model and the prescribed slip are physically reasonable unless the true nature of the medium and its motions are known ahead of time, a situation clearly impossible in the case of earthquakes, since the slip occurs at depths of many kilometers where the physical conditions are not known, and since there are no available dynamic solutions for the problem of actual fault motion. Kinematic models commonly involve non-physical singularities, or parameters for which appropriate values are unknown, and thus constraints have to be determined by trial and error

to be consistent with available data. Unfortunately, when the data base is severely limited, as is the case for normal faults, there remain large uncertainties in choosing the range of values appropriate for various parameters, and thus large uncertainties in the predicted values of ground motion.

RATIONALE FOR FOAM-RUBBER MODELING

Physical models of faulting , as distinct from numerical or mathematical models, are guaranteed to obey static and dynamic mechanical laws, and thus can be used to gain insight into the physical processes involved. Although in laboratory physical models there are inherent problems of scaling and matching of physical conditions, such models can provide important constraints on numerical and theoretical models; for example, by modeling dynamic geometrical effects on actual fault slip.

Foam-rubber is very flexible; i.e., has a low rigidity, so that it is easy to produce large strains and particle motions. Since it is light-weight, relatively large models can be constructed, enabling the scale of dynamic phenomena to be enlarged. This allows dynamic features to be more easily observed and recorded using relatively simple electronic devices, such as tiny accelerometers and position sensing devices. Foam-rubber models automatically assure that motions are physically realistic (no singularities or unreasonable specified slips). However, this does not guarantee that the motions will correspond to motions from actual earthquakes, since there are inherent difficulties with any laboratory size scale model of large scale earth phenomena.

Great effort has been expended in rock mechanics laboratories to determine the properties of slip along interfaces between small blocks (centimeters to meters) of rock in the hope that these results could somehow be scaled up to the dimensions of rocks involved in real earthquakes (tens of kilometers or more). However, such scaling has never been justified in the literature. There are two dynamic scaling considerations not satisfied by ordinary rock mechanics experiments which are satisfied by the foam-rubber model. First, the stressing apparatus for the foam model is effectively infinitely rigid compared to the rigidity of the model, assuming that the dynamics of the model are not influenced by interaction with the stressing apparatus. We have verified this by placing a small accelerometer on the piston. No measurable motion (i.e., no interaction) of the piston at the time of a stick-slip event was found. Secondly, the overall dimensions of the foam model are large compared to the dimension of dynamic slip pulse which propagates along the interface between the two blocks. This allows the slip pulse to propagate predominantly under the influence of conditions local to the slip pulse itself, with minimized effects of the boundaries of the model and the stressing apparatus. This obviously corresponds better to the conditions in the real earth, for which the length of slip pulse is small compared to the dimensions of the fault (Heaton, 1990). In rock mechanics experiments this is not the case. (Foam-rubber has a Poisson's ratio of about 0.25, close to that for rocks, and thus satisfies one of the dimensionless scaling requirements (ratio of P-wave to S-wave velocities).)

Some of the major limitations of foam-rubber modeling include:

1. Intrinsic Q is low (of the order of 10) and cannot be controlled. This constrains the usefulness of foam-rubber modeling to wave propagation distances which are not to large compared to the wavelengths involved. Thus it is most useful to gain insight into near-source phenomena. (An ancillary advantage of the low Q is that there is relatively little energy scattered back from the distant sides of the model, which could interfere with the dynamics).

2. The fault surface friction conditions are difficult to control. The lattice of foam-rubber vesicles produces extreme roughness on a small scale (scale of the order of a millimeter). The coefficient of friction is on the order of 10, whereas that for rocks is on the order of 0.5. Thus to produce fault slip, the strains must be very large, on the order of 10^{-2}, whereas in the earth the corresponding strains are on the order of 10^{-4}. As long as strains are approximately linear, the difference can be corrected for. However, in both the foam-rubber and the real earth, the fault behavior is not linear on the fault trace, and there is no guarantee that the non-linearities in the foam model correspond to those in the real earth. (A similar problem is common to kinematic modeling as well).

Foam-rubber modeling studies have been reported in a number of publications (see references), with funding for these studie s coming from EPRI, NSF, and USGS. We believe that foam-rubber modeling has been established as a useful tool for seismology, but the results must be interpreted with care, and the inherent limitations must be kept in mind. This is of course true for any type of modeling.

DESCRIPTION OF MODEL

The model consists of two large blocks of foam-rubber , one driven horizontally over the other by a hydraulic piston (Fig. 1). We have confirmed that the direction of gravity is not critical to dynamics by testing the model in a tilted position. The lower block is securely glued to a plywood sheet which is in turn anchored to the concrete floor. The upper block and the attached rigid frame are supported by four steel pipes, and are equipped with scaffolding jacks and guiding rollers at each corner. Normal force at the contact (fault) is provided by the weight of the upper block and is varied by lowering or raising the jacks. A hydraulic piston placed between a concrete wall and the upper block frame, pulls the upper block, creating the normal fault stress geometry. The rollers guiding the moving block ensure a shear motion. As the upper block is pulled backwards over the lower block,

the strain in the blocks increases until the stress at the interface exceeds the frictional resistance and a stick-slip event occurs over the whole boundary (fault plane). These major events correspond to "characteristic" events for the system, analogous to "characteristic earthquakes'" in the earth. Successive "characteristic" events usually cause about the same amount of average slip (~1 cm) between the blocks, but the pattern of slip can vary markedly, with the rupture initiating at different points and propagating in different directions. If the driving displacement is steady, the characteristic events repeat more or less regularly until the upper block has slipped about 30 centimeters. At this point, the hydraulic piston is fully contracted, and one experimental run is complete. The stress is relieved and the upper block is lifted and moved backward to the starting position for repeat of the procedure.

This study compares normal fault motion with strike-slip motion. To record normal fault motion, the motion sensors are installed along the front center of the model in arrays of sensors extending from near the fault tip to deep inside the model, and along the surface to a distance of about 20 centimeters from the fault tip. To record, strike-slip motion sensors are installed on each side of the model. Rupture nucleation is typically deep in the model, with the rupture propagating to the front surface for normal fault geometry, and to the side for strike-slip geometry, as is typical of actual normal and strike-slip fault earthquakes.

INSTRUMENTATION

Ultra-light Accelerometers

Due to foam-rubber's low density and high elasticity, particle accelerations in a stressed foam-rubber model of earthquakes can exceed several hundred gravities (the acceleration due to gravity). Slips of the order of one (1) centimeter can take place in a few milliseconds, resulting in very large accelerations at high frequencies. In order to measure these accelerations, accelerometers with a high dynamic range and low mass (to minimize the mass loading effects) are needed. We have 16 state-of-the-art, ultra-light ENDEVCO Model 25A accelerometers. The Model 25A, with a mass of 0.2 grams and a dynamic range of +/- 1000 g, is the world's smallest piezoelectric accelerometer. In order to further reduce the mass loading effects, each accelerometer is mounted on a 1.5-inch styrofoam disk before inserting them in the foam; the 1/8-inch thick Styrofoam disk (with the same density as the foam-rubber used in the model but far more rigid), distributes the accelerometer's mass over a much larger area (about 50 times larger).

On the surface near the tip of the normal fault model (corresponding to the ground surface in the earth), due to the overall smaller particle accelerations relative to the accelerations on the fault surface, we used more sensitive accelerometers with a dynamic

range of +/- 50 g. These SenSym Model SXL050G accelerometers were also mounted on 1.5-inch styrofoam disks in order to distribute the mass over a larger area, and reduce the mass-loading effects.

Data Acquisition System

The data acquisition system consists of a 486 PC with a state-of-the-art 330 kHz analog-to-digital board (DAP 1200e/6 manufactured by Microstar Laboratories). Particle motions during stick-slip events at 16 sites were digitized at the rate of 5000 samples-per-second and recorded on the PC.

CALIBRATION

Each ENDEVCO Model 25A accelerometer comes with the manufacturer's calibration data sheet, which is traceable to the National Institute of Standards and Technology. However, we calibrate each accelerometer by subjecting it to a sinusoidal motion and recording the harmonic accelerations and displacements (using the position detector) simultaneously on the digital data acquisition system. The accelerometer's response (in counts/g) is then determined by calculating the peak-to-peak input acceleration amplitude from the measured peak-to-peak displacement and angular frequency of the input motion .

SenSym Model SXL050G accelerometers were calibrated both by subjecting them to sinusoidal motion (similar to ENDEVCO Model 25A calibration), and by tilting them at 90 degrees from their null position, and recording the output corresponding to 1 g (one gravity). Both types of accelerometers were normalized (in the data acquisition software) to have identical outputs when subjected to a common input motion.

EXPERIMENTAL PROCEDURES

Figures 2a and 2b show the locations of 16 miniature accelerometers that are embedded on the fault surface, and on the ground surface (indicated by numbers 1-16). Sensors at sites 1 through 6 measure horizontal particle motions (parallel to the surface), and are embedded on the surface (corresponding to earth's surface) on both sides of the fault along a line perpendicular to the tip). Sensors 7 through 16 are embedded on the fault surface; 7, 9 and 11, enclosed in parenthesis, indicate the accelerometers in the upper block that are approximately located above accelerometers 8, 10, and 12 in the lower block,

respectively (the relative position changes several centimeters as the upper block is pushed over the lower one). The sensors, embedded on the fault surface (7-16), measure particle motions on the fault plane parallel to the direction of external shear force (provided by the hydraulic piston).

Digital data from each stick-slip event is recorded on 16 channels, at a rate of 5000 samples per second. The Analog-to-Digital sensitivity of the data acquisition system is 6554 counts/volt. Data files are saved on the PC and backed up on ZIP disks.

DATA

The appendix gives playouts of the accelerations for channels 1-16, for numerous events. In order to illustrate the general features of the seismograms in the appendix, we show here several examples typical of particle motions for different points of nucleation of the rupture at depth (Figs. 3 a-f).

ANALYSIS

The obvious points illustrated by the data are:

1. The surface accelerations near the fault outcrop (channels 1-6) are systematically lower than the accelerations at the side sensors where the rupture breaks out at the surface (channel 14 or 15 when the rupture propagates and breaks out in those directions, respectively). The average ratio of the largest acceleration at any of stations 1-6 to the amplitude of the acceleration at 14 or 15, for the cases in the figures is about 0.10 +/- 0.07.

   We estimated average ratios of the largest acceleration on the horizontal sensors(sensors 1-6) to the acceleration on the strike slip sensor(sensor 14 or 15) partly because the horizontal component is the most important in engineering design, and partly because the horizontal component is typically larger on actual eathquake strong motion seismograms. However, near the fault tip in the foam model, since the primary motion is parallel to the fault dip(60 degrees), the vertical component is actually about 1.73 times the horizontal. In the real earth, refraction in near surface low velocity layers may change the ratio of horizontal to vertical motion somewhat, depending on the velocity of sediments on the hanging wall side of the fault, the near-surface dip of the fault, and other complications in the hanging wall side of

the fault.

2. For dislocation modeling the important parameter is the dislocation ac celeration near the surface, i.e., the accelerations for sensor 9 compared to the shallow dislocation accelerations for the strike-slip case. The average ratio of the acceleration at sensor 9 to that at sensor 14 or 15 is about 0.15 +/- 0.12. The near-surface dislocation is clearly asymmetric, with the hanging wall dislocation acceleration (sensor 9) being about twice as large as that for the footwall(sensor 10). (The particle velocities and displacements of the shallow dislocations are also approximately twice as high for the hanging wall). Dislocatiom modeling typically forces the hanging wall and footwall accelerations to be the same at high frequencies.

If the results above are applicable to real-earth situations, kinematic modeling of ground motion using classical dislocation theory should apply some adjustment of the fault slip time function on the shallow part of the fault. In order to apply these results to the real earth, we must consider the typical ratios of the wavelengths involved to the thickness of the weak layer, as well as other factors which might qualify the results.

We interpret the difference between the accelerations at the front sensors and the accelerations at the side sensors to be due to two factors:

(1) Dynamic and geometrical effects of the mode II (particle motion in direction of rupture propagation) rupture plane intersecting the surface at an angle of 60 degrees in one case (normal fault geometry), and mode I (particle motion perpendicular to rupture direction) rupture intersecting the surface at an angle of 90 degrees (strike-slip geometry).

(2) The low stresses (normal and shear) at the tip of the normal fault.

Condition (1) is also inherent in real-earth differences between normal and strike-slip faults, because it is a dynamic geometrical effect. Condition (2) also applies in normal faulting in the real earth, but the comparison with strike-slip faulting depends on the strength of strike-slip faults at the surface. Thus the results from this modeling study should be taken into account when using kinematic dislocation theory to compare ground motion from normal faults with data from primarily strike-slip faults. The weight to be given to these results depends on the actual stress conditions for any particular case and also how the results are scaled to real-earth situations.

Factor (1), the dynamic and geometrical effects between normal faulting and strike-slip faulting, will apply if the dislocation pulse nucleating at depth and arriving at the surface is similar in the real earth to the situation for the foam-rubber model; i.e., rupture of the fault interface occurs so that the fault surface cannot transmit shear waves across the fault during

rupture. Although this may seem obvious, standard dislocation theory modeling does not take this into account, and assumes the fault is transparent during rupture (Brune, 1995, 1996). Another factor that effects the dynamics of the fault motion near the fault tip is that the polarity of the energy arriving from the deeper part of the fault arrives at the free surface as a dilatational wave, but changes phase at the surface to become a compressional wave, which tends to stabilize the fault when it impinges upon it (Brune, 1996).

In order to scale the dynamic and geometrical effects to the real earth we also need to know the ratio of the wavelength of the energy involved to the dimension of the dislocation pulse traveling up the fault plane, the so-called Heaton pulse (Heaton, 1990). The other factors involved in scaling are geometrical, and thus scale independent. In previous studies of foam-rubber modeling we have found that the dimension of the dislocation pulse; i.e., the distance between the leading edge of the rupture and the following edge (locking edge) is about 10 centimeters. (This seems to be primarily controlled by the characteristic roughness dimension of the interface, in the case of foam-rubber, about 1 millimeter). In the real earth, Heaton (1990) has estimated that the typical dislocation width is about 1-5 kilometers (rise-times of about 0.3 to 2.0 sec.) Thus for the purely geometrical effects, a wavelength of about 2 kilometers (about 1 Hz) in the earth corresponds to about 10 centimeters in the foam rubber model. The shear wave velocity in the foam-rubber is about 35 m/sec, so that 10 centimeters corresponds to periods of about 4 ms. The acceleration pulses for the side sensors (strike-slip case), have energy of this frequency, but for most of the normal fault pulses the high frequencies have been significantly removed, and typical periods are around 10 ms or longer. The dynamic geometrical effects should apply to higher frequencies also, if they had propagated toward the fault tip.

Factor (2), the low stress level at the normal fault tip, causes the dislocation pulse to lose energy as it propagates toward the outcrop of the normal fault. The high frequency energy is removed by fault friction and the fact that the pulse has to propagate through a zone with a relatively low level of shear strain energy to re-energize the pulse. This is to a certain extent counteracted by the fact that the frictional force needed to cause sliding also decreases, and also by the fact that the free surface causes an amplification of about a factor of 2.0. In the real-earth case of normal faults with large offsets, the stresses near the normal fault tip are probably even more reduced, because of the presence of a thick sedimentary alluvial section on the hanging wall side of the fault. This, of course, is not represented in the model, and thus the model may overestimate the accelerations on the hanging wall side of such normal faults. However, in the cases of normal faults near Yucca Mountain, the effect of thick alluvium on the hanging wall side of the fault may not be as important because most of the faults have small total offsets, and there is no thick sedimentary section on the hanging wall side (e.g., the Solitario Canyon fault). In this sense the model's results for the hanging wall side of the fault may be realistic for the Solitario Canyon Fault (more so than would be the case, for example, for the Bare Mountain fault, or other Basin and Range faults with a thick alluvial section on the hanging

wall side of the fault).

The Role of Shallow Fault Creep in Normal Faulting

Because the fault normal stress approaches zero at the surface, any extensional strain in the model causes some quasi-static (i.e., non-dynamic) fault slip near the tip of the fault. We refer to this a fault creep. The amount of creep depends on the amount of extensional strain ocurring after the last event, and the depth at which the fault locks, preventing creep. We can control this to a certain extent by tilting the stressing posts to force down the tip of the fault, but for the geometry shown in figure 1, we could not prevent some shallow creep from ocurring. We tilted the stressing posts to the point at which the fault was just touching the tip. If we tried to put further normal stress at the tip by tilting the posts, a counter-torque was produced on the hanging-wall wedge, causing the tip to open up even though the fault normal stress further into the model was increased.

Because a significant amount of shallow creep always occurs between events, and essentially no creep occurs at depth, the fault offset at the surface during events is consistently less than that at depth. Averaged over time, the slip at the surface(creep plus dynamic fault slip) must be equal to that at depth(primarily dynamic slip). The consequence of this is that just prior to rupture in any event, the shear stress along the shallow part of the fault fault is lower than would be the case if there had been no inter-event creep. This in turn effects the rupture dynamics as the rupture approaches the surface, because there is less energy availabe to overcome friction. Thus the effect of inter-event creep is to reduce available shear stress near the fault tip at the time of the event. This is similar to the situation that would be created if a weak(low friction) surface had been artificially introduced on the fault (as has been done for the case of strike slip faulting and described in an accompanying report, Brune and Anooshepoor, 1997). The reduced stress at the fault tip clearly contributes to reducing the accelerations near the fault tip. Application of the results of these model studies will require an assessment of how closely the model stresses correspond to fault stresses for actual normal faults in the earth.

How much inter-event creep occurs on real-earth normal faults is not known. As extensional strain increases between major normal faulting events it seems that there must be some fault creep or other type of stress relaxation in any thick alluvial section on the hanging wall side of the fault. Although there have been some geodetic indication of inter-event stress relaxation and creep, there is not enough evidence to say for sure whether it is common or not. This is partly because in the Basin and Range the inter-event times are so long that creep or stress relaxation rates are very low.

As discussed above there are clearly physical reasons why normal fault stresses in the earth must approach zero in extensional regimes. This of course does not guarantee that the stess pattern in the model is exactly like that in the model, but in a general way the stress patterns

are similar, and the consequences in the earth must be similar, i.e., there is less shear energy avaialable near the fault tip to feed into the fault rupture, and this will reduce the acceleration at the fault tip.

CONCLUSIONS

Results of particle motion studies in a foam-rubber model of normal faulting, compared with similar results for a strike-slip geometry, show surface horizontal accelerations for normal faulting that are systematically lower, by an average factor of about 0.10 -/+ 0.07, relative to the accelerations representing strike-slip motion. The dislocation acceleration on the shallow hanging wall fault surface reduced by a factor of 0.15 +/- 0.12. The foot wall acceleration, in turn, is about half that for the hanging wall. Since for normal faults there are essentially no near-fault data from large earthquakes, the foam-rubber modeling results could be very important to constrain dislocation modeling, and suggest that a significant adjustment of the fault slip time function on the shallow part of the fault should be applied. In a normal faulting regime the static normal and shear stresses along the fault must approach zero at the surface, and thus the upper few kilometers of the fault are inherently weaker than is the case for strike-slip faults. In addition there are dynamic effects from geometry and fault surface physics which reduce the fault motion. Thus there are clear physical reasons for the foam-rubber mod - eling results, reasons which apply to the real earth as well. We conclude that estimates of accelerations for normal faults should be scaled down considerably from values based on current regression curves or simulations.

FIGURE CAPTIONS

Figure 1 Diagram of the foam-rubber normal fault model. Dimensions and description are given in the text.

Figure 2a Diagram showing setup for sensors in the normal fault model for ruptures which breakout at sensor 15.

Figure 2b Diagram showing setup for sensors in the normal fault model for ruptures which breakout at sensor 14.

Figure 3 a-f Examples of accelerations recorded at the normal fault outcrop (sensors 1 - 6), and the strike-slip breakout (15 or 14). Selections were made to represent maximum, minimum, and average values of the ratio of the normal fault acceleration to the strike-slip acceleration.

Appendix figures

A 1 a Diagram of sensor layout for recordings for which the strike-slip rupture breaks out at sensor 15.

A 1 b-p Acceleration recordings for examples for which the strike-slip rupture breaks out at sensor 15.

A 2 a Diagram of sensor layout for recordings for which the strike-slip rupture breaks out at sensor 14.

A 2 b-o Acceleration recordings for examples for which the strike-slip rupture breaks out at sensor 14.

REFERENCES

Anooshehpoor, A., and J.N. Brune (1989): Foam rubber modeling of topographic an dam interaction effects at Pacoima Dam. Bull. Seis. Soc. Amer., 79, 1347-1360.

Anooshehpoor, A. And J.N. Brune (1994): Frictional Heat Generation and Seismic Radiation in a Foam Rubber Model of Earthquakes. PAGEOPH 142(3/4), 735-747.

Archeluta, R.J., and J.N. Brune (1975): Surface strong motion associated with a stick-slip event in a foam rubber model of earthquakes. Bull. Seis. Soc. Amer., 65(5), 1059-1071.

Brune, J.N. (1996): Dynamic wave effects on particle motions in thrust, normal and strike-slip faulting. AGU Fall 1996 Meeting, EOS, Transactions, 77(46), November 12, 1996, S31B6, F505.

Brune, J.N. (1973): Earthquake modeling by stick-slip along pre-cut surfaces in stressed foam rubber. Bull. Seis. Soc. Amer., 63, 2105-2119.

Brune, J.N. (1996): Particle motions in a physical model of shallow angle thrust faulting. Proceedings of the Indian Academy of Science, 105(2), 1-10.

Brune, J.N., and R. Anooshehpoor (1991): Foam rubber modeling of the El Centro terminal substation building. EERI: Earthquake Spectra, 7, 45-79.

Brune, J.N., and R. Anooshehpoor (1991): Foam rubber modeling of the Lotung large-scale seismic experiment. EERI: Earthquake Spectra, 7, 165-178.

Brune, J.N., R. Anooshepoor, Modeling the effect of a shallow weak layer on strong ground for strike-slip ruptures, Draft Report, presented at PSHA strong motion workshop #3, in Salt Lake City, January 9, 1997.

Brune, J.N., R. Anooshehpoor, and R.H. Loveberg (1988): Foam rubber modeling of soil-structure interaction. Proceedings of the Earthquake Engineering and Soil Dynamics Conference 2. Sponsored by the American Society of Engineers Geotechnical Engineering Division, June 17-30, 1988, 218-232.

Brune, J.N., S. Brown, and P.A. Johnson (1993): Rupture mechanism and interface separation in foam rubber models of earthquakes: a possible solution to the heat flow paradox and the paradox of large overthrusts. Tectonophysics, 218, 59-67.

Brune, J.N., P.A. Johnson, and C. Slater (1990): Nucleation, Predictability, and Rupture Mechanism in Foam Rubber Models of Earthquakes. Journal of Himalayan Geology, 1(2), 155-166.

Hartzell, S.H., G.A. Frazier, and J.N. Brune (1978): Earthquake modeling in a homogenous half-space. Bull. Seis. Soc. Amer., 68, 301-306.

Heaton, T.H. (1990): Evidence for and implications of self-healing pulses of slip in earthquake rupture. Physics of the Earth and Planetary Interiors, 64, 1-20.

King, J.L., and J.N. Brune (1981): Modeling the seismic response of sedimentary basins. Bull. Seis. Soc. Amer., 71, 1469-1487.

FIGURES

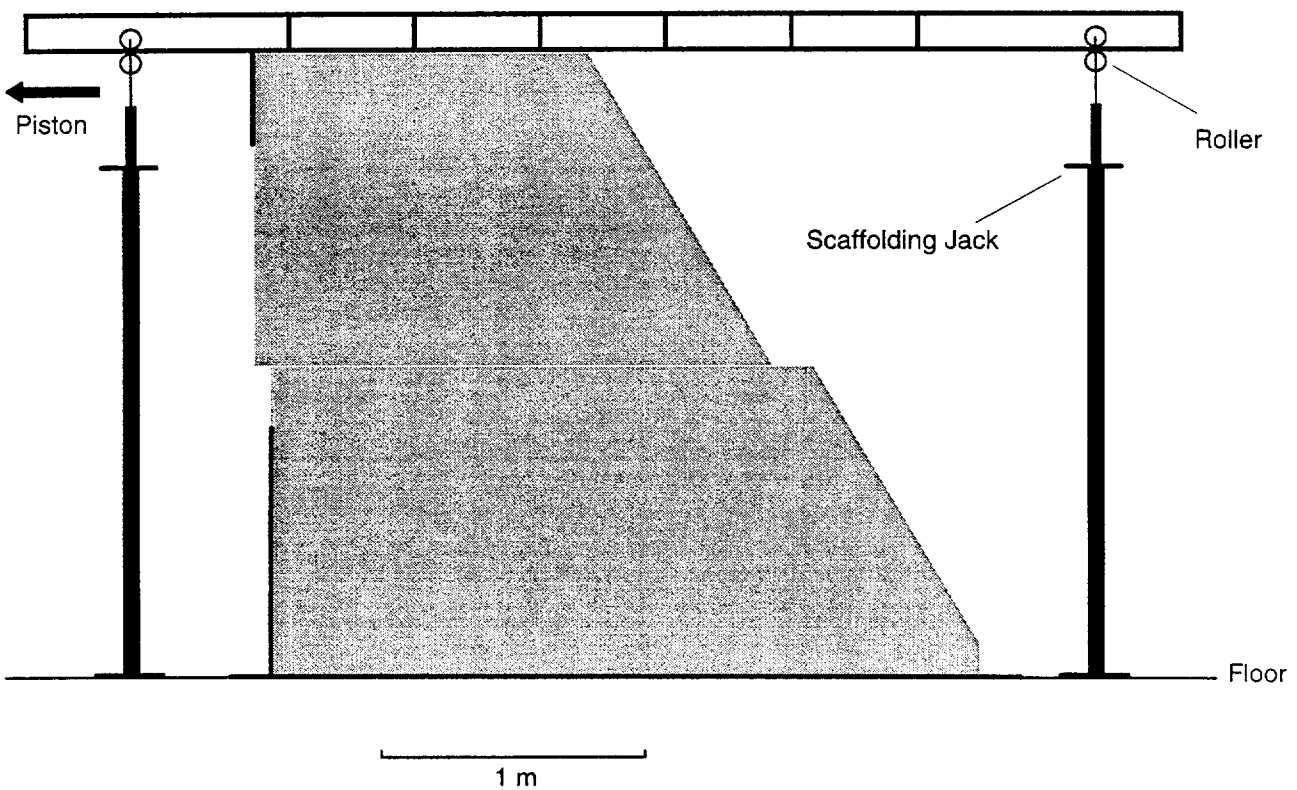

Figure 1

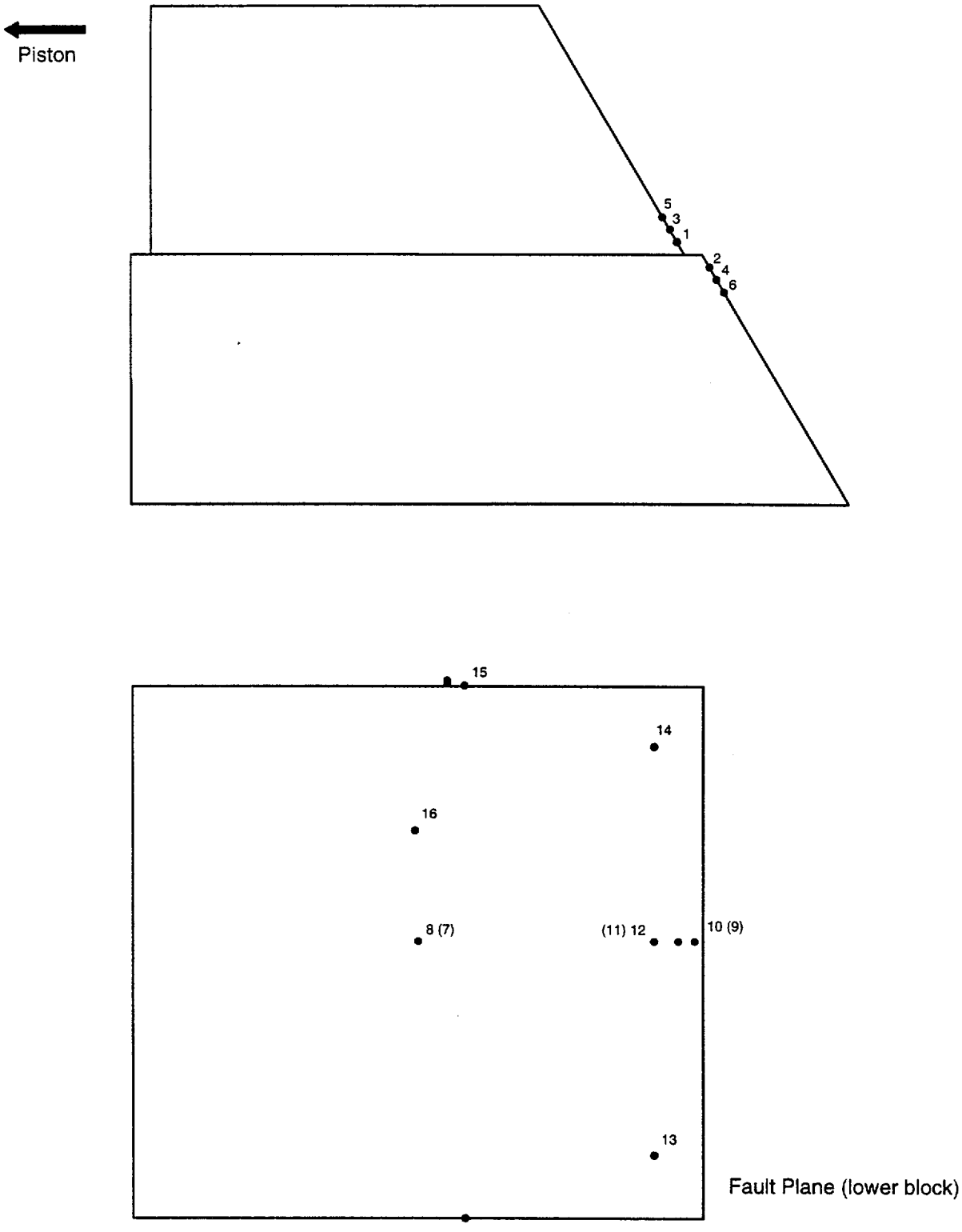

Figure 2a

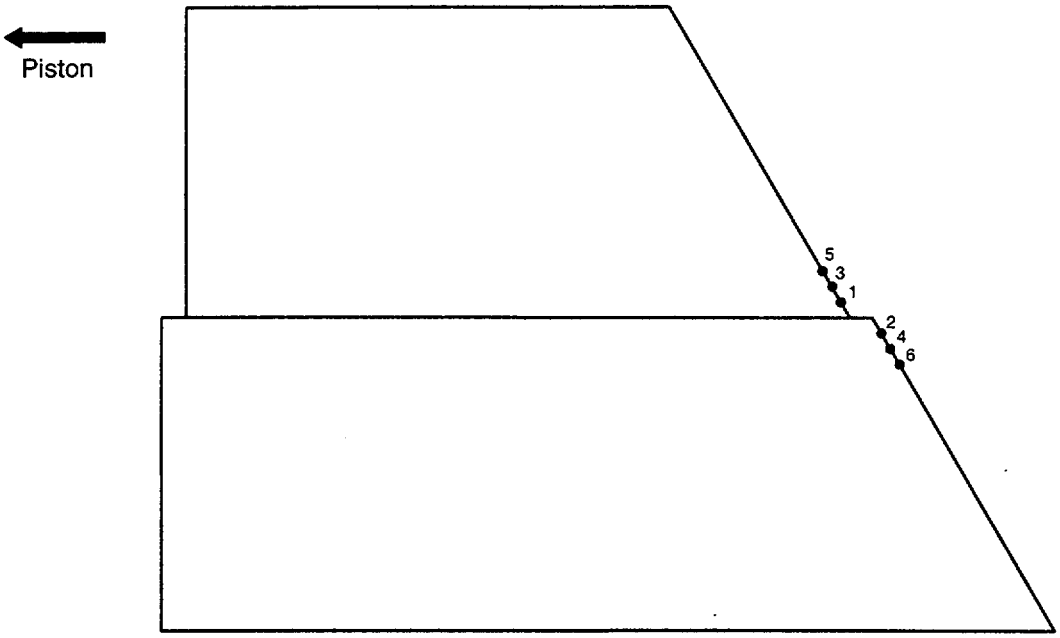

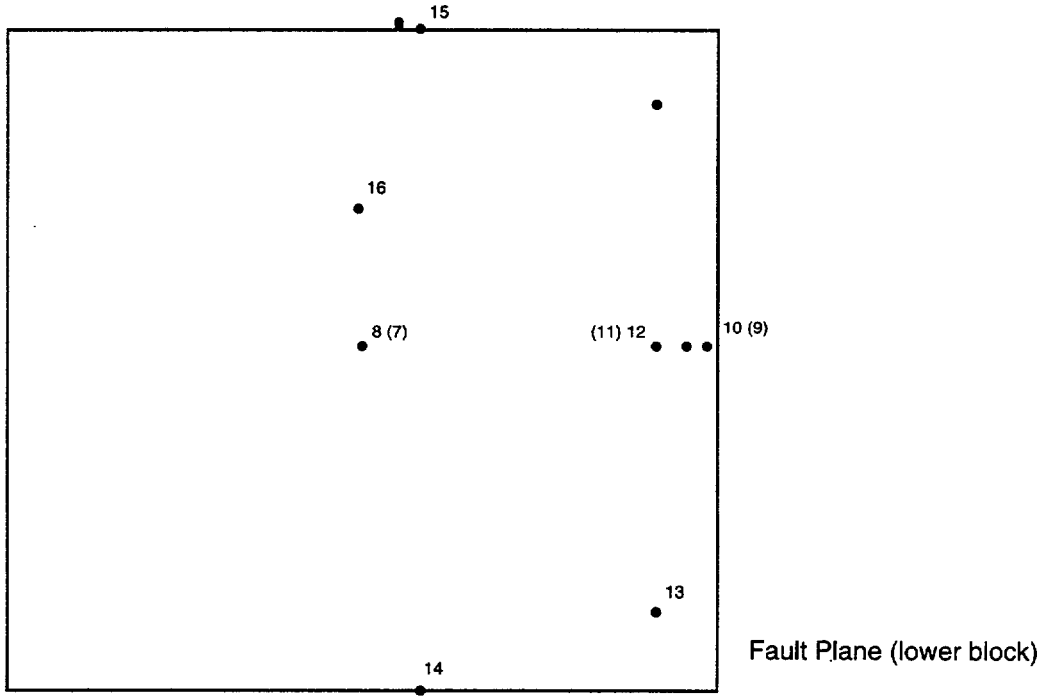

Figure 2b

NRM17.LOG

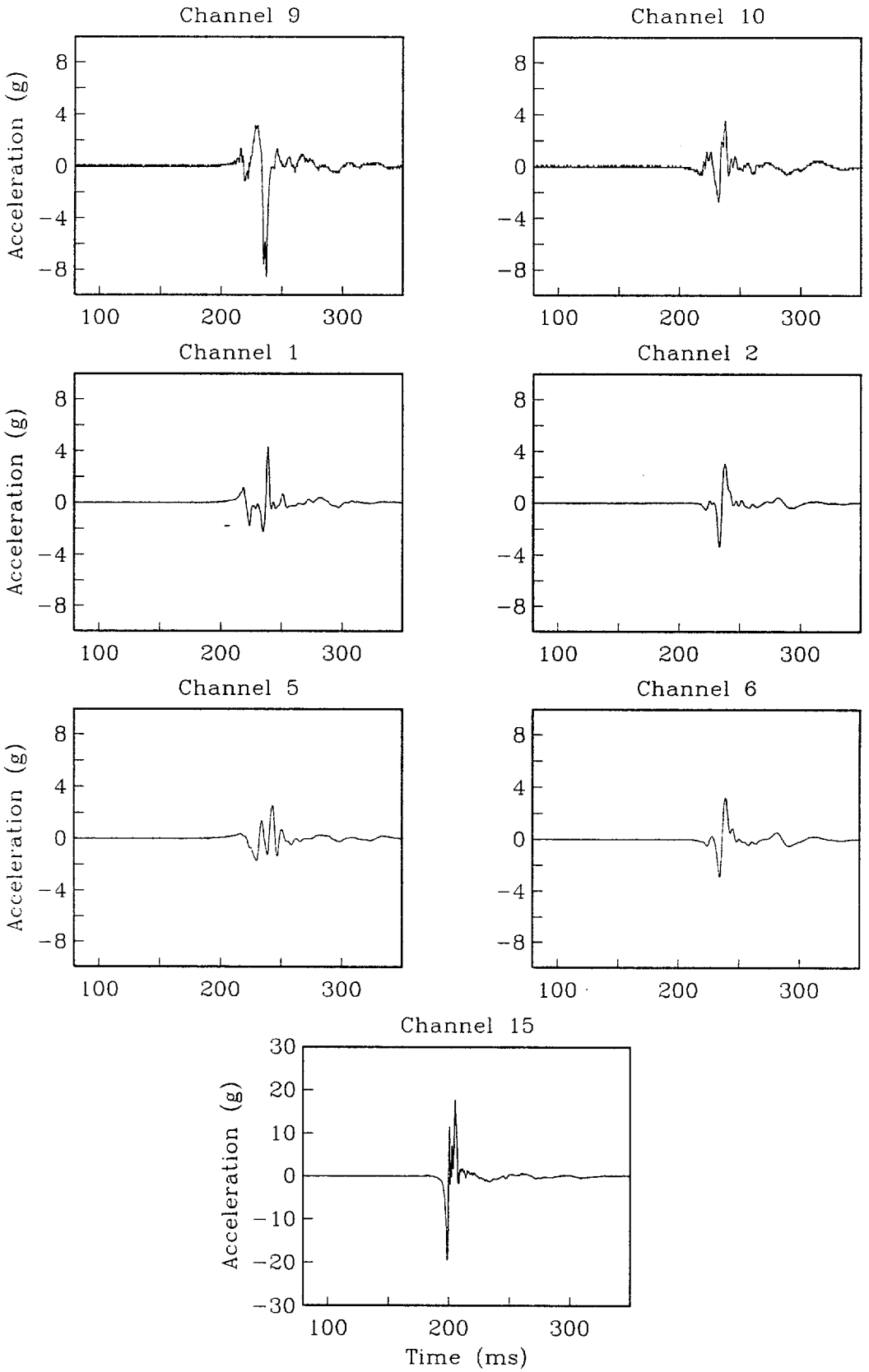

Figure 3a

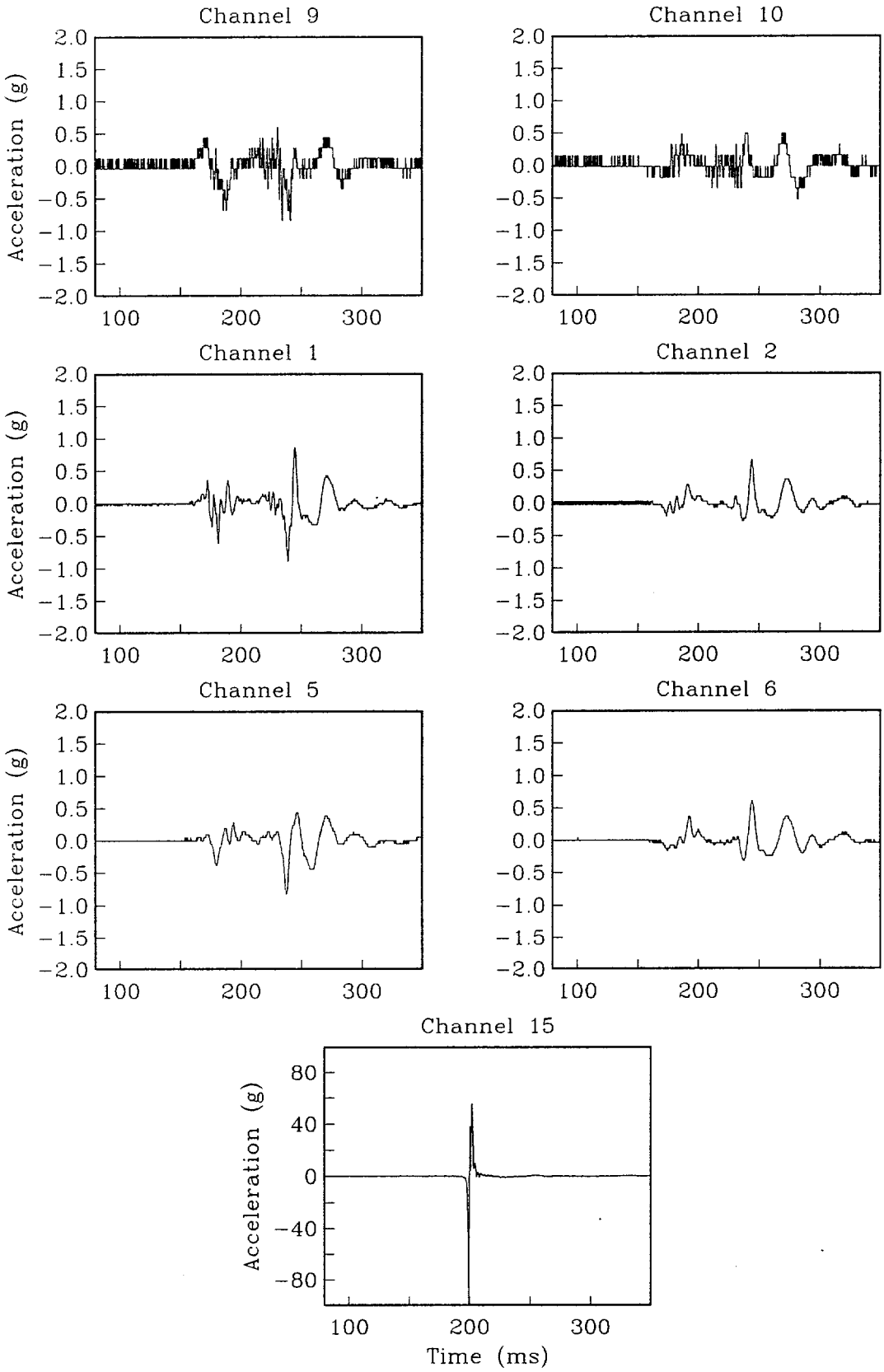
Channel 9
Channel 10
Channel 1
Channel 2
Channel 5
Channel 6
Channel 15
Acceleration (g)
2.0
1.5
1.0
0.5
0.0
−0.5
−1.0
−1.5
−2.0
80
40
0
−40
−80
100
200
300
Time (ms)

Figure 3b

NRM20.LOG

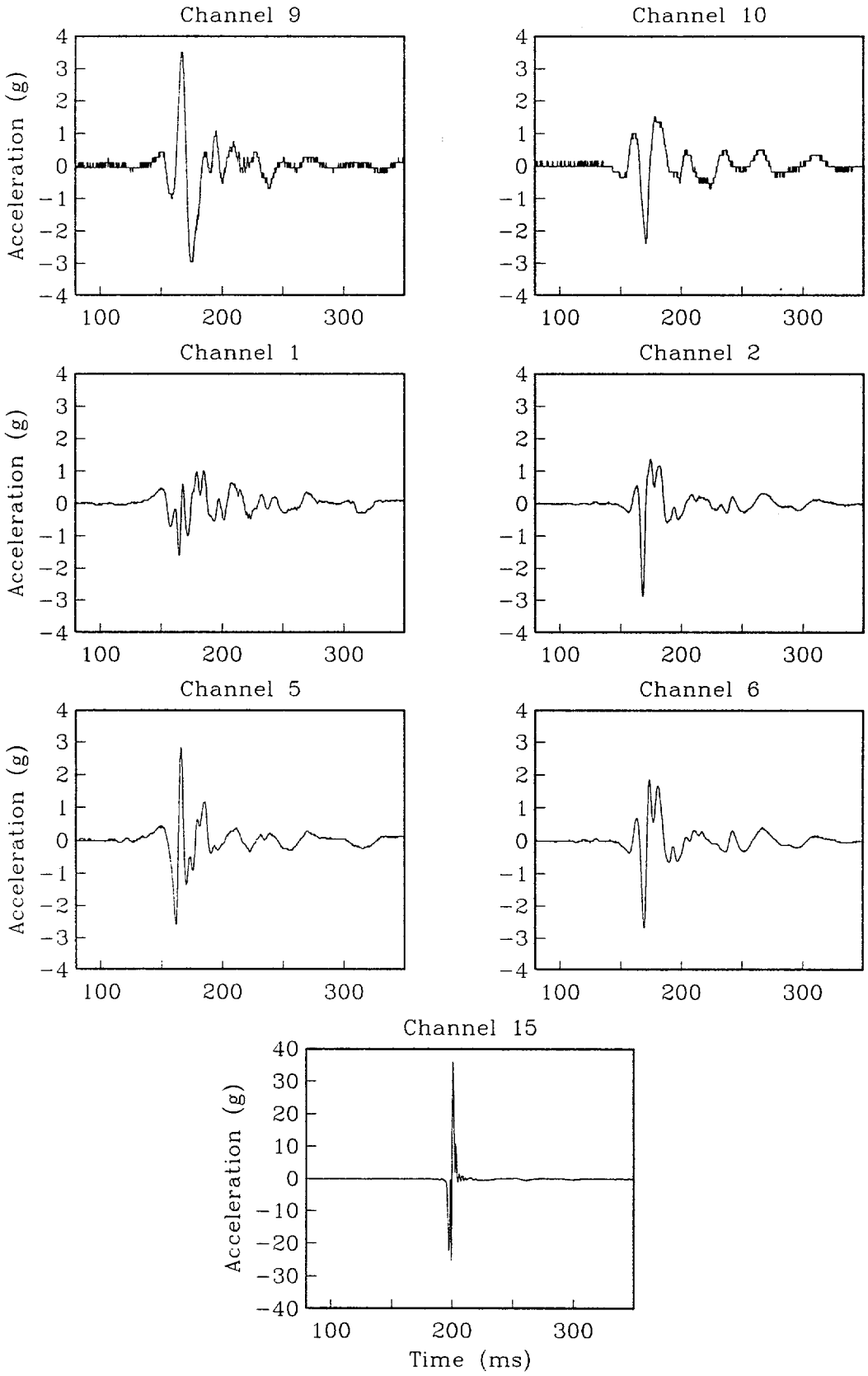

Figure 3c

NRM41.LOG

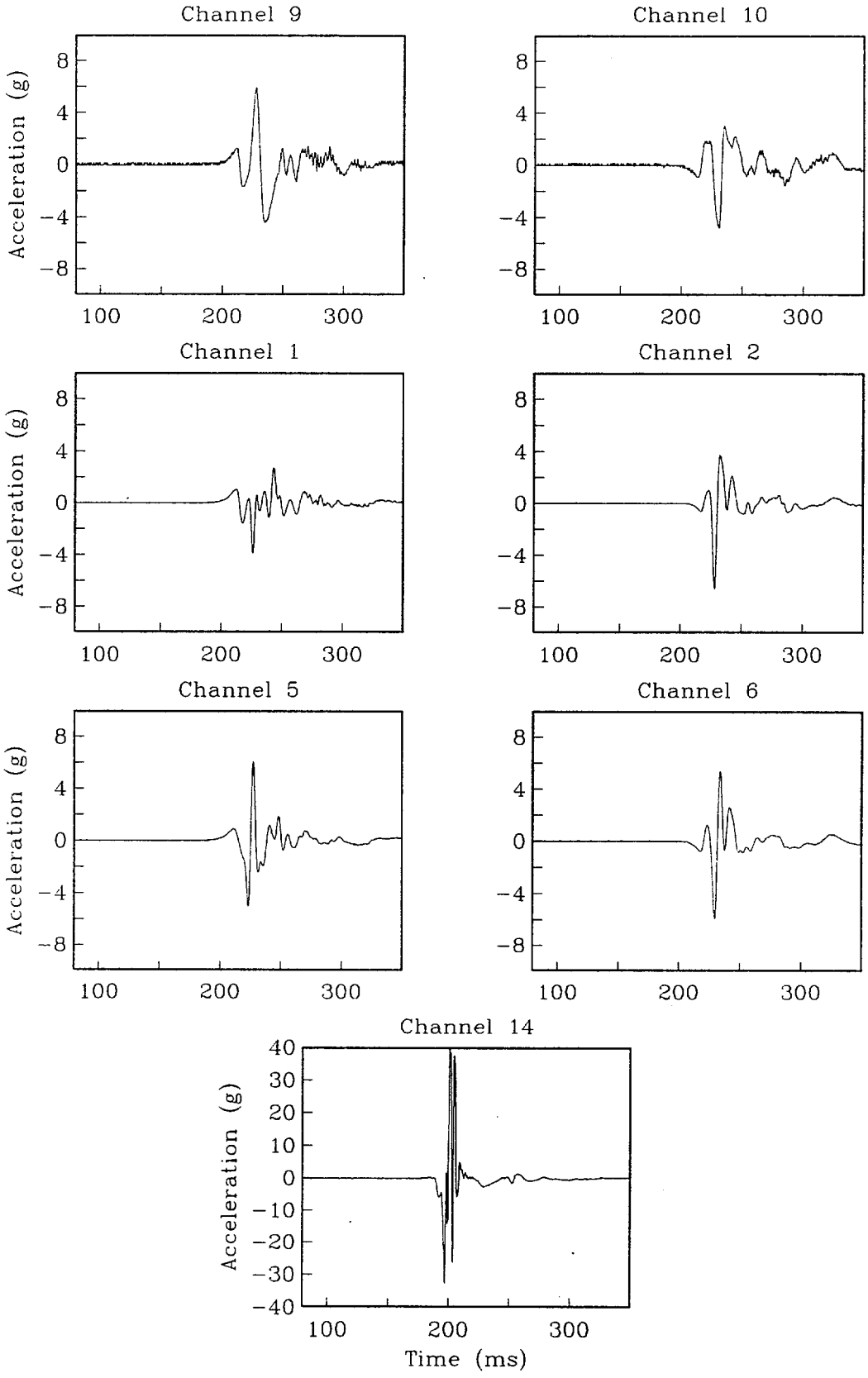

Figure 3d

NRM49.LOG

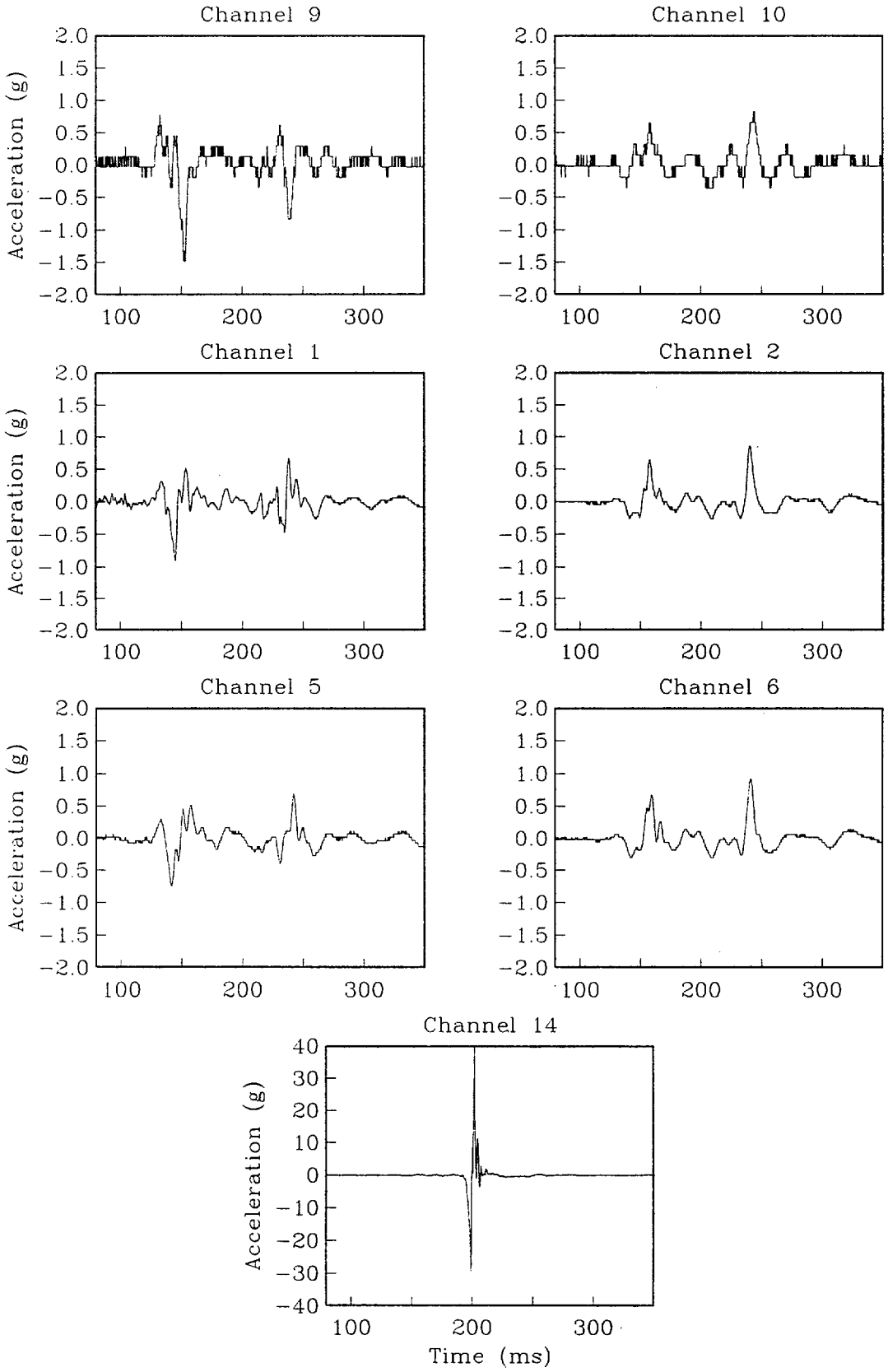

Figure 3e

NRM50.LOG

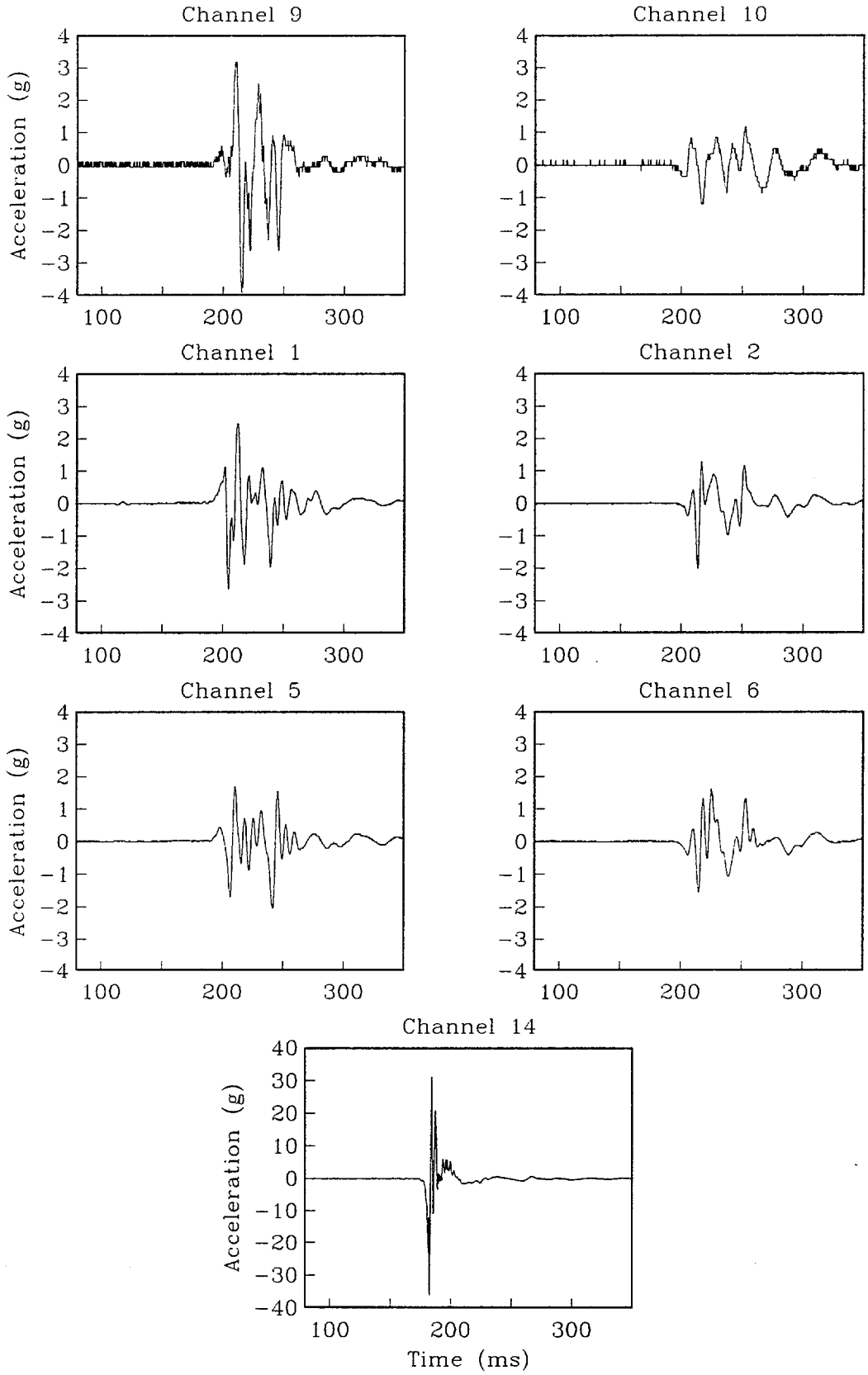

Figure 3f

DRAFT REPORT

MODELING THE EFFECT OF A SHALLOW WEAK LAYER ON STRONG GROUND MOTION FOR STRIKE-SLIP RUPTURES

YMP WBS: 1.2.3.2.8.4.1, Task SPT 38PM4 (FY97)

James N. Brune and Rasool Anooshehpoor

Seismological Laboratory, University of Nevada, Reno

ABSTRACT

We report results of foam-rubber modeling of the effect of a shallow weak layer on ground motion from strike-slip ruptures. Computer modeling of strong ground motion from strike-slip earthquakes has involved somewhat arbitrary assumptions about the nature of slip along the shallow part of the fault (e.g, fixing the slip to be zero along the upper 2 kilometers of the fault plane) in order to match certain strong motion accelerograms. Most modeling studies of earthquake strong ground motion have used what is termed kinematic dislocation modeling (e.g., studies reported at the Georgetown Conference). In kinematic modeling the time function for slip on the fault is prescribed, and the response of the layered medium is calculated. Unfortunately, there is no guarantee that the model and the prescribed slip are physically reasonable unless the true nature of the medium and its motions are known ahead of time.

There is good reason to believe that faults are weak along the upper few kilometers of the fault zone and may not be able to maintain high levels of shear strain required for high dynamic energy release during earthquakes. Physical models of faulting , as distinct from numerical or mathematical models, are guaranteed to obey static and dynamic mechanical laws. Foam-rubber modeling studies have been reported in a number of publications. The object of this report is to present results of physical modeling using a shallow weak layer, in order to verify the physical basis for assuming a long rise time and a reduced high frequency pulse for the slip on the shallow part of faults. It appears a 2 kilometer deep, weak zone along strike-slip faults could indeed reduce the high frequency energy radiated from shallow slip, and that this effect can best be represented by superimposing a small amplitude, short rise-time pulse at the onset of a much longer rise-time slip. A weak zone was modeled by inserting weak plastic layers of a few inches in thickness into the foam rubber model. The pulse observed in the model for the 3-inch layer has been reduced by a factor of 0.4 compared to the average value for the case with no weak zone; but because only one observation was available, this value is quite uncertain. For the 6-inch weak zone the average pulse is reduced by a factor of 0.46. The factor for the 8-inch case reduction is 0.11. For the 12-inch case it is 0.045. From these results we can see that, the thicker the weak layer, the more difficult it is for a short rise-time acceleration pulse to push its way through the weak layer to the surface. This is thus an approximate justification for reducing the high frequency radiation from shallower parts of strike-slip faults.

INTRODUCTION

Modeling of strong ground motion from strike-slip earthquakes has involved somewhat arbitrary assumptions about the nature of slip along the shallow part of the fault (e.g, studies reported at the Georgetown conference) in order to match certain strong motion accelerograms. It was realized that this was an ad-hoc and unsatisfactory situation from a physical point of view, since it is well known that the fault slip at the surface is commonly of the same magnitude as slip at depth.

It is generally accepted that the static normal and shear stresses along a vertical strike-slip fault must approach zero if the surface consists of incompetent sediments, because such materials could not maintain permanent stresses. Even in competent rocks the shear stresses in bore holes are commonly observed to approach zero near the surface in strike-slip faulting regimes. Since the shear stresses are related to the normal stresses by the coefficient of friction, μ, and since the weight of the overlying rocks approaches zero, the shear stresses held by rock weight should also approach zero. Of course if tectonic normal forces are present, then normal shear stresses near the surface in competent rocks could theoretically be quite high. However, in most developed fault zones the fault zone itself is a layer of relatively incompetent fault gouge, which would not be expected to be able to maintain large shear strains over inter-seismic time periods. Most measurements of shear stress in the Western United States show values at zero near the surface. Therefore there is good reason to believe that faults are weak along the upper few kilometers of the fault zone, and may not be able to maintain high levels of shear strain required for high dynamic energy release during earthquakes. This in turn might be the explanation for the presumed requirement to reduce dynamic slip along the shallow parts of faults in strong-motion modeling.

However, given the fact that the slip is known not to be zero, it seems that, rather than locking the fault at shallow depths, a more reasonable solution would be to decrease the fault slip velocity (lengthen the rise-time of the fault slip) , thus decreasing the amount of high frequency energy radiated, but allowing slow slip to continue to match the final fault offset.

The object of this report is to present results of physical modeling using a shallow weak layer, to verify the physical basis for assuming a long rise-time and a reduced high frequency pulse for the slip on the shallow part of faults.

Difficulties with Kinematic Dislocation Modeling

Most modeling studies of earthquake strong ground motion have used what is termed kinematic modeling (e.g., studies reported at the Georgetown Conference). In kinematic modeling the time function for slip on the fault is prescribed, and the response of the layered medium is calculated. Unfortunately, there is no guarantee that the model and the prescribed slip are physically reasonable unless the true nature of the medium and its motions are

known ahead of time. This situation is clearly impossible in the case of earthquakes, because the slip occurs at depths of many kilometers where the physical conditions are not known, and since there are no available dynamic solutions for the problem of actual fault motion. Kinematic models commonly involve non-physical singularities, or parameters for which appropriate values are unknown. Constraints must be determined by trial and error in order to be consistent with available data. Unfortunately, when the data base is limited, there may remain large uncertainties in choosing the range of values appropriate for various parameters; and thus there remain large uncertainties in the predicted values of ground motion.

RATIONALE FOR FOAM-RUBBER MODELING

Physical models of faulting , as distinct from numerical or mathematical models, are guaranteed to obey static and dynamic mechanical laws. Thus these models can be used to gain insight into the physical processes involved. Of course here are inherent problems of scaling and matching of physical conditions in laboratory physical models. Such models can nonetheless provide important constraints on numerical and theoretical models; for example, by modeling dynamic geometrical effects on fault slip.

Foam-rubber is very flexible; i.e., it has a low rigidity, making it is easy to produce large strains and particle motions. Since foam-rubber is light-weight, relatively large models can be constructed, enabling the scale of dynamic phenomena to be enlarged. This allows dynamic features to be more easily observed and recorded using relatively simple electronic devices, such as tiny accelerometers and position sensing devices. Foam-rubber models automatically assure that motions are physically realistic (no singularities or unreasonably specified slips). However, this does not guarantee that the motions will correspond to motions from actual earthquakes, because there are inherent difficulties with any laboratory size scale model of large-scale earth phenomena.

Great effort has been expended in rock mechanics laboratories to determine the properties of slip along interfaces between small blocks (centimeters to meters) of rock in hopes that these results could somehow be scaled up to the dimensions of rocks involved in real earthquakes (tens of kilometers or more). However, such scaling has never been justified in the literature. There are two dynamic scaling considerations not satisfied by ordinary rock mechanics experiments which are satisfied by the foam-rubber model. First, the stressing apparatus for the foam model has effectively infinite rigidity compared to the rigidity of the model, assuming that the dynamics of the model are not influenced by interaction with the stressing apparatus. We have verified this by placing a small accelerometer on the piston. No measurable motion of the piston (no interaction) was found at the time of a stick-slip event. Secondly, the overall dimensions of the foam model are large compared to the dimension of dynamic slip pulse which propagates along the interface between the two blocks. This allows the slip pulse to propagate predominantly under the influence of conditions local to the slip pulse itself, with minimized effects of the boundaries

of the model and the stressing apparatus. This obviously corresponds better to the conditions in the earth, for which the length of slip pulse is small compared to the dimensions of the fault (Heaton, 1990). This is not the case in rock mechanics experiments. (Foam-rubber has a Poisson's ratio of about 0.25, close to that for rocks, and thus satisfies one of the dimensionless scaling requirements, the ratio of P-wave to S-wave velocities.)

Some of the major limitations of foam-rubber modeling include:

1. Intrinsic Q is low (on the order of 10) and cannot be controlled. This constrains the usefulness of foam-rubber modeling to wave propagation distances which are not too large compared to the wavelengths involved. Thus it is most useful to gain insight into near-source phenomena. An ancillary advantage of the low Q is that there is relatively little energy scattered back from the model's distant sides, which could interfere with the dynamics.

2. The fault surface friction conditions are difficult to control. The lattice of foam-rubber vesicles produces extreme roughness on a small scale (scale of the order of a mm). The coefficient of friction is on the order of 10, whereas that for rocks is of the order of 0.5. Thus to produce fault slip, the strains must be very large, of the order of 10^{-2}, whereas in the earth the corresponding strains are of the order of 10^{-4}. As long as strains are approximately linear, the difference can be corrected for. However, in both the foam-rubber and the real earth, the fault behavior is probably not linear on the fault trace, and there is no guarantee that the non-linearities in the foam model correspond to those in the real earth. (A similar problem is common to kinematic modeling as well.)

Foam-rubber modeling studies have been reported in a number of publications (see references) with funding for these studies coming from EPRI, NSF, and USGS. We believe that foam-rubber modeling has been established as a useful tool for seismology; but the results must be interpreted with care and the inherent limitations kept in mind (of course this is true for any type of modeling).

DESCRIPTION OF MODEL

The model consists of two large blocks of foam rubber (1m x 2m x 2.5m), one driven horizontally over the other by a hydraulic piston (Fig. 1). The lower block is securely glued to a plywood sheet which is in turn anchored to the concrete floor. The upper block and the attached rigid frame are supported by four steel pipes equipped with scaffolding jacks and guiding rollers at each corner. Thin sheets of plywood are glued to the front and the back of each block. These sheet are free to rotate about the hinges connecting them to the two horizontal plywood sheets attached to the top of the upper block and the bottom of the lower

block. When the model is under shear force, these sheets prevent the foam blocks from tearing off the horizontal plywood plates.

Normal force at the contact (fault) is provided by the weight of the upper block (650 lbs) and is varied by lowering or raising the jacks. Normal force is measured by subtracting the force exerted on the jacks from the total weight of the upper block. Shear force is provided by a hydraulic piston that is placed between a concrete wall and the upper block's frame; the rollers guiding the moving block ensure a pure shear motion.

As the upper block is forced to slide over the lower block, the strain in the blocks increases until the stress at the interface exceeds the frictional resistance and a stick-slip event occurs over the whole boundary (fault plane). These major events correspond to "characteristic" events for the system, analogous to "characteristic earthquakes" in the earth. Successive "characteristic" events usually cause about the same amount of average slip (1 cm) between the blocks; but the pattern of slip can vary markedly, with the rupture initiating at different points and propagating in different directions. If the driving displacement is steady, the characteristic events repeat more or less regularly until the upper block has slipped about 30 centimeters, corresponding to about 30 characteristic events with some additional smaller events. At this point, the hydraulic piston is fully extended and one experimental run is complete. The stress is removed and the upper block lifted and moved back to the starting position for repeat of the procedure.

INSTRUMENTATION

Position-sensing Detectors

Displacement at the foam surface is measured by a telescopic, 2-axis, position-sensing detector, which is focused on a small light emitting diode (LED) embedded in the foam. The Dual Axis Super Linear Position Sensor (DLS10, manufactured by the United Detector Technology Sensors, Inc.), is a square of photovoltaic material, 1cm on a side. The sensor locates the centroid of a light spot (image of the embedded LED) projected upon it, and provides continuous output as the light spot moves from the null point to either direction along each of the two perpendicular axes. The output of the position-sensing detector depends on the location as well as the intensity of the bright spot. Therefore, it is necessary to calibrate each detector before and after each experimental run. (The position detectors have a built-in calibrating mechanism.) The resolution of the DLS10 sensors is limited only by the intensity of the light source and the signal resolving circuitry. In our experiments, the resolution is better than 0.01centimeter.

Ultra-Light Accelerometers

Due to foam rubber's low density and high elasticity, particle accelerations in a stressed foam rubber model of earthquakes can exceed several hundred g (the acceleration due to gravity). Slips of the order of 1 centimeter can take place in a few milliseconds, resulting in very large accelerations at high frequencies. In order to measure these accelerations, accelerometers with a high dynamic range and low mass (to minimize the mass loading effects) are needed. We have 16 state-of-the-art, ultra-light ENDEVCO Model 25A accelerometers. The Model 25A, with a mass of 0.2 gm and a dynamic range of +/- 1000 g, is the world's smallest piezoelectric accelerometer. In order to further reduce the mass loading effects, each accelerometer is mounted on a 1.5-inch styrofoam disk before inserting them in the foam; the 1/8-inch thick styrofam disk (with the same density as the foam rubber used in the model, but far more rigid) distributes the accelerometer's mass over a much larger area (about 50 times larger).

Data Acquisition System

The data acquisition system consists of a 486 PC with a state-of-the-art 330 kHz analog-to-digital board (DAP 1200e/6 manufactured by Microstar Laboratories). Particle motions during stick-slip events at 16 sites were digitized at the rate of 5000 samples-per-second and recorded on the PC.

CALIBRATION

Since the response of the sensors differ slightly, each position detector and accelerometer is calibrated prior to experiments to correct for the difference in the instrument response. Position detectors have a built-in calibrating mechanism, which moves the image of the LED (embedded in the model at a site that the particle displacement is to be measured) a known amount on the position sensor by moving the entire detector relative to the stationary LED along either of the two orthogonal axes. The change in the detector's output voltage corresponding to the known displacement is digitally recorded on the PC and used to normalize the response of all detectors to a pre-defined value (1920 counts/mm).

Each ENDEVCO Model 25A accelerometer comes with the manufacturer's calibration data sheet which is traceable to the National Institute of Standards and Technology. However, we calibrate each accelerometer by subjecting it to a sinusoidal motion and recording the harmonic accelerations and displacements (using the position detector) simultaneously on the digital data acquisition system. The accelerometer's response (in counts/g) is then determined by calculating the peak-to-peak input acceleration amplitude from the measured peak-to-peak displacement and angular frequency of the input motion.

EXPERIMENTAL PROCEDURES

In this study, we are modeling strike slip motion, so the motion sensors are installed along the right side of the interface looking from the piston in the direction of motion of the upper block (in effect the model is like a strike-slip fault rotated 90 degrees on its side). We had verified in previous experiments that the particle motions are approximately symmetrical on opposite sides of the fault in the model with no plastic strip inserted. Thus we assumed that the main features of the distribution of particle motion could be determined by recording on only one side of the fault.

Figure 2 shows the location of fourteen miniature accelerometers that are embedded in the lower block (indicated by numbers 1-13, and 15) and one in the upper block (number 14) near the fault surface. Accelerometer 14 in the upper block is approximately located above accelerometer 15 in the lower block (the relative position changes by about +/- 10 centimeters as the upper block is pushed over the lower one). A light emitting diode inserted at site 16 (on the surface) is used to monitor the slip during each stick-slip event and cross check the accuracy of double-integration process in calculating displacements from accelerations. Sensors at all 16 sites measure particle motions on the fault plane parallel to the direction of external shear force (provided by the hydraulic piston).

In order to determine the effect of a shallow weak layer we carried out several experiments with a strip of low-friction plastic of different widths inserted along the edge of the model (corresponding to the surface of the earth). The measured quasi-static friction of the plastic is about 0.17 of the rupture strength of the foam block interface. The thicknesses of the strips were 0 (no strip), 3 in., 6 in., 8 in., and 12 in. (Fig. 2). We perturbed the stresses in the model to cause nucleation of the rupture to occur at depth, and thus caused the rupture front to arrive at the surface with a steep angle of incidence, as is typical of actual strike-slip earthquakes.

DATA

Appendix B gives playouts of the accelerations for channels 1-15, and displacement for channel 16 (LED) for numerous events. The main variable is thickness of the weak layer (plastic strip). In order to make clear the effect of the shallow weak layer, we recorded rupture events with and without the plastic strip inserted.

In order to illustrate the general features of the seismograms in the appendix, we show examples typical of each of five configurations: no weak layer (no plastic strip), and four widths of weak layer (3in. ,6in., 8in., and 12 in.), (Figs. 3-7).

Long Rise-Time Slip

In all of the cases with weak layers, even though the peak accelerations were greatly reduced by the weak layer, the total slip was not. This can easily be seen by comparing the total slips shown on the LED, channel 16, for the cases with and without the weak zones. We have also confirmed this fact by integrating the accelerometer channels to get fault displacement. Thus the shallow weak layer reduces the amplitude of the short rise-time pulse, but not the overall slip, which is accomplished by long rise-time slip. Typical rise-times of the displacement time functions shown in the figures are about 50 milliseconds. In general, there is also a small high velocity pulse near the beginning of the ramp, the pulse amplitude depending on the thickness of the weak layer.

Short Rise-time Pulse Propagating Through The Weak Layer

In most cases with a shallow weak zone, a short rise-time pulse propagates through the weak zone and arrives at the surface, but with reduced amplitude compared to the case with no weak zone. This is illustrated in Figs. 3-7. In order to determine the average effect of the shallow weak layer, we have averaged the accelerations for each case and shown the results in Fig. 8. (We only had one example for the 3-inch layer, so the individual result represents the average). Since the average amplitude of the dislocation at depth varied for each of theses cases, in Figure 9 we show the curves in Figure 8 normalized to the amplitude interpolated for a position half way between sensor 1 and sensor 2.

From the results in Figure 9 we see that the pulse observed for the 3-inch layer has been reduced by a factor of 0.4 over the average value for the case with no weak zone; but because only one observation was available, this value is quite uncertain. For the 6-inch weak zone the average pulse is reduced by a factor of 0.46. The factor for the 8-inch case reduction is 0.11. For the 12-inch case it is 0.045. From these results we see that, the thicker the weak layer, the more difficult it is for a short rise-time acceleration pulse to push its way through the weak layer to the surface.

ANALYSIS

It is clear from the results above that the effect of the shallow weak layer (strip of plastic) is in all cases to reduce the surface acceleration at the surface site 15 relative to the acceleration observed there with no weak layer (and also relative to the accelerations occurring deeper in the model, corresponding to accelerations deeper in the earth). However, in most cases, a small, short rise-time pulse propagates through the weak zone and reaches the surface, although with much reduced amplitude compared to the case without a weak shear zone. If the results above are applicable to real earth situations, kinematic modeling of ground motion using classical dislocation theory should apply some adjustment of the fault slip time function

on the shallow part of the fault. In order to apply these results to the real earth, we must consider the typical ratios of the wavelengths involved to the thickness of the weak layer, as well as other factors which might qualify the results.

The physical reason that the shallow weak zone reduces the surface ground accelerations near the fault is that energy is taken out of the dislocation pulse as it propagates through the weak near-surface zone. This is because this zone has no stored up energy to replace the energy lost by damping and high velocity sliding friction. It is certain that, in many cases in the real earth, a similar situation occurs, especially where there is a thick and deep weak zone of fault gouge near the surface, or a thick layer of incompetent sediments which cannot store long term stresses. To scale these results to the real earth, the critical parameter is the ratio of the wavelength, λ, of the energy involved to the thickness, h, of the weak layer. In the model, the predominant period of the peak pulse of energy reaching the surface for the case of no weak layer is about 10 milliseconds. Multiplying by the typical shear wave velocity, 30m/sec., we estimate a predominant wavelength of about 30 centimeters. In the case of the 3-inch (7.5 cm) weak layer, the high frequency pulse for deep nucleation was observed at the surface, reduced by a factor of 0.46, whereas only very much weaker pulses were observed for the thicker weak layers (6 in., 8in., and 12 in.; 15 cm, 20 cm, and 30 cm). A 1-inch (2.5 cm) layer would have been essentially ineffective in damping out the sharp acceleration pulse. The critical ratio of λ/h for transition of effectiveness in damping out the sharp acceleration pulse is about 30cm/20cm $\approx$1.5. In the real earth, peak accelerations are typically caused by energy of about 5 Hz. If the surface velocities are about 3 km/sec, this corresponds to wavelengths of about 600 meters. Thus a weak layer of about 900 meters would be expected to significantly reduce 5 Hz energy. For 2.5 Hz energy, the corresponding thickness would be 1.8 kilometers, close to the value suggested by some studies of strong ground motion (about 2 kilometers).

Another factor important in scaling is the ratio of the wavelength of the energy involved to the dimension of the dislocation pulse at depth traveling up the fault plane, the so-called Heaton pulse (Heaton, 1990). In previous studies of foam-rubber modeling we have found that the dimension of the dislocation pulse; i.e., the distance between the leading edge of the rupture and the following edge (locking edge) is about 10 centimeters. (This seems to be primarily controlled by the characteristic roughtness dimension of the interface, in the case of foam-rubber, about one (1) millimeter.) In the real earth, Heaton (1990) has estimated that the typical dislocation width is about 1-5 kilometers (rise-times of about 0.3 to 2.0 seconds). Thus a wavelength of about 2 kilometers (about 1 Hz) in the earth corresponds to about 10 centimeters in the foam model. The shear wave velocity in the foam-rubber is about 35m/sec, so that 10 centimeters corresponds to periods of about 3 ms. The acceleration pulses have energy of this frequency and lower. Similar dynamic geometrical effects should apply to higher frequencies also, if they had been present in the upcoming pulse.

Thus it appears a shallow weak zone along strike-slip faults could indeed reduce the high frequency energy radiated from shallow slip. This effect can best be represented by superimposing a small amplitude, short rise-time pulse at the onset of a much longer rise-time

slip. The average rise-times can be estimated from the LED displacement sensor plots in each figure. The average rise-times are about 3-5 times longer for the 6-12 inch strips, compared to the case for no weak layer. This is thus an approximate justification for increasing the rise-time in modeling the radiation from shallower parts of strike-slip faults.

CONCLUSIONS

Results of foam-rubber modeling of the effect of a shallow weak layer on ground motion from strike-slip ruptures indicate a strong damping of the surface acceleration by such a weak layer. Since modeling of ground motion from strike-slip earthquakes has involved somewhat arbitrary assumptions about the nature of slip along the shallow part of the fault (e.g., studies reported at the Georgetown Conference), there is need for a physical basis to constrain the parameterization. There is good reason to believe that faults are weak along the upper few km of the fault zone, and the physical consequences of this need to be better understood. Results presented here give a physical basis for assuming a long rise-time and a reduced high frequency pulse for the slip on the shallow part of faults. The acceleration pulses observed at the surface are reduced by factors of (0.4), 0.46, 0.11, and 0.045 for the 3-inch, 6-inch, 8-inch, and 12-inch cases, respectively. From these results we can see that, the thicker the weak layer, the more difficult it is for a short rise-time acceleration pulse to push its way through the weak layer to the surface. It appears that this effect can best be represented by superimposing a small amplitude, short rise-time pulse at the onset of a much longer rise-time slip. These results give an physical justification for reducing the high frequency radiation from shallower parts of strike-slip faults.

FIGURE CAPTIONS

Figure 1 Diagram of foam-rubber model setup for testing the effect of shallow weak layers on strike-slip motion. Dimensions and description are given in the test.

Figure 2 Diagram showing setup for sensors in the strike-slip, weak layer, model.

Figure 3 Acceleration records for the case of strike-slip motion with no shallow weak layer(no plastic strip).

Figure 4 Acceleration records for the case of strike-slip motion with a 3-inch shallow weak layer(plastic strip).

Figure 5 Acceleration records for the case of strike-slip motion with a 6-inch shallow weak layer(plastic strip).

Figure 6 Acceleration records for the case of strike-slip motion with a 8-inch shallow weak layer(plastic strip).

Figure 7 Acceleration records for the case of strike-slip motion with a 12-inch shallow weak layer(plastic strip).

Figure 8 Plot of approximate average acceleration as a function of sensor position between sensor 1(deepest) and sensor 15 (surface) for the cases of no shallow weak layer, and 3-inch, 6-inch, 8-inch, and 12-inch weak layers(plastic strips), respectively.

Figure 9 Plot of normalized average acceleration as a function of sensor position between sensor 1(deepest) and sensor 15 (surface) for the cases of no shallow weak layer, and 3-inch, 6-inch, 8-inch, and 12-inch weak layers(plastic strips), respectively. Curves are normalized to the average acceleration of sensors 1 and 2 at a point halfway between them.

Appendix A

Figure A 1-5 Plots of acceleration as a function of sensor position between sensor 1(deepest) and sensor 15 (surface) for the cases of no shallow weak layer, and 3-inch, 6-inch, 8-inch, and 12-inch weak layers(plastic strips), respectively.

Appendix B

Figure B 1-25 Plots of acceleration for all sensor locations for various thicknesses of weak layer: 0(no weak layer), 3 inches, 6 inches, 8 inches, and 12 inches. The first number in the identification of each figure gives the thickness of the weak layer.

REFERENCES

Anooshehpoor, A., and J.N. Brune (1989): Foam rubber modeling of topographic and dam interaction effects at Pacoima Dam. Bull. Seis. Soc. Amer., 79, 1347-1360.

Anooshehpoor, A. And J.N. Brune (1994): Frictional Heat Generation and Seismic Radiation in a Foam Rubber Model of Earthquakes. PAGEOPH 142(3/4), 735-747.

Archeluta, R.J., and J.N. Brune (1975): Surface strong motion associated with a stick-slip event in a foam rubber model of earthquakes. Bull. Seis. Soc. Amer., 65(5), 1059-1071.

Brune, J.N. (1996): Dynamic wave effects on particle motions in thrust, normal and strike-slip faulting. AGU Fall 1996 Meeting, EOS, Transactions, 77(46), November 12, 1996, S31B6, F505.

Brune, J.N. (1973): Earthquake modeling by stick-slip along pre-cut surfaces in stressed foam rubber. Bull. Seis. Soc. Amer., 63, 2105-2119.

Brune, J.N. (1996): Particle motions in a physical model of shallow angle thrust faulting. Proceedings of the Indian Academy of Science, 105(2), 1-10.

Brune, J.N., and R. Anooshehpoor (1991): Foam rubber modeling of the El Centro terminal substation building. EERI: Earthquake Spectra, 7, 45-79.

Brune, J.N., and R. Anooshehpoor (1991): Foam rubber modeling of the Lotung large-scale seismic experiment. EERI: Earthquake Spectra, 7, 165-178.

Brune, J.N., R. Anooshehpoor, and R.H. Loveberg (1988): Foam rubber modeling of soil-structure interaction. Proceedings of the Earthquake Engineering and Soil Dynamics Conference 2. Sponsored by the American Society of Engineers Geotechnical Engineering Division, June 17-30, 1988, 218-232.

Brune, J.N., S. Brown, and P.A. Johnson (1993): Rupture mechanism and interface separation in foam rubber models of earthquakes: a possible solution to the heat flow paradox and the paradox of large overthrusts. Tectonophysics, 218, 59-67.

Brune, J.N., P.A. Johnson, and C. Slater (1990): Nucleation, Predictability, and Rupture Mechanism in Foam Rubber Models of Earthquakes. Journal of Himalayan Geology, 1(2), 155-166.

Hartzell, S.H., G.A. Frazier, and J.N. Brune (1978): Earthquake modeling in a homogenous half-space. Bull. Seis. Soc. Amer., 68, 301-306.

Heaton, T.H. (1990): Evidence for and implications of self-healing pulses of slip in earthquake rupture. Physics of the Earth and Planetary Interiors, 64, 1-20.

King, J.L., and J.N. Brune (1981): Modeling the seismic response of sedimentary basins. Bull. Seis. Soc. Amer., 71, 1469-1487.

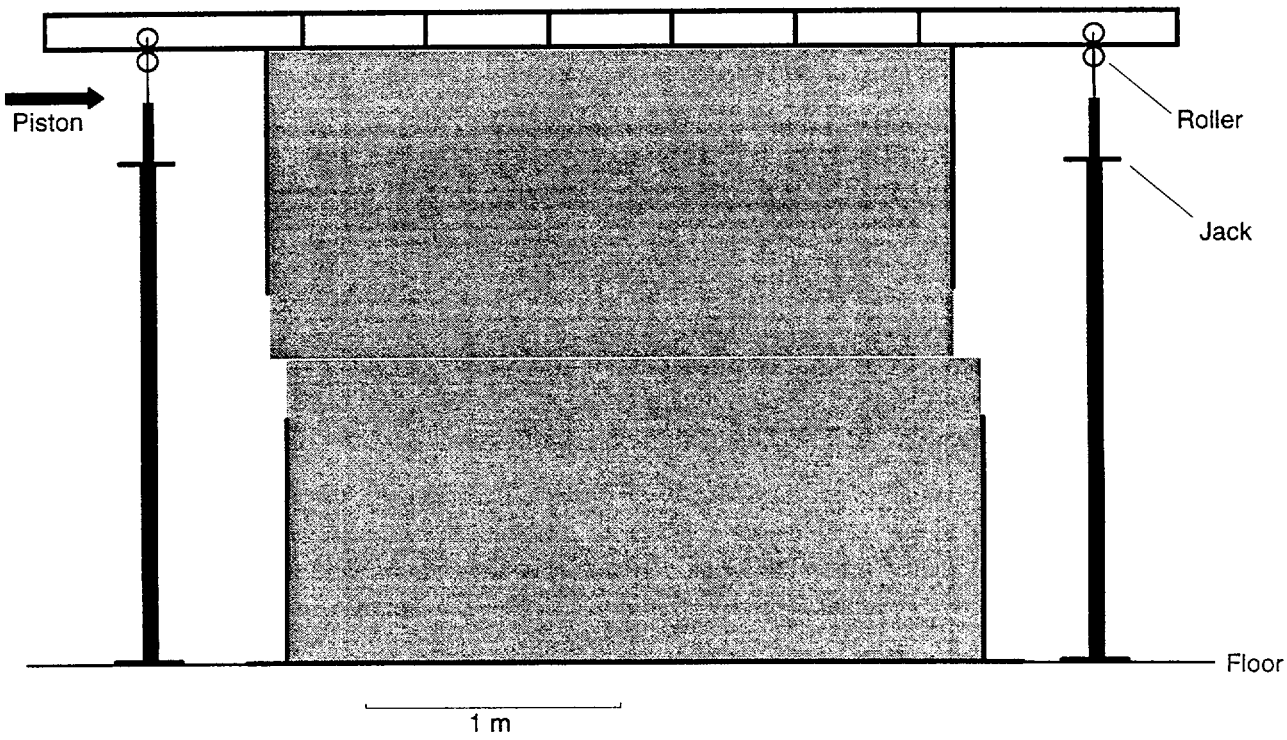

Figure 1

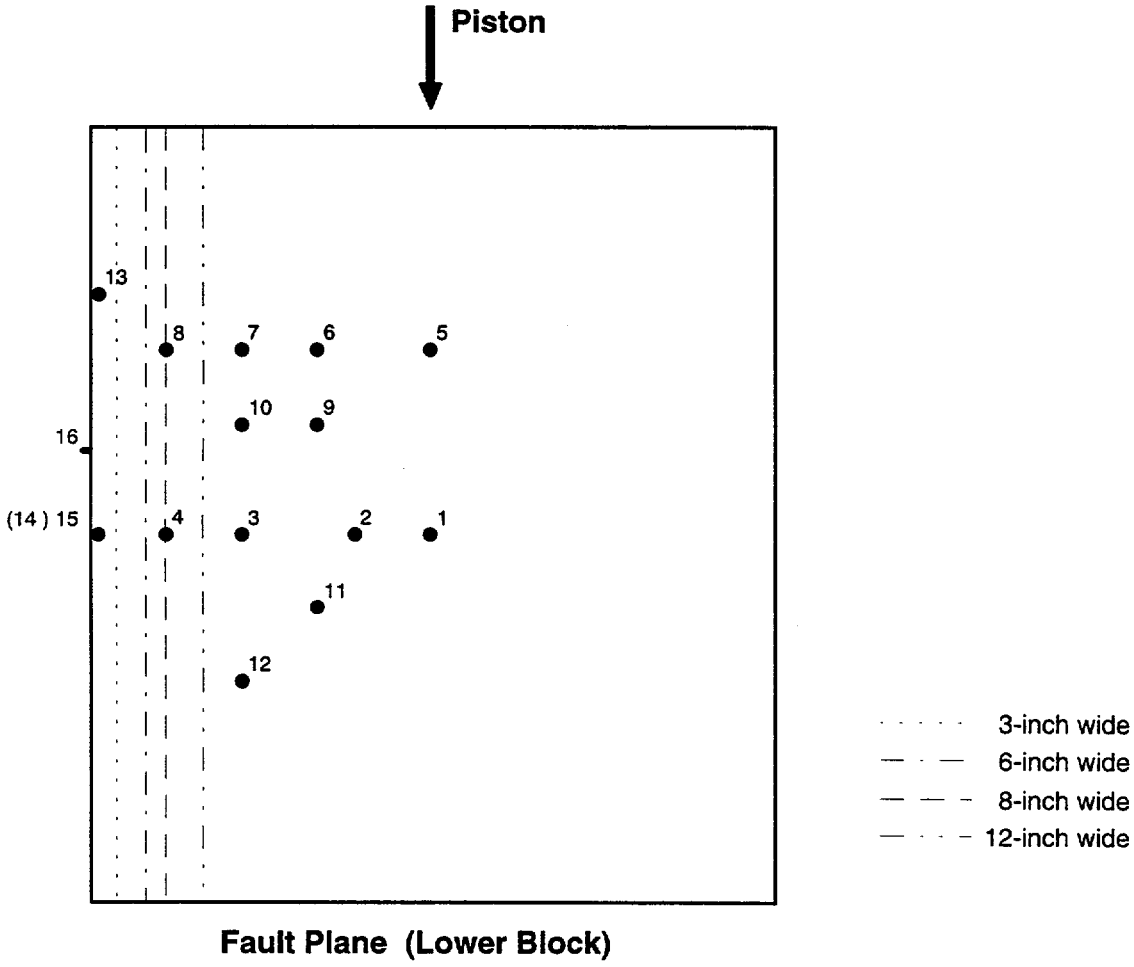
Piston
13
8
7
6
5
10
9
16
(14) 15
4
3
2
1
11
12
3-inch wide
6-inch wide
8-inch wide
12-inch wide
Fault Plane (Lower Block)

Figure 2

No Plastic Strip

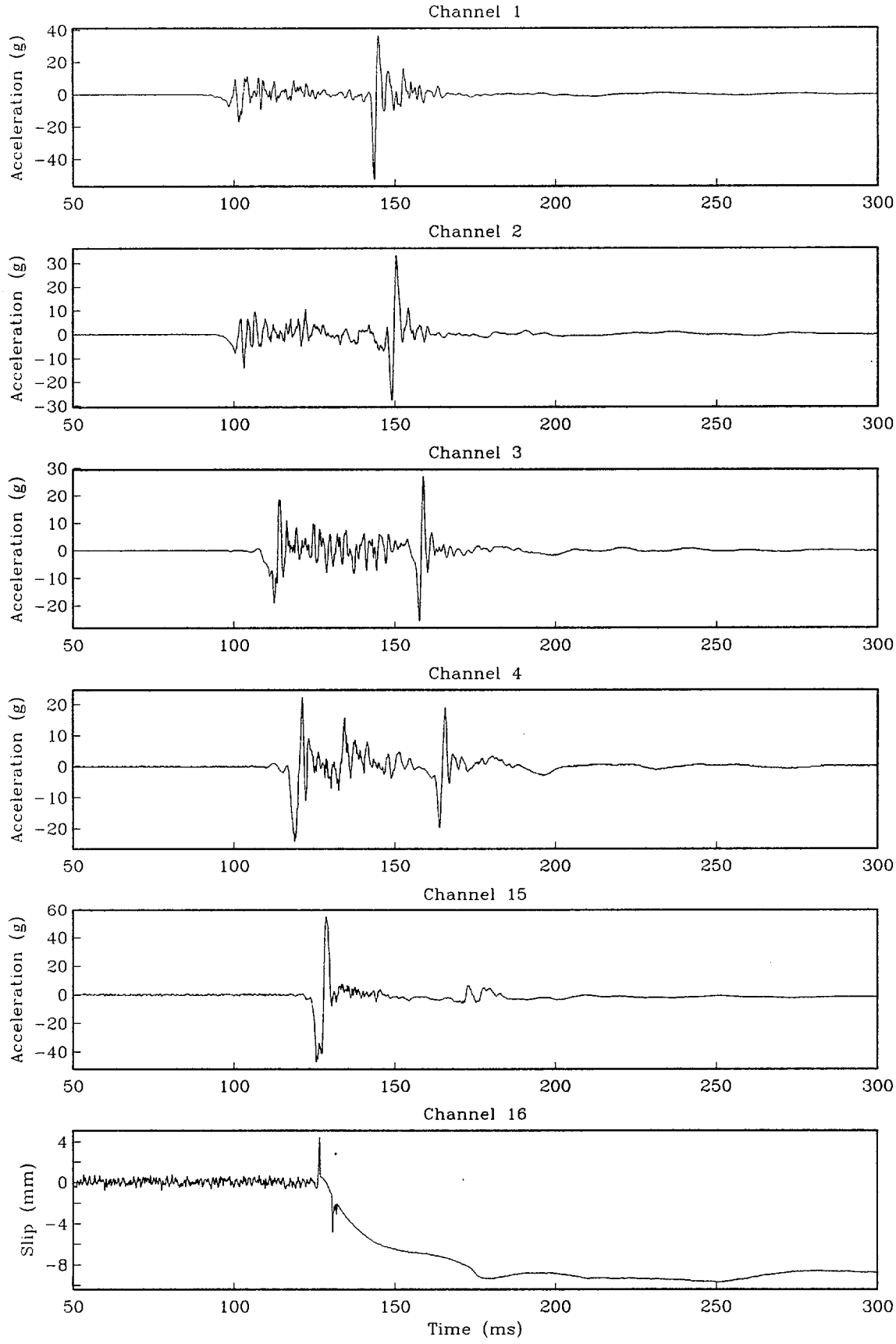

Figure 3

3-inch Wide Plastic Strip

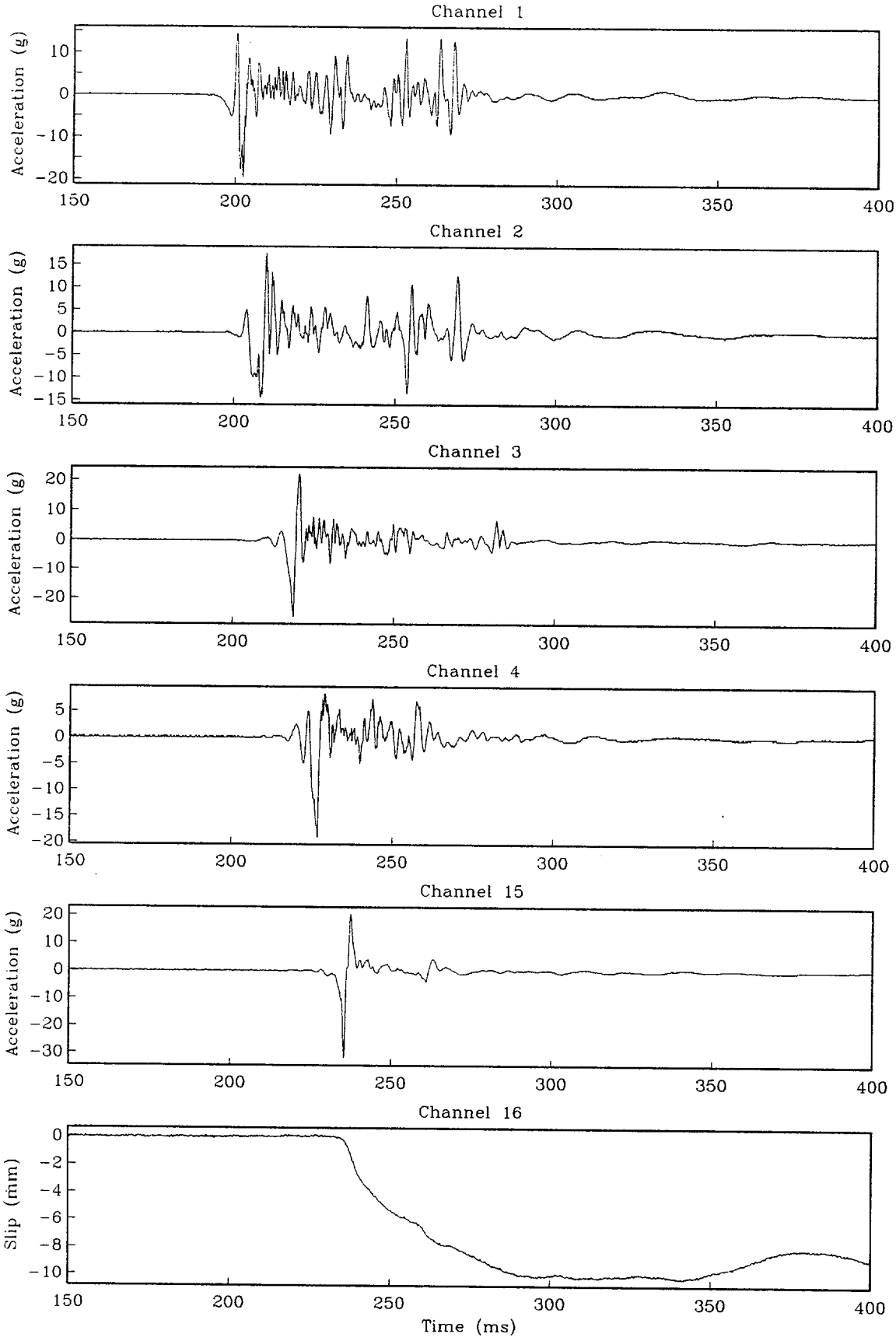

Figure 4

6-inch Wide Plastic Strip

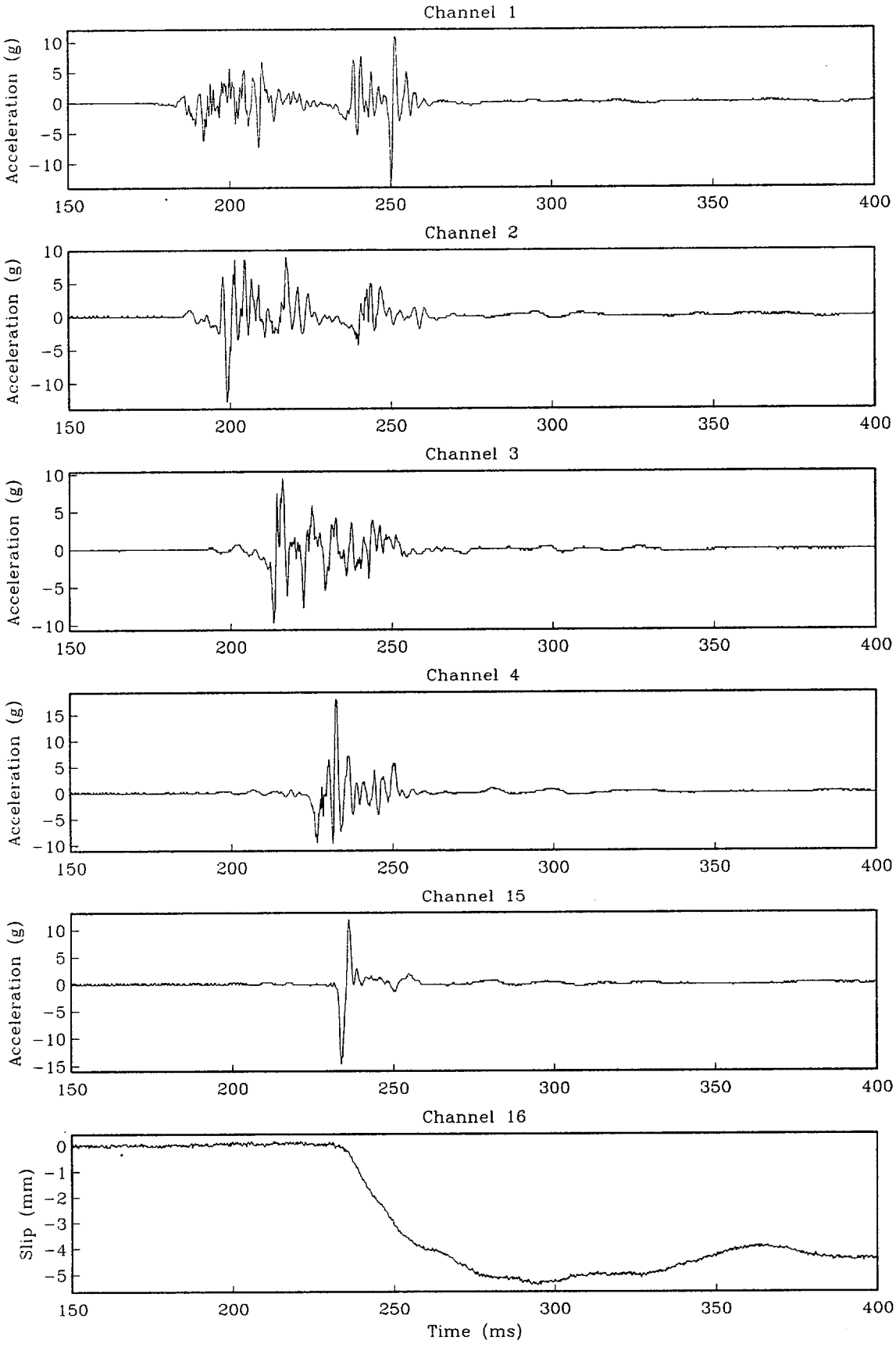

Figure 5

8-inch Wide Plastic Strip

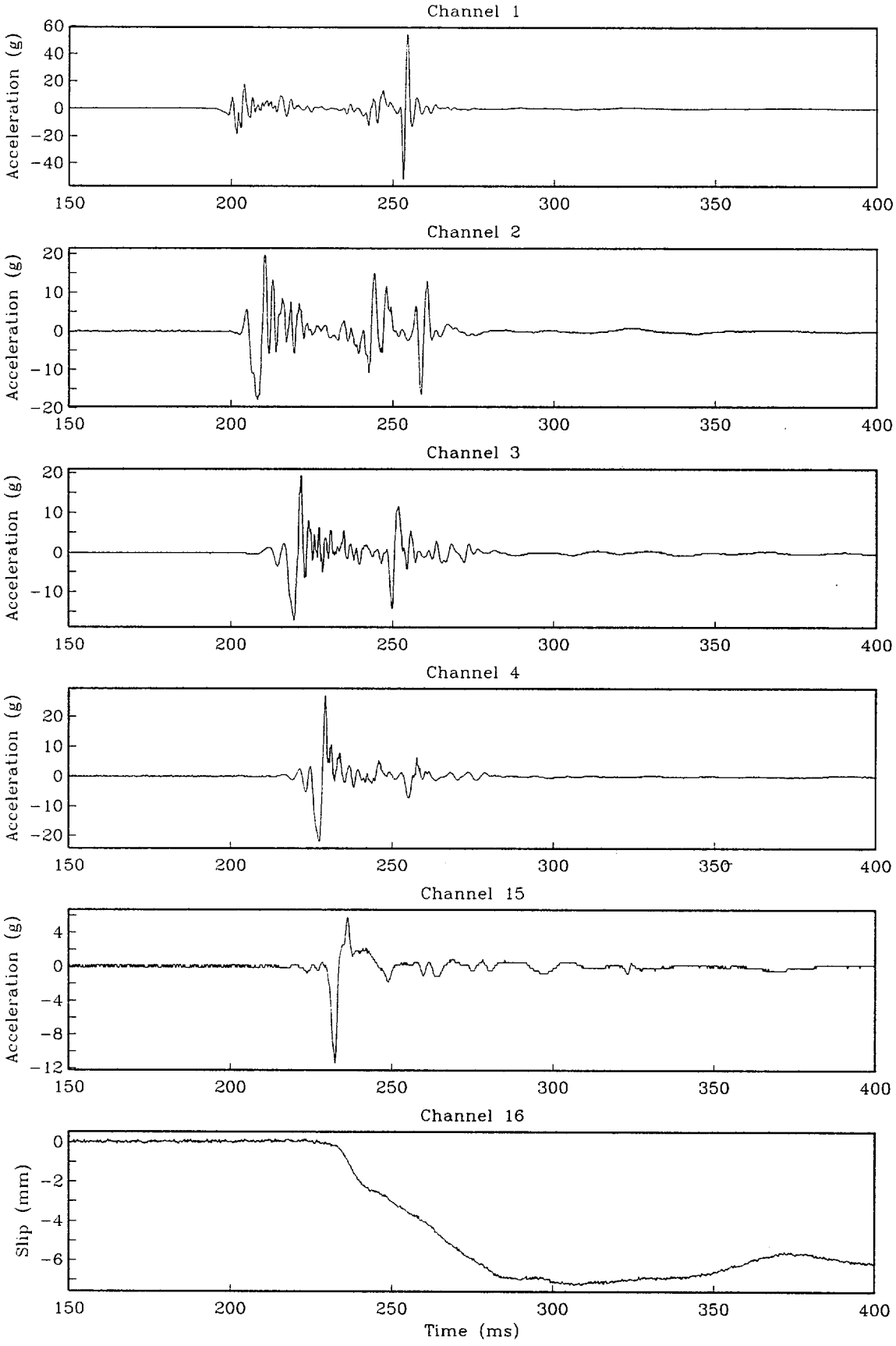

Figure 6

12-inch Wide Plastic Strip

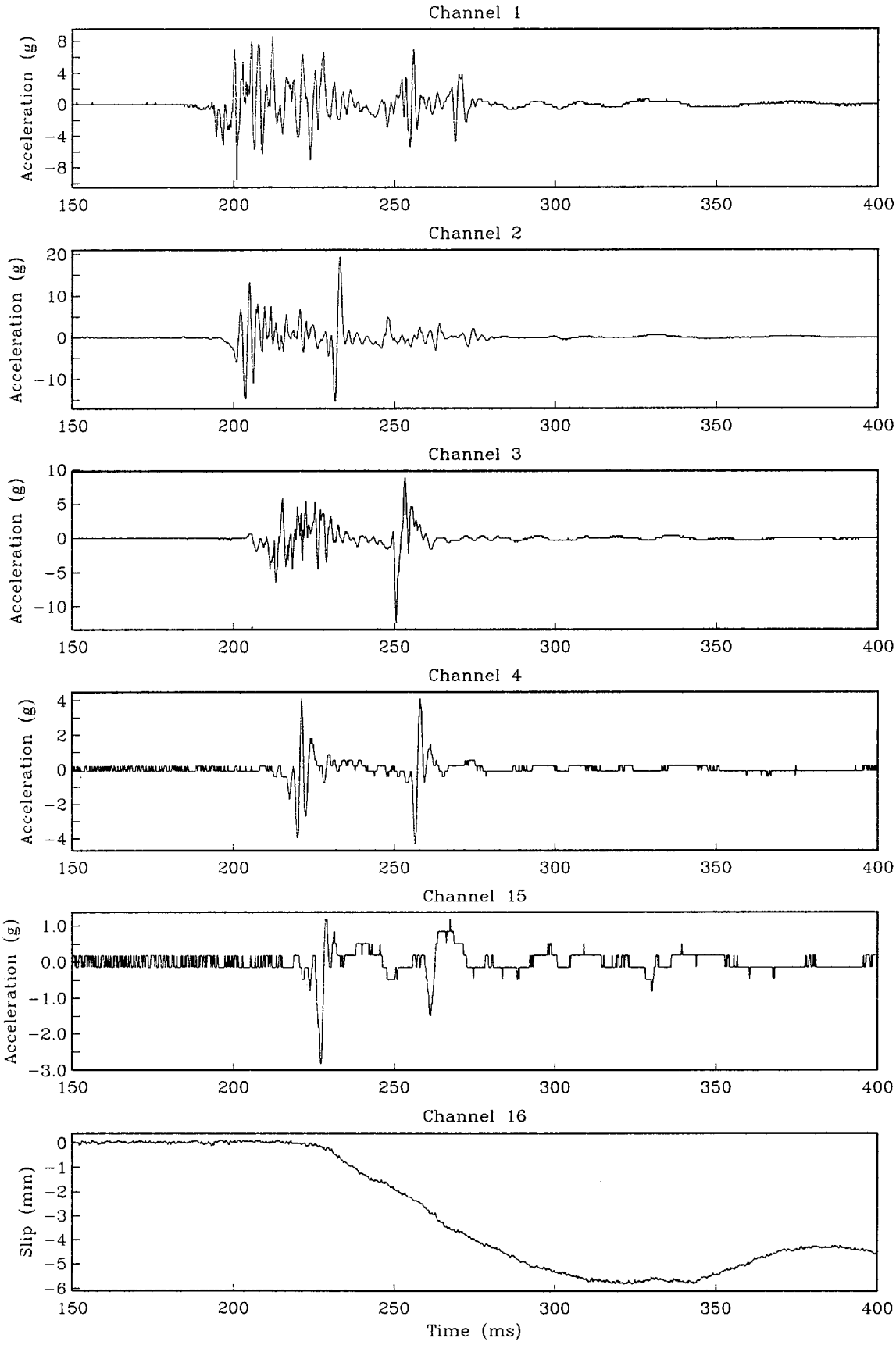

Figure 7

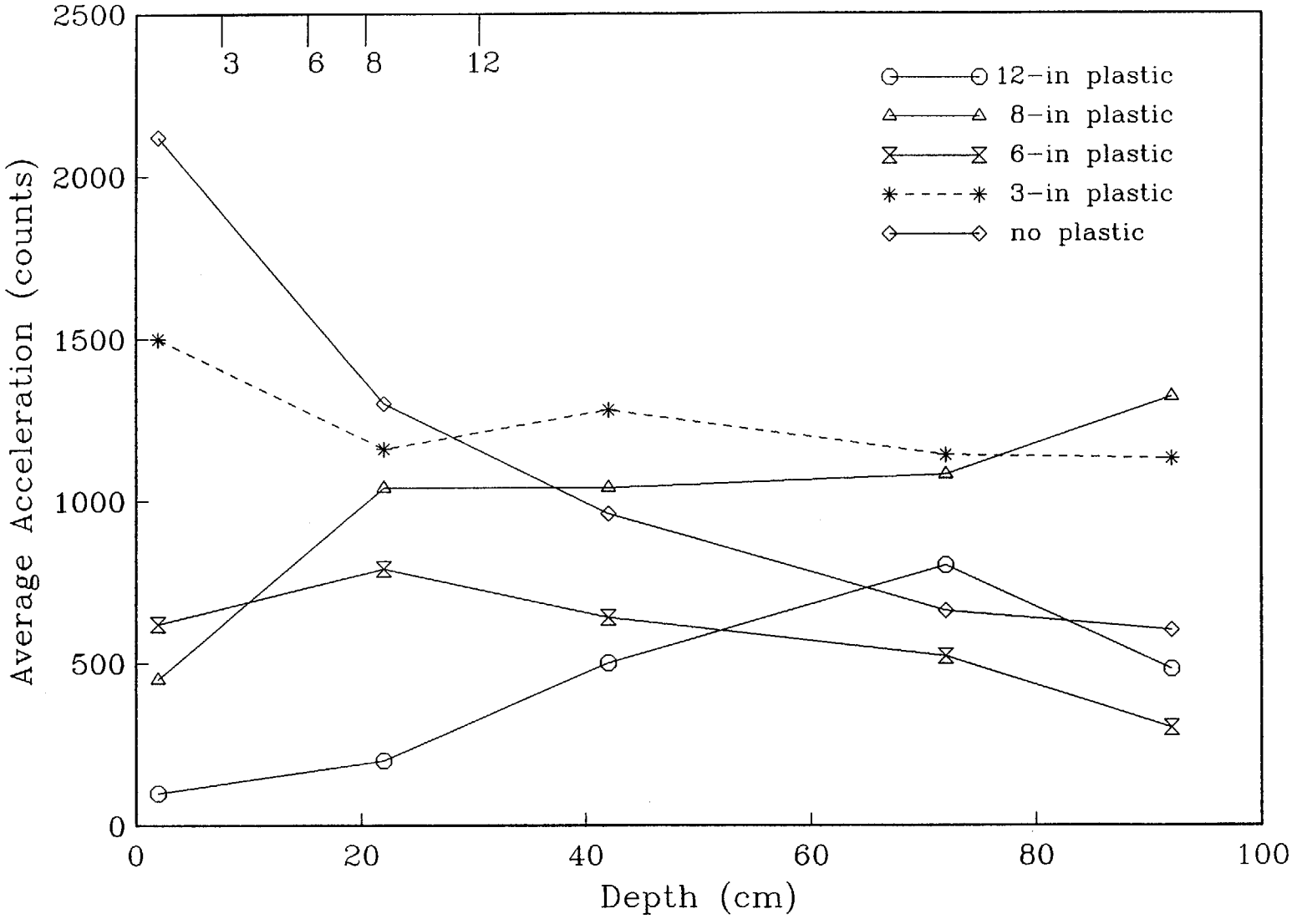
2500
2000
1500
1000
500
0
3
6
8
12
Average Acceleration (counts)
0
20
40
60
80
100
Depth (cm)
12-in plastic
8-in plastic
6-in plastic
3-in plastic
no plastic

Figure 8

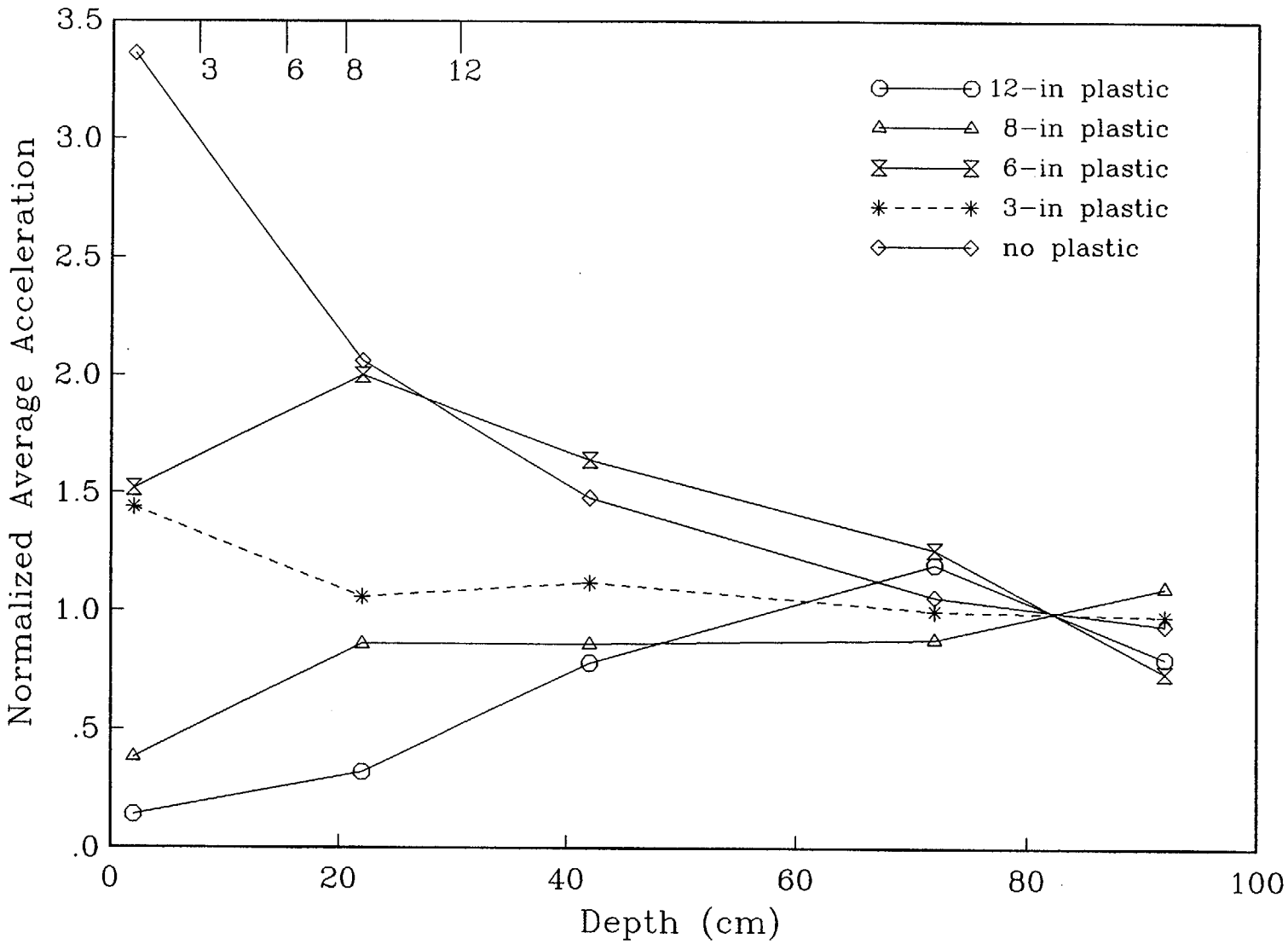
3.5
3.0
2.5
2.0
1.5
1.0
.5
.0
Normalized Average Acceleration
3
6
8
12
12-in plastic
8-in plastic
6-in plastic
3-in plastic
no plastic
0
20
40
60
80
100
Depth (cm)

Figure 9

Dynamic Wave Effects on Particle Motions in Thrust, Normal and Strike Slip Faulting

James N Brune (Seismological Laboratory, University of Nevada-Reno, Reno, NV 89554; (702) 784-4974; email: brune@seismo.unr.edu)

Dynamic wave effects generated by the faulting process can destroy the plane symmetry often assumed in models of faulting. In the idealized symmetric models there are no fault-normal stresses propagated ahead of the rupture front. However, on actual faults a number of effects can destroy this symmetry and cause fault-normal stresses ahead of the rupture front, with consequent fault rupture and particle motions deviating significantly from the idealized models.

In strike-slip ruptures, fault-normal stresses ahead of the rupture front can be caused by differences in material properties on the two sides of the fault (Weertman waves), asperity impact during fault slip, or Riedel shears in the zone of fault gouge. The tensile stresses propagated ahead of the rupture front by Riedel shears are approximated by the formula: $\sigma_t = 0.1\ (r^2/R^2)\ \sigma$, where σ_t is the tensile stress, R is the distance along the fault ahead of the Riedel shear, and r and σ the radius and stress-drop of the Riedel shear. Depending on the fault failure conditions, fault-normal stresses can radically alter the rupture propagation and particle motions.

In shallow angle thrust faulting, a dislocation starting at the heel of the hanging-wall wedge sends a compressional wave upward and forward in the hanging-wall plate, which changes polarity upon reflection at the free surface, and then impinges on the fault plane as a tensile wave, reducing the normal stress and destabilizing the fault, thus altering the dynamics and particle motions. In a foam rubber model of shallow angle (25deg.) thrust faulting, interface waves associated with fault opening are reinforced by the reflected wave, decoupling the overlying hanging-wall plate from the foot-wall plate, thus trapping energy in the hanging-wall wedge and resulting in a spectacular increase in particle motions at the fault tip (Brune, SRL, V 67, No. 2, 1996; Proc. Indian Acad. Sci. (Earth Planet. Sci.), V. 105, No. 2, June 1996, pp. L197-L206).

In shallow angle normal faulting, a dislocation at the heel of the hanging-wall wedge sends a dilatational wave upward and forward in the hanging-wall wedge, which changes polarity upon reflection at the free surface, and then impinges on the fault as a compressional wave, which stabilizes the fault. A foam rubber model of a shallow angle (25 deg.) normal fault dramatically illustrates the differences between normal faulting and thrust faulting. The shallow angle normal faulting is accomplished by numerous small dislocations which have very weak ground motion at the hanging-wall fault tip.

Although the strong motion data set for ground motions near the outcrop of large normal and thrust earthquakes is very limited, it appears to be consistent with these dynamic effects being operative in some large earthquakes. If so, they may have drastic effects on the resulting near-source ground motions and on estimates of seismic hazard, with surface intersecting thrust faults being more dangerous, and surface intersecting normal faults less dangerous.

Brune, J. N. (1996): Dynamic Wave Effects on Particle Motions in Thrust, Normal and Strike-Slip Faulting, AGU Fall 1996 Meeting, EOS, Transactions, Vol. 77, No. 46, November 12, 1996.